University of California
Santa Barbara

Instrumentation and Method Development for Efficient DNP in Electron Spin-Spin Coupled Systems.

A dissertation submitted in partial satisfaction
of the requirements for the degree

Doctor of Philosophy
in
Chemistry

by

Kan Allan Tagami

Committee in charge:

Professor Songi Han, Chair
Professor Bernard Kirtman
Professor Raphaële Clement
Professor Mark Sherwin

June 2022

The Dissertation of Kan Allan Tagami is approved.

Professor Bernard Kirtman

Professor Raphaële Clement

Professor Mark Sherwin

Professor Songi Han, Committee Chair

June 2022

Instrumentation and Method Development for Efficient DNP in Electron Spin-Spin Coupled Systems.

by

Kan Allan Tagami

Acknowledgements

Grad school was one of the hardest things I have ever done, and I certainly could not have done it alone. I am incredibly grateful to all the mentors that I had along the way including all the postdocs and fellow grad students in the Han lab. I'd like to thank Asif Equbal for being an incredible teacher, friend, and collaborator who taught me almost everything I know about DNP theory, and constantly challenged me to understand more about magnetic resonance in general. I wouldn't have gotten through my first year of grad school if it wasn't for Alisa Leavesly, Alicia Lund, and Ilia Kaminker offering their invaluable help showing me the ropes of high field DNP instrumentation and generally getting started in the lab. My gratitude also goes out to Sheetal Jain and Miranda Li for their incredibly useful discussions on magnetic resonance and for being great lab-mates and friends. I know I'm missing people here so I'd also like to thank all the members of the Han lab that I got the chance to work with over the years, their friendship and support made grad school possible for me. Finally, I am beyond grateful to Songi Han herself for being the best possible advisor I could have hoped for. I know I was never the best communicator but you always supported and encouraged me, and allowed to to really explore the areas of DNP that truly interested me.

Next, I would like to thank some of our outside collaborators who really helped me along the way as well. From Revolution NMR I would like to thank David and Ed who always put up with my naive questions about our MAS NMR probes. I also need to thank Toby Zens who taught me so much about NMR probes and basically got me a job out of grad school. Anthony Siaw also helped greatly with my understanding of NMR and DNP instrumentation.

I wouldnt be where I am today without all the teachers and mentors I had along the way including my awesome undergraduate advisor Kristen Wustholz. My time in the

Wuszтholz lab cultivated my interest in spectroscopy and physical chemistry, and research in general– I would certainly not have pursued grad school without that experience.

In my opinion making it through grad school requires a delicate work/life balance. I might have had a bit too much fun, and for that I'd like to thank all my friends who kept me sane and attended maybe 1 too many pint nights and chill bonfires with me. In no particular order: Pavel, Sheng, Jocelyn, Payton, Nick, Randerson, Emily, Manny, Zollner, Mia, Sarah, Max, Marko, Daniel, Julianne, Sam, Chris, Karl, Alex and everyone in the IM Hoops groupme. I know I forgot someone please forgive me. I also need to shout out my roomates/friends; Grant, Shona, and Richard who made COVID-19 quarantine manageable through all our shenanigans and who still supported me even though I may have left the tortilla bag open in the fridge too many times.

Finally I would like to thank my family, in particular my parents Lori and John who have always supported me in whatever I do and pushed me to follow my ambitions. I couldn't have done it without you guys.

Curriculum Vitæ

Kan Allan Tagami

Education

2022	Ph.D. in Chemistry (Expected), University of California, Santa Barbara.
2016	B.SC. in Chemistry, College of William and Mary

Research Experience

2017-present	Graduate Researcher University of California Santa Barbara Supervisor: Dr. Songi Han Project: Instrumentation and method development for high field dynamic nuclear polarization
2013-2016	Undergraduate Researcher College of William and Mary Supervisor: Dr. Kristen Wustholz Project: Photobleaching dynamics of purpurin and alizarin artists dyes.

Presentations

2018	Determination of Exchange Coupling in AMUPOL Towards Efficient MAS DNP, ENC Poster
2019	Investigation of J Coupling in Dynamic Nuclear Polarization NMR, JSU/UCSB Chemistry Conference Talk
2019	Arbitrary Waveform Enhanced DNP NMR under MAS, ENC Poster
2021	Progress on a Helium Free 7T 10K Static DNP/EPR Probe, ENC Poster
2021	Design of an Ultra Low Temperature Cryogen-Free High Field Dual EPR/DNP Probe, ISMAR Poster
2021	Dual NMR-EPR Detection in a high field (7T) Low Temperature (8.5K) DNP Spectrometer, Global NMR Discussion Meeting Talk

Publications

[1] Tan, J. A., Garakyaraghi, S., Tagami, K. A., Frano, K. A., Crockett, H. M., Ogata, A. F., Patterson, J. D., & Wustholz, K. L. (2017). Contributions from excited-state proton and electron transfer to the blinking and photobleaching dynamics of alizarin and purpurin. Journal of Physical Chemistry C, 121(1), 97–106.

[2] Li, Y., Equbal, A., Tagami, K., & Han, S. (2019). Electron spin density matching for cross-effect dynamic nuclear polarization. Chemical Communications, 55(53).

[3] Tagami, K., Equbal, A., Kaminker, I., Kirtman, B., & Han, S. (2019). Biradical rotamer states tune electron J coupling and MAS dynamic nuclear polarization enhancement. Solid State Nuclear Magnetic Resonance, 101.

[4] Equbal, A., Tagami, K., & Han, S. (2019). Pulse-Shaped Dynamic Nuclear Polarization under Magic-Angle Spinning. Journal of Physical Chemistry Letters, 10(24).

[5] Equbal, A., Tagami, K., & Han, S. (2020). Balancing dipolar and exchange coupling in biradicals to maximize cross effect dynamic nuclear polarization. Physical Chemistry Chemical Physics, 22(24).

[6] Equbal, A., Jain, S. K., Li, Y., Tagami, K., Wang, X., & Han, S. (2021). Role of electron spin dynamics and coupling network in designing dynamic nuclear polarization. Progress in Nuclear Magnetic Resonance Spectroscopy, 126–127.

[7] Li, Y., Chaklashiya, R., Takahashi, H., Kawahara, Y., Tagami, K., Tobar, C., & Han, S. (2021). Solid-state MAS NMR at ultra low temperature of hydrated alanine doped with DNP radicals. Journal of Magnetic Resonance, 333.

[8] Oh, S., Nikolaev, A., Tagami, K., Tran, T., Lee, D., Mukherjee, S., Segalman, R. A., Han, S., Read De Alaniz, J., & Chabinyc, M. L. (2021). Redox-Active Polymeric Ionic Liquids with Pendant N-Substituted Phenothiazine. ACS Applied Materials and Interfaces, 13(4).

Tagami, K., Thicklin, R., Jain, S., Equbal, A., Li, M., Zens, T., Siaw, A., & Han, S.Design of a Cryogen-Free High Field Dual EPR and DNP Probe (paper in progress)

Tagami, K., Equbal, A., Mattia, S., & Han, S., Hetero-spin DNP using Radical Mixtures (paper in progress)

Tagami, K., & Han, S., Butterfly Surface Coil Design for dual EPR/DNP detection (paper in progress)

Abstract

Instrumentation and Method Development for Efficient DNP in Electron Spin-Spin Coupled Systems.

by

Kan Allan Tagami

Solid state nuclear magnetic resonance (NMR) is a powerful technique that gives access to molecular structures and dynamics not accessible via other methods. However, the Achilles heal of NMR is the inherently low polarization of nuclei in a magnetic field in temperatures above the milli-Kelvin range, resulting in very poor sensitivity compared to other forms of spectroscopy. Fortunately, the much larger polarization of a paramagnetic electron can be transferred to the nuclei in a process known as dynamic nuclear polarization (DNP). However, the efficiency of state of the art DNP techniques drops of significantly at high magnetic fields >5T and fast magic angle spinning (MAS)– conditions favourable for high resolution NMR spectroscopy. Furthermore the scope of state of the art DNP methodology has been limited to a narrow set of paramagnetic electrons, pulse sequences, and instrumentation, which has limited the widespread applicability of DNP

This dissertation will seek to enhance the efficiency of DNP high magnetic field and fast MAS via electron spin analysis and manipulation of the coupled electron spin network. Advanced DNP instrumentation was also developed and applied to novel DNP systems in an effort to expand the scope of DNP to presently "exotic" paramagnetic systems.

In an effort to rationalize DNP performance of current state of the art DNP radicals, an electron paramagnetic resonance (EPR) case study was undertaken that revealed a

previously unknown distribution of magnetic spin-spin exchange coupling. The origin of this distribution was rationalized to be rotamer states via DFT calculations, and its effect on DNP was elucidated via quantum mechanical DNP simulations.

The magnetic properties of the spin system is only half the recipe for DNP, as μw irradiation of the EPR transitions is also necessary to facilitate polarization transfer. Thus, we have also developed a new method for shaped μw irradiation to boost the efficiency of DNP under MAS. This technique promises to be even more efficient compared to standard μw irradiation at higher temperatures, higher magnetic fields, and at higher μw power as new μw source technology is developed.

Finally, we have developed a new versatile cryogen free dual EPR/DNP probe for in situ EPR and NMR analysis of non-traditional DNP systems. This probe been designed to provide optimal μw (EPR) and radiofrequency (NMR) performance simultaneously for a broad range of nuclei and electron centers. This system has been used to analyze and demonstrate DNP between paramagnetic centers of different spin quantum number for the first time, opening up an entirely new avenues of DNP methodology using hetero-spin systems. The versatility of this system also allows testing of novel DNP instrumentation, as well as addition of various capabilities to enable a wide range of magnetic resonance experiments including ENDOR and light activated DNP.

Contents

Curriculum Vitae **vi**

Abstract **viii**

1 Introduction **1**
1.1 Motivation and Objectives 1

2 Theory and Background **8**
2.1 Permissions and Attributions 8
2.2 Overview of DNP Mechanisms 8
2.3 State of Art DNP methodology as of 2016 21

3 Role of Electron Exchange Coupling in DNP **28**
3.1 Permissions and Attributions 28
3.2 Introduction 28
3.3 Methods 32
3.4 Results and Discussion 36
3.5 Conclusions 50

4 AWG DNP **54**
4.1 Permissions and Attributions 54
4.2 Introduction 54
4.3 Results and discussion 57

5 Probe Building **75**
5.1 Introduction 75
5.2 Methods: Design Considerations 76
5.3 Results: Design and Performance of Dual DNP/EPR Probe 91
5.4 Results: Dual DNP/EPR Experiments 111
5.5 Conclusion 116

6 High Spin DNP **118**
6.1 Introduction . . . 118
6.2 Methods . . . 121
6.3 Results and Discussion . . . 122
6.4 Conclusion . . . 133

7 Conclusion and Outlook **140**

A Appendix A **144**
A.1 EPR . . . 144
A.2 DFT . . . 148
A.3 DNP Simulations . . . 152

B Appendix B **153**
B.1 1. Experimental Setup . . . 153
1. Experimental setup . . . 153
B.2 2. Experimental results on TEMTriPol-1 . . . 160
2. Experimental results on TEMTriPol-1 . . . 160
B.3 3. Numerical simulation . . . 161
3. Numerical simulation . . . 161

C Appendix C **170**
C.1 Temperature Performance . . . 170
C.2 NMR Design . . . 173
C.3 μw Design . . . 181

Bibliography **192**

Chapter 1

Introduction

1.1 Motivation and Objectives

In 1922 the Stern-Gerlach experiment demonstrated that nuclei have an intrinsic "spin" angular momentum property that can impart a small magnetic moment to the nuclei.[9] This discovery paved the way for the field of nuclear magnetic resonance (NMR), first demonstrated in molecular beams by Rabi in 1938,[10] and later in solids and liquids by Bloch and Purcell in 1946.[11, 12] NMR operates on the principle that when a (magnetic) nuclei with a nonzero spin is placed in an external magnetic field they partially align with the field, and non-degenerate quantum energy levels form which represent either parallel (low energy) or antiparallel (high energy) alignment with the external field. The energy separation between these states is related to the external field strength (B_0) and the nuclear gyro-magnetic ratio (γ_n) which is unique for every nuclear isotope. This energy separation is referred to as the nuclear Larmor frequency because the nuclear spins can also be described as "precessing" (or spinning at a certain frequency) around the axis of the external magnetic field.

These energy levels are further split by small electric and magnetic interactions within

the nucleus, and from the local environment around the nuclei. The structure of the energy levels can give incredibly detailed information about the environment and dynamics of the nuclei being probed. As a result these interactions are also what give NMR spectra their characteristic line-shapes and splittings, from which the desired properties are extracted. This information make NMR useful in a wide variety of fields from chemistry to structural biology and material science.

1.1.1 NMR Sensitivity

Despite its widespread use, NMR is plagued by intrinsically low sensitivity compared to most other forms of spectroscopy. This stems from the very small separation between nuclear spin energy levels when placed in an external magnetic field, leading to very low Boltzmann polarization. This means that only a small fraction of the nuclear spins will align with the external magnetic field and contribute to NMR signal. This is reflected in the relatively low electromagnetic frequencies used to probe NMR transitions which are on the order of 10s-100s of MHz, while much more sensitive optical spectroscopy techniques use orders of magnitude higher frequencies at 100s of THz (i.e 100s of nm wavelength). Furthermore, not all nuclear isotopes of a particular element are NMR active, and low natural abundance of NMR active nuclei can lead to even lower sensitivity.

Resolution and Sensitivity in Solid State NMR

The problem of low sensitivity is exacerbated when the sample of interest is as solid, as opposed to a liquid or solution. In solution state NMR rapid tumbling of the nuclei/molecule of interest averages out magnetic interactions between NMR active nuclei. In solid state no such tumbling occurs, and the NMR line-shape is broadened by orders of magnitude (proportional to the strength of chemical shift, quadrupolar, and dipolar

couplings present). This loss of resolution also translates to a loss in sensitivity, as the spectral intensity is spread out over a wide frequency range.

To combat the the loss of resolution and sensitivity in solid state NMR (ssNMR), magic angle spinning (MAS) techniques were developed. MAS operates on the principle that all anisotropic interactions that broaden NMR line-shape contain the term $3cos^2(\theta)-1$, where θ is the angle between the interaction tensor and the external magnetic field. If this term is minimized by setting θ to 54.7°, then the magnitude of the interaction, and thus broadening is also minimized. However, for samples that aren't single crystals the direction of the interaction tensor (i.e molecular orientation) is random. Thus to set $3cos^2(\theta) - 1$ to 0, the sample is rapidly rotated at 54.7° to the main magnetic field, such that all orientations of the tensor pass through this angle. If the speed of rotation (generally in kHz) is larger than the strength of the interaction, then the anisotropy is averaged out.

While MAS does partially alleviate the sensitivity problem of solid state NMR, its effectiveness is limited by the maximum achievable spinning speed (around 100-200kHz maximum with current technology) and aforementioned inherent sensitivity issues in NMR. Furthermore, the quadrupolar interaction is not fully averaged out by MAS and can still impede sensitivity. Even with MAS some ssNMR experiments can take up to days or even weeks of signal averaging to complete, and some experiments are rendered impossible due to the limited spectrometer time available.

Boltzmann Polarization

As stated above, the inherent sensitivity of NMR is limited by the Boltzmann polarization of the nuclei in an external magnetic field. This polarization is described by the

Boltzmann equation:

$$\frac{N+}{N-} = e^{-\Delta E/kT} \tag{1.1}$$

N+ and N- represent the populations of the high and low energy levels respectively. When this ratio is 1 (i.e the populations are equal) the system has no polarization and thus cannot be detected by NMR. ΔE is the energy difference between the two energy levels and is given by $h\gamma_n B_0$. T is the temperature of the system. For NMR a more useful equation is given below:

$$P_n = 1 - \frac{N+}{N-} = 1 - e^{-h\gamma_n B_0/kT} \tag{1.2}$$

P_n is the percentage polarization of the nuclear spins. When $P = 1$, all of the spin population resides in the lower energy state and the system is fully polarized, giving the maximum sensitivity. However, typical NMR polarization levels are $<< 1$ due the factor γ_n being very low. Much effort has been put into maximizing the field B_0 to raise the sensitivity. But increasing B_0 comes with diminishing returns and exponential cost as modern resistive and superconducting magnet technology reaches its limit. As of the time of this writing the highest B_0 achieved for NMR is 36 Tesla corresponding to a 1H Larmor frequency of ∼1.5 GHz (although the vast majority of ssNMR spectrometers operate between 7-14 Tesla). At room temperature the 1H polarization at this field would only be 0.025%, and even lower for other, lower γ_n nuclei. Another way to increase the sensitivity is to decrease the temperature. Modern solid state MAS NMR experiments routinely use liquid nitrogen to cool to ∼77 - 100K. At 77K and 36 Tesla the polarization of 1H would still only be 0.095%. To get more than 1% polarization a temperature of under 7.5K would be needed at this field. While achievable, these ultra low temperatures are expensive to reach and can introduce other issues such as extremely long nuclear T_1

relaxation rates which can end up lengthening experiment times.

γ_n is specific to each nuclear isotope. However it is possible to transfer polarization from a higher γ_n nuclei to a coupled lower γ_n nuclei in a process called cross polarization (CP). This process is used widely in modern NMR and can theoretically give a lower γ_n nuclei the same sensitivity as the higher γ_n nuclei. A typical example of this would be transferring polarization from 1H to 13C, with a polarization enhancement for 13C up to $\sim$4 times (the ratio of 1H to 13C γ_n. However this technique is limited by the maximum polarization of the higher γ_n nuclei, which still leaves the total polarization at less than a fraction of a percent.

Fortunately another, more effective polarization transfer method known as Dynamic Nuclear Polarization (DNP) exists that offers significant gains in sensitivity over other methods of increasing polarization. DNP is similar to CP in that polarization is transferred between two magnetically active spins. However instead of a high γ_n nuclear spin, DNP makes use of paramagnetic electron spins as the polarization source. Similar to nuclei, electrons also possess spin angular momentum which can be non-zero when the electrons are unpaired (such as with a radical). Compared to nuclei, electron spins have a much higher gyro-magnetic ratio (γ_e) which is typically $\sim$660 times larger than 1H, and absorb electromagnetic energy in the microwave rather than radio frequency range. This means the sensitivity and signal to noise (s/n) can be theoretically improved by up to 660 times, potentially shortening experimental times by a factor of 435,600.

DNP was first proposed by Overhauser, and subsequently demonstrated by Slichter in 1953,[13, 14] but for decades was limited to low field (i.e low resolution) applications by the lack of high frequency microwave technology needed to excite the electron spins. In 1997 the first high field (5 Tesla) MAS ssNMR DNP experiment was demonstrated on biomolecules mixed with paramagnetic polarizing agents (PAs) using a (140GHz) gyrotron to generate high power (100W) microwaves resulting in a renaissance for DNP applications

in NMR.[15] Now, commercial MAS DNP instruments up to 9.4 Tesla (260 GHz) using both high power gyrotrons and solid state transistor based microwave amplifiers are routinely used for high resolution, high sensitivity NMR experiments. As a result DNP has been successfully used for a wide variety of previously difficult/impossible NMR applications including protein structure and dynamics,[16, 17, 18, 19] low γ_n and natural abundance nuclei,[20, 21] and surface studies of functional materials.[22, 23, 24, 25, 26, 27, 28]

However the actual polarization enhancement in modern DNP methods is often much less than the theoretical value of 660. This issue is compounded at higher magnetic fields due to microwave instrumentation limitations as well as the electron spin physics of DNP mechanisms. Subsequently much effort has been put in to designing and analyzing the magnetic properties of PA systems to optimize the polarization transfer process. Even so, the scope of current state of the art DNP methodology (discussed in chapter 2) has been limited to a narrow range of radicals classes, conditions, and instrumentation. Thus, the goal of this thesis is twofold: 1) to enhance the efficiency and understanding of existing DNP systems, and 2) to broaden the scope of DNP by introducing new instrumentation and PA systems to open up new potential avenues to efficient and accessible DNP.

Most efforts to develop efficient radical coupling for high field DNP have so far focused on optimizing the inter-electron distance of bi-radicals to tune electron-electron dipolar coupling coupling. In chapter 3 we will present a study elucidating the distribution and origin of exchange coupling in state of the art biradicals– an alternative coupling mechanism to dipolar coupling.

High field DNP has also been limited in very basic μw irradiation schemes. Chapter 4 will present a study of a novel irradiation scheme for enhancing DNP under MAS for existing radical systems using unique hardware available in the Han lab.

The scope of DNP has also been limited by standard DNP instrumentation, which

typically limits DNP experiments to a lower temperature limit of 80K, and a narrow μw frequency range allowing DNP of only a narrow range of radicals with specific g factors. Furthermore, most DNP spectrometers do not allow in situ EPR analysis of the DNP radicals to diagnose the factors affecting the efficiency of DNP. In chapter 5, the development of a static (non MAS) 8.5K cryogen free dual EPR/DNP probe is described. The probe has been optimized to give simultaneous EPR and NMR performance.

Finally, chapter 6 will describe the use of this probe to investigate unique heterogenous mixtures of DNP radicals with different spin properties. Here, DNP between two radicals of different spin is recorded, and analyzed for the first time.

Chapter 2

Theory and Background

2.1 Permissions and Attributions

1. Part of the content of chapter 2 has been published in "Progress in Nuclear Magnetic Resonance Spectroscopy".[29] It is reproduced here with the permission of Elsevier: `https://www.sciencedirect.com/science/article/pii/S0079656521000236`.

2.2 Overview of DNP Mechanisms

In general there are four distinct mechanisms by which the DNP process can proceed. These are (1) the Overhauser effect (OE), (2) the solid effect (SE), (3) cross effect (CE), and (4) thermal mixing (TM). The simplest DNP mechanisms are OE and SE which require that a paramagnetic electron spin be coupled to a nuclear spin. An idealized, minimal OE/SE system consisting of an isolated electron-nuclei pair is described by the Hamiltonian:

$$H = H_e + H_n + H_{en} + H_{\mu w} \tag{2.1}$$

Here the subscript "S" denotes the electron spin and "I" represents the nuclear spin. The term H_e is the Zeeman interaction of the electron (i.e energy splitting due to the external magnetic field) which is described by the electron Larmor frequency ω_{0S} and the electron spin operator S. Similarly H_n is the nuclear Zeeman interaction with ω_{OI} being the nuclear Larmor frequency and the nuclear spin operator I. H_{en} represents the electron-nuclear hyperfine interaction with A and B being the isotropic and dipolar components of the interaction respectively. $H_{\mu w}$ is the microwave perturbation to the system where ω_1 is the strength of the microwave field perpendicular to the external magnetic field, and $\omega_{\mu w}$ is the frequency. The form of the component interaction terms is shown below:

$$H_e = \omega_{0S} S_z \tag{2.2}$$

$$H_n = \omega_{0I} I_z \tag{2.3}$$

$$H_{en} = A_{iso}(S_z I_z + S_y I_y + S_x I_x) + A_{dip} S_x I_z \tag{2.4}$$

$$H_{\mu w} = \omega_1 [S_x \cos \omega_{\mu w} t + S_y \sin \omega_{\mu w} t] \tag{2.5}$$

The Hamiltonian shown in equation 2.1 results in 4 energy levels arising from the electron and nuclear Zeeman interactions. These energy levels correspond to the electron and nuclear spin states as shown in Fig. 2.1

For **OE** DNP to occur, the central microwave transition must be saturated, and cross relaxation along the zero quantum or double quantum (W_0 and W_2) must occur. For this cross relaxation to occur the hyperfine interaction must be time dependant due to molecular tumbling in solution or electron mobility in conducting solids. For this reason OE DNP is not useful for ssNMR of insulating solids (the vast majority of use cases). Noteably, in 2014 the Griffin group reported OE in an insulating solid using a

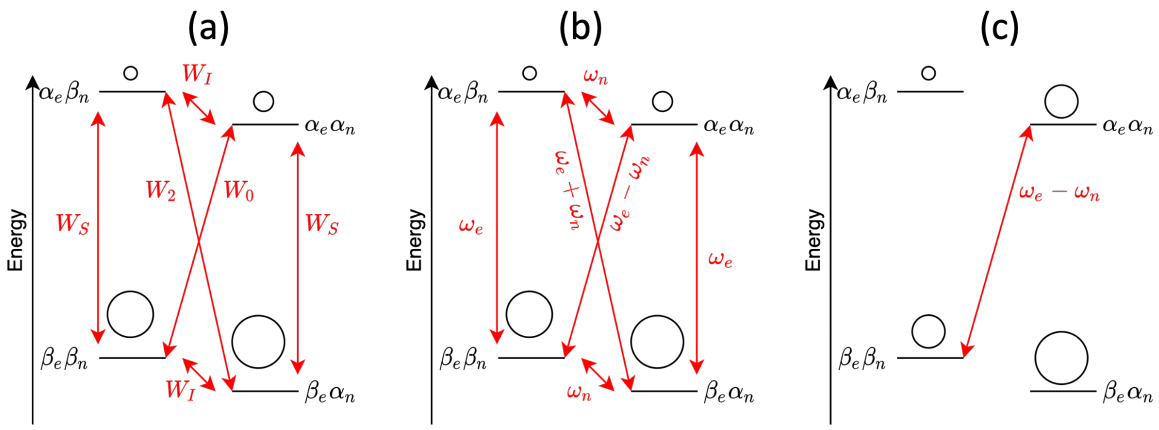

Figure 2.1: Magnetic energy levels diagram for a coupled electron nuclear spin system in an external magnetic field. α and β denote whether the spin is parallel or antiparallel to the external field, and the subscript indicates if it is the spin of an electron or nuclei. The relative populations of each state is illustrated by the size of the ball shown on each energy level. (a) shows the transition probabilities between each state denoted as W. (b) shows the transition energies (frequencies) between each state. (c) illustrates the polarization of states as a result of irradiating on the zero quantum transition.

BDPA radical. However, recent results suggest that this might be a TM effect instead. Although this is a rich area of research, for most modern ssNMR DNP systems, OE is not considered and investigation of this effect for ssNMR is beyond the scope of this work

SE is a much more commonly used effect than OE for ssNMR applications. For SE to occur, the zero or double quantum transition must be saturated with microwaves ($\omega_e \pm \omega_n$) as illustrated in Fig. 2.1 (right). This results in increased polarization between nuclear spin states (i.e between $\alpha_e\beta_n$ and $\alpha_e\alpha_n$, as well as $\beta_e\beta_n$ and $\beta_e\alpha_n$). While SE is very effective at low fields, it the efficiency drops at higher fields. The reasons for this are twofold: 1) the transition probability along the single quantum and double quantum transitions scales with ω_{0I}^{-2} which is itself a field dependant quantity. 2) the single quantum and double quantum transitions are forbidden transitions, and to effectively drive them requires a large amount of microwave power (ω_1), and the power output of microwave sources decreases at higher frequency. Thus DNP at high field requires a

different mechanism.

The most widely used method for DNP at high fields is **CE**. This 3 spin mechanism has 3 main requirements:

1. Spin System Coupling: 2 paramagnetic electrons coupled together, that are also coupled to a nucleus ($e - e - n$).

2. CE Frequency Matching Condition $\Delta\omega_e = \omega_n$: The 2 electrons must be separated in frequency by the nuclear larmor frequency.

3. Polarization Difference ΔP_e: The two electrons must have a polarization difference between them.

Taking into account these requirements, the minimum Hamiltonian needed to describe CE is as follows:

$$H = H_e + H_n + H_{en} + H_{ee} + H_{\mu w}$$

(2.6)

H_{ee} is the interaction between the two electron spins (also known as the zero field interaction or electron-electron $e - e$ coupling). This interaction consists of two components: the dipolar interaction (H_D), and the scalar exchange interaction (H_J). Compared to equation 2.1, H_e and H_{en} contain multiple terms due to the multiple electrons in the system. The component terms are expanded below:

$$H_e = \sum_{i=1,2} \omega_{0S_i} S_z, i \tag{2.7}$$

$$H_n = \omega_{0I} I_z \tag{2.8}$$

$$H_{en} = \sum_{i=1,2} A_{iso}(S_{z,i} I_Z + S_{y,i} I_y + S_{x,i} I_x) + A_{dip} S_{x,i} I_z \tag{2.9}$$

$$H_{ee} = H_D + H_J \tag{2.10}$$

$$H_D = D(2S_{z1}S_{z2} - S_{x1}S_{x2} - S_{y1}S_{y2}) \tag{2.11}$$

$$H_J = J(S_{z1}S_{z2} + S_{x1}S_{x2} + S_{y1}S_{y2}) \tag{2.12}$$

$$H_{\mu w} = \omega_1[(S_{x1} + S_{x2}) \cos \omega_{\mu w} t + (S_{y1} + S_{y2}) \sin \omega_{\mu w} t] \tag{2.13}$$

Where d is the value of the dipolar coupling, and J is the value of the scalar exchange coupling. The subscript "i" refers to the multiple electrons in the system (i.e 1 and 2)

The resulting energy levels are shown in Fig. 2.2a. For CE to occur one of the electron EPR transitions (ω_{e_1} or ω_{e_2}) must be selectively saturated by microwaves resulting in a polarization gradient between $\alpha_{e_1}\beta_{e_2}\beta_n$ and $\alpha_{e_1}\beta_{e_2}\alpha_n$. If the CE condition $\Delta\omega_e = \omega_n$ is met then the levels $\alpha_{e_1}\beta_{e_2}\beta_n$ or $\alpha_{e_1}\beta_{e_2}\alpha_n$ are nearly degenerate and will equalize their polarization through the transition W_{CE} (known as the CE transition) with a probability determined by J and D.

If the lower energy electron is excited then an excess of polarization is built up on $\alpha_{e_1}\beta_{e_2}\alpha_n$ resulting in a positive DNP enhancement (positive polarization difference) shown in Fig. 2.2b, while if the higher energy electron is excited then polarization is built up on $\alpha_{e_1}\beta_{e_2}\beta_n$ resulting in a negative DNP enhancement (i.e population inversion across the NMR transition) shown in Fig. 2.2c.

Unlike SE, the μw driven ω_e transitions and the W_{CE} transitions are allowed, resulting

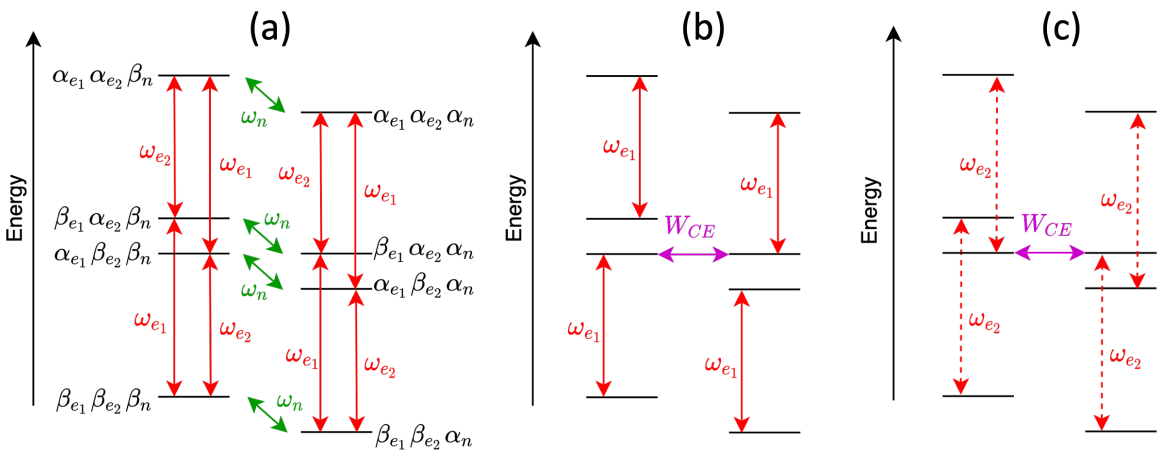

Figure 2.2: Relevant magnetic energy levels for the CE mechanism. (a) labels the spin states responsible for the energy levels as well as the possible EPR and NMR transitions for the system. (b) shows the transitions relevant for positive DNP enhancement. (c) shows the transitions relevant for negative DNP enhancement.

in a much lower μw power requirement, as well as better efficiency at high fields. In fact CE only scales down as ω_{0I}^{-1} (as opposed to ω_{0I}^{-2} for SE). Thus CE DNP is currently the most promising mechanism for DNP at high fields, and will be the focus of this thesis.

2.2.1 Factors Affecting DNP

The factors that affect the efficiency of CE DNP arise predominantly from the individual terms of the CE Hamiltonian of equation 2.6. These factors can be grouped into 3 categories based on the 3 aformentioned conditions for CE: the frequency matching condition, the coupling condition, and the polarization difference condition which will be discussed below. In addition spinning the sample (i.e MAS experiments) will introduce an additional time dependence i

2.2.2 Frequency Matching Condition $\Delta\omega_e = \omega_n$

EPR Line-shape The Zeeman term H_e is dominant in determining an the EPR frequency ω_e of an electron. This in turn determines if the system fulfills the CE condition $\Delta\omega_e = \omega_n$. For a real DNP system containing paramagnetic electrons and nuclei, the magnetic properties do not strictly fulfill CE the DNP condition. A CE system containing multiple electrons will have a distribution of EPR frequencies and couplings depending on their local environment and orientation in space. This is what gives rise to the distinct "line-shape" of EPR spectra for various paramagnetic electrons. To describe an EPR spectra the overall structure of the Hamiltonian is identical to equation 2.6 but the terms must be expanded to represent a real system. At high fields the electron Zeeman interaction H_e typically dominates the EPR line-shape. H_e is determined by the EPR g factor which describes the magnetic moment of the electron arising from its spin angular momentum and takes the form of a 3x3 tensor. The interaction of the g factor with the magnetic field is what gives the Zeeman interaction:

$$H_e = \mu_b B_0^T g S = \mu_b \begin{bmatrix} B_x & B_y & B_z \end{bmatrix} \begin{bmatrix} g_{xx} & g_{xy} & g_{xz} \\ g_{yx} & g_{yy} & g_{yz} \\ g_{zx} & g_{zy} & g_{zz} \end{bmatrix} \begin{bmatrix} S_x \\ S_y \\ S_z \end{bmatrix} \tag{2.14}$$

Here B_i represents the cartesian components of the external B_0 field in the lab frame (where only B_z is present for a good magnet). S_i are the cartesian components of the spin operator. g_{ij} are the components of the g factor which depend on the orientation of the unpaired electron in the lab frame. The unpaired spin density that gives rise to the directionality of the g tensor is illustrated on a tempo molecule in Fig. 2.3a. The g matrix is generally symmetric and can be rotated to only give the 3 principle values g_x, g_y, and g_z. The frame that gives a diagonal g tensor is shown in Fig. 2.3b. The reference

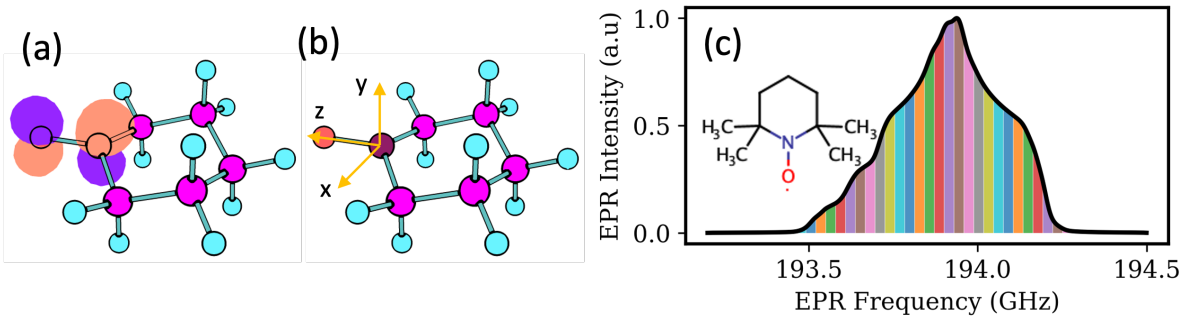

Figure 2.3: (a) DFT optimized geometry of a tempo nitroxide radical with unpaired spin density indicated by the purple and orange orbitals. (b) Direction of the symmetric (diagonal) g tensor for the nitroxide radical. (c) EPR profile of a typical nitroxide at 6.9 Tesla. Different colors represent different spin packets whose energy is predominantly determined by the g anisotropy. Inset is the 2D structure of tempo.

frame is aligned along the N-O bond, as well as with the plane of the ring.

For many radicals the distribution of EPR frequencies ω_e (and thus EPR line-shape) is dominated by the g anisotropy at high field. Large g anisotropy will lead to a broad distribution of ω_e caused by the various individual electrons all facing different, random directions relative to the main magnetic field B in a typical non-crystalline sample.

The effect of g anisotropy is shown in Fig. 2.3c. The EPR lineshape shown here is illustrated to be composed of different "spin packets" of electrons oriented differently in space. Here we can see that not all of these spin packets fulfill the CE condition $\Delta\omega_e = \omega_n$. Furthermore, irradiating at the center of an EPR line can cause both negative and positive DNP enhancement simultaneously which cancel out, which can be detrimental to the NMR signal. Thus CE DNP requires that two electrons have the correct g factors as well as orientations to fulfill $\Delta\omega_e = \omega_n$.

Hyperfine coupling, and electron-electron $(e-e)$ coupling can also influence the shape of the EPR line via splitting of the Zeeman energy levels. Hyperfine coupling can often be in the 10s of MHz for radicals in which the unpaired electron orbital is on a nuclei of non-zero spin such as with a nitroxide radical (the Nitrogen is strongly coupled to the

free electron). However, for typical DNP radicals at high fields these interactions are generally weaker than the g anisotropy, and thus only slightly broaden the EPR spectra.

2.2.3 Coupling Condition

Electron Electron Coupling

As stated above the electron-electron coupling plays a minor role in determining EPR lineshape. The main effect e-e coupling has on DNP is affecting the rate at which the CE transition can occur by facilitating the triple spin flip transition W_{CE}. The dipolar component of the coupling can be described by the tensor D as shown below in equation 2.18. In the frame of the inter-electron vector, D contains only diagonal terms and is trace-less. However, in general the dipolar matrix will not be aligned with the laboratory frame and thus will have off diagonal terms.

$$H_D = S_1^T D S_2 = d \begin{bmatrix} S_{x1} & S_{y1} & S_{z1} \end{bmatrix} \begin{bmatrix} d_{xx} & d_{xy} & d_{xz} \\ d_{xyx} & d_{yy} & d_{yz} \\ d_{zx} & d_{zy} & d_{zz} \end{bmatrix} \begin{bmatrix} S_{x2} \\ S_{y2} \\ S_{z2} \end{bmatrix} \tag{2.15}$$

The result of equation 2.18 gives equation 1.13 for H_D. In the secular approximation (1st order) for 2 alike spins (i.e 2 electrons, or 2 of the same nuclei) equation 1.13 can be expressed in terms of the ladder operators S^+ and S^-:

$$d[S_{z1}S_{z2} + \frac{1}{4}(S_1^+ S_2^- + S_1^- S_2^+)] \tag{2.16}$$

Here we can see that the terms in this equation account for the EPR double quantum transition that is necessary for CE transition to occur, and thus the rate of the transition relies on d.

In reality, there are higher order terms present that are responsible for the double

quantum and single quantum transitions that are necessary for SE DNP. However these terms are less relevant for CE and will not be discussed.

The value d is the strength of the dipolar coupling (typically expressed in MHz for electrons), and is dependant only on the distance and angle between the two spins relative to the magnetic field.

$$d = \frac{\mu_0 \gamma_e^2 \hbar}{4\pi r^3}(1 - cos^3(\theta)) \tag{2.17}$$

Where γ_e is the electron gyro magnetic ratio, r is the inter-electron distance, and θ is the angle between the vector connecting the two spins and the external magnetic field B. Thus, the strength of the dipolar coupling is dependant on the orientation of the two electron spins in space. For a typical non-crystalline sample, all orientations are present and thus the effective dipolar coupling will vary from $-d/2$ to d, with the weight of the distribution heaviest towards $-d/2$. This also means that different orientations of electrons will have different CE transition rates, and will thus give different DNP enhancements. The effect of dipolar anisotropy will be discussed further in Chapter 3.

The isotropic component of the $e - e$ coupling is generally referred to as J coupling. The J component of the $e - e$ coupling Hamiltonian is as follows:

$$H_J = S_1^T J S_2 = J \begin{bmatrix} S_{x1} & S_{y1} & S_{z1} \end{bmatrix} \begin{bmatrix} S_{x2} \\ S_{y2} \\ S_{z2} \end{bmatrix} \tag{2.18}$$

Which yields equation 1.14 for H_J. Similar to d, the value of J is a scalar value generally given in MHz, but unlike d, J does not have a directional dependence, and all orientations of electrons in the system will have a single value of J. Additionally, the value of J is not strictly dependant on distance, but on the overlap of the unpaired

electron orbitals.

Most radicals that exist in a physical mixture will rely on dipolar coupling to facilitate CE as through space dipolar coupling falls off as $1/r^3$, while through space J coupling is dependant on the shape of the molecular orbital. However radicals tethered together through a bond typically rely on a combination of of dipolar and J coupling to facilitate CE. Because J does not change with orientation, radicals coupled primarily through J can have a more well defined e-e coupling.

Due to its importance in CE DNP, $e-e$ coupling is a central theme of this thesis. Chapter XX details a study on the origin and analysis of J coupling in common tethered radicals. Chapter XX describes a method to enhance DNP in biradicals with certain e-e coupling properties. Chapter XX will show DNP using high spin radicals formed from very strongly J coupled spins, subsequently coupled with spin 1/2 radicals.

Hyperfine coupling The hyperfine coupling between an e and n with non-zero spin is necessary for polarization to transfer from electrons to nuclei and is crucial for any DNP mechanism. The hyperfine interaction has the following form:

$$H_{en} = S^T A I = \begin{bmatrix} S_x & S_y & S_z \end{bmatrix} \begin{bmatrix} a_{xx} & a_{xy} & a_{xz} \\ a_{yx} & a_{yy} & a_{yz} \\ a_{zx} & a_{zy} & a_{zz} \end{bmatrix} \begin{bmatrix} I_x \\ I_y \\ I_z \end{bmatrix} \tag{2.19}$$

Here, I denotes the nuclear spin operator, where S is the electron spin operator. A is the 3x3 hyperfine tensor which consists of dipolar and isotropic components (similar to D and J in H_{ee}). Notably this matrix can be symmetric when aligned along the $e-n$ vector similar to the dipolar tensor D. However, in the laboratory frame the hyperfine tensor has off diagonal terms which are essential for DNP. For CE DNP, the pseudo-secular

terms from equation 2.19 are needed which gives:

$$H_{en,CE} = a_{zx} I_x S_z + a_{yz} I_y S_z \tag{2.20}$$

These two terms account for the single quantum (single spin flip) transition of the nuclear spin that needs to happen during the CE transition W_{CE}, and can be expressed in terms of ladder operators:

$$H_{en,CE} = a[I^+ S_z + I^- 1 S_z] \tag{2.21}$$

$$a = \frac{1}{2}(a_{zx} - i a_{zy}) \tag{2.22}$$

In most DNP systems, the paramagnetic electrons have a large hyperfine coupling to a nuclei on the same molecule as the electron. However, nuclei on the same molecule as the paramagnetic electron are generally not the target for DNP. For most solid state DNP experiments, the PA is mixed in a solvent with the target nuclei/molecule. This means the hyperfine coupling tensor A is stochastic and can be coupled to either or both of the electrons. However, the multitude of nuclei surrounding the electrons means that there will almost always be a nuclei that fulfills the conditions necessary for CE DNP. The polarization is transferred from the PA to the solvent nuclei (typically 1H) that fulfill the conditions for CE, and subsequently propagated through spin diffusion to the target nuclei. This thesis will not focus much on the effect of hyperfine coupling, but does acknowledge that factors such as DNP solvent/glassing agent used can play a large role in the distribution of hyperfine couplings, and thus DNP.

2.2.4 Polarization Difference Condition ΔP_e

uW

In CE DNP μw irradiation is needed to generate a polarization difference between the two spins. This is typically achieved by selectively irradiating on one spin to destroy its polarization. The effect of μw irradiation on the spin system can be described similar to the Zeeman interaction, except that the external field is oscillating in time, and is applied along the X or Y axis (as opposed to the Z axis for B_0). The hamiltonian for μw excitation of one of the electron spins is:

$$H_{\mu w} = B_1^T S = \begin{bmatrix} cos(\omega_{\mu w} t) & sin(\omega_{\mu w} t) & 0 \end{bmatrix} \begin{bmatrix} S_x \\ S_y \\ S_z \end{bmatrix} \tag{2.23}$$

Unlike with typical NMR experiments, or low field EPR experiments the μw irradiation used for high field DNP uses cw irradiation or pulses whose bandwidth is much less than the width (in frequency) of the the EPR spectra/transitions. Thus the effect of μw iradiation can be visualized as "burning a hole" in the EPR spectra.

The resulting polarization difference built up then drives the CE transition. μw irradiation is a crucial part of the DNP process and will be discussed further in section 2.3 and chapter 4.

Relaxation

In DNP, there is a tug of war between μw saturation and electron spin relaxation. Specifically, the selective saturation of an in-homogeneously boradened EPR spectrum

gives rise to a large electron spin polarization differential, ΔP_e, while T_{1e} relaxation pushes the polarization back to its thermal equilibrium, reducing ΔP_e. Short T_{1e} rapidly reduces the polarization gradient and can lead to low DNP efficiency. In fact, the requirement of long T_{1e} is the reason that DNP typically requires cryogenic temperatures to work.

Relaxation has been shown to be a crucial factor for DNP in studies that vary both temperature and radical structure. For example a study by Ouari, Emsley and coworkers demonstrates a series of bis-nitroxide radials in the family of bTbk and TEKPOL exhibiting long T_{1e} that correlated with higher DNP enhancements.[30, 31] The strategy was to increase the bulkiness or the molecular weight of the nitroxide-based PA, and in turn slow down its motional dynamics to yield longer T_{1e} with a more rigid molecular framework around the radical center. The T_{1e} values of the PA ($\sim$ 15 mM concentration, measured at 100 K, 3.5 T) that varied from 10 to 45 μs. The DNP enhancements measured at 100 K, 9.4 T and 15 kHz MAS, showed a direct correspondence between T_{1e} and enhancement. Increasing T_{1e} increased the observed DNP enhancement. However, long T_{1e} can also induce the detrimental effect of nuclear depolarization under MAS (explained in section 6). We hence posit that there is an optimum regime for T_{1e} that should be long enough to maintain saturation, but short enough to replenish electron spin polarization after each rotor event, and to avoid the undesirable nuclear depolarization effect under MAS (details in section 6).[32]

2.3 State of Art DNP methodology as of 2016

In the past 20 years DNP has rapidly been gaining momentum as a mainstream technique for NMR, and as of 2016 powerful commercial systems were available for MAS DNP experiments. A typical DNP experiment requires a radical system mixed in a

glassing agent with the NMR sample of interests, as well as a microwave irradiation source to excite the electron transitions. Furthermore the sample must be cooled down to cryogenic temperatures typically while spinning under MAS. Much effort has been put into optimizing each one of these factors which has lead to the current state of modern DNP experiments.

2.3.1 DNP Radicals

The DNP radical is at the heart of every DNP experiment and is perhaps the most important aspect of the DNP process. Most of the factors that affect DNP are a direct result of the magnetic properties of the DNP radical. Thus, radical development has been a very active part of DNP research.

Many classes of free radicals exist that can be used for DNP but historically development efforts have focused on spin 1/2 radicals that can roughly be classified as "narrow line" or "broad line". The "narrow" and "broad" classification refers to the width of the EPR line due to the magnetic properties of the radical. Typically broad line radicals are nitroxide radicals while narrow line radicals are carbon based radicals.

Nitroxide Radicals

As of 2016 bis-nitroxides were the radical of choice for the vast majority of CE DNP applications. These molecules are essentially 2 nitroxide moieties connected by a linker chain. The length, rigidity, composition, and angle of the linker chain all play a role in determining DNP efficiency by modulating the electron-electron coupling and g-tensor orientations of the nitroxides. Three of the most popular of these radicals are Totapol, Amupol, and Tekpol (shown in Fig. 2.4).

These commercially available radicals account for a large chunk of the DNP experi-

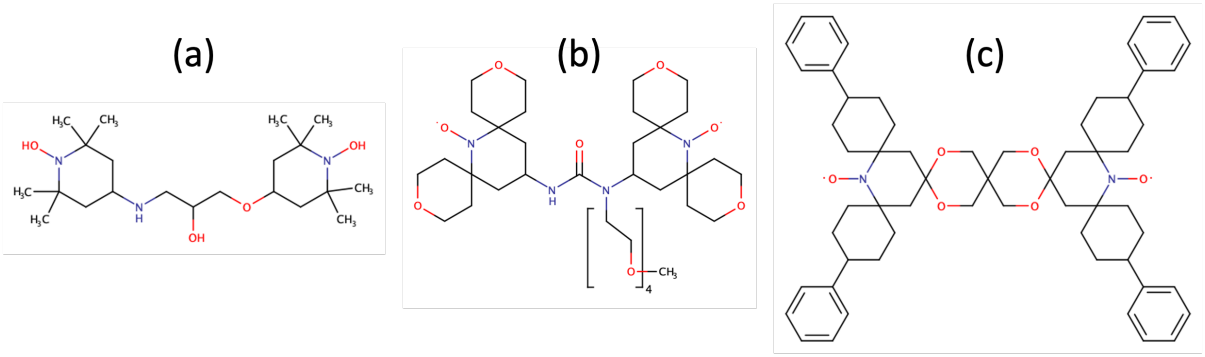

Figure 2.4: Commonly used bis-nitroxide radicals (a) Totapol, (b) Amupol, (c) Tekpol.

ment carried out to date and work well up to moderate magnetic fields ($\sim 9.4T$). However, under MAS these radicals undergo a process known as "depolarization" which can reduce the NMR signal. Additionally, the g anisotropy of these radicals is field dependant, and thus the spin density of the radicals spreads out at high field, thereby reducing the spin density fulfilling $\Delta\omega_e = \omega_n$ at any given μw frequency. Thus at ideal conditions for ssNMR (high fields and fast MAS) nitroxide radicals become less effective for DNP.

Mixed Radicals

More recent developments have seen the use of "mixed" radicals which employ both broad line nitroxide radicals and narrow line carbon radicals. The first use of these radicals employed a physical mixture of nitroxide and trityl (carbon based) radicals.[33] By using 2 separate types of radicals, greater spin density can be tailored to meet the CE condition $\Delta\omega_e = \omega_n$ as shown in Fig. 2.5a. These radicals also don't suffer from the same depolarization effect under MAS as nitroxide-only radicals due to their non-overlapping spin density.

Similar to bis-nitroxides, tethered tempo-trityl type radicals have recently been developed to constrain the dipolar coupling between the two radical moieties. The first of these tethered mixed radicals were aptly named temp-tripol series (one of which is

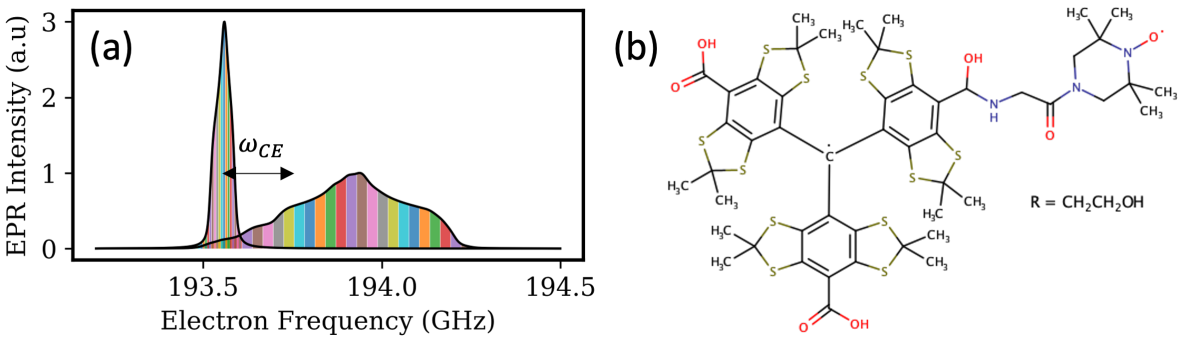

Figure 2.5: (a) EPR spectra and spin density of a Trityl and nitroxide type radicals overlayed. (b) Temp-Tripol-1 tempo-trityl type biradical.

shown in Fig. 2.5b).[34] Unlike bis-nitroxide radicals, the relatively symmetric g-tensor of the trityl radical does not require specific alignment with the g tensor of the nitroxide radical to optimally fulfill the CE condition $\Delta\omega_e = \omega_n$, meaning more orientations can participate in DNP at a time.

The focus of this thesis will be to analyze and exploit the properties of various state of the art DNP radicals, as well as novel radical systems currently not used for DNP, to enhance DNP methodology. Specifically, chapter 3 of this thesis will focus on a thorough analysis of the origin and effect electron-electron coupling in current state of the art DNP radicals.

2.3.2 DNP Pulse Sequences

The other half of the DNP recipe is the μw irradiation used to excite the EPR transitions and transfer the e polarization to the nuclei. Typical state of the art high field DNP experiments use monochromatic continuous wave (CW) moderately high power (10's to 100's of watts) irradiation from a gyrotron. This irradiation typically has no gating, pulsing, or frequency ramping typical of time domain EPR or NMR pulse sequences as shown in Fig. 2.6

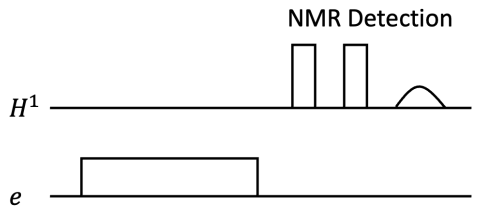

Figure 2.6:

Other

Recently time-domain modulation of μw irradiation has been shown to offer superior control of EPR transitions for DNP. These time domain DNP techniques can be grouped into two approaches: (i) *Coherent DNP* that uses high μw powered pulses to (coherently) drive a certain transition of an *e*-*n* spin system resulting in nuclear polarization enhancement; and (ii) *Incoherent DNP* that relies on low-to-intermediate μw powered shaped pulses to induce broadband, or deliberately shaped, saturation of the EPR transitions in a select frequency range. Here, time-domain modulation can compensate for the lack of μw power by saturating a larger number of EPR transitions in the frequency domain, thereby recruiting a larger number of electron spins in DNP process. However, this method did not work under MAS at high field until the work of this thesis. Chapter 4 will describe a method to enhance DNP using time modulated microwaves under MAS.

Notably, over the last few years, Griffin and coworkers have tested a series of coherent DNP mechanisms for a coupled *e*-*n* system that in principle do not scale down with B_0, unlike CE and SE. These DNP methods get inspiration from the coherence transfer processes routinely used in solid-state NMR using RF pulses.

2.3.3 DNP Instrumentation

μw Sources

The choice of μw irradiation scheme is largely determined by the power, bandwidth, frequency agility, and pulse gating abilities of the available μw source. Coherent DNP requires high power (100s of watts) paired with nanosecond pulsing. Incoherent DNP can be effective with much lower power (of the order of 100s of milliwatts) delivered in CW or pulse trains, and optional time-domain modulation, but still benefits greatly from increased power.

Gyrotrons are currently the μw source of choice for high-field DNP and deliver up to 10s of watts of power in monochromatic CW mode, which translates into a nutation frequency of up to a few MHz. While this is not enough μw power for coherent DNP, gyrotrons are effective for achieving incoherent DNP. Recently, frequency agile gyrotrons have become available that demonstrated the option for sweeping the μw frequency over 120 MHz.[35, 36] However, such gyrotrons span limited frequency bandwidth (compared to the EPR line width and proton Larmor frequency) and cannot be used to achieve direct pulsing at the required nanosecond timescale to achieve coherent DNP. Thus, state-of-the-art gyrotrons are a robust option for incoherent DNP at high field, but are unable to perform coherent DNP and EPR detection due their limited power, versatility and phase stability. Notably, pulse slicing technologies to achieve external pulse gating of high-powered sources such as the free electron laser (FEL) exist and have been utilized for pulsed EPR.[37] However, FELs have not yet been developed yet for the duty cycles necessary for pulsed DNP applications.

Solid-state devices as μw sources have complementary and orthogonal qualities for DNP applications compared to gyrotrons. They are compact devices driven by lower frequency μw signals, typically generated by a YIG synthesizer or voltage controlled os-

cillator (VCO) operating at X-band (10 GHz) or W-band (35 GHz) frequencies. This low frequency signal is multiplied and amplified with an amplifier multiplier chain (AMC) to generate frequencies in the 100s of GHz range. Currently, at 200 - 260 GHz, such device can produce up to 100s of milliwatts of μw power, which yields a nutation frequency of hundreds of kHz; with gains in output power and maximum frequency seen every year. Critically, the solid-state source drivers are easily tune-able in frequency and amplitude with an accuracy of <100Hz, and can be phase-locked to be exceptionally stable. Moreover, these sources can be combined with fast arbitrary waveform generators (AWGs) with a 2-10 GHz bandwidth, allowing for fine control over the amplitude, frequency, phase, and pulse gating with sub-ns time scales at the final high frequency output.[38] This capability to achieve modulation of the μw source using AWG in the time-domain with high accuracy and speed provides opportunities to test new DNP methods, mechanisms, or samples. Furthermore, the precise control of μw irradiation offered by solid state sources allows EPR detection, making "in situ" EPR analysis of the DNP mechanism possible.

The work of this thesis will focus on the use of these solid state sources for both AWG DNP under MAS (chapter 4) as well as EPR analysis of DNP radicals (chapter 5-6).

Equally important as the μw source is the DNP/NMR probe used cool the sample, as well as transmit the μw's to the sample and detect the NMR signal. One major thrust of this thesis is the development of a sub-cryogenic dual EPR/DNP probe described in chapter 5, and aspects of state of the art DNP probes will be discussed there.

Chapter 3

Role of Electron Exchange Coupling in DNP

3.1 Permissions and Attributions

1. The content of chapter 2 and appendix A has been published in the Journal of Solid State Nuclear Magnetic Resonance.[3] It is reproduced here with the permission of Elsevier: https://www.sciencedirect.com/science/article/abs/pii/S0926204019300098.

3.2 Introduction

Since its discovery over 50 years ago, Dynamic Nuclear Polarization (DNP) has gained prominence as a hyper polarization technique in which spin polarization is transferred from an unpaired electron to a nuclear spin via saturation of the electron paramagnetic resonance (EPR) frequency. This allows the NMR signal to be enhanced, in theory, by up to 660 fold for ^{1}H, dramatically enhancing the scope of NMR applications.[13, 39]

The cross effect DNP (CE-DNP) mechanism using tethered bis-nitroxide type radicals has become of particular interest for solid state DNP NMR, given its efficiency at high magnetic fields (B_0)[40, 41, 42, 43] and under magic angle spinning (MAS).[44, 45] Under MAS, the electron spin energy levels associated with anisotropic interactions undergo periodic level crossings and anti-crossing in what are known as *rotor events*.[46] The CE transfer is associated with an anti-crossing that fulfills the resonance condition, i.e. $\Delta\omega_{0e} = \omega_{0n}$ where $\Delta\omega_{0e}$ is the energy difference between two electron spins, and ω_{0n} the nuclear Larmor frequency. Among other factors, the efficiency of the CE-inducing *rotor event* is dependent on the strength of the $e-n$ coupling and, most importantly, on the magnitude of the $e-e$ coupling between the two CE-fulfilling electron spins.[45, 47] Thus, quantifying these parameters is important for radical design, and so to optimize the CE-DNP.

A variety of tethered bis-nitroxide radicals[48, 31] including TOTAPol[44] and later pyPOL derivatives[49, 50] have been designed in order to maximize and/or tune the magnetic electron-electron spin ($e-e$) coupling. Among them, AMUPol is currently one of the most widely used polarizing agents, owing to its high performance across a wide range of experimental conditions relevant for DNP applications, water solubility, bio-compatibility and commercial availability.[49] Despite its widespread use, the precise mechanistic basis for its broad applicability for MAS DNP is still not entirely clear. The role of T_{1e},[49, 51, 52, 53, 54, 55, 30] higher rigidity, [48, 31, 49, 50, 44, 56] high dipolar (D) coupling, near orthogonal g tensor orientation of the electron spin pair[45], as well as spin exchange (J) coupling have all been suggested as contributors to the favorable CE-DNP performance of AMUPol compared to TOTAPol.[57, 58] Still, their characterization remains incomplete. A key question is what the biradial design parameters should be to improve the DNP performance, especially in the regime of high B_0 and fast MAS frequency, where the performance of most radicals used for DNP significantly

deteriorates, including that of AMUPol. Faster spinning and higher B_0 field reduce the transition probability of CE rotor events, as can be understood through the Landau-Zener theory.[59]

Enhancing the strength of the $e-e$ spin coupling can be an important pathway to increase the CE-DNP transition probability. There are two spin-spin coupling terms in the biradical Hamiltonian: the dipolar coupling (DS_1S_2) and the J coupling ($-2JS_1S_2$) terms. Until recently, only the dipolar coupling has been considered when simulating DNP enhancements and DNP profiles through quantum mechanical calculations.[45, 58] In a very recent article by Griffin and coworkers[60] the J coupling parameter in AMUPol was found to be around 15 MHz, by multi-frequency EPR spectra of frozen samples, which is in agreement with assumptions made in the literature.[61] Similarly, J has been shown to have a value of around 21-22 MHz according to X-band EPR lineshape analysis in solution state (in Gast et al. the Hamiltonian JS_1S_2 was used instead of $-2JS_1S_2$, doubling the apparent J value).[57, 50]

Interestingly, the $e-e$ J coupling for bis-TEMPO radicals with identical linker lengths and similar composition to AMUPol (structures not shown) have been determined to be 25-40MHz, again in solution and from X-band EPR lineshape analysis.[62] No molecules analogous to TOTAPol have been examined to determine their J values. However a comprehensive analysis of a multitude of biradicals suggests that the additional CH_2 groups in the linker chain of TOTAPol would drastically decrease the extent of exchange coupling by >16 times.[63] On the other hand, even longer biradicals have been shown to be able to flex into conformations with high J coupling, even in the absence of conjugation.[63] In light of the e-e J coupling being a relatively new parameter to consider for DNP and given the sparsity in the literature, there is no clear consensus on the prediction, measurement method, value and range for J coupling values for common DNP radicals, justifying our study.

It is important to note that the value of J can, in general, be temperature dependent for the following reasons: (i) electron spin exchange is modulated by inter-radical collisions, (ii) the population of the different conformational rotamer states of the biradical is governed by the Boltzman factor, and (iii) the population of the triplet/single state of the exchanged coupled state is temperature dependent. Here, the temperature dependence of (iii) will lie at liquid helium temperatures given the miniscule exchange coupling values of the order of tens of MHz, and hence not of direct relevance for AMUPol under DNP conditions. Our study will show that factors (i) and (ii) play a role in most nitroxide-based biradicals employed for DNP since more than one conformation is readily accessible. In vitrified samples the relevant temperature, in principle, is that at which the sample was incubated before vitrification. However, vitrification is non-trivial to achieve for MAS DNP samples, given the sample size and geometry, as well as the probe and cryostat configuration. Thus in practice, the freezing and equilibration history will still affect the resultant J coupling for the sample frozen to <100 K for DNP experiments.

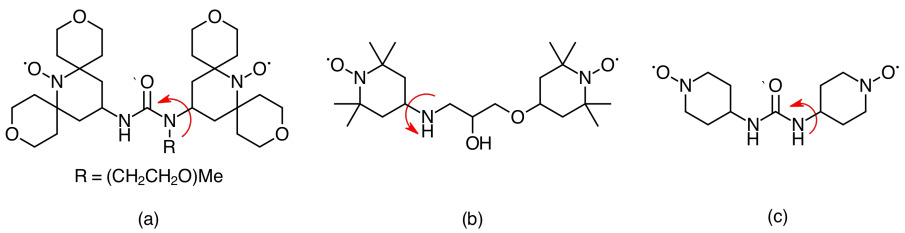

Figure 3.1: Radicals investigated in the present work. (a) AMUPol, (b) TOTAPol, (c) truncated AMUPol used in testing of broken symmetry DFT as discussed in sec 3.2.

In this study, we obtain electron spin J coupling values for TOTAPol and AMUPol - the two most widely used biradicals for DNP - at multiple temperatures and in a series of solvents under well-defined sample conditions. To gain insight into the factors that determine J coupling, we accompany our experimental study with DFT calculations of J coupling for both AMUPol and TOTAPol using Yamaguchi's[64] broken symmetry

approach. In addition, we examine the potential role of J coupling in solid-state DNP by carrying out fully quantum-mechanical simulations of MAS DNP for a 3 spin (eeH) system using the SpinEvolution[65] simulation package. Our results demonstrate that even a small J coupling between the two dipolar coupled electron spins can dramatically boost the DNP enhancement.

The outline of our paper is as follows. In the next section we describe the experimental conditions along with the computational methods used to simulate the EPR spectra, the DNP enhancement, as well as the broken symmetry calculation of J. Then we present the procedure whereby the J value and distribution is determined as a function of temperature and solvent through EPR line shape analysis. The temperature and solvent dependence of the J value and distribution in AMUPOL and TOTAPOL will be used to obtain the conformational dependence of J in these biradical molecules. Subsequent broken symmetry DFT calculations show that the dependence of J on torsional angle– and thus, rotamer states– is consistent with the experimental findings. Finally, we show that even very small J coupling can significantly enhance the CE-DNP performance, especially at high MAS frequency.

3.3 Methods

3.3.1 Sample Preparation

For EPR experiments, solutions of AMUPol (Fig. 3.1a) and TOTAPol (Fig. 3.1b) were prepared at 100μM concentration to avoid broadening by collisional Heisenberg exchange. Solvents used include: 60/30/10 $\%V$ d_8-Glycerol:D_2O:H_2O DNP Juice, 50/50 DMSO:H2O, H_2O, DMSO, and Toluene. d_8-Glycerol was obtained from Cambridge Isotope Laboratories, Inc. AMUPol was obtained from Cortecnet; TOTAPol was obtained

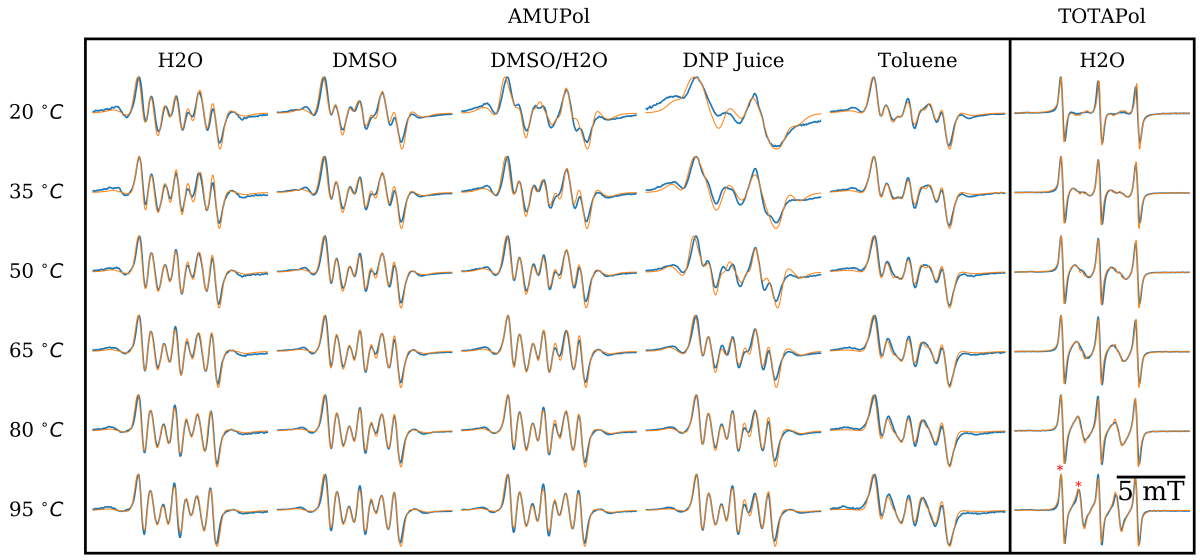

Figure 3.2: Experimental data (blue) and fits (orange) of AMUPol and TOTAPol X-band EPR spectra in different solvents at various temperatures. In the DNP Juice and DMSO/H2O solutions at lower temperatures, the incomplete averaging of the anisotropic A and D tensors manifests as asymmetric broadening in the spectra. Toluene spectra are visibly different due to increased isotropic line broadening most likely due to a change in T_2. Peaks used to evaluate the cage effect mechanism are marked with *.

from DyNuPol.

3.3.2 X-Band EPR

X-band EPR experiments were performed with a Bruker EMX spectrometer equipped with a ER041MR microwave bridge and a rectangular cavity (Bruker 4102ST) with variable temperature control. The sample was placed in a 0.8 mm ID round quartz capillary which was held in the cavity by a 4 mm quartz EPR tube. Temperatures were varied from 20°C to 95°C with a stability of ±2°C using a heated nitrogen line. The microwave power was 6 mW, the modulation amplitude set to 1 Gauss, and the modulation frequency to 100kHz.

3.3.3 Simulation of EPR spectrum

The simulations of EPR spectra were preformed using the 'pepper' function of the EasySpin package for Matlab.[66] Although 'pepper' is explicitly for solid state spectra, it is sufficient for our purposes since the solution EPR spectrum is isotropic (or nearly isotropic) and has the virtue of being much faster for computation than the "slow motion" algorithm. The spin system simulated was two coupled spin 1/2 electrons, with isotropic g and A interactions, and residual dipolar coupling (D). Additional simulation details and parameters are described further in the discussion section and appendix A.

3.3.4 DFT Calculation of J Coupling

Unrestricted DFT calculations of J were performed using the Orca software package[67, 68] and the Broken Symmetry (BS) formalism.[69, 64] Geometry optimizations were performed in all cases at the B3LYP-D3/TZVP level of theory (for initial structures and other details see appendix A). In the BS treatment, the first step of this approach is to obtain the value of $\langle \hat{S}^2 \rangle$ and the self consistent field (SCF) energy (E) of the high spin triplet (T) spin state (corresponding to two unpaired electrons in the same spin state $\uparrow\uparrow$) obtained at the triplet molecular geometry. Subsequently, one of the two spins is flipped, and the same quantities ($\langle \hat{S}^2 \rangle$ and E) calculated for the resulting (BS) singlet state (corresponding to a nearly equal mixture of the $M_S = 0$ component of the triplet and true singlet $\sim\uparrow\downarrow + \downarrow\uparrow$).[70, 71] Thus, $\langle \hat{S}^2 \rangle$ is expected to be close to 2 for the triplet and close to 1 for the BS singlet state. The Yamaguchi equation was then used to calculate the J coupling as follows:[64]

$$J = \frac{E_T - E_{BS}}{\left\langle \hat{S}^2 \right\rangle_T - \left\langle \hat{S}^2 \right\rangle_{BS}} \tag{3.1}$$

The optimized triplet geometry was employed for the BS singlet state geomery as

well.[71] Even though an improved J value might be obtained by optimizing the geometry of the latter,[72] we do not think our basic conclusions would be altered. Several DFT functionals and different basis sets were tested as described later in the Results and Discussion section. Because the S-T gap in AMUPol and TOTAPol is very small ($\sim 10^{-9}$ Hartree) compared to the energy of the individual states, it is critical to ensure sufficient numerical accuracy in the calculations, and thus the SCF energy must be converged to a precision at or below the J coupling value.

3.3.5 DNP Simulations

Simulations of the DNP performance were carried out using the fully quantum mechanical density matrix formalism-based SpinEvolution package, which has been recently upgraded to perform DNP simulations.[65, 73, 32, 73] In this study, simulations were performed for a spin system consisting of two coupled e spins and one coupled proton (^{1}H) spin under MAS condition at high B_0 field (9.4T). The calculations were performed in the rotating frame of electron spins and the lab frame of nuclear spin using the commercial SpinEvolution simulation package. The calculation was based on solving on the master-equation, in the Liouville space. For high level of accuracy, local tolerance for the integration of the equation of motion was set to $2 * 10^{-5}$. The form of dipolar and J coupling Hamiltonians used are standard and very well documented in the SpinEvolution reference.[65] The program incorporates relaxation, assuming that all the relaxation of spins is due to random fluctuations of single-spin operators (I_x, I_y, I_z), and hence use phenomenological rate constants (T_1 and T_2) as inputs. All relevant spin parameters can be found in Sec.3.2 as well as the simulation script included in the appendix A.

3.4 Results and Discussion

Determination of J by EPR The determination of the electron spin J coupling of biradicals can be done in solution state by CW EPR lineshape analysis at Q- or X-band, or lower B_0, where the anisotropy of the g, A and D tensors is readily averaged out. When the condition $\{\Delta g, \Delta A, D\} << 1/\tau_{corr}$ is fulfilled, where τ_{corr} is the rotational correlation time of the molecular motion and Δ indicates the anisotropy, an EPR splitting pattern emerges that depends only on the ratio J/A_{iso}.[62] Here A_{iso} is the isotropic hyperfine coupling constant. At higher B_0, the dispersion of the g anisotropy, Δg, is greater, and thus it is harder to achieve complete motional averaging of the g tensor, $i.e. \Delta g \not<< 1/\tau_{corr}$. Incomplete motional averaging in solution state or a fully anisotropic g, A or $e-e$ D tensor found at cryogenic temperatures (operational for DNP) will gives rise to line broadening, and thus obscure the signature of electron spin J coupling in the EPR line. This is true especially when J coupling is a small contributor to the EPR line, as is the case in a non-conjugated biradical molecule, yielding values on the order of a few to tens of MHz. Thus, EPR lineshape analysis at lower fields and in solution (as opposed to solid) state is the method of choice for quantifying the electron spin J coupling. In a recent study J was determined in the frozen state using a comprehensive multifrequency EPR approach.[60] In general, however, the effect of J coupling in the solid state can be easily hidden by the large $e-e$ dipolar coupling and other anisotropic line broadening mechanisms. Under such circumstances, with as many as 10 other parameters required to fit the spectrum, the determination of J will be quite challenging.

EPR lineshape analysis To determine the J coupling at each temperature based on the splitting pattern of the EPR spectrum in solution, we first evaluated the isotropic A value from the field separation between the 3 hyperfine lines. Then, an approximate

value of J was obtained by fitting the line positions of the EPR spectrum. Given this approximate value of J, a linewidth (FWHM) was determined by fitting the first hyperfine peak to a Gaussian broadened test spectrum with all other features ignored. In order to obtain a satisfactory fit we, subsequently, considered a range of J values. Since we do not know the distribution of J *a priori*, we first simulated the EPR line for multiple values of J. These EPR lines were then summed together and weighted according to a distribution function. This distribution function was then varied until a satisfactory fit was achieved. Typically, the broadening of an EPR line takes the form of a Gaussian and/or Lorentzian shape.[74] For convenience, a single distribution function (Gaussian or Lorentzian) was used to characterize the distribution of J, specified by its central value and FWHM. In all cases for AMUPol and TOTAPol, a purely Lorentzian distribution gave between $2-10\%$ superior fit than a purely Gaussian distribution. However, an interpretation of the shape of the distribution in terms of the molecular basis underlying this distribution function is beyond the scope of this paper. The importance of including this distribution is illustrated in Fig. 3.3. A residual dipolar coupling (D) was also included in order to account for asymmetric features present in the low temperature spectra. For each point in the three dimensional (J, FWHM, D) parameter space the resulting weighted distribution of the spectra was normalized and the squared deviations (χ^2) from the observed spectrum obtained. D was varied in steps of 1 MHz from 0 MHz to 16 MHz. For AMUPol, J was varied from 15 MHz to 40 MHz in 0.5 MHz steps; and the FWHM was varied from 1 MHz to 50 MHz in 0.5 MHz steps. For TOTAPol, we initially assumed negligible J coupling, and thus varied J from 0 MHz to 250 MHz in 0.5 MHz steps and the FWHM from 1 MHz to 500 MHz in 0.5 MHz steps. The set of parameters that gave the minimum sum are the ones used in this paper. J and FWHM are presented in Fig. 3.4a-d, and D is shown in Fig. 2 in the appendix A. Error bars were determined from J and FWHM values (at the optimal D value) that were within

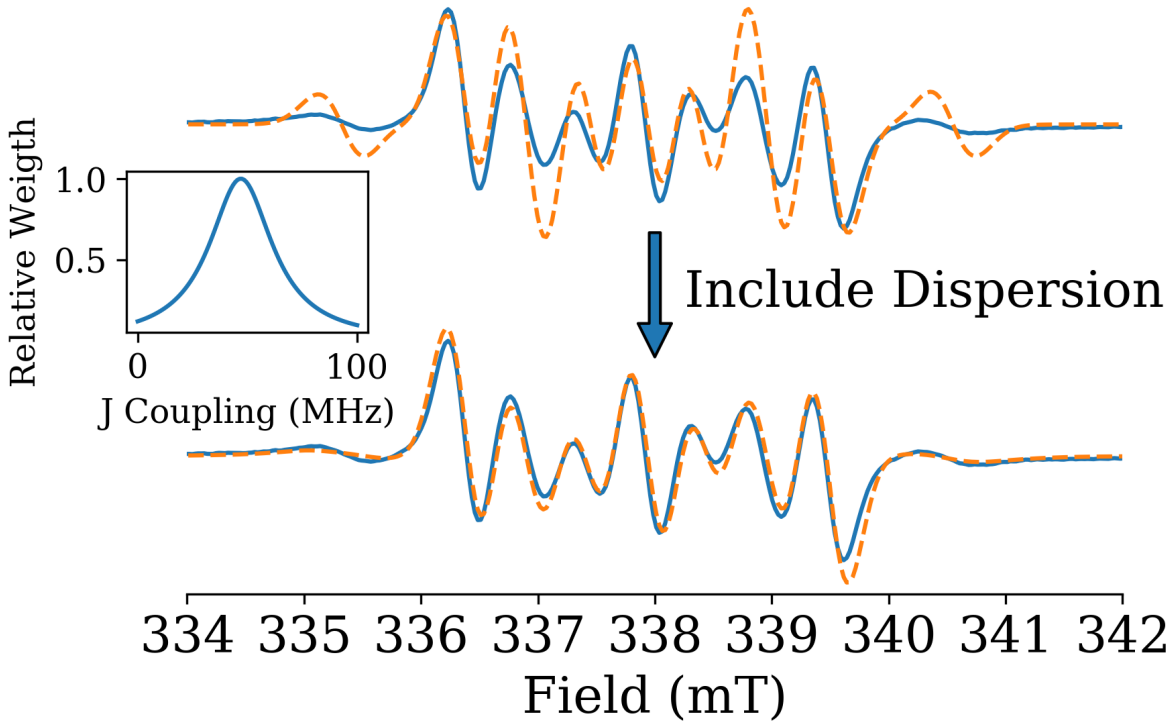

Figure 3.3: Comparison of simulation fit with (bottom) and without (top) a Lorentzian distribution of J values for AMUPol in H_2O at $95C°$. Inset is the distribution of J used to generate the bottom fit.

$1.25\chi^2$ of the global minimum (forming an ellipse), similar to what was done in the study by Soetbeer et al.[60]

AMUPol For AMUPol, the fitted mean J values ranged from 18 to 27 MHz (Fig. 3.4a) across all solvents and temperatures examined. These J values are comparable to those reported in the literature for biradicals of similar length and linker composition, as well as previously reported values for AMUPol.[50, 57, 63, 62]. However, each individual spectrum also revealed a broad distribution of J values (FWHM) which, when modeled with a Lorentzian function, ranged from 10 to 34 MHz, as shown in Fig. 3.4b. Both, the mean J and its distribution increased linearly with temperature in all solvents (Fig. 3.4a-b). The rate for the increase in J and FWHM is similar in all cases, with the exception

of toluene at higher temperatures. This trend breaks down below 20°C in DNP Juice due to residual anisotropic interactions. We also observe that the J value is higher by ∼7 MHz at a given temperature in toluene and H_2O compared to in DMSO or DNP juice. Similarly, the FWHM in toluene is 10-15 MHz greater than in the other solvents.

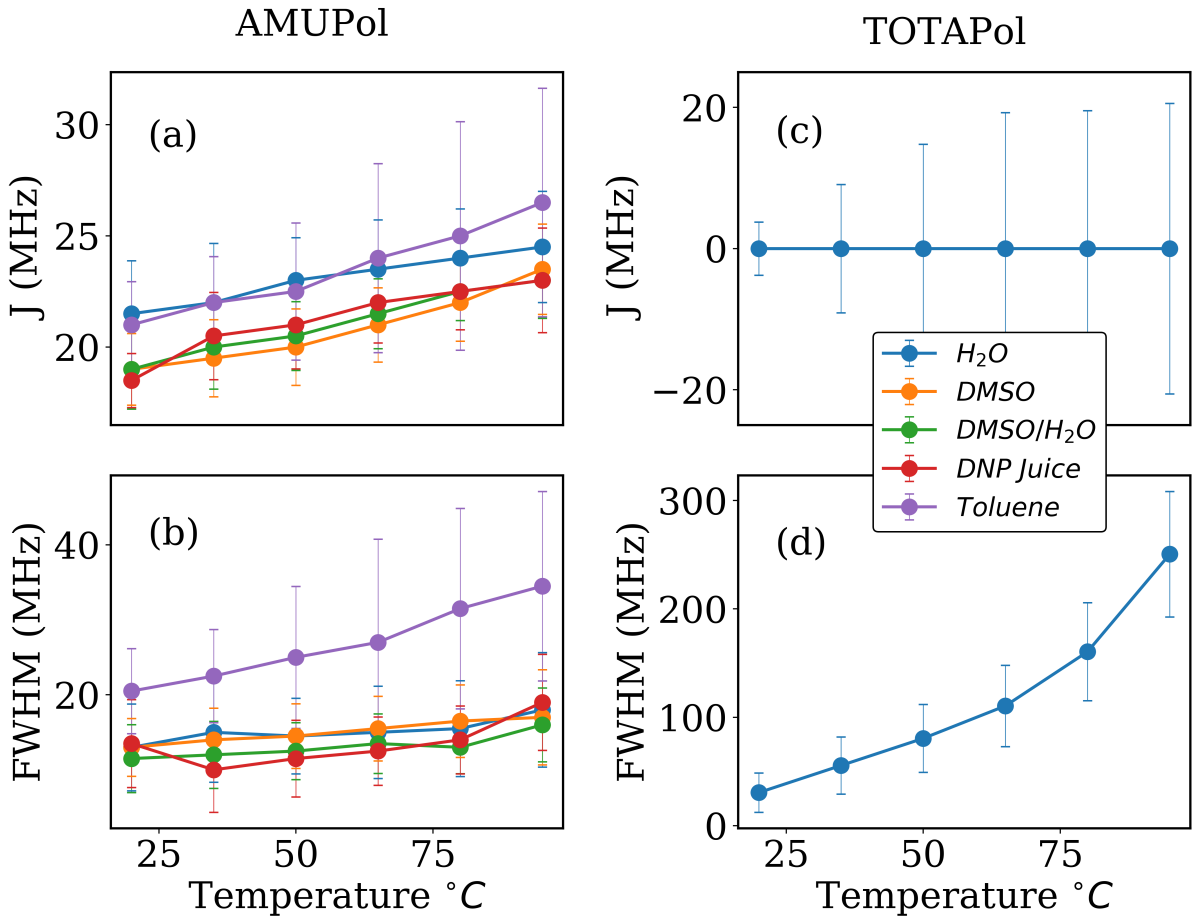

Figure 3.4: (a) Change in J coupling due to Temperature and Solvent for AMUPol. (b) Change in the FWHM of the lorentzian distribution of J coupling with temperature for AMUPol. (c) Change in J coupling due to Temperature and Solvent for TOTAPol. (d) Change in the FWHM of the lorentzian distribution of J coupling with temperature for TOTAPol.

The increase in J values and their distribution with temperature indicate that a range of conformations of AMUPol exist in solution, and that additional conformations with higher J are populated at higher temperature. The nature of the distribution

described by a single, broadened, Lorentzian function can be explained by fast chemical exchange between a ground state with low J and excited state(s) with higher J, resulting in an effective J value that shifts upwards with temperature as the population shifts towards the excited states. The width of the J distribution may be ascribed to the superposition of many spectra, in slow chemical exchange between excited states with different J values.[62, 74] However, we do not know the source of these conformational changes *a priori*, but the shift in J and FWHM with temperature and solvent indicate that molecular dynamics of AMUPol is key to understanding the underlying mechanism.

An obvious source for the distribution of J values would be collisional/inter-nitroxide distance modulation. However, studies of nitroxide spin probes exchanging through water show that such $e-e$ J coupling drops off very quickly with inter-nitroxide distance.[75] At the inter-nitroxide distance of $\sim 1.32nm$ present in AMUPol, as validated by DFT calculations[49] and consistent with the experimentally determined dipolar coupling ($\sim 23MHz$)[57], the through-space J coupling should be negligible ($<< 1MHz$). This is supported by DFT calculations of through-space J coupling.[76, 77] Therefore, the J coupling must involve a through-bond mechanism that depends on the conformation of the molecular backbone of AMUPol. A previous study by Bryantsev et al. calculated the rotational energy barrier around the N-C(sp3) bond in substituted urea derivatives to be between 2 and 5 kcal/mol, making this rotation very feasible in solution state.[78] The equivalent rotation in AMUPol is indicated in Fig. 3.1a. Moreover, the large moments of inertia of the attached groups will lower the torsional frequencies and thereby increase the accessibility of excited torsional states. Hence, we postulate that conformational degrees of freedom, particularly internal rotations, give rise to the temperature-dependent distribution of J values in AMUPol. The underpinning for this hypothesis will be sought from broken symmetry calculations DFT.

TOTAPol EPR spectral analysis of TOTAPol were carried out only on the sample dissolved in H2O, given that the analysis of AMUPol found similar temperature dependence of J in all solvents tested. The temperature dependence of the X-band EPR spectrum of TOTAPol is even more dramatic than that of AMUPol. In Figure 3.2, the EPR spectra show the evolution of two additional lines with increasing intensity at elevated temperatures, clearly indicating the presence of additional spectral component(s). The additional peaks become readily apparent in the range 50 - 95 $°C$, leading to a total of 5 spectral lines associated with very high J coupling relative to the hyperfine splitting ($J >> A$). Notably, the experimentally observed ratio of these lines (close to 2.2:1:2.5:1:2.2 at 25$°C$ and 1:1:1.5:1:1 at 95$°C$) is not what is expected of a strongly J coupled triplet system (1:3:5:3:1).[74] In fact, according to the model of Parmon et al.[62] the unexpected ratio of spectral lines can be described as being due to the superposition of at least two solvent-stabilized structures: one in an extended (negligible J coupled) conformation and one in a contracted (strongly J coupled) conformation. Additionally the lines in our experimental spectra demonstrate alternate broadening in which the line width of the 5 lines are not all equal. According to Parmon's model, the alternate broadening of the 5 spectral lines demonstrates that molecular motion in the strongly J coupled conformation leads to a range of J values over which $J >> A$ is not always true.

Given the above description, the temperature dependence of the TOTAPol spectrum can be modeled by a distribution of J values as we have done for AMUPol. The fits are shown in Fig. 3.2, and the resulting values for J and FWHM are shown in Fig. 3.4c-d. It is noteworthy that both solvent-stabilized structures can simultaneously be accounted for by a single Lorentzian distribution of J values centered around $J = 0$, as illustrated in Fig. 3.5. This suggests that we are sampling a distribution of conformations that exist between the extreme cases of extended ($J = 0$) and contracted ($J >> A$) forms.

In contrast to AMUPol, the central J value does not shift with temperature, indicating

slow exchange between conformations.[62, 79] However, the FWHM of the Lorentzian distribution increases drastically with temperature from 30 to 250MHz (Fig. 3.4d) as more population is shifted to higher J coupled states. To illustrate the severity of this effect, as well as offer a comparison to AMUPol, the best fit distribution of J for the low and high temperature conditions were plotted together for both molecules in Fig. 3.5. We clearly can recognize the increase of J coupled components with temperature in TOTAPol. We conclude that increasing temperature leads to the population of a second structure in TOTAPol which, in turn, strongly increases the accessibility of states with a broad distribution of J values. This conclusion is consistent with the DFT calculations that will be presented in the following sub-section.

The strong temperature dependence for TOTAPol, in particular, suggests that the glassing method and freezing history can dramatically alter the distribution of J values encountered under DNP conditions ($< 100K$). For the two biradical studied here, J generally decreased with decreasing temperature in solution state, because temperature affects the conformational equilibrium of these radicals and the e-e collision frequency. Hence, rapid freezing would effectively lock the distribution of J, as the J in and of itself is not temperature dependent at the cryogenic temperatures relevant for DNP. This might explain the dramatic, but also consistent, variation in absolute DNP enhancement seen as a function of the type of solvent and glassing agent, as well as freezing history used, for the DNP sample preparation.[80]

3.4.1 DFT Calculations of J Coupling

AMUPol In order to justify our qualitative interpretation of J coupling in AMUPol and TOTAPol we have carried out broken symmetry DFT calculations as described in Sec.2.4. It has been shown by Barone et al. and others that in small, planar, nitroxide biradicals

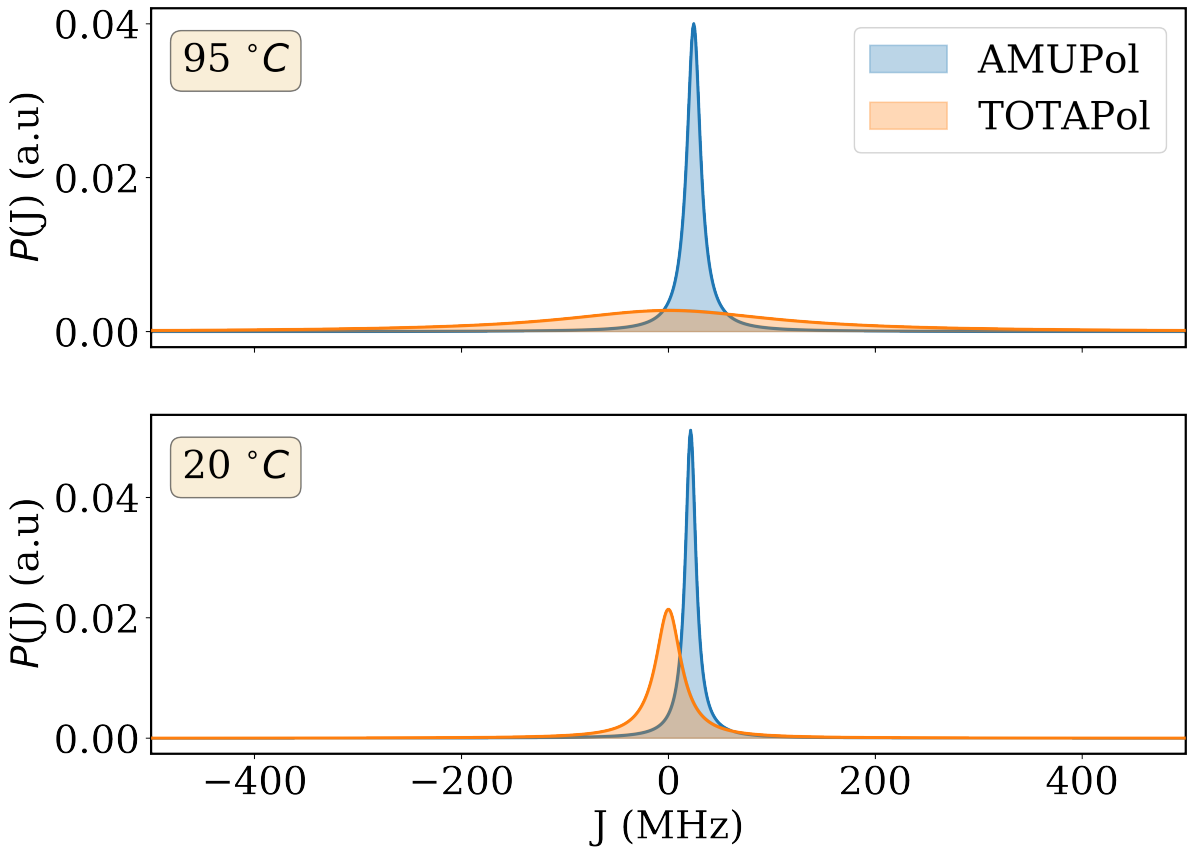

Figure 3.5: Comparison of J Coupling in TOTAPol and AMUPol in water at 20°C and 95°C. Note that the effects of negative and positive J are indistinguishable from each other in solution state spectra (i.e -5 and 5 MHz of J coupling would have the same effect.

the dihedral angle between the radical moieties greatly affects the J value.[77, 81, 82, 83] For the molecules of interest here, the situation is more delicate because the nitroxide mono-radicals are further apart and the J values are much smaller. Thus, we must be very careful with regard to the precision of our calculations. Figure 3.6a shows the effect of numerical precision in the SCF calculation. In this Fig. we present the average absolute deviation of J from the value obtained with 10^{-9} Hartree convergence tolerance for 18 equally spaced torsional angles around the N(H)-cyclohexyl bond (shown in Fig. 3.1c) of a trimmed AMUPol molecule (Fig. 3.1c) using the CAM-B3LYP functional and SVP basis set. We see that the average absolute deviation in J is converged to less than 1

MHz at 10^{-8} hartrees. To ensure sufficient accuracy, all calculations were carried out with a tolerance of 10^{-13} hartrees.

Broken symmetry DFT is known to overestimate the magnitude of J coupling, although this effect is minimized by using hybrid functionals.[72] Here we tested several functionals for the evaluation of J. Figure 3.6b shows J as a function of torsional angles for the same trimmed AMUPol molecule discussed, using the same SVP basis set and the B3LYP optimized triplet state geometry (see Fig. 3.1c). The GGA functionals BP86 and PBE substantially overestimate the J values for AMUPol from the experimental results. This overestimate is reduced for the hybrid functionals B3LYP and PBE0, which gave nearly identical results. Finally, considering that the interaction between the nitroxide radicals is over a long range, we examined the range-separated hybrid functionals CAM-B3LYP, wb97x, and LC-BLYP. The range-separated functionals reduced the J values further still, and yielded results in excellent agreement with each other. Thus, these functionals appeared most promising to us.

In order to justify the use of the relatively small SVP basis set[84] in the above discussed tests we compared it to the larger TZVP[84] basis set. As can be seen from Fig. 3.6c, this simplification has only a minimal effect on the J values. The result shown here is from using the CAM-B3LYP functional.

The above tests on the trimmed AMUPol structure suggest that CAM-B3LYP calculations of the rotational dependence of J should be suitable for the full molecule. Moreover, a comparison between the trimmed and full molecules, shown in the appendix A, exhibits very similar trends in the behavior of this property. We use this comparison to justify the use of the same DFT parameters (functional, basis set, integration accuracy, etc.) for the full molecule that were used on the trimmed version, while the final broken symmetry calculations of J (with settings determined using the trimmed molecule) was carried out using the full molecule. The so determined J values for the full molecule,

as given in Fig. 3.7a, gave remarkably close values to the experimental results of 18-27 MHz.

In Fig. 3.7a we observe that even a small change in the relative orientation of the nitroxide g-tensors, induced by a small change in the dihedral angle of only a few degrees, can lead to a significant ($5MHz$) change in the value of J. The change in J appears jagged with the change in the relative torsion angle, which is likely due to specific interactions involving the bis-nitroxide side chains. This is supported by the observation that J is a much smoother function of the torsion angle in a smaller and lower complexity bis-nitroxide radical with larger J values (shown in Fig. S8). As expected, we also observed substantially higher values of J for the two torsional energy minima visible in Fig. 3.7a (corresponding to rotamer states of the molecule). While the large rotational energy barriers at $-100°$ (26 kcal/mol) and $140°$ (28 kcal/mol) preclude tunneling at reasonable temperatures in solution, the low energy torsional states of the equilibrium configuration could very well be rapidly exchanging at room temperature; leading to the behaviour of J observed at various temperatures.

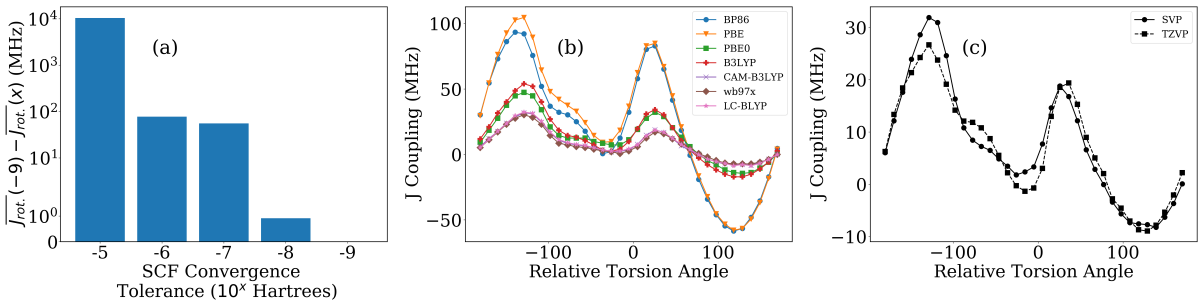

Figure 3.6: Tests of broken symmetry DFT calculations using the trimmed AMUPol molecule, shown in Fig. 3.1c, for dependence of J on (18 equally spaced) torsional angles. (a) Effect of SCF energy convergence criterion (numerical precision). Shown is the CAM-B3LYP/SVP average **absolute** deviation with respect to a convergence tolerance of 10^{-9} Hartree. (b) Effect of various functionals (SVP basis).(c) Comparison of TZVP and SVP basis sets using the CAM-B3LYP functional.

TOTAPol To verify that there exists at least 2 states relating to the extended/contracted conformations of TOTAPol found experimentally, we carried out geometry optimization of TOTAPol starting from a cis and a trans conformation. Indeed, two distinct, locally stable, geometries were found depending on the starting conformation, as illustrated in Fig. 3.7b-c (top). The energy difference between these two structures is only 1.63 kcal/mol, with the extended one being the ground state, suggesting significant populations of both conformations in solution. To provide a basis for the observed distribution of J, we repeated the analysis used on AMUPol (CAM-B3LYP/SVP) for both conformations (Fig. 3.7b-c bottom). The J values for the contracted, cis, conformation ranged from -800 to 400 MHz with higher potential energies generally corresponding to higher absolute values of $|J|$. For the extended, trans, conformation the J coupling vanished at all torsional angles.

The broken symmetry analysis shows that the contracted conformation of TOTAPol possesses significantly higher J coupling than the extended conformation. This supports our EPR data since the Boltzmann population will increasingly populate the contracted conformation at higher temperatures, thus increasing the density of states with high J coupling. J values can be positive or negative. Hence, given that the mean J value is around 0, increasing J will be reflected in a broadened J distribution. Thus the dynamic equilibrium between these states is likely the origin of the alternatively broadened EPR lineshape, which gives rise to the large distribution of J coupling.

The broken symmetry DFT calculations provide a glimpse at the complicated conformational landscape of TOTAPol and its role in the origin of the distribution of J values. Because of the many nuclear degrees of freedom, however, it provides only a limited picture of the results described by our EPR lineshape analysis.

The broken symmetry DFT calculations of J presented in this paper yield experimentally reasonable values, even when they are as small as 3×10^{-9} hartrees (20 MHz).

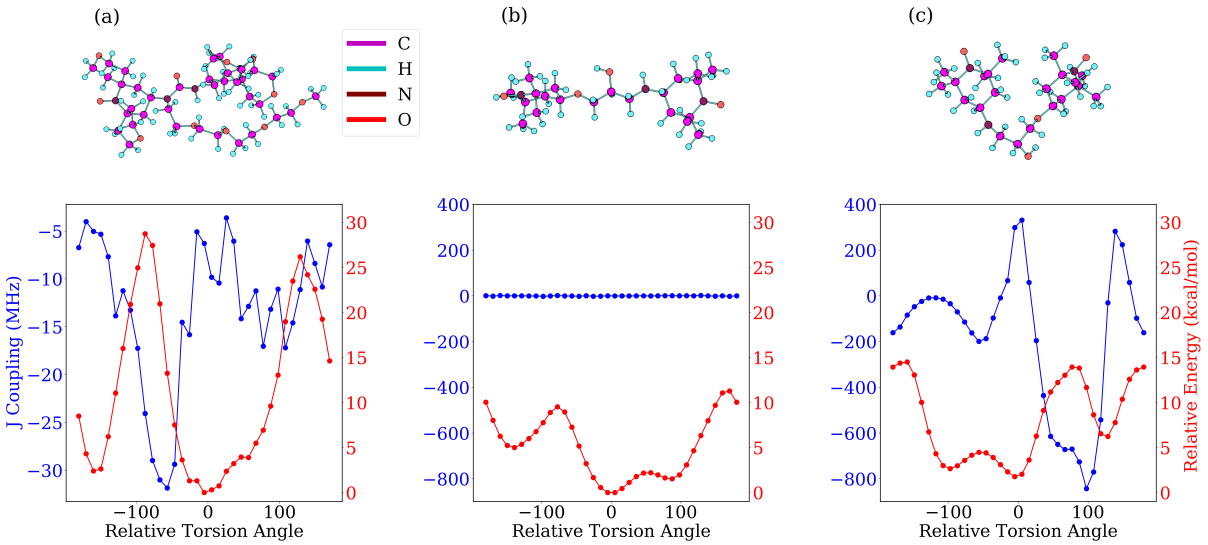

Figure 3.7: Broken symmetry DFT J values as a function of torsional angle for AMUPol and TOTAPol (extended and contracted structures). The equilibrium geometries are shown at the top. J values are shown in blue and relative torsional energies are shown in red. (a) Torsion around the R-N-C-C dihedral angle in AMUPol (see Fig. 3.1a). (b) Torsion around the C-N-C-C dihedral angle in the extended form of TOTAPol (see Fig. 3.1(b)). (c) Torsion around the same C-N-C-C dihedral angle in the contracted form of TOTAPol (see Fig. 3.1(b)). The torsional energies in (b) and (c) are with respect to the equilibrium extended geometry, which is the global minimum.

However, we should also emphasize that such calculations are the subject of current theoretical development and require refinement and further validations.

While the dihedral angle, by itself, plays an important role in the determination of J coupling, it is almost certainly not the only structural factor that does so. In molecules as large as AMUPol or TOTAPol, there are many other nuclear and molecular degrees of freedom that can modify the J value, either independently or through interaction with the dihedral angle. For example, the cyclohexane ring structure" is expected to affect J. [85] In any case, our study clearly demonstrates that a distribution of biradical conformations leads to a distribution of J values.

Hence, the next question is what effect the J coupling has on DNP enhancement. This is, in fact, still an open question because it is experimentally impossible to fully

separate the effect on DNP of J coupling *vs.* D coupling *vs.* g-tensor orientation. Thus, to single out the effect of J coupling on DNP, we turn next to quantum mechanical DNP simulations.

3.4.2 DNP Simulations

In order to ascertain the role of J coupling in CE-DNP of the biradicals studied here, and thus of their rotamer states, quantum mechanics - based numerical simulations were carried out for a 3 spin ($e_1e_2^1H$) system under MAS, at 100 K and 9.4 T conditions. Figure 3.8 is a plot of the simulated ^{1}H enhancement (ε) as a function of the J value, for different relative g-tensor orientations determined by β in the Euler angle set [107°, β, 124°] (zyz convention) that describes the orientation of e_2 with respect to e_1. The microwave field amplitude (nutation frequency) and the $e-e$ dipole coupling were set to 0.8 MHz and 19 MHz (r_{ee}=1.39 nm), respectively. The e_1-H and e_2-H dipolar couplings are set to 2 MHz and 0.04 MHz, respectively. From Fig. 3.8a, it can be seen that the g tensor orientation (at a spinning speed of 10 kHz) plays a significant role in determining ε. Even for J = 0 the optimum ^{1}H ε varies from negligible enhancement up to 200 fold as a function of merely the g tensor orientation. Figure 3.8a clearly shows that the impact of J is modulated by the g tensor orientation. Importantly, we also observe that increasing J increases ^{1}H ε, regardless of the g tensor orientation, up to a threshold J value of about 15 MHz. Since the J value and the g tensor orientation are intrinsically linked to the torsional angle, the rotamer states of the biradical will critically modulate ε. We also note that for J exceeding a value of the order of the nuclear Larmor frequency (a few hundred MHz) a further increase in J leads to a decrease in ^{1}H ε (data not shown). This has been shown experimentally for mixed and tethered TEMPO-trityl type radicals in which too large J coupling impedes DNP enhancement.[34, 86]

A major boost in ε comes with inclusion of J-coupling above a threshold (and below a ceiling) value. At the optimum g-tensor orientation (β=90°), a gain by a factor of > 2 is observed for $|J| \sim 15$ MHz, at 9.4 T. The reason a $|J|$ value comparable to $|D|$ has a much larger effect is that, unlike $|J|$, the dipolar coupling constant ($\frac{\mu_0 \gamma_e^2}{4\pi r_0^3} = 19$ MHz for $r_0 = 1.39$ nm) is scaled down by orientation averaging (due to sample spinning) as will next be illustrated.

The effect of orientation averaging on DNP can be seen in Figure 3.8b where we plot ε for ^{1}H as a function of spinning speed, with and without J coupling. The conditions used for this calculation were taken from the highlighted point in Fig. 8a. Without J coupling the enhancement drops significantly with increasing spinning speed from ^{1}H ε 500 to a small value. The inclusion of J completely mitigates this effect entirely, with almost no loss observed in ^{1}H ε at higher spinning speeds.

To gain a deeper insight from DNP simulations under MAS, we present a map of ε at 10 kHz spinning for a powder sample with 100 random molecular orientations. The same two cases as in Fig. 3.8b are shown. Evidently, in the presence of J (as well as D) coupling, a large number of orientations ($\sim 80\%$) show an enhancement close to the theoretical maximum of 660. On the other hand, when only dipole coupling is present, just a few orientations contribute to such high enhancements. This is because dipolar coupling is anisotropic, and only fully effective for select few molecular orientations. Under fast MAS and high B_0, this anisotropy attenuates the Landau-Zener adiabatic transition probability for rotor events leading to CE-DNP polarization. It also reduces the $e - e$ spin exchange probability at a given $e - e$ (degenerate) level crossing, thereby reducing the steady state polarization difference between the two electronic spin states. These effects have been proposed by Mentink *et al.* to rationalize the reduced DNP depolarization effect seen with strongly dipolar coupled biradicals.[61] Unquestionably, the presence of J coupling significantly augments the CE-DNP performance, especially

at faster spinning frequency, which is an increasingly important experimental condition for contemporary solid state NMR.

In the two cases presented here, our X-band EPR results suggest that it would be advantageous to vitrify AMUPol or TOTAPol from higher sample incubation temperatures to ensure the J coupling density exceeds 15 MHz. Figure 3.5 shows that for AMUPol and TOTAPol, a significant population density with very low J coupling remains, especially at temperatures below room temperature and especially for TOTAPOL. Moreover, the decrease in J with temperature is expected to continue at lower temperatures (down to above the freezing temperature). It seems that the DNP enhancement can be quite sensitive to the incubation temperature of the sample before vitrification through its effect on J.

3.5 Conclusions

EPR lineshape analysis of biradical samples equilibrated in different solvents and at different temperatures show that there exist multiple electron spin J coupling values for TOTAPol and AMUPol. Moreover, the mean value and the width of the distribution increase with temperature, in solution state. From temperature and solvent dependent EPR lineshape analysis, as well as Broken Symmetry DFT calculations, we conclude that for AMUPol this behavior is due to the varying population of different rotamer states that are undergoing rapid chemical exchange with one another. This effect is observed because even small changes in torsional angle can induce significant change in J due to variation in the relative g-tensor orientation of the nitroxide moiety. For TOTAPol, the extreme dependence of J on temperature is due to both rotamer, and extended *vs.* contracted states. Our results illustrate that biradicals in solution can have dramatically differing J coupling values, depending on the equilibrium temperature, as well as the

solvent type and, of course, the biradical structure. Consequently, the equilibration conditions and freezing history of the sample can significantly alter the J coupling effect in frozen biradicals used for DNP.

The significance of the above findings is recognized through quantum-mechanical simulations illustrating that the CE-DNP efficiency is dramatically boosted under MAS up to a value for ^{1}H $\varepsilon \sim 500$ in the presence of a small/moderate J value (> 15 MHz, but less than a few hundred MHz, in the case considered). In contrast, the effectiveness of a comparable dipolar coupling value is negligible and eliminated under MAS.

The results reported here provide important insight into the role of J coupling in CE-DNP of binitroxide radicals. However, a more firm and detailed understanding of the molecular basis of J coupling remains desirable. One aspect that requires further consideration is the BS DFT calculation of small J values. Although our BS DFT treatment remarkably reproduced the experimental values, additional authentication is needed and, perhaps, even methodological development necessary. Moreover, we have focused on the effect of a given torsion angle and neglected other low frequency nuclear motions that could be significant by themselves, or in combination with torsion, on the J coupling and DNP efficiency..

Acknowledgement

This work was supported by the National Science Foundation (NSF) (CHE #1505038 to SH) and the Binational Science Foundation (Grant #2014149 to S.H.) The content is solely the responsibility of the authors and does not necessarily represent the official views of the funding agencies. I.K. acknowledges support of the long-term postdoctoral fellowship by the Human Frontier Science Foundation. We also acknowledge Phillip Chen for his work with broken symmetry DFT calculations.

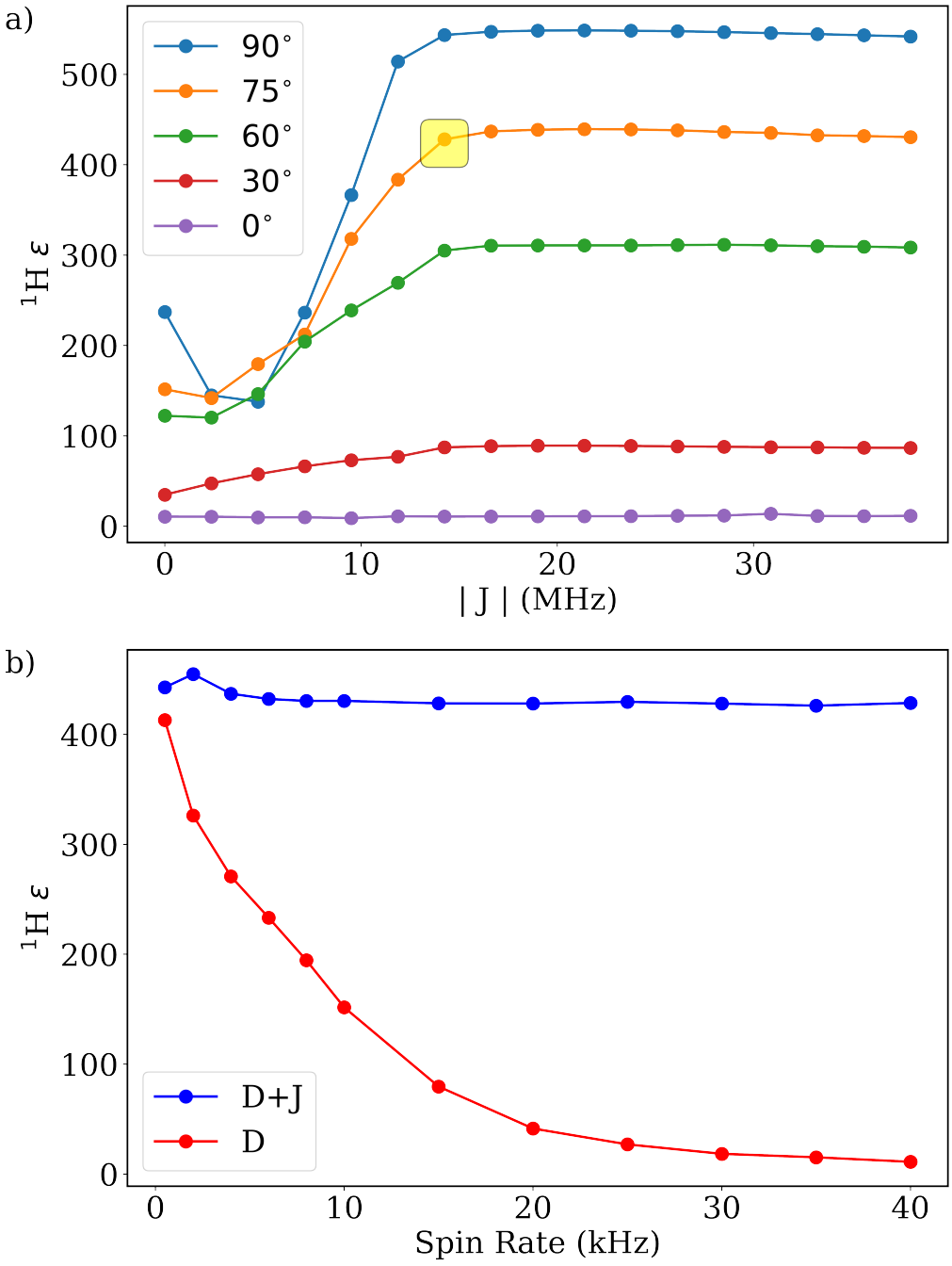

Figure 3.8: (a) ^{1}H DNP enhancement as a function of $|J|$ for different relative g-tensor orientations (varied with β; see text) of two nitroxide radicals with a dipolar coupling of 19 MHz, spinning speed of 10 kHz, B_0 field of 400 MHz (9.4T), and μw amplitude of 0.8 MHz. T_1 of electron spins was set to 3ms. (b) ^{1}H ϵ *vs.* spin rate in presence (blue) and absence (red) of J coupling for the parameter highlighted with a yellow box in (a), i.e. $|J|$=15 MHz and β=75°.

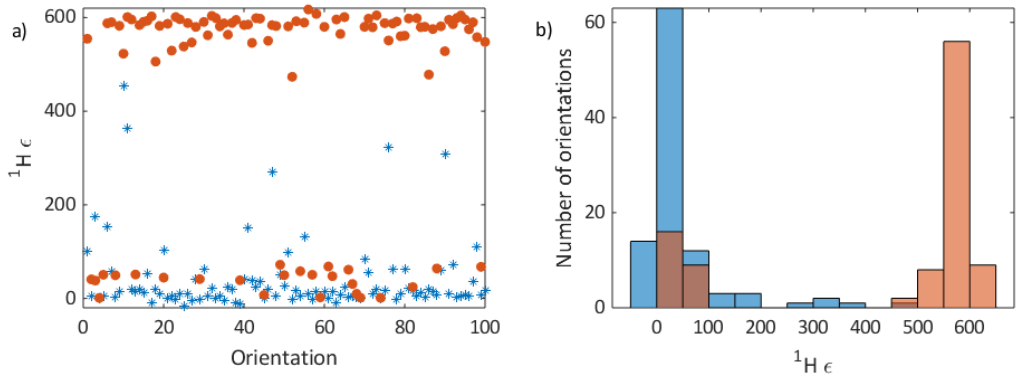

Figure 3.9: (a) ^{1}H DNP enhancement for 100 different molecular orientations in a powder sample under the same conditions as Fig. 3.8b : (i) only dipolar coupling (blue) and (ii) dipolar and J-coupling (red); (b) Histogram distribution of enhancement in (a).

Chapter 4

AWG DNP

4.1 Permissions and Attributions

1. The content of chapter 3 and appendix B are reprinted with permission from the Journal of Phyiscal Chemistry Letters.[4]. Copyright 2019 American Chemical Society. https://pubs.acs.org/doi/10.1021/acs.jpclett.9b03070

4.2 Introduction

The DNP process is mediated by microwave (μw) irradiation of the electron spin's paramagnetic resonance; and occurs through distinct mechanisms that can be broadly classified into three categories, the Overhauser Effect (OE)[13], Solid Effect (SE) [87], and Cross Effect (CE) [40]. Of these, the CE is the most effective mechanism to achieve DNP for insulating solids at high magnetic fields. Recently, OE was also reported for insulating 1,3-bisdiphenylene-2-phenylallyl (BDPA) dispersed in polystyrene [88]. But deeper insight into the mechanistic basis of OE in insulating solids under cryogenic temperature is needed before its utility can be relied upon [89]. CE is based on a three-spin

system - two coupled electron (e) spins, coupled to a nuclear (n) spin. The polarization transfer mechanism operates through simultaneous flip-flop-flip of the three spins ($e-e-n$) when the difference in the electron paramagnetic resonance (EPR) frequencies of the two e spins matches the Larmor frequency of the n spin. This ensures that the process is energy conserving [90].

The extent of polarization transfer from e to n is proportional to the polarization difference (ΔP_e) between the two CE-fulfilling e spin ensembles, which is created by μw irradiation of the e spins of the polarizing agent (PA). Note that even in the absence of μw irradiation at thermal equilibrium, the CE-fulfilling e spin can have a polarization difference that constructively contributes to polarization, or destructively to depolarization.[91] Typically, continuous-wave (CW) μw irradiation is used to selectively or differently depolarize (or saturate) the two CE e pair. However, the saturation efficiency is substantially decreased at higher B_0 field, higher temperature and faster MAS frequency because of decreased Landau-Zener (adibatic) transition probability [45, 47]. Consequently, the resulting DNP transfer efficiency also decreases under these regimes. Additionally, efficient CW-DNP is limited to a select few PAs and sample types. To broaden the scope of DNP and improve its efficiency in the above mentioned experimentally important regimes, concerted efforts have been invested at two key fronts: (i) the design and development of PAs and (ii) versatile high frequency μw technology.

The PA design has to be tailored to the underlying DNP mechanism. For MAS-DNP, tethered-radicals fulfilling the CE conditions are being developed [92, 49, 31]. Despite significant investment and impressive advancements made in PA design, the DNP performance is typically far below the theoretical maximum of γ_e/γ_n (660x for ^{1}H spins) at thermal equilibrium. With CW μw irradiation, the DNP performance relies exclusively on the complex and intrinsic e spin dynamics of the PA. Therefore, an important requirement for efficient and robust DNP is user-controlled manipulation of the e spin po-

larization. This can be achieved via time-dependent μw irradiation using recent advances in μw technology.

Time-domain ($non\text{-}CW$) methods such as nuclear orientation via electron spin locking (NOVEL) [93, 94], off-resonance NOVEL [95] and time optimized pulse (TOP) [96] offer solutions to overcome the field dependence of CW-DNP methods. However for all of these methods, the μw power or Rabi frequency ($\nu_{\mu w}$) needed to meet the $e-n$ cross-polarization resonance condition is enormous (tens to hundreds of MHz), and further increases with higher nuclear Larmor frequency (or the B_0 field). The high power demands restrict their applicability to lower B_0 fields ($\sim$1 T) with the current state-of-the-art μw technology.

Compared to the just discussed power-stringent techniques, broadband frequency or phase modulated/swept saturation of an e spin ensemble is a more accessible approach to boost DNP efficiency at high B_0 field. It also confers user-controlled spin manipulation capability, even with modest μw power. Previously, Hovav et al. [97], Bornet et al. [98], and Thurber et al. [99] (using field modulation) demonstrated this at a $\sim$ 3.3 T, 6.7 T, and 9.4 T magnetic field, respectively. In the first 2 studies, modulation was achieved by oscillations of the μw source in the frequency domain using voltage controlled oscillators; and in the last study, field modulation was achieved via an EPR modulation coil fed by a lock in amplifier. Arbitrary waveform generated (AWG) time-domain manipulation of the μw has principal advantages of versatility, speed and reaching a broader frequency span. Recently, Kaminker et al. demonstrated dramatically enhanced (up to 4x) CE DNP under static (non-MAS) conditions at 7 T by μw saturation relying, for the first time, on AWG pulse shaping in the time domain [100, 38]. Subsequently, static AWG-DNP has been exploited to achieve enhanced DNP using highly anisotropic (broad EPR line) PAs, such as transition metal complexes including Vanadium(IV).

Notably, all AWG techniques for DNP transfer reported in the literature have hitherto

been conceived and/or applied under static (sample) conditions only. MAS, however, is indispensable to achieve high resolution NMR of solid-state samples. Thus, there is an insistent need for AWG DNP techniques that work under MAS. Unfortunately, concepts learned from static DNP cannot be directly translated to and implemented under MAS, as fundamentally demonstrated by Thurber et al. and Mentik et al. [45, 47]. This is because the sample spinning renders additional time-dependence to the e spin dynamics compared to the μw dynamics, making the DNP process much more complex.

In this study we debut a novel concept to achieve enhanced DNP by AWG pulse shaping of electron spin polarization under MAS. Our study is based on experiments done using a custom 7 T DNP instrument with AWG capabilities, and quantum mechanical simulations. We discover that AWG-DNP (pulse shaped) has two major advantages over conventional CW-DNP. Firstly, AWG pulse shaping *broadens* the optimum DNP condition in the μw frequency domain, thereby recruit more e spins to actively and constructively contribute to the DNP effect. Secondly, it paves the way towards achieving *faster* e saturation for efficient CE DNP under short T_{1e} (e spin-lattice) relaxation conditions. Essentially, this fast and broadband (FAB) saturation using AWG will be vital for DNP using PAs that exhibit significantly heterogeneously-broadened EPR lines and fast relaxation properties, for polarizing agents with distinct non-overlapping spin populations.

4.3 Results and discussion

To explore AWG-DNP under MAS, we examined two classes of PAs that are commonly employed for DNP measurements: bis-nitroxide [48] and mixed narrow (Trityl) – broad (Nitroxide) line radicals (including a physical mixture, as well as chemically tethered PA) [2, 34]. Both PAs have their distinct advantages and limitations. Bis-nitroxide

radicals are stable and readily available, and therefore widely used, but their performance deteriorates severely at higher B_0 [101]. Mixed radicals are better performers at high B_0 field conditions, require much lower μw power and also exhibit a smaller depolarization effect, but are more challenging to synthesize [34, 102, 103, 61, 104]. We note that the choice for PAs in this study was based on availability and proving the principle, not by optimizing the expected performance.

To achieve *non-CW* pulse shaped irradiation, we upgraded our 7 T MAS-DNP spectrometer by implementing AWG pulse shaping capabilities, similar to what has been demonstrated with the dual EPR-NMR capable static DNP instrument [105, 38]. The AWG-DNP experimental schematic is shown in Fig. 4.1A. AWG irradiation has two defining parameters: (1) the frequency sweep width $\Delta\nu_{AWG}$, and (2) the AWG modulation rate given as a function of N, where N is the number of repetition of AWG blocks per rotor period, *i.e.* $\tau_r = N * \tau_{AWG}$, where τ_r and τ_{AWG} are the lengths of the MAS rotor period and the AWG-repeating unit, respectively. With AWG, any waveform can be implemented, but we first present conceptual advances with easy-to-implement linear chirp schemes, unless mentioned otherwise.

AWG-DNP using bis-nitroxide

Our first goal was to understand whether broadband AWG-DNP can improve the ^{1}H polarization enhancement compared with CW-DNP for a bis-nitroxide radical (simulated EPR spectrum using Easy-spin [66] shown in Fig. 1B.) under optimized conditions (i.e. PA concentration of 10 mM and glassing matrix composition of 60/30/10 v% d-glycerol/D_2O/H_2O). To this end, we chose the standard AMUPOL radical [49], which has previously been shown to yield 70% greater ^{1}H-DNP enhancement (ϵ_{DNP}) by AWG-DNP over CW-DNP under static conditions at 7 T [100]. In Fig. 1C the normalized

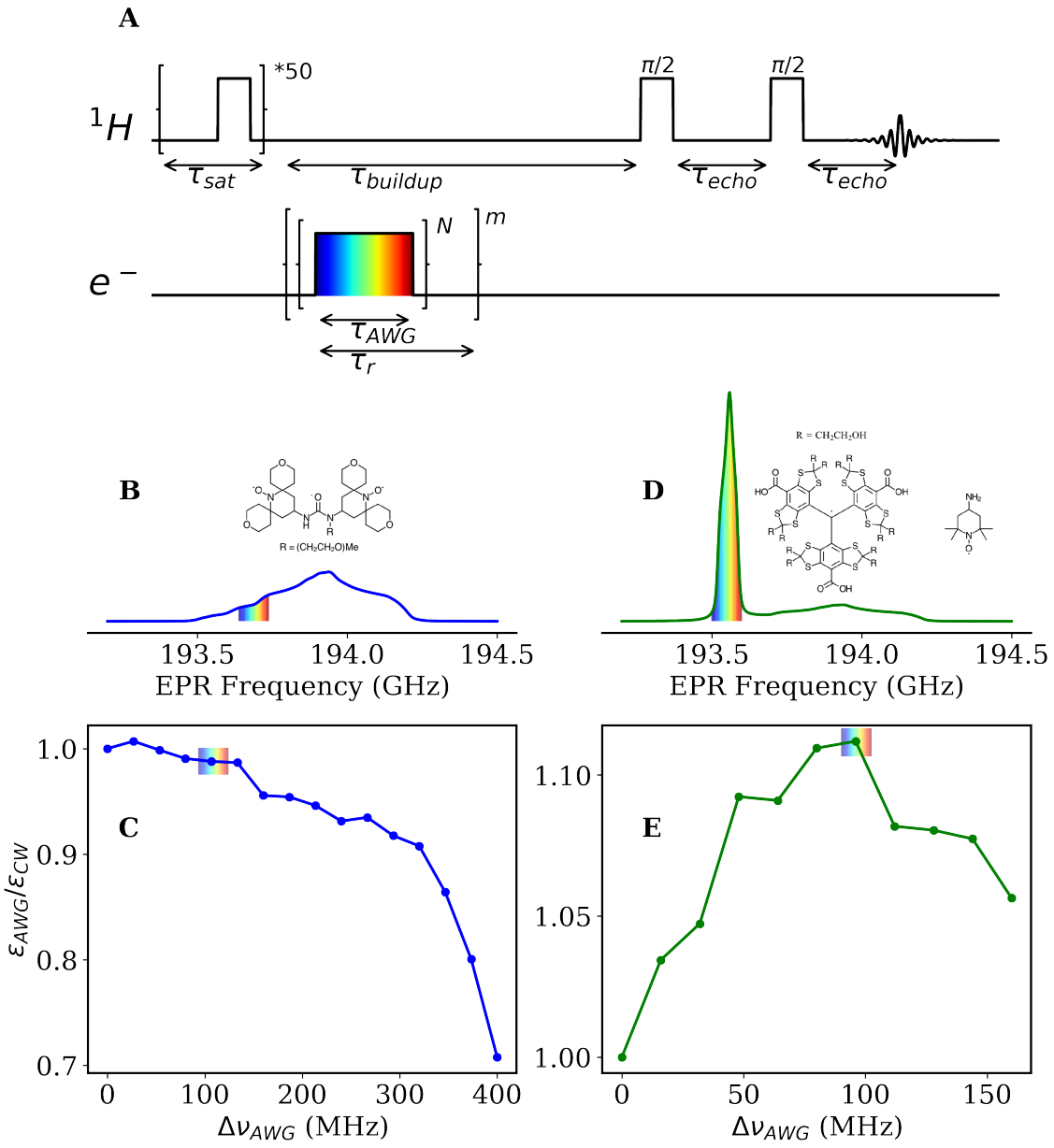

Figure 4.1: **Pulse schematic and AWG profiles for bis-nitroxide and mixed radical. (A)** Solid-echo pulse sequence, with pre-saturation pulses, used for detection of ^{1}H NMR signal. N blocks of AWG shaped μw pulses (rainbow) were synchronized with a rotor period, i.e. $N * \tau_{AWG} = \tau_r$. The DNP buildup time, $\tau_{buildup}$ was set to m times τ_r. AWG-DNP enhancement (normalized with CW-DNP) as a function of frequency sweep-width ($\Delta\nu_{AWG}$), acquired under 3 kHz MAS and 32 K conditions for **(C)** 10 mM AMUPOL radical with ν_0 =193.7 GHz and **(E)** physical mixture of 4-Amino Tempo (26.6 mM) and Trityl-OX063 (13.33 mM) with ν_0 =193.6 GHz. N=4. Their simulated EPR spectra are shown in **B** and **D**, respectively.

ϵ_{DNP} enhancement is plotted as a function of the frequency sweep width ($\Delta\nu_{AWG}$) of the linear-chirp pulse train. All experiments were done under conditions of MAS frequency (ν_r) of 3 kHz and at 32 K. The normalized $\varepsilon_{AWG}/\varepsilon_{CW}$ data ensures that the nuclear spin depolarization effects and bleaching effects are taken into consideration, as these factors are independent of μw irradiation. Clearly, compared to CW irradiation ($\Delta\nu_{AWG}$=0), ϵ_{DNP} decreased with increased $\Delta\nu_{AWG}$. Even with more sophisticated waveforms, the AWG-DNP did not lead to better ϵ_{DNP} for AMUPOL at the available 350 mW μw power at the μw source output. Hence, contrary to the results found under static conditions, we found that AWG (here chirp) μw irradiation deteriorated the ϵ_{DNP} of AMUPOL under MAS compared to CW irradiation. A priori, this might appear surprising; however, analytic insight can help us understand and rationalize this phenomenon. The DNP mechanisms for static and MAS samples are different [45, 47, 106]. While the energies of the spins are fixed in time for a static sample, under MAS they are time-modulated because of anisotropic g and dipolar interactions. Modulation of the EPR frequencies over the course of the MAS rotor period leads to multiple different resonance/degeneracy conditions (a.k.a rotor events [47]). These events can lead to various diabatic and adiabatic transitions between the coupled $e-e-n$ spin states, as detailed by Thurber and Tycko using the Landau−Zener (LZ) model [59]. Therefore, under MAS, the prominent interactions in the CE DNP mechanism, the spin-B_1 (μw induced e spin transition/saturation), and the spin-spin (e–e flip-flop and e–e–n flip-flop-flip) fields are time modulated. The LZ model provides an analytic solution to the transition dynamics for a time-dependent Hamiltonian in a two energy-level system. According to the LZ model, the adiabatic transition probability (P) at the resonance condition scales down with an increasing energy crossing-rate ($\dot{E} = dE/dt$), and scales up with the magnitude of perturbation (E_1); $P = 1 - exp(-\pi {E_1}^2/\dot{E})$. For example, the μw induced e spin saturation caused at the μw rotor-events depends on (a) the strength of the μw power (perturbations); and (b)

the rate of the energy change at the crossing, which in turn depends on the g-anisotropy and the MAS rate.

There are two challenges in improving the CE-DNP efficiency of bis-nitroxide radicals using AWG: (i) The two nitroxide e spins have similar EPR characteristics (line-width and relaxation rate); therefore, the selective saturation of one of the two CE e becomes unfeasible with increased irradiation bandwidth ($\Delta\nu_{AWG}$). (ii) μw modulation on top of the large EPR energy modulation of the broad nitroxide radical under MAS increases the effective energy crossing-rate, (dE/dt), at μw resonance conditions, and therefore lowers the μw induced EPR saturation probability. From this cogent LZ based description, it can be understood why the DNP performance of AMUPOL (bis-nitroxide radical) deteriorates with broad-band AWG-irradiation when using a low power μw source. However, numerical simulations also predict that a high power μw source (μw nutation frequency greater than 4 MHz) will increase the AWG-DNP efficiency of AMUPOL, but only marginally, as the selective e spin manipulation of such radical is still not straightforward (see SI, Fig. S6). With the availability of very high power and coherent μw sources, pulse schemes designed using optimal control theory may achieve maximal polarization differential (ΔP_e), but this is beyond the realm of state-of-the-art μw source technology.

AWG-DNP using mixed-radicals

Choosing a PA where the two e spins participating in the CE mechanism are already separated in their isotropic frequencies or non-overlapping in the frequency space, will circumvent the above discussed bottlenecks. Such PA will easily facilitate the selective μw perturbation or saturation of one of the e population. For this purpose, an ideal system would be a mixed narrow-broad PA. This is already available in the form of a Trityl-TEMPO physical mixture which was first introduced by Hu et al. and its tethered

biradical by Mathies et al. [107, 34]. Here, the smaller EPR line-width (g-anisotropy) of the narrow radical species will help increase the LZ μw transition probability, even at low-moderate μw power available with current μw source technology. This type of PA has shown promising potential to overcome the inefficiency of DNP at high B_0 field where the standard bis-nitroxide PAs failed to deliver high enhancements [34, 103]. Therefore, further improving the performance of these PAs using shaped pulse, *non-CW*, irradiation would be a momentous step forward towards efficient and robust DNP developments.

It is important to note that time modulation of spin energies under MAS allows a much larger number of e spin pairs to participate in the DNP mechanism as compared under static operation. Therefore, MAS by itself exhibits a *self-chirping* effect. A question arises: will AWG irradiation have an additional benefit if MAS by itself exhibits a *self-chirping*[45] effect ? Based on our analysis presented here, we reckon that AWG will indeed be crucial for further improving the DNP efficiency. The saturation of e spins with CW under MAS occurs at a rate governed by the MAS rate and rely predominantly on the relative orientations of e spins interaction tensors, leaving not much external and rational (user) control in such an experiment. In contrast, AWG permits enhanced control over the manipulation of e spin polarization, granted sufficient knowledge of the e spin system and necessary μw technology. Taken together, AWG MAS-DNP should be able to: (a) help saturate e spins at a much faster rate than MAS alone can do, and importantly (b) mitigate the e spin orientation dependence on saturation through broadband irradiation. Next, we test the validity of this concept.

TEMPO-Trityl physical mixture

To test AWG-DNP under MAS by exploiting non-overlapping spin populations for CE DNP, we chose the physical mixture of 4-Amino TEMPO and Trityl-OX063 in a 2:1 ratio as optimized by Li et al. in a recently published study [2]. A simulated EPR spectrum for

this mixture is shown in Fig. 4.1D which clearly shows the separation of spin populations. In Fig. 4.1E, the normalized ^{1}H-ε_{DNP} procured using AWG irradiation at $\nu_r = 3$ kHz is plotted as a function of the sweep width, $\Delta\nu_{AWG}$. The carrier frequency was set to the center of the Trityl resonance. Clearly, the ^{1}H-DNP enhancement for rotor-synchronized AWG (linear chirp) irradiation increased with $\Delta\nu_{AWG}$ until it reached an optimum at 85 MHz, close to the line-width of the Trityl-OX063 resonance at 7 T. Here $N = \tau_r/\tau_{AWG}$ was set to 4. The 10% increase in DNP enhancement represents the first successful demonstration of improving MAS-DNP using shaped pulse ($non\text{-}CW$) μw irradiation with a low power μw source. Importantly, this modest gain can be significantly improved by careful pulse shaping and higher microwave power, as well as optimized PA design. To prove this point, we showcase the benefit of moving beyond linear chirp irradiation towards shape optimized saturation later in this paper.

Tethered TEMTriPol-1

It has been reported in the literature that efficient CE-DNP is obtained using a tethered radical which has strong $e-e$ coupling, in particular, exchange (J) coupling because of its isotropic component [61, 108, 109, 3, 60]. However, owing to different radical conformers (e.g. rotamers), a wide variation in the relative g-tensors and the J-coupling between the two e spins is observed in the widely used biradical PAs [3]. Strong J-coupling splits the e spin density population away from the isotropic g value of a narrow line radical. And therefore, different J-coupling conformers will have different DNP optimum conditions with respect to the CW μw frequency [34, 61]. Monochromatic CW irradiation cannot simultaneously achieve optimum DNP for all conformers. Contrarily, AWG-DNP can encompass a significant fraction or all of the different spin populations, given its multi-frequency and broadband e spin saturation capabilities. This prospect is demonstrated using SpinEvolution based numerical simulation [65] for the tethered

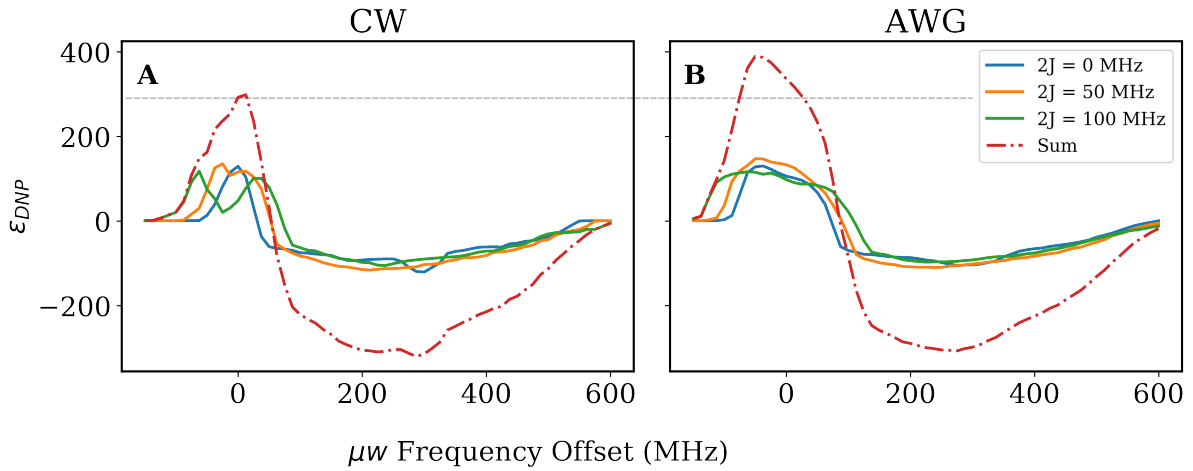

Figure 4.2: **Simulated DNP frequency profiles.** Numerically simulated ^{1}H-DNP enhancement vs. μw frequency offset for **(A)** CW-DNP and **(B)** AWG-DNP. The simulations were performed using $e_1 - e_2 - ^1$H spin system, taking g-tensors of the tethered Tempo(e_2)-Trityl(e_1) radical. Three different J-coupling conformers were considered. Averaging over three relative g-tensor orientations were done for each J-coupling conformer. MAS and $\nu_1^{\mu w}$ were set to 10 kHz and 0.8 MHz, respectively.

Tempo-Trityl PA. For simplicity, we take only three J-coupling components (with $2J$= 0, 50 and 100 MHz) weighted equally, while fixing all other spin parameters to be equal. Under CW irradiation, all components have different ϵ_{DNP} optimum conditions, as highlighted with dashed lines in Fig. 4.2A. Therefore, it is clear that we cannot fulfill these different optimum conditions simultaneously using CW irradiation for a PA populating multiple conformers giving rise to different J coupling values. In contrast, broad-band irradiation using linear chirp can fulfill the optimum condition over a broader and/or multiple frequency range, leading to larger overall ϵ_{DNP} than using CW irradiation. This is illustrated by simulation (Fig. 4.2B) that shows ∼30% gain in ϵ_{DNP} under the condition of MAS frequency of 10 kHz, $\nu_1^{\mu w} = 0.8$ MHz, $\Delta\nu_{AWG} = 100$ MHz and $N = \tau_r/\tau_{AWG}$ set to 4.

To illustrate this experimentally, we chose tethered TEMTriPol-1 radical provided to us by Yangping Liu (Tianjin Medical University, China) who originally designed and

synthesized this PA [**?**]. This is the most efficient water soluble PA at high magnetic fields (18T) reported in the literature to date [34]. Figure 4.3A shows the normalized ϵ_{DNP} frequency profile for this radical using CW and AWG irradiation. Clearly, the optimum DNP enhancement condition with respect to the μw resonance frequency for CW-DNP is very narrow. The shoulders (at the frequencies 193.47 GHz and 193.53 GHz) in its DNP frequency profile indicate multiple J-coupled conformers of the bi-radical. In such scenarios, AWG can be used to efficiently encompass a range of conformers in the DNP process, maximizing ε_{DNP}, as illustrated in Fig. 4.3A-B. Using a simple linear chirp irradiation scheme, with $\Delta\nu_{AWG}$ and N set to ∼200 MHz and 5 respectively, we observed a ∼15 % increased enhancement compared to CW irradiation at $\nu_r = 3$ kHz and a sample temperature of 32 K.

Custom AWG-DNP under MAS

Next, we applied AWG pulse train irradiation schemes using more advanced broad-band pulses than linear chirp, including WURST (wideband, uniform rate, smooth truncation) and custom broad-band pulses to the underlying EPR lineshape. The results are shown in Fig. 4.3D. For the same sample and experimental conditions as used for the linear chirp DNP, WURST irradiation led to a ∼25% higher DNP enhancement. The optimum $\Delta\nu_{AWG}$ of this scheme similar to that of chirp, as shown in SI (Fig. S5). In general, the AWG-DNP enhancement is expected to be increased using a more sophisticated irradiation scheme where the frequency is swept non-linearly for a fixed μw power for more effective saturation. In fact, the WURST scheme is widely used in NMR and EPR for broadband excitation and decoupling when limited RF power is available [110].

In the experimental regime of low power μw perturbation (rabi frequency) and comparable relaxation rate as present here, e spins cannot be coherently manipulated. Hence,

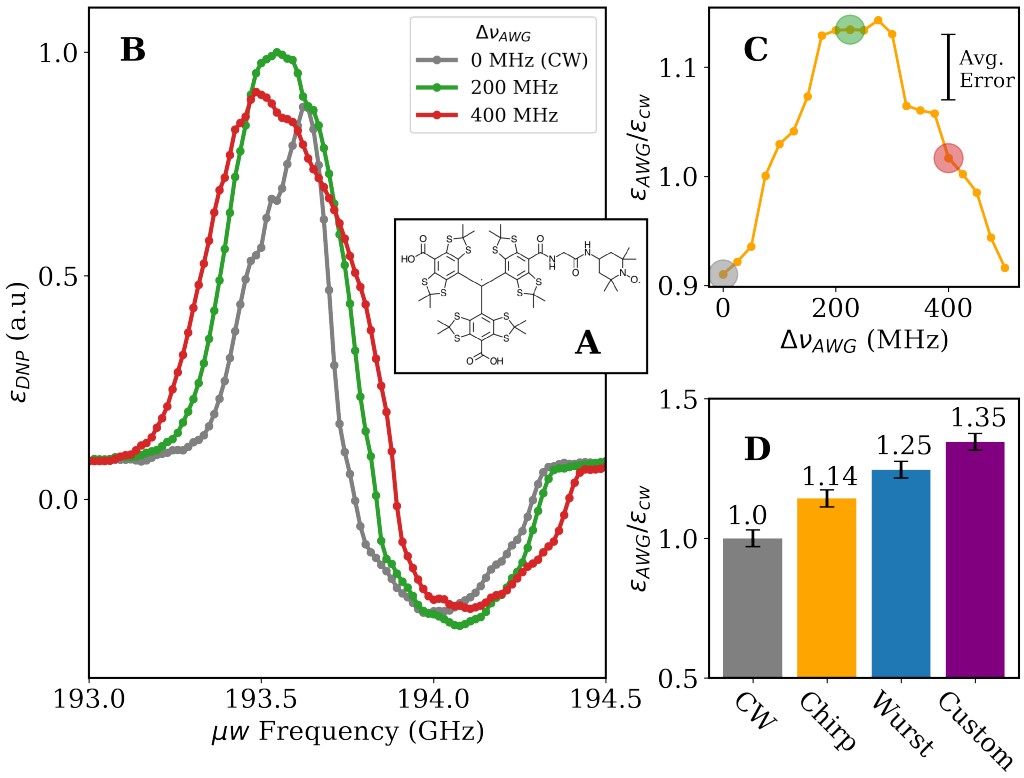

Figure 4.3: **AWG-DNP performance for TEMTriPol-1 radical. (A)** Chemical structure of TEMTriPol-1. **(B)** Experimental ^{1}H ε_{AWG} vs. $\nu_{\mu w}$ recorded for three μw irradiation schemes: CW (blue) and linear chirp with $\Delta\nu_{AWG}$ equal to 200 MHz (Orange) and 400 MHz (green). **(C)** Dependence of normalized ε_{AWG} on $\Delta\nu_{AWG}$ using the centre frequency set to the optimum (green) obtained in Fig. **3B**. **(D)** Experimental comparison of ε_{DNP} for various AWG schemes normalized with the maximum of CW-DNP. Optimization protocols as well as NMR spectra are provided in SI (section 2). All the experments were done under 3 kHz MAS, 32 K temperature, with $P_{\mu w} = 350$ mW and $t_{buildup} = 10$ s for 20 mM TEMTriPol-1 in DNP-juice. Error bars were determined from the maximum deviation of 10 consecutive runs of CW DNP.

broadband saturation in this regime will benefit from a non-linear μw power distribution across the EPR frequency as weighted by the EPR line intensity. To test the benefit of custom broadband saturation under MAS, we designed a waveform with $\Delta\nu_{AWG}$ set to 200 MHz and power distribution around the carrier frequency weighted by the CW-DNP profile. The relative DNP enhancement for various μw irradiation shapes are presented in Fig. 3C. We observe an even greater ($\sim$35%) increase in DNP enhancement with custom pulses compared to CW irradiation. For reference, a visual representation of this power profile and the corresponding waveform is shown in appendix B, Fig. 4.

DNP under fast electron spin-lattice relaxation conditions

One critical objective for broadening the scope of DNP is improving enhancement under fast relaxation conditions. Here we highlight the advantages of AWG towards DNP with fast relaxing PAs. The CE DNP mechanism, the method of choice, involves two essential spin transitions: (i) μw transition that saturates/depolarizes one of the two CE e spins, thereby creating a large polarization difference (ΔP_e) relative to the n spin polarization, and (ii) simultaneous flip-flop-flip of all three spins induced by the CE Hamiltonian when the resonance condition, $|\omega_{e1} - \omega_{e2}| = |\omega_n|$, is satisfied. The latter transition is intrinsic to the spin system, independent of the use of an optimized μw irradiation scheme. The amplitude of the CE Hamiltonian is solely dependent on the orientation of the e spin tensors because ω_{ei} changes with orientations (e.g. with sample rotation). In general, given the large g-anisotropy of a nitroxide radical, different rotor events are separated in time under MAS. At present, DNP under MAS is limited to the experimental conditions or PAs which have relatively long (100sμs to few ms at below 80 K) e spin T_{1e} compared to rotor period (τ_r). This is to ensure that the effect of different rotor events (separated in time) prevail over time and add up constructively,

leading to a net desirable DNP transfer. Hence, long T_{1e} is required so that the large ΔP_e created by μw rotor event is retained at the CE matching rotor event which leads to net DNP enhancements. Time delays between these two rotor events would essentially be proportional to τ_r, i.e. the time scale taken to change the orientation of molecule ($e-e-n$ spin system) from the μw rotor event to the CE rotor event. If T_{1e} is shorter than τ_r, then the delay between the resonances considerably attenuates ΔP_e at the CE resonance condition, and thereby the net achievable DNP. In the limit of very fast relaxation where T_{1e} is shorter than τ_r, CW-DNP becomes extremely inefficient, even in the high μw power regime. This is because the two events are separated in time longer than T_{1e}, so that the effect of saturation has vanished by the time the CE matching is satisfied. Of course, very short T_{1e} also reduces the efficiency of electron spin saturation of the μw rotor event itself. Theoretical consideration predict that fast frequency sweeps using AWG across the narrower EPR line at a rate faster than the sample spinning frequency will ensure that saturation or large ΔP_e is maintained at all the CE events. Here, we illustrate this effect through quantum mechanical simulation using SpinEvolution. Figure 4.4 shows electron and nuclear spin polarization profiles as a function of time (for one rotor period) when the e spins have reached their quasi steady-state conditions. Here, T_{1e} was set 10 times shorter than τ_r. As a result, the large ΔP_e created at the μw rotor event (Blue-bar) is reduced significantly (due to relaxation) by the time the CE matching condition (Red-bar) is reached. As a result, the increase in n spin polarization is minuscule under CW irradiation (Fig. 4A). Thus in a powder sample, CW irradiation leads to efficient DNP only for select spin packets, where the time delay between the μw and the CE rotor events happen to be negligible relative to T_{1e}. In contrast, a large ΔP_e can be maintained by AWG shaped irradiation, repeated at a rate much faster ($N = \tau_r/\tau_{AWG}$=20) than the MAS rate (Fig. 4.4B). Under this condition, AWG-DNP leads to large enhancements for a larger number of orientations ($e - e - n$ triplets), independent of orientations. This

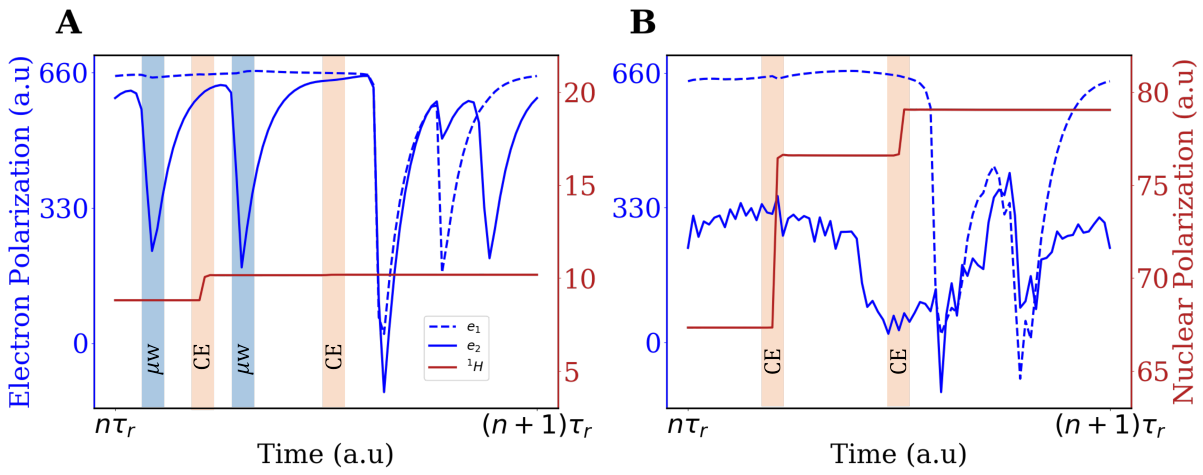

Figure 4.4: **Spins polarization trajectories.** Numerically simulated electron (blue, left y-axis) and nuclear (red, right y-axis) spins polarization trajectories measured for a single crystal orientation of $e_1-e_2-^1$H spin system with e_1 and e_2 mimicking Trityl and TEMPO, respectively. The polarizations are plotted for one rotor period at the steady-state conditions for e spins using **(A)** CW, and **(B)** AWG (linear chirp, N=80 and $\Delta\nu_{AWG}$=100 MHz) μw irradiation. Polarization sampling was done after every 5μs, i.e. the length of τ_{AWG}. MAS was set to 2.5 kHz and T_{1e_1}=T_{1e_2}=0.1τ_r.

is effectively illustrated in Fig. 4.5 which shows enhancement for 232 different α and β orientations in repulsion powder averaging scheme. For this case, AWG-DNP (Fig. 4.5B) leads to a 2.5x greater enhancement than CW-DNP (Fig. 4.5A) for the powder sample on average. It can inferred from Fig. 4.5, that AWG-DNP will lead to more uniform polarization enhancement of the nuclear spins in space whereas CW-DNP will be highly orientation selective under the above experimental conditions. Therefore, for conditions where T_{1e} $\leq$10μs, typically found with transition metals even at cryogenic temperatures (100 K) or with organic bi-radical PA at elevated temperatures $\epsilon_{AWG}/\epsilon_{CW}$ can be significantly boosted. A way to increase T_{1e} relative to τ_r would be to increase the spin rate but this will also lower the adiabatic transition probabilities of all the other rotor events [45, 47]. Moreover, spin rate is also governed by instrumental limitations as well experimental requirements.

As illustrated, the benefit of AWG is maximum under fast relaxation, but our exper-

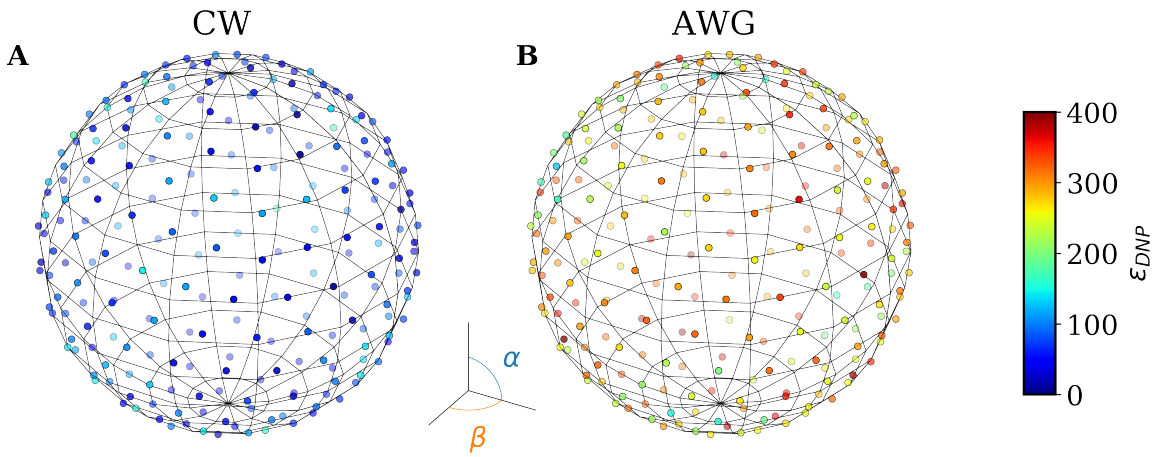

Figure 4.5: **Powder orientation dependence of CW and AWG-DNP.** (a)Simulated ^{1}H ε_{DNP} mapped for for 232 powder orientations of a $e_1 - e_2 - ^1$H spin-system mimicking TEMTriPol-1 PA, acquired using optimized **(A)** CW, and **(B)** AWG irradiation schemes at MAS = 10 kHz and $\nu^1_{\mu w}$ = 1.5 MHz. N=20 and $\Delta\nu_{AWG}$=100 MHz for AWG scheme. T_{1e_1}=0.1τ_r and T_{1e_2}= 0.5T_{1e_1}.

imental data shown so far is at 32K to compensate for the low μW power available with our source. However, at higher temperature the relative gain $\epsilon_{AWG}/\epsilon_{CW}$ becomes larger as T_{1e} becomes shorter as shown experimentally in appendix B Fig. 5b.

Microwave power dependence

Frequency agile, solid-state μw sources such as the ones used in this experiment have a limited power output. Fortunately, advancements in μw technology is constantly raising the power output of frequency agile sources. Here we analyze how these higher μw power sources would improve AWG-DNP performance relative to CW-DNP. To this end, quantum mechanical numerical simulations of the 3-spin system were performed as a function of μw nutation frequency (power) using the linear chirp scheme. Although a realistic system consist of much more than three spins, previous discoveries have shown the successful applicability of this model system in the design of polarizing agent as

well understanding of CE mechanism [109, 108, 58, 89]. Clearly, as shown in Fig. 4.6, increasing μw power enhances both CW and AWG-DNP, but the gain in AWG-DNP is much larger than in CW-DNP. The plot shows that an impressive relative gain of up to 4x can be obtained for a nutation frequency of 2.5 MHz. Currently, powers achieved by gyrotrons (at 9.45 T) are estimated to be $\sim 0.5 - 1$ MHz which would correspond to a 2.5x enhancment over CW.[111] Additionally, simulations show the effectiveness of AWG-DNP is maintained even at higher B_0 field (14 T) as shown in the appendix B, Fig 9. Higher μw power increases the adiabatic transition probability for AWG irradiation and thus the effectiveness of AWG over CW, as explained using the Landau-Zener theory and shown experimentally in appendix B Fig. 5d.

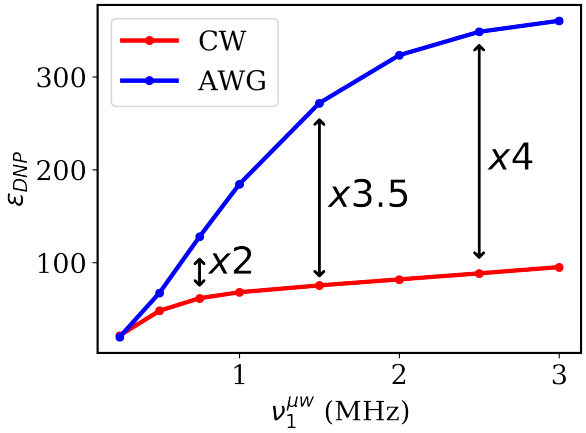

Figure 4.6: **Microwave nutation frequency dependence on CW and AWG.** Simulated ^{1}H ε_{DNP} vs. μw nutation frequency for CW and AWG (linear chirp) schemes. The simulations were performed for $e_1 - e_2 - ^1$H spin-system mimicking TEMTriPol-1 PA for MAS = 10 kHz. For AWG-DNP, $\Delta\nu_{AWG}$ and N were set to 100 MHz and 20, respectively. T_{1e_1}=0.1τ_r and T_{1e_2}= 0.5T_{1e_1}. All the relevant spin parameters are provided in the ESI (section 3).

Conclusion and Outlook

We have experimentally and conceptually demonstrated the impact of AWG μw modulation to enhance the efficiency of DNP at high B_0 field, and to enhance the scope of MAS-DNP to include polarizing agents with fast T_{1e} relaxation times, found for a broad range of paramagnetic species and experimental conditions. Even with low μw power of only 350 mW, we could achieve significant improvements by 35% in enhancement with AWG-DNP compared to monochromatic CW-DNP. Additionally, quantum mechanical simulations predict that higher μw power will lead to a remarkable 400% gain for AWG over CW-DNP.

This study only scratches the surface of what is possible with AWG-DNP. Fast and broadband saturation enables recruitment of a larger number of electron spins in a shorter amount of time, potentially opening up avenues for DNP at elevated temperatures and using short-lived photo-excited paramagnetic species to address important new questions about biological and chemical systems. As μw technology progresses towards higher power and greater frequency tunability, the impact of AWG-DNP will increase. AWG-DNP capabilities will likely broaden the application of electron-nuclear spin hyperfine spectroscopy for detailed structural characterization of paramagnetic surface sites in regimes deemed inaccessible to solid-state NMR, or enhance NMR spectral resolution under DNP conditions via electron-nuclear spin decoupling during NMR signal acquisition. The latter has already been experimentally demonstrated for ^{13}C NMR by Barnes et al. [112].

High power μw sources providing a μw nutation frequency of a few MHz with frequency modulation capabilities are being developed expeditiously[113]. The frequency-agile gyrotrons [112] by the group of Barnes is one example. However, a frequency-agile gyrotron is currently limited in the modulation scheme that it can achieve in the fre-

quency domain. In contrast, the combination of solid-state μw sources that allow for more versatile and rapid time-domain (as opposed to frequency-domain) manipulation of μw phase and frequency, in conjunction with a broad-band amplifier would be most beneficial. Optimization of μw transmission pathway [114, 115], optimization of NMR rotor dimensions [103], and addition of resonator or lens to maximize μw intensity at the sample position will further increase the B_1 power generated with the given μw power available, and hence further enhance the capacity of AWG-DNP, especially at higher field and temperatures. This study paves the way for time-dependent AWG μw manipulated MAS-DNP that has the prospect to become a mainstay of DNP.

Our study will demonstrate that as a result of these benefits, AWG leads to more efficient and robust DNP for state-of-the-art PAs under favourable conditions for NMR. Additionally, the benefits of AWG-DNP widen the scope of MAS-DNP, for example: (i) the *broadband* property of AWG-DNP is expected to include a greater selection of endogenous metal centers with stronger spin-orbit couplings and greater zero-field splitting than currently accessible to DNP [116], and (ii) the *fast* saturation properties of AWG-DNP technique are advantageous to the potential realization of near room temperature DNP–achieving such conditions is a crucial for high-resolution bio-solids studies by DNP-enhanced MAS NMR.

We thank Dr. Yangping Liu (Tianjin Medical University, China) for providing us with the TEMTriPol-1 radical. Part of the AWG-DNP instrument development was supported by the National Institute of Health through Grant No. R21EB022731 awarded to SH. The Binational Science Foundation through Grant No. 2014149 provided partial support for AE. KT was partially supported by the John H. Tokuyama Memorial Fellowship. We thank David Lewis and Ed Twehouse from Revolution NMR, LLC for collaboration on designing and operating the low-temperature MAS-DNP probe.

Supporting information concerning the setup of AWG-DNP instrument, experimental

results on TemTriPol-1 radical and numerical comparisons of CW and AWG-DNP under MAS are provided.

Chapter 5

Probe Building

5.1 Introduction

DNP has yet to reach its full potential due to incomplete knowledge of of the electron-nuclear spin system, further aggravated by DNP's decreasing efficiency at high fields over 14 Tesla.[45, 47] Hence, DNP studies can be critically enhanced with diagnostic tools to evaluate the spectral and spin dynamics of both the nuclei and electrons in the sample system under DNP conditions. It has been shown that electron spin lattice relaxation time (T1e), the g anisotropy, electron-electron couplings, electron spectral diffusion and nuclear spin diffusion all play critical roles in the DNP efficiency.[30, 31] Studies often evaluate these parameters with EPR at X or Q band, i.e. lower magnetic fields, but many of the relevant EPR parameters are either field dependent or difficult to resolve at lower magnetic fields. Thus, an accurate assessment of DNP parameters requires dual NMR and EPR detection capabilities under DNP conditions to characterize spin dynamical properties of samples containing the same PA concentration and solvent, subjected to the same microwave irradiation power, cryogenic temperature and magnetic field. To fulfill these requirements a dual EPR/DNP probe with simultaneous EPR and NMR

capabilities are needed.

While dual EPR/DNP probes would be critical tools for DNP studies, only a handful of such diagnostic instruments exist. Some currently existing cryogenic "high field" ($> 3T$) EPR/DNP probes include a dissolution system from Kockenberger et. al at 3.35T, [117, 118], a system from the Griffin group at MIT at 5T,[119] a system from the Goldfarb group at the Weizman institute at 3.35T [120], and a system from the Han lab at 7T[121]. An important bottleneck is the lack of commercial availability of dual EPR/NMR probes and spectrometers, as well as the limited availability of high field EPR hardware components including solid state microwave (MW) sources, amplifiers and receiver systems sensitive enough to detect EPR signal. Most commercial DNP systems are powered by a gyrotron as the microwave source due to the need of high power in the in the 10s of Watts range. However, these sources are non-trivial to achieve quick pulsing/gating and phase cycling of the radiation of the high power μw source.[37] In theory, any DNP probe can be adapted for EPR detection. However, the probe should be simultaneously optimized for NMR radio frequency (RF) receive and transmit andμw receive and transmit, as well as minimizedμw reflection at the EPR frequency. Most DNP (in particular MAS) probes are only optimized for transmitting a single polarization of μw irradiation, which limits their applicability for the highly sensitive induction mode EPR detection (i.e detection of μw emission with orthogonal polarization to the excitation).[122] However, even in a static DNP setup, it is non-trivial to achieve optimal NMR and pulse EPR detection with high fidelity at high magnetic fields.

5.2 Methods: Design Considerations

In this paper we will outline design considerations for the construction and performance of a dual EPR/DNP instrument and probe, designed to work with a low power

solid state μw source at cryogenic temperatures down to liquid helium temperatures. The design of the probe is focused around simultaneously optimizing three main aspects: 1) efficient cooling the sample to cryogenic temperatures; 2) robust, sensitive and versatile NMR circuit; and 3) efficient μw transmission and reflection for optimal EPR (and by extension DNP) performance.

5.2.1 Thermal Design Considerations

Temperature performance is critical for the operation of a DNP/EPR probe. Typically, lower temperatures will yield larger Boltzmann polarization, more impressive DNP enhancements,[15] and access to slower dynamics that permit DNP and cross polarization transfer to methyl groups (which freely rotate at typical DNP temperatures of $\sim$100K).[123, 124, 125, 126, 127] Furthermore, MAS using cold nitrogen gas is limited in the achievable spinning frequency, while cold helium gas has fluid dynamical properties similar to air and hence can be used to achieve much higher MAS frequencies.[126, 128, 129, 130, 131] Hence, performing DNP at temperatures lower than liquid nitrogen (77K) is of great interest to the magnetic resonance community. To achieve these temperatures, the right choice of cryostat must be made, followed by adequate thermal design of the probe. Practical factors must be also considered when deciding on the design of a cryostat, including cost, cooling time, freeze quench capability, and available space.

There are a variety of cryostat designs used for DNP/EPR spectrometers; but they can be roughly broken down into 3 categories: closed cycle cryostats, bath cryostats, and continuous flow crysotats.[132, 133, 134, 135] *Bath cryostats* are essentially a specialized dewar containing liquid helium or nitrogen in which the sample or cold finger is placed. The sample is cooled by thermal contact with the cyrogenic liquid or cold finger. These

cryostats can hold very low temperatures ($\sim$ 4K) for long experimental times, and can cool large sample volumes (such as the coils of superconducting magnets). However, these cryostats are not optimal for achieving thermal cycling or variable temperatures, but have nonetheless been used effectively in dissolution DNP setups.[136, 137] *Continuous flow* cryostats use the latent heat of vaporization from boiling helium to cool a cold finger, and subsequently the sample. The boiling helium is constantly replaced from an external dewar (hence continuous flow), while the boiled off helium is allowed to escape the cryostat. This method consumes the most cryogens, but can easily reach a wide range of temperatures of $> 4K - 300K$, and can be thermally cycled quickly and easily. Additionally, these cryostats become more efficient for small sample volumes such as those used in DNP. Many high field EPR/DNP probes have used this style of cryostat effectively (such as the Oxford Spectrostat or Janis SuperTrans),[119, 120, 138, 117, 139, 140] including the cryostat that was previously used in the Han lab to achieve dual EPR and DNP transmit and receive.[51] *Closed cycle cryostats* use a mechanical compressor to cool a cold finger to cryogenic temperatures. This cold finger can subsequently cool a sample chamber via thermal contact with an exchange gas or can cool a supply of helium gas which can then flow over the sample chamber. These cryostats have much less overall cooling power, and tend to cool down much more slowly when compared to bath or continuous flow cryostats. Therefore they require much more careful thermal design of the DNP/EPR probe to reach their minimum and desired temperatures. The benefit of these cryostats is that they can readily achieve temperatures below $\sim$4K, continuously and without the need for continuous replenishing of the cryogens. This makes them ideal for long experiment times or experiment runs requiring multiple samples. These cryostats are becoming more popular due to the rising cost of liquid helium, and a number of NMR/DNP/EPR systems exist that rely on such cryostats.[126, 136, 141, 142, 143] We should note that there exists another type of cryostat known as a "stinger" system,

which combines a closed cycle helium system with a bath or continuous flow cryostat. In these systems the helium evaporates from a bath or a flow cryostat and is recaptured and re-condensed.

Thermal Design of Probe

In most cases, cryostats are purchased commercially (often custom commissioned), leaving the user or developer with the need to come up with a thermal design for the DNP/EPR probe. The thermal design of the probe is crucial for optimizing the temperature performance that relies on minimizing heat exchange with the ambient environment. The two dominant mechanisms of unwanted heating are thermal conduction along temperature gradients in the probe, and blackbody radiation emitted and absorbed from non-reflective surfaces.[144]

Thermal conduction is dictated by the shape and materials that compose the probe. Heat transfer can be minimized by constructing the probe out of low thermal conductivity materials such as fluoropolymers (e.g. PTFE,KEL-F), G-10 fiberglass, carbon fiber or stainless steel; instead of high thermal conductivity materials such as copper and aluminum. The thermal conductivity of some cryogenic materials is shown in section 1.1 of appendix C. Furthermore, material shapes with a higher cross section (across a thermal gradient) will conduct more heat, and thus thin structures are preferred. These materials must also maintain structural stability at cryogenic temperatures (i.e not become too brittle) and have matched coefficients of thermal expansion to avoid structural failure, while the structure of the probe must be strong enough to support its own weight. Furthermore, material selection and shape must be balanced with other requirements for the probe such as RF and μw transmission. The RF transmission lines must be conductive enough to efficiently transmit RF, which means constructing them out of highly (electrically) conductive materials such as copper and/or making them thicker, hence

directly contradicting the design for minimizing thermal conduction. The μw waveguide must also be made out of a conductive material and be wide enough to support the desired μw transmission mode (i.e the hybrid HE_{11} mode for efficient coupling to a free space gaussian beam). Unfortunately, good electrical conductors are also generally good thermal conductors. However, the conductivity and geometrical requirements of the waveguide can be relaxed by plating a thin layer of electrically conductive material on a less thermally conductive material such as stainless steel. At the desired high RF and μw frequencies, the skin effect makes a thin layer sufficient for maximum RF transmission and electrical conductivity. Besides thermal conduction through solid material, gas filled cryostats must contend with undesired heat transfer through the helium gas present in the cryostat. This effect can be mitigated by confining the cooled helium gas to a small area containing the cold finger and sample, e.g. by adding baffles that restrict gas flow.

Thermal radiation is another mechanism of heat transfer that can be crucial in achieving ultra-low temperature DNP/EPR operation. This mechanism occurs because surfaces emit and absorb electromagnetic radiation based on their temperature (i.e black body radiation). Thus, care must be taken to reduce radiation absorbed by cold parts of the probe, such as the RF probehead. One way to reduce the emission and absorbance of radiation is to construct the probe from reflective, low emission materials, such as polished metals. Another method is to physically block/absorb radiation from the source before it reaches colder parts of the probe. This can be accomplished through radiation shields such as baffles or multilayer insulation. Notably, materials at a lower temperature emit far less radiation, and thus radiation shields which are cooled to lower temperatures preform much better.

5.2.2 RF Performance Design

RF performance dictates the usefulness of the probe for both NMR and DNP applications, but is perhaps the most difficult part to design due to space constraints imposed by the cooling setup and the μw waveguide. There are a myriad of factors that determine NMR performance and applicability including B_0 homogeneity, B_1 homogeneity, RF Power handling, nutation frequency, sample filling factor, circuit filling factor, Q factor, isolation, tuning range and tuning mechanism. A comprehensive review of all the factors that go into designing an ideal NMR RF probe is beyond the scope of this paper and can be found elsewhere.[145, 146, 147, 148] However, the two main measures of performance for a solid state NMR probehead are a strong RF B_1 field (i.e nutation) and large signal to noise ratio (s/n). In general, the B_1 has the following dependency:[146]

$$B_1 \propto \sqrt{P_{RMS}\eta_{CFF}Q_T}, \tag{5.1}$$

where P_{RMS} is the RMS power (in watts) delivered to the circuit, η_{CFF} is the circuit filling factor (i.e the percent of RF energy that is stored in the sample coil and Q_T is the (unmatched) quality factor (see appendix C section 2.2). The Q_T is related to the resistance of the circuit components, where a higher Q means less RF energy lost to heat. The probehead factors that affect s/n are:[146]

$$s/n \propto \sqrt{\eta_{CFF}\eta_S Q_T}, \tag{5.2}$$

where η_S is the sample filling factor which is the fraction of the magnetic field generated by the sample coil that intersects with the sample. Thus to maximize NMR performance, P_{RMS}, η_{CFF}, Q_T and η_S must be considered in the RF design, along with other practical factors, such as the ease of tuning/matching and the tuning bandwidth.

RF Circuit Design

A variety of RF circuits (both double and single resonance) have been used for cryogenic solid state DNP applications including transmission line circuits,[149, 119, 35, 120] and cryogenically tuned circuits,[150, 138, 126, 121]. The choice of circuit design will impact η_{CFF}, P_{RMS}, Q_T, and the practical utility of the probe.

Transmission line circuits have the tuning and matching elements of the RF circuit far from the sample outside the cryostat. These circuits connect to the NMR sample coil via coaxial lines that are pruned to a specified length (generally a multiple of $\lambda/2$) that provides the necessary distributed capacitance and inductance to give resonance at a specified frequency, while still being the correct length to reach the sample from outside the cryostat.[135, 151] Fine tuning and matching capacitors are placed outside the cryostat/magnet, and are connected to the sample coil via the coaxial lines. These circuits have higher power handling (allowing higher P_{RMS}) due to the high power handling of coaxial cables and large externally mounted variable capacitors. Furthermore the variable capacitors are placed outside the cryostat at room temperature, making adjustments easier, freeing up precious space in the cryostat, and allowing the use of non-cryogenics rated, variable, capacitors. However, the reliance on frequency-specific length of the transmission line means that the tuning bandwidth is often limited to a single nuclei per channel. Furthermore, transmission line circuits can have lower Q and η_{CFF} due to the use of long (slightly lossy) transmission lines as resonant components, while larger diameter (higher Q) transmission lines can conduct more heat into the probe.[152, 135]

Cryogenically tuned circuits[138, 126, 132] are generally based on discrete lumped element inductors and capacitors rather than transmission lines (not to be confused with cryogenically cooled circuits which are still external to the cryostat[153]). These circuits have all the tuning and matching elements inside the cryostat near the sample. These

probes have the advantage of achieving a wide tuning range (depending on the variable capacitors used), higher Q due to cryogenic cooling of the resonant circuit elements[153], and a higher η_{CFF} because energy is not stored in the inductance of the coaxial lines. However, the discrete tuning elements take up a large amount of space in the cryostat, mechanical tuning of capacitors can become challenging at cryogenic temperatures (although commercial capacitors exist which can handle cryogenic conditions), and the helium atmosphere in the cryostat causes capacitors to be more prone to arcing at high RF power (though this problem is partially mitigated at low temperatures).[154, 135]

Matching the circuit to the input impedance of the RF signal is another design aspect that must be considered. This matching can either be done capacitively or inductively. To date, most solid state cryogenic NMR and DNP probes have used capacitive coupling.[150, 138, 126] We have previously suggested that an inductively matched circuit can provide benefits over capacitive matching for cryogenic DNP NMR.[155] Inductively matched probes are inherently balanced without additional components, which eliminates ground loops, reduces dielectric losses between the resonant circuit and ground, and reduces noise interference from outside sources.[156, 157] Furthermore, it has recently been shown that inductive matching can offer higher η_{CFF} for multi resonant probes.[158]

Circuit Components

Once a circuit layout is chosen the next step is to choose the components necessary to physically build the circuit, including the capacitors and inductors.

Capacitors are a crucial component to any NMR probe, as the ability to tune and match are essential for maximizing B_1 and s/n at a desired frequency. For a solid-state NMR probe, the most important factor for these capacitors are their power handling (which determines the maximum P_{RMS}).[147] Other major concerns include the mechanical and electrical robustness of the variable capacitors under thermal cycling between

room temperature and liquid helium temperatures, and the physical size (with larger capacitors having larger parasitic inductance). Most probes use a combination of fixed capacitors and variable capacitors. Fixed capacitors can be made to have favourable mechanical properties (i.e robustness and small size) and electrical properties (i.e high voltage handling and low resistance), but dont provide the flexibility to make the small adjustments to tuning and matching necessary for resonant probes, which necessitates the incorporation of variable capacitors.

Fixed capacitors are generally commercially available nonmagnetic NPO/C0G ceramic chip capacitors with a capacitance of around one to a few hundred picofarad (pF), a (DC) voltage rating of up to a few kV, and a Q of a few hundred to a few thousand. A more in-depth review of fixed capacitors for NMR is available elsewhere.[147]

The selection of variable capacitors is more challenging as they need to be variable within the desired range (often $\sim$ 1 - 10s or 100s of pF), and have a tuning mechanism that may not be robust enough to survive hundreds to thousands of thermal cycles between cryogenic and room temperatures. Commercial capacitors exist that can handle cryogenic temperatures,[159, 150] but they tend to be very large in size relative to the space available in the cryostat and costly. Our own experience with commercially available variable capacitors has shown they can be mechanically unreliable when subject to extreme temperatures and thermal cycling for prolonged times; however other groups have successfully built cryogenic probes using commercially available variable capacitors from companies such as Voltronics.[135, 132, 160, 161]

RF Coils are the most important part of a typical NMR spectrometer as they generate the magnetic field necessary to interact with the nuclear spins. Good NMR coils will have low resistance/high Q (which affects the overall Q_T of the circuit), high η_s along with low electric fields at the sample, and high magnetic field homogeneity to achieve maximum s/n and high B_1. To date, non-spinning solid state DNP probes have made use

of solenoids,[149, 119, 150] saddle (Helmholtz) coils,[162, 121, 120, 99] and Alderman-Grant (AG) coils[121]. Traditionally, solid state NMR probes use solenoids as sample coils due to their high Q and high η_s.[147] However, the axial nature of these coils mean μw's transmitted down the length of the magnet must pass through the winding of the solenoid coil to reach the sample, which can attenuate the incident μw power. Furthermore, the sample exchange mechanism of our probe requires the sample to be removed vertically (parallel to B_0) rather than horizontally. This can be achieved with saddle coils that also provide good magnetic field homogeneity, and hence have been used extensively in DNP applications. AG coils show similar B_1 homogeneity to saddle coils, and are a type of slotted cylinder resonator that is tuned with capacitors in series.[163] The series tuning increases the operating frequency of the coil readily to the ^{1}H NMR frequency range at high magnetic fields and reduces the overall voltage across the coil, resulting in less dielectric loss and sample heating.[156] However the low overall inductance of AG coils leads to difficulty tuning to lower frequencies < 100 MHz, and often decreased RF efficiency due to parasitic inductance.

The auxiliary coils are a necessary component to generate multiple resonances in a multi-frequency tuned circuit. They are also important components of the circuit as they can affect Q and η_{CFF}. For most double resonant circuit designs, a higher value of inductance for the auxiliary coil will result in a higher H channel η_{CFF} and a lower X channel η_{CFF}. Good auxiliary coils will have as high a Q as possible, as small parasitic capacitance as possible (high self resonant frequency), and be easy to magnetically couple to (in the case of inductively coupled circuits). Solenoids are a good choice because they provide the highest Q for a given inductance, and are also fairly easy to magnetically couple to. Additionally, care must be taken that the lead lengths connecting the coil to other components are accounted for when measuring the inductance of the coil as long leads can add inductance, resulting in a different balance of η_{CFF} in the RF circuit than

expected.

5.2.3 μw Design

The design to achieve optimal μw transmission is critical to both the EPR and DNP performance of the probe. Maximum μw power at the sample ensures large μw B_1 which contributes to enhanced DNP performance, especially at higher temperatures where faster $T1_e$ relaxation counteracts μw-driven saturation or simultaneous electron-nuclear spin transitions. Furthermore, maximizing the μw power transmitted to and from the sample enhances the EPR signal to noise (s/n).

Strategies to maximize the μw power in the probe itself (discounting μw sources, quasi optics, ect. outside the probe) can be broken down into 2 parts: to optimize μw transmission through the probe to the sample and to optimize the μw properties of the sample holder. These two aspects will be discussed next.

μw Transmission

At high frequencies transmission lines become very lossy due to the skin depth effect. Thus traditional methods of 2 conductor electromagnetic propagation using coaxial lines become extremely inefficient for long transmission distances, such as the length of the EPR/DNP probe (spanning$\sim$1 m). In EPR probes, coaxial lines for μw transmission are only used up to Q band ($\sim$45 GHz). Most EPR and DNP spectrometers rely on waveguides for μw transmission. Low field (X and Q band) and early high field ($\geq$ W band) systems relied on metallic **rectangular waveguides** to transmit μw's in the fundamental TE_{10} mode. However, the dimensions of these waveguides is on the order of the wavelength of the desired frequency, and thus they become very small at high fields/frequencies. Additionally, the decrease in waveguide size paired with the skin ef-

fect leads to more losses in the wall of the waveguide (although not as much as in coaxial lines).[164] This problem was first overcome in early high field EPR experiments when the Freed group developed the first **quasi-optical** high field EPR probe operating at 250 GHz.[165] This probe relied on a μw beam propagated in free space (in a fundamental gaussian TEM_{00} mode) instead of confining the beam inside a conventional single mode waveguide. This design has the advantage of no conductor losses, and can achieve a transmission loss of $\sim$1.5dB/m at 250GHz, which is much less than the loss with traditional rectangular (TE/TM mode) waveguides. However for long transmission distances at high frequency, this approach requires refocusing of the gaussian beam using components that are either large (mirrors) and/or are lossy/reflective (teflon dielectric lenses). Additionally it requires precise alignment of optics, and the beam cannot be turned or tapered without additional large, precise quasi optical components (mirrors and lenses), which can be problematic in the limited space of a dual DNP/EPR probe/cryostat. **Corrugated waveguides** were first introduced in EPR probes by Smith et. al to achieve optimal coupling through the cryostat to the sample with minimal losses of $<$0.01dB/m at 200 GHz,[166] and were later implemented in gyrotron-based DNP systems by Woskov et. al ($\sim$0.3dB/m loss at 250 GHz).[167] These oversized, cylindrical waveguides support the hybrid HE_{11} mode which is very similar to the fundamental Gaussian TEM_{00} mode, which allows low loss transmission (due to minimal current on the metallic walls), as well as good coupling to Gaussian beams such as those propagated through quasi optics, and can thus be easily paired with a quasi optical detection/pulse forming stage. Additionally, these waveguides generally require a smaller diameter than quasi-optics and can be tapered to focus μw power on a small sample volume. These advantages have lead to corrugated waveguides to become the de-facto standard for μw transmission in high field DNP and EPR probes. However, corrugated waveguides are often one of the most expensive components of the EPR probe as they require a complex manufacturing process.

Recently, evidence has been presented that cheaper, smooth walled, cylindrical waveguides could also be effective for DNP μw transmission,[168, 150] but losses associated with mode conversion make them non-ideal for EPR detection.

Sample Holder

Perhaps a more important aspect of μw design for a high field EPR/DNP probe is the sample holder. The sample holder must have favourable μw and RF properties to allow both types of irradiation to effectively penetrate to the sample.

Many EPR probes have the sample inside a μw resonator to increase the μw power experienced by the sample many fold. However, these resonant structures must be compatible with concurrent RF penetration to the sample for NMR experiments. To date, a number of DNP resonators have been introduced, including single mode TE_{01} resonators,[169] fabry-perot (FP) type resonators,[170, 171] and a newly introduced photonic bandgap resonator.[162] Of these, *single mode cylindrical cavities* have so far found the most use for solid state DNP experiments. Most single mode cavities for DNP follow the design of Weis et. al,[169] which uses a flat helical coil as the main body of the resonator and as the NMR coil. The dimensions of single mode cavities must be on the order of the wavelength of the desired frequency, and hence at higher frequencies the dimensions become smaller and much harder to machine to tolerance. This small size also leads to low sample volumes, which can reduce both the EPR and NMR sensitivity (3nL at 260 GHz)[172]. Additionally, the skin depth effect paired with the small size creates resistive losses in the sample cup, leading to a lower quality factor "Q" (analogous to the NMR circuit Q). The single mode design also does not allow for induction mode EPR detection (only reflection mode), which can result in lower s/n.[173]

Fabry Perot (FP) type resonators are essentially two reflectors spaced at a distance from each other such that a standing wave forms between them at a certain frequency.

FP's can be larger than the wavelength, and have already been shown to work for solution state DNP setups at 260 GHz,[170], and a low Q standing wave structure has been used for cryogenic solid state DNP/EPR experiments at 140 GHz[120]. However, FP resonators have "nodes" of alternative magnetic and electric fields, and thus care must be taken such that the sample is only in the magnetic field node to avoid sample heating, and to maximize μw B_1 homogeneity. Therefore the sample volume is often still very small, with the maximum reported so far of 90 nL at 260 GHz.[174]

Recently a resonator based on a 1D *photonic band gap structure* has been developed by Nevzorov et. al.[162] This resonator consists of an alternating stack of dielectric disks between two reflective surfaces. Here, a standing wave pattern is formed similar as in a traditional FP resonator, except that the sample can be placed in each node (i.e between each disk) which allows for larger sample volumes, demonstrated for 2.5μL by Nevzorov and coworkers.

With all resonators, sample volumes remain small, and the precise mechanisms needed to tune the resonators often present a problem, especially when space inside the magnet bore is at a premium. Additionally, precise mechanical tuning at cryogenic temperatures, while possible, presents a costly design challenge. Furthermore, high Q cavities have an inherently narrow bandwidth, and thus need to be re-tuned for each μw frequency, which renders frequency swept experiments very challenging. To perform multi-frequency experiments such as ELDOR, the Q of the resonator must be somehow reduced to give an appropriate bandwidth or a double resonant structure designed.

However, at very high fields where μw sources can often only provide milliwatts of power, or for samples containing lossy (μw attenuating) materials such as liquid water,[173] resonators may be the best choice to permit both efficient EPR detection, as well as new and efficient methods of time-domain modulated DNP such as TOP-DNP.

An alternative approach is to use a non-resonant sample holder, which allow for a

much larger sample volume (>10 μL at 200 GHz)[175, 121, 176] and frequency bandwidth at the cost of μw power. In this design the μw field propagates through a sample holder (ideally) without standing waves or mode conversion. In the case of a corrugated waveguide, the μw beam is launched at the sample as a nearly gaussian beam. With a non-resonant EPR/DNP probehead, the goal is to guide the μw radiation to and from the sample with as little loss as possible, and without sacrificing NMR performance. To this end, the geometry and materials of the sample holder are important. Due to diffraction of the μw beam outside the waveguide,[177] the sample should be placed inside, or as close to the waveguide as possible, while reconciling this with an RF coil design that does not sacrifice RF performance. Alternatively, waveguide extensions can be used to guide the μw's to the sample positioned outside the waveguide.[121] Here, the sample diameter should not be much smaller than the waveguide aperture to maximize the μw filling factor. Furthermore, the sample geometry should be as thin as possible in the dimension parallel to the direction of the μw beam propagation– preferably no more than a quarter wavelength thick to avoid effects of B_1 in-homogeneity throughout the sample. However these considerations, again, restrict sample volume and can cause a reduction in NMR filling factor and B_1 for typical NMR coil geometries.

For optimal μw transmission to the sample from the waveguide, the path of the μw should not contain high dielectric constant or conductive materials that could reflect μw's before they reach the sample. Similarly, materials with high loss tangent should not be placed near the μw path to reduce dielectric loss to heat. Materials such as PTFE (teflon), PFA, and Kel-F are excellent choices due to their suitability at cryogenic temperatures, low dielectric constant and loss tangents, and lack of protons (allowing ^{1}H NMR detection).[178] To further enhance the μw power at the sample, a mirror can be placed opposite at the bottom of the sample cup, causing the μw radiation to pass through the sample twice, theoretically doubling the μw power.[121, 176, 120]

5.3 Results: Design and Performance of Dual DNP/EPR Probe

The design of the Han lab probe described here made every effort to incorporate what we determined were the optimal design choices described in the previous section.

5.3.1 Thermal Design

Cryostat

The Han lab chose a close cycle cryostat to replace our continuous flow cryostat with a close cycle cryostat for the dual DNP/EPR probe for the reasons listed earlier. A new DNP/EPR probe was designed and built from scratch to fit into a close cycle cryostat custom designed by Janis (described below), replacing the continuous flow cryostat (Janis STVP-200-NMR) and DNP/EPR probe design used for DNP studies until 2019.[179, 52, 155, 51, 180, 105, 38, 181, 32, 182, 73, 183, 100, 184, 185, 2, 29] The Han lab close cycle cryostat consists of a Sumimoto CKW-21 helium compressor paired with a Janis custom SHI-500T-5 Gifford-McMahon (GM) cold head. The cryostat consists of a cold finger surrounded by a radiation shield which is maintained in a vacuum jacket as shown in Fig. 5.1a-b. The copper cold finger located at the bottom of the cryostat is cooled by the cold head, which is powered by the helium compressor (Fig. 5.1c). The cold finger is in (conductive) thermal contact with the sample chamber which is filled with helium gas and the sample cooled by gas conduction between the cooled inner bore and the sample. The cryostat is pressurized at 0.5 psi using an external helium tank, a pressure sensor, and a solenoid valve, electronically controlled by an Arduino microcontroller. This cryostat can reach an unloaded temperature of 4.2K (without a probe inserted).

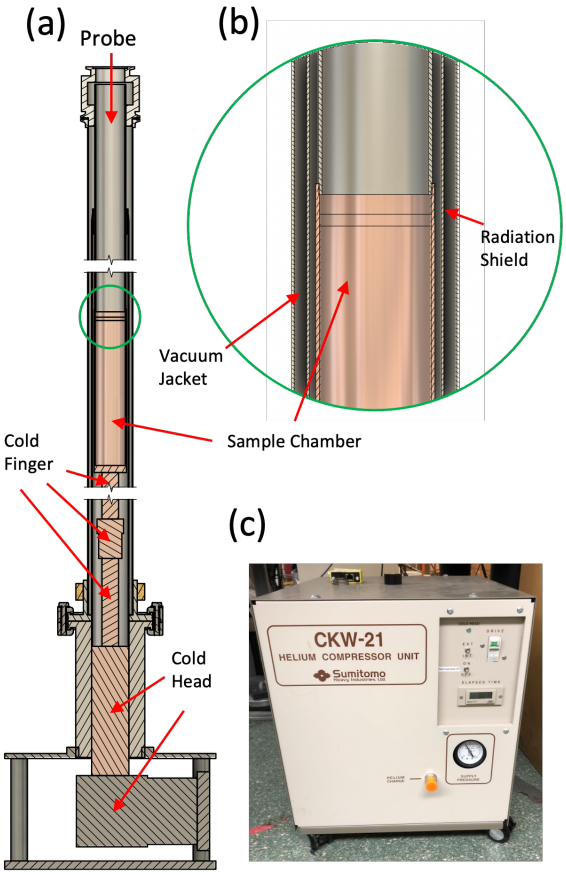

Figure 5.1: A) Cross section CAD model of the Janis Cryostat described in this paper. B) Zoomed in picture showing the concentric tubes used to form the radiation shield and vacuum jacket. C) Picture of the helium compressor used to power the cryocooler.

Probe

Our dual DNP/EPR probe is built to minimize heat exchange between the ambient environment and the probehead containing the sample. To achieve that, the structural frame is constructed of a perforated thin cylinder of 316 stainless steel (316-SS), supported by disks made from soldered together FR-4 printed circuit boards (PCBs) that act as baffles to block gas conduction (Fig. 5.2a). The FR-4 PCBs are soldered to an aluminum PCB polished on one side to reduce thermal radiation. Polishing both sides could improve thermal performance and can be incorporated in the future. The waveguide (held within the afformentioned structural frame) is constructed of German silver, and the waveguide taper is made of gold plated copper to minimize interference with B_0 homogeneity around the sample from the German silver (which can be slightly magnetic due to its nickel content).[186] Notably, the waveguide presents a large, thermally conductive cross section that will facilitate unwanted heat transfer. A cross section of a probe baffle with all feedthroughs is shown in Fig. 5.2b.

The sample is held at the bottom of the waveguide by a "J arm" structure consisting of a 0.25" tube running the length of the probe, cross-connected to a sample mounting piece, as shown in a zoomed out photo, in Fig. 5.2c. The bottom 12" of the "J arm" nearest the sample cup is built from copper, while the upper part ($\sim$24") is built from 316-SS. The use of copper is to reduce any B_0 inhomogeneities that may be induced from the slightly magnetic 316-SS material near the sample, while the 316-SS reduces heat transfer along the thermally conductive copper to the sample.

The sample temperature is measured via a Lakeshore Cernox "SD" package negative temperature coefficient sensor mounted on the sample holder via an aluminum PCB (to facilitate thermal contact with the sample) as shown in Fig. 5.2c, and connected to a Lakeshore 350 temperature controller via wires fed through the J arm. Variable

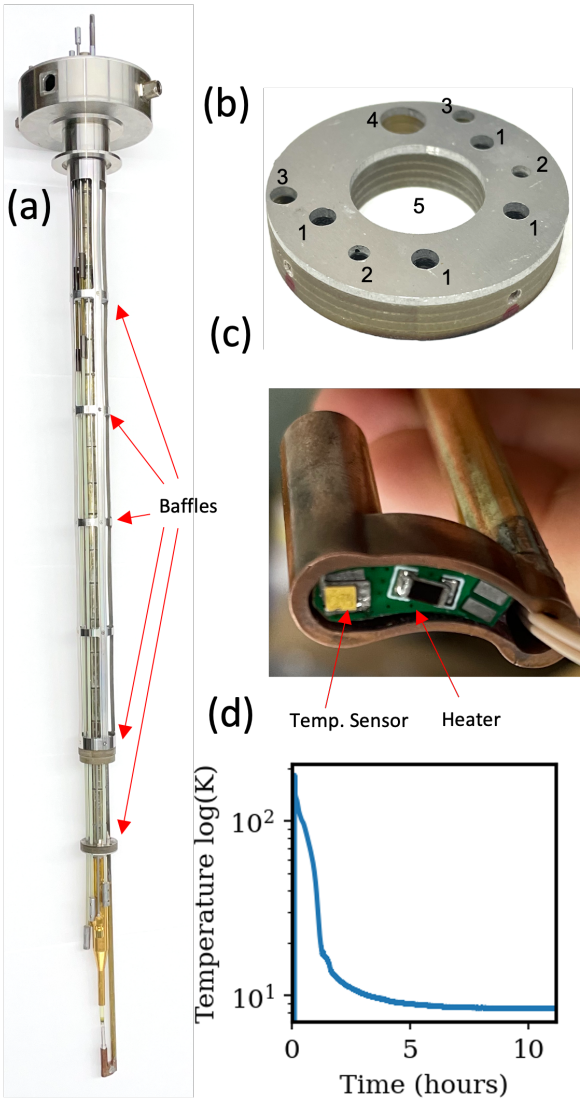

Figure 5.2: (a) Picture of probe without NMR circuit. The top of the probe is at room temperature while the bottom of the probe is at the lowest temperature. (b) Picture of FR-4/aluminum probe baffle with labeled feedthroughs: 1) G-10 tuning rods, 2) 0.085" 316-SS Coaxial cables, 3) 1/8" holes for future use, 4) J arm cutout, 5) waveguide.(c) J arm piece with PCB containing temperature sensor and heater. (d) Probe cooldown time when the cyrostat is already at the minimum temperature.

temperature is achieved by the addition of a 100 Ohm metal foil resistor to the PCB as a heater (Fig. 5.2c), which is fed current and controlled with a PID loop by a Lakeshore 350 temperature controller. The loaded cryostat with the probe can reach a minimum sample temperature of 8.5 K after about 6 hours of cooling, as shown in Fig. 5.2d. Additionally, a sweep coil is placed around the cryostat, inside the magnet, to enable field swept EPR experiments. Further information about the sweep coil is available in section 1.2 of appendix C.

Improvements in Thermal Performance

The cryo-free cryostat can reach 4.2K without a probe, but only 8.5K with the probe inserted. This means modifications to the probe can potentially result in a lower sample temperature. The lowest temperature of the probe is mostly limited by the conduction of heat down the length of the corrugated waveguide. Hence, the thermal performance can be improved by adding a thermal break to the waveguide (i.e cutting a section of the waveguide out and leaving an air gap), which should have minimal implications to the μw performance.[187] This can help reduce the largest contribution to thermal conduction in the probe. Furthermore, the waveguide could be constructed from thermally less conductive material than German silver (i.e stainless steel or titanium) and plated with gold to maintain surface conductivity. Finally, proper multi-layer insulation consisting of foam layers interspersed with reflective foil sheets can be implemented along the length of the probe to further block helium gas flow, and so reduce thermal radiation effects.

5.3.2 RF Design

The design aspects of the RF circuit and components were chosen to optimize the B_1 and detection sensitivity of both the NMR and EPR spins.

RF Circuit Design

Our DNP probe design relies on a cryogenically tuned circuit by inductive matching. The basic principle of our cryogenically tuned, inductively coupled, rf circuit is schematically shown in Fig. 5.3. The design is based on the principle developed by Zens et. al[158]. Here, the "inner" resonant section of the circuit uses a doubly resonant 3 inductor "ladder" configuration, with the RF energy for each channel inductively coupled into the resonant portion through two equivalent auxiliary inductors as shown in Fig. 5.3. Matching is achieved by adjusting the series and parallel capacitance of the outer matching coupling inductors. This circuit provides all the advantages of a balanced, inductively coupled, circuit that also has a high inherent η_{CFF} due to the minimal number of discrete inductors used (the 2 auxiliary inductors shown are equivalent and only count as 1). Additionally, the design requirements (Q_T, power handling, etc.) of the matching sections (i.e coupling inductors and matching capacitors) can be relaxed as they are not part of the resonant circuit.

Capacitors

The fixed capacitors used in our probe are commercially available nonmagnetic Knowles Syfer 1111 package chip capacitors with a nominal DC voltage rating of 2kV (e.g. Digikey part number 1608-1268-1-ND). For the resonant portions of the circuit made up by tuning capacitance, 3 of these capacitors are used in series to increase the voltage handling (shown in Fig. 5.6a).

The variable capacitors used in our probe are mechanical capacitors, home-built from copper and zirconia to mitigate relatively frequent breaking and avoid the high cost of the commercially available variable capacitors, and to achieve the desired tuning and matching range. These capacitors work by actuating a copper piston (via a G10 tuning

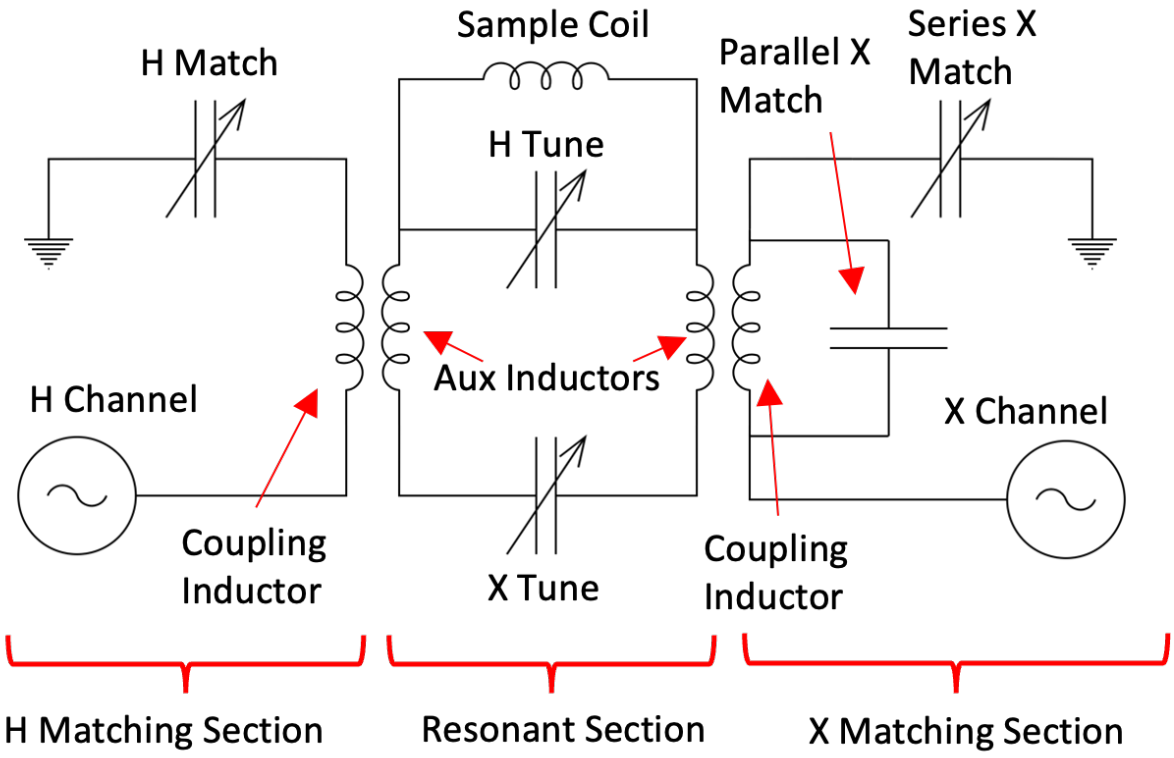

Figure 5.3: Layout of the inductively coupled double resonance circuit. The "inner" resonant portion of the circuit consists of the Sample Coil, the tuning capacitors "H Tune" and "X Tune", and the Auxiliary Inductors necessary to generate multiple resonances. The matching portion of the circuit consists of the matching capacitors "H match" and "X match" as well as the coupling inductors. The RF energy is fed into the matching portion of the circuit which transforms the 50 ohm impedance of the RF pulse to the impedance of the resonant portion of the circuit through the inductively coupled coils.

rod) in and out of the zirconia tube, which is itself wrapped in copper foil. The G10 rods are actuated via a simple screw mechanism located towards the top of the probe. The copper piston acts as one plate of the capacitor, while the copper foil cylinder acts as the other, with the cylindrical zirconia tube serving as the dielectric in between. The design for this variable capacitor illustrated in Fig. 5.4(a)-(c). A ceramic zirconia dielectric was chosen to achieve good mechanical properties (i.e high fracture resistance) at low temperature, a high dielectric constant (allowing the capacitor to be smaller), a large dielectric strength (allowing larger P_{RMS}), and a fairly well matched coefficient of thermal expansion to copper (of which the foil and piston is made of) which prevents jamming of the capacitor.[188] Many capacitors use sapphire or alumina as the dielectric due to their low loss tangent, but in our experience the Q of the capacitor is larger compared to that of the inductors, such that it has a minimal effect on the overall Q of the circuit. Even using slightly more lossy zirconia as the dielectric has only a small effect (i.e $> 10\%$), while zirconia is a much stronger material less prone to breaking.

One major issue we encountered with this capacitor design is arcing/partial discharge on the surface of the inner copper piston into the slight air gap that exists between the inner copper piston and the zirconia dielectric. Simulations show that for a simplified 3 plate capacitor design, the electric field density will always be greatest across a (low dielectric constant) air gap, as illustrated in Fig. 5.4 (d) and (e). This air gap always exists to some degree due to manufacturing tolerances that allow the inner piston to move vertically to adjust the capacitance. Since air has a much lower dielectric constant than zirconia, most of the electric field generated between the inner copper piston and outer copper foil is concentrated in the air gap, which also has a much lower breakdown voltage (especially when filled with helium). Furthermore the electric field in the air gap will always be strongest near the surface of the metal conductor. To solve this problem we used an 0.01" thick FEP heat shrink around the inner piston. This heat shrink creates

a tighter fit around the inner piston and largely eliminates the air gap on the surface of the piston. The highest electric field is thus concentrated in the FEP layer which has a much higher dielectric strength than air or helium. One drawback of this FEP layer is a smaller capacitance range, since the FEP layer is much thicker than any air gap that would otherwise exist, and it has a much lower dielectric constant than zirconia.

The overall construction of the tuning capacitor is shown in Fig 5.4c-e. Fig 5.4d shows the X channel capacitor that has a maximum capacitance range of 1-6pF, can handle ∼1000 volts peak to peak at 300 MHz without arcing, and has a $Q >> 300$ (measurement methods shown in sections 2.2 and 2.3 of appendix C). The observed breakdown occurs across the gap between the two outer pieces of copper foil, and thus the capacitance range can be traded for increased power handling by making the outer copper foil pieces shorter and further apart. This was done for the H channel capacitor (as shown section 2.4 of appendix C) where the capacitor plates are also horizontally arranged to provide shorter lead lengths to the sample coil, and so yielding a ∼1100 Vpp power handling on the X channel at higher frequency.

The matching capacitors are similarly constructed using a zirconia tube, copper piston and copper foil, however no FEP heat shrink was used and one end of the capacitor is directly grounded (as shown in section 2.5 of appendix C). This is because the matching capacitors do not need to handle high voltages unlike the tuning capacitors, as they are not part of the resonant circuit; but, a larger capacitance range still can extend the tuning/matching range of the circuit.

These homebuilt variable capacitors are much cheaper than commercial capacitors (the major cost is the Zirconia dielectric tubes), are mechanically much more robust to resist repeated thermal cycling between liquid helium and room temperature, and are customized to suit our specific needs in terms cryogenic operation, RF tuning range and RF voltage handling.

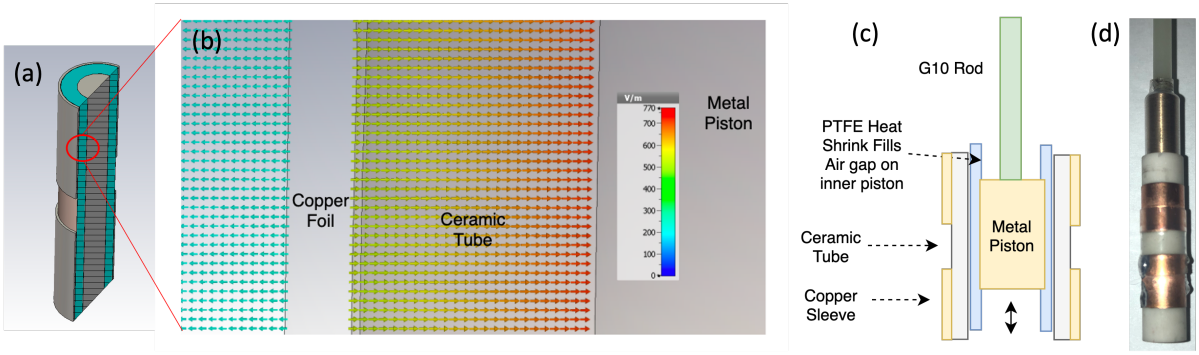

Figure 5.4: (a) Schematic of the capacitor construction. (b) rendering of the X channel tuning capacitors used. (c) Cross section of the X channel tuning capacitor. (d) Simplified 3 plate capacitor with high dielectric constant ceramic material (i.e zirconia) between the plates, and an air gap around the central plate. The two ends of the capacitor connected to an outside circuit are indicated by + and -. (e) Simulation result showing the relative electric field density on a cutout of the simplified 3 plate capacitor. The electric field of the capacitor is concentrated in the air gap.

Inductors

We chose a 4 turn saddle coil for NMR signal detection to allow for axial μw irradiation and to achieve a (relatively) high inductance (compared to an alderman grant coil) necessary to double tune our RF circuit to the correct frequencies (~300 MHz and 74 MHz), and to ensure high RF efficiency. The coil is constructed from vertical copper rods (1mm/18 AWG wire) connected by horizontal copper wire to form the saddle coil as shown in Fig. 5.5a-c. The coil diameter is 9.5mm, the window angle is 110° (although any angle over 90° is sufficient)[189], and the window height is 7mm. The vertical wires are supported by holes machined into 2 PTFE rings (Fig. 5.5a) which are mounted around a 7mm OD zirconia support tube. Copper foil guard rings (shown in the cutout of Fig. 5.5c) are placed inside the zirconia tube to focus the RF field onto the sample, as well as prevent excess μw scattering, as will be discussed later.

The coil parameters were measured by resonating the coil at the desired frequency (300 MHz for H and 74 MHz for X nuclei) using a chip capacitor across the coil leads (not within the RF circuit) and coupling the coil to a VNA (vector network analyzer) using

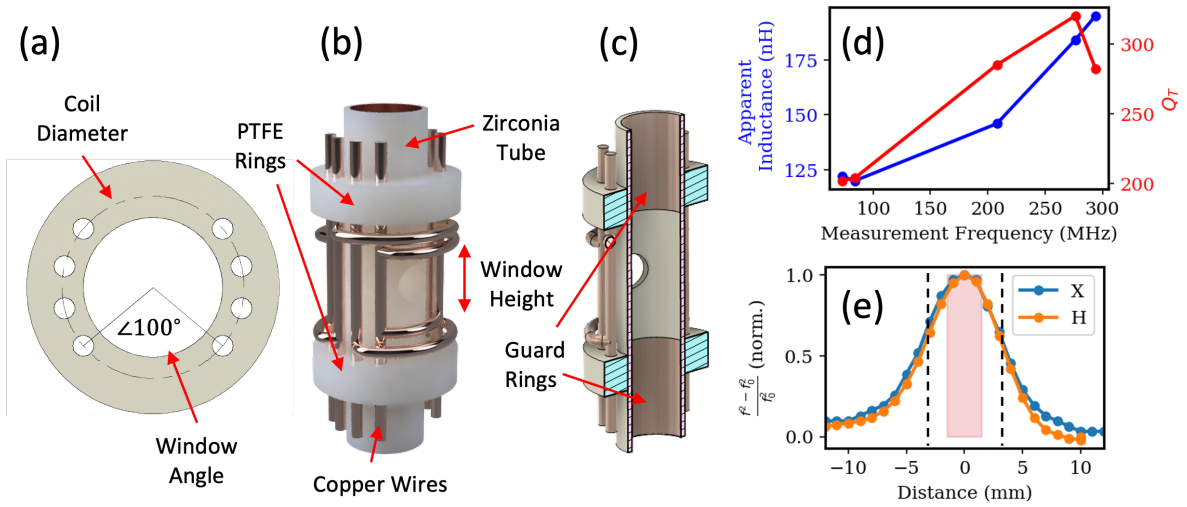

Figure 5.5: (a) Top down schematic of the PTFE Support rings used to form the saddle coil. (b) Rendering of the 4 turn saddle coil with PTFE rings, zirconia support tube, and copper foil guards. The coil is formed by inserting vertical copper wires into the holes in the PTFE rings and cross connecting them by soldering horizontal lengths of copper wire. (c) Cutout of coil showing copper foil guard rings. (d) Coil inductance and Q_T at different frequencies. (e) Ball shift measurement at 74 MHz (X) and 300 MHz (H). The window height is indicated by the black dashed lines, and sample region is shaded in red.

a pickup loop. The coil was found to have an inductance of 125nH, and a measured Q_T of 205 at 74 MHz and 275 at 300 MHz (as shown in Fig. 5.5d). The z axis homogeneity of the coil was determined from a ball shift measurement (see section 2.6 of appendix C) using a 1/8" aluminum ball.[190] The ball shift profile is shown in Fig. 5.5e with the 3mm tall sample region shaded in red. This measurement suggests that a fairly good RF homogeneity (less than 10% variation in amplitude along the z axis) for the H and X channel is achieved in this sample region.

For the circuit described in this paper, the auxiliary coils are two-turn solenoid coils with an ID of 7mm wound from 14 AWG wire (shown in Fig. 5.6c below). These coils have an inductance of 51.5 nH when the lead lengths are included, and a Q_T of 410. The coupling inductors used to couple to the auxiliary coils are two- and three-turn (for H and X channel respectively) 7mm ID solenoid coils wound from 18 AWG copper wire. These

coils are aligned axially with the auxiliary coils to achieve the desired magnetic coupling k. The exact inductance, Q, and coupling factor k (i.e the overlap of magnetic flux from the matching and auxiliary inductors) does not necessarily need to be tightly controlled as they minimally affect the circuit performance. A higher k and larger inductance will generally make the circuit easier to match (especially at lower frequencies), but caution must be taken not to increase k too much as this will be deleterious to the RF efficiency and Q. If optimal matching can be achieved (>25 dB return loss) a lower k and inductance value can be used that will slightly increase the circuit performance (as less magnetic energy will be stored in the coupling inductors). For lower frequencies and lower coupling factors, the coupling inductors can be made resonant near the desired tuning frequency (i.e 74 MHz for the X channel) by placing a capacitor across the coupling inductor (as shown in Fig. 5.3a) to facilitate matching. [158]

RF Circuit Construction

The RF circuit constructed from the capacitors and inductors are shown in Fig. 5.6. The exact circuit diagram with each discrete component used and their value is shown in Fig. 5.6a (for a circuit dually tuned to ^{1}H and ^{13}C). The circuit components are supported by grounded aluminum plates and standoffs as shown in Fig. 5.6b, and can be divided into two parts which are separated by the aluminum plates. The upper "deck" contains the matching circuitry, coaxial cable feeds, and auxiliary coils; and the lower deck contains the sample coil and tuning capacitors. Most of the coaxial cable consists of a 0.085" 316-SS coaxial cable, but the bottom 5" length feeding the RF circuit is made of a 0.141" copper coaxial cable to minimize disturbance to the B_0 homogeneity by the slightly magnetic 316-SS material. All leads that connect the discrete RF circuit components are made of 14 AWG copper wire with occasional application of FEP heat shrink to prevent shorting components together or to ground, and are soldered with a

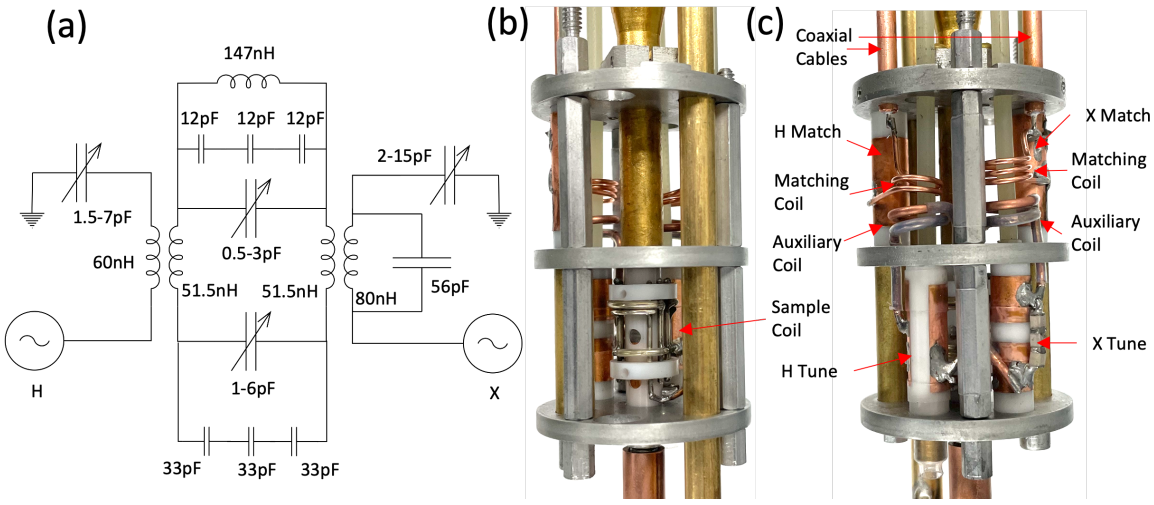

Figure 5.6: (a) Schematic of inductively coupled (H-X) double resonance circuit with all discrete component values shown. (b) Picture of the constructed circuit attached to the waveguide taper with components indicated.

60/40 tin-lead solder. The distance between the coupling inductors and tuning inductors is about 4mm, but can be adjusted by hand to get k between the coupling inductors and the auxiliary inductors into the correct range to match the circuit. Most of the capacitance for the H channel is placed directly across the coil leads in the form of three 12 pF chip capacitors in series, as shown in Fig. 5.6a. This improves η_{CFF}, as most of the H channel current travels directly through the chip capacitors and not through the leads to the variable capacitor, which have inductance and can reduce overall circuit efficiency η_{CFF}. The X channel tuning capacitor is brought into the correct range by the addition of three 33 pF capacitors in series. For both the H and X channel the chip capacitors are placed in series to extend their voltage handling to be equal or better than the variable capacitor.

The performance of this circuit is shown in table 5.1. The Q_T for the circuit is 281 and 170 for the H and X channels respectively. These are not very impressive numbers in comparison to a typical solid-state NMR probe, but the lower Q values can be mostly attributed to the small size and construction of the sample-holding saddle coil (which

itself has a similar Q as shown in Fig. 5.5d). The max power handling of the circuit is 150 W for the H Channel and 125 W for the X Channel, which is mostly determined by the power handling of the variable capacitors. The η_{CFF} was measured experimentally using ball shifts (described in section 2.6 of appendix C), which yielded a H channel η_{CFF} of 32.9% and an X channel η_{CFF} of 63.3%. The η_{CFF} balance between these channels was deliberately optimized through the design of the auxiliary coils to maximize the X channel detection sensitivity after cross-polarization (CP). The total η_{CFF} of 96% is high, which is due to the minimal parasitic and unnecessary inductance in the circuit design. At 125 W input power, the B_1 was measured to be 50 kHz (corresponding to a 5 μs 90° pulse) for the H channel and 31.25 kHz (corresponding to a 8 μs 90° pulse) for the X channel, respectively. Additionally, the tuning range of the X channel in the shown configuration is 69-81 MHz, which gives access to ^{55}Mn, ^{79}Br, ^{13}C, ^{27}Al, ^{51}V, ^{23}Na and ^{63}Cu nuclei. This performance is low compared to most solid-state NMR probes using solenoid coils (as is the case for most MAS systems), but is excellent for saddle coil-based systems, especially considering the large diameter of the saddle coil.

Improvements to RF Design

While the RF circuit performs well, and care has been taken to optimize most aspects of the circuit, there is still room for improvement, mainly through modifications of the sample coil. If the coil could be wound from a single wire (instead being soldered together), the Q and η_s would be higher. Additionally a flat coil made from foil could increase the η_s over the round wire used here. Guard rings outside the coil could be placed to focus the B_1 field more onto the sample and further increase the η_s. The variable capacitor geometry could also be changed to provide a shorter path for the RF current, hence increasing η_{CFF} by reducing parasitic inductance.

Channel	Q_T	Max Power	η_{CFF}	B_1 (125 W)
^{1}H	281	150 W	32.9%	50 kHz
^{13}C	170	125 W	63.3%	31.25 kHz

Table 5.1: Performance and parameters of the inductively coupled double resonance NMR circuit.

5.3.3 μw Design

μw Transmission

The μw transmission down the probe is via a 12.7mm ID corrugated waveguide (Bridge12 Inc) constructed from nickel silver (i.e German silver) with a gold plated waveguide taper to 5.5mm to focus the μw's onto the sample, as shown in Fig. 5.7(a). The top of the waveguide is vacuum sealed with an epoxy sealed rexolite window. The waveguide is fed with a gaussian beam from a quasi-optical table, as described in a previous paper.[121]

Sample Cup Construction

The sample holder for our probe is constructed of a 3/16" OD, 1/8" ID PFA tube with 1/8" PTFE rod inserts to hold the sample in place, as well as an aluminum insert that acts as a mirror, as shown in Fig. 5.7(c)-(d). The bottom of the PFA tube is threaded to enable mounting to the "J arm". The sample volume can be adjusted by adjusting the length of the PTFE inserts according to the homogeneous region of the NMR coil. The advantage of this design is that all parts are readily and cheaply commercially available, and the sample holder is easily assembled so that re-use of sample cups is not necessary, and samples can be simply saved in the sample cup for later use, if needed.

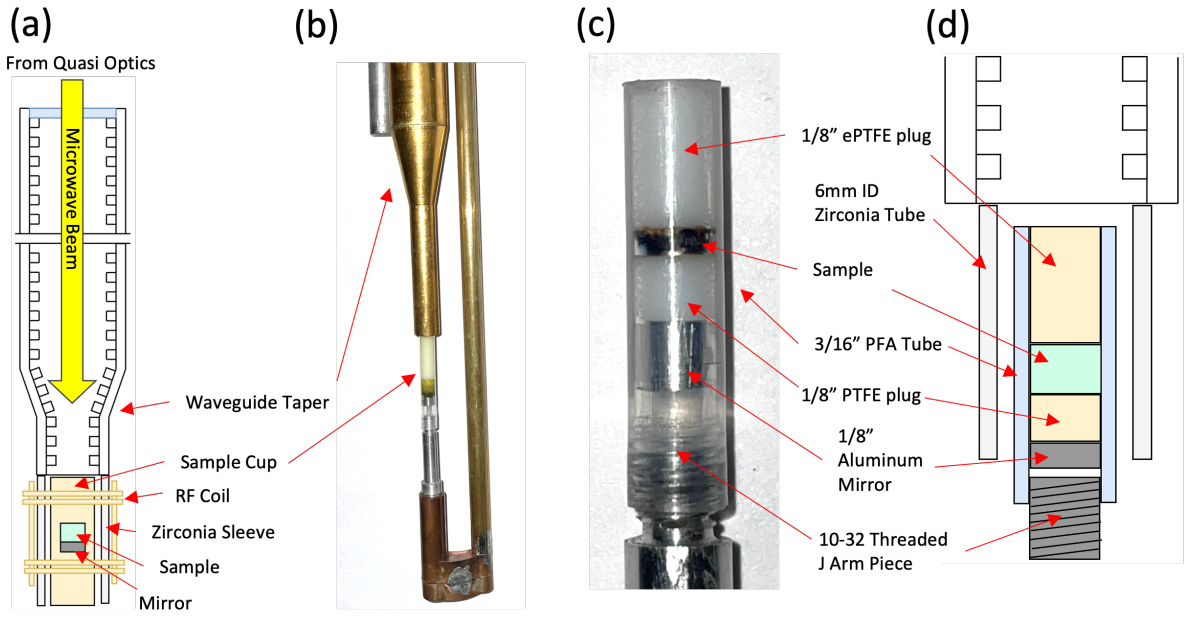

Figure 5.7: (a) μw pathway to sample. (b) Picture of waveguide taper, sample cup, and J arm without RF circuit. (c) Picture of sample cup. (d) Schematic of sample cup.

Sample Cup Optimization

Although the sample cup is made from commercially available parts, the geometry was carefully designed to ensure maximum transfer of μw power to the sample. The PFA/PTFE sample cup itself acts as a dielectric waveguide, which was inspired by the work of Zilm et. al. Here, the μw's are confined in the PTFE structure due to the higher dielectric constant of PTFE compared to free space. Additionally, PTFE/PFA has a low enough dielectric constant to not cause too much reflection off the surface of the sample cup. The geometry of this PFA/PTFE waveguide was optimized using finite difference time domain (FDTD) techniques in CST Studio. Selected geometric features that were optimized, in feedback with FDTD simulations, are shown in Fig. 5.8a as well as appendix C Fig. C.7.

In these simulations the μw power was measured as a function of the various ge-

ometric features, with a typical simulation result/setup shown in Fig. 5.8b. Here, a cross section of the RMS B_1 field amplitude in the sample cup/waveguide extension is shown for a frequency of 194 GHz. The simulation model shown here includes the corrugated waveguide, PFA/PTFE waveguide extension, sample, and support tube. The μw output of the corrugated waveguide exit was simulated using a TE_{11} to HE_{11} mode converter structure with the same output ID as the actual waveguide.[191] For simplicity the waveguide was simulated as a perfect electrical conductor. The PFA/PTFE waveguide extension/sample cup was modeled as a solid PTFE rod (dielectric constant $\epsilon = 2.1$), and the sample was simulated as a puck of frozen DNP Juice ($\epsilon = 3.5$).[192] This model does not include the aluminum mirror as this feature greatly increases the simulation time and makes interpretation of the results more complicated.

Fig. 5.8b shows the simulated B1 field in the sample cup geometry described in Fig. 5.7d and Fig.5.8a. Here, it is qualitatively apparent that most of the μw power is confined to the PFA/PTFE waveguide extension, and is not radiated away from the sample. Thus, most of the μw power will intersect the sample yielding higher B1 which is useful for EPR and DNP. Similarly, EPR s/n will be high as the signal emitted from the spins will be directed mostly to the waveguide.

The final sample cup geometry used in our probe was optimized using such calculations of the percent B1 field to sample plotted in Fig. 5.8c-f, with the select geometrical dimension indicated by the dashed lines.

Fig. 5.8c shows the results of the waveguide extension diameter (labeled as "diameter of sample cup" in Fig. 5.8a) on the effective "filling factor" (i.e how much of the μw power intersects the sample– here we refer to filling factor as the percentage of microwave power that passes through the sample rather than the typical definition of filling factor for a EPR or NMR resonator). Here, the filling factor is measured as the % of μw power that passes through the upper face of the sample (more information is available in section

3.1 of appendix C). Fig. 5.8c shows that for larger diameters, the % of μw power that gets to the sample decrease from almost 80% for a 3mm diameter to ∼30% for a 10mm diameter. This data indicates that for a larger diameter the μw's are more spread out inside the waveguide extension and the "filling factor" will be lower. This effect can be qualitatively seen in appendix C Fig. C.10. A 3/16" (4.76mm) waveguide extension diameter (dashed line on Fig. 5.8c) was chosen to give an optimal filling factor while maintaining a reasonable sample diameter/volume. Additionally, confining the μws to a smaller volume makes the sample thinner, allowing a thinner NMR coil which can give a higher NMR B_1.

Fig. 5.8d shows the effect of the gap between the waveguide extension and the RF coil support tube. This parameter affects the diameter of the sample cup and/or the inner diameter of the coil support sleeve. The gap can be seen as the white space between the grey coil support sleeve and the blue sample cup labeled as "gap between sample cup and coil support sleeve" in Fig. 5.8a, as well as in appendix C Fig. C.7. From the simulation results we can see that larger gaps will yield higher μw filling factor, with a 0mm gap (no gap) giving ∼28% filling factor and a 2mm gap giving ∼80% filling factor. If this gap is too small the μws in the waveguide extension will couple to the tube and be scattered away from the sample. This concept is illustrated in appendix C Fig. C.11. However if the gap is too large, then the NMR filling factor will decrease as the NMR coil will have a larger diameter than necessary (either the sample cup is thinner or the RF coil is larger in diameter). Noteably, the gap dependence of filling factor on gap is not linear, and thus a sufficiently large gap is optimal for filling factor. The dashed line indicates the gap chosen for our geometry which is ∼1.2mm.

Fig. 5.8e shows a simulation of how the waveguide extension length affects μw power to the sample. This determines how long the waveguide extension can be before μw's scatter out of the PFA/PTFE structure. It is important that the waveguide extension is

long enough so that the metallic corrugated waveguide taper does not interfere with the NMR coil, but short enough that most of the μw power reaches the sample. The results suggest that the waveguide extension is very efficient at transmitting μw power, even at longer distances exceeding 10 mm. For our probe we chose length of $\sim$9.5mm which separates the NMR coil sufficiently from the corrugated waveguide, while not sacrificing any μw filling factor.

Fig. 5.8f shows the dependence of μw filling factor on the position of PTFE waveguide extension relative to the waveguide (i.e the "sample cup distance from waveguide" as shown in Fig. 5.8a, and appendix C Fig. C.7). Here a negative distance corresponds to the PTFE waveguide extension being placed partially inside the corrugated waveguide, and a positive distance corresponds to a gap between the output of the corrugated waveguide and the PTFE waveguide extension. The simulations show that in general, a larger gap results in less μw coupling between the corrugated waveguide and PTFE waveguide extension, leading to less μw power to the sample. Additionally the results suggest placing the PTFE extension inside the waveguide doesn't necessarily provide better coupling, but doesn't diminish the coupling by much either. These results are further illustrated in appendix C Fig. C.13. However, placing the PTFE extension inside the corrugated waveguide could potentially have some downsides including contaminating the corrugated waveguide or damaging the corrugations. Thus we decided to position the PTFE extension directly at the output (0mm distance) of the corrugated waveguide for most situations.

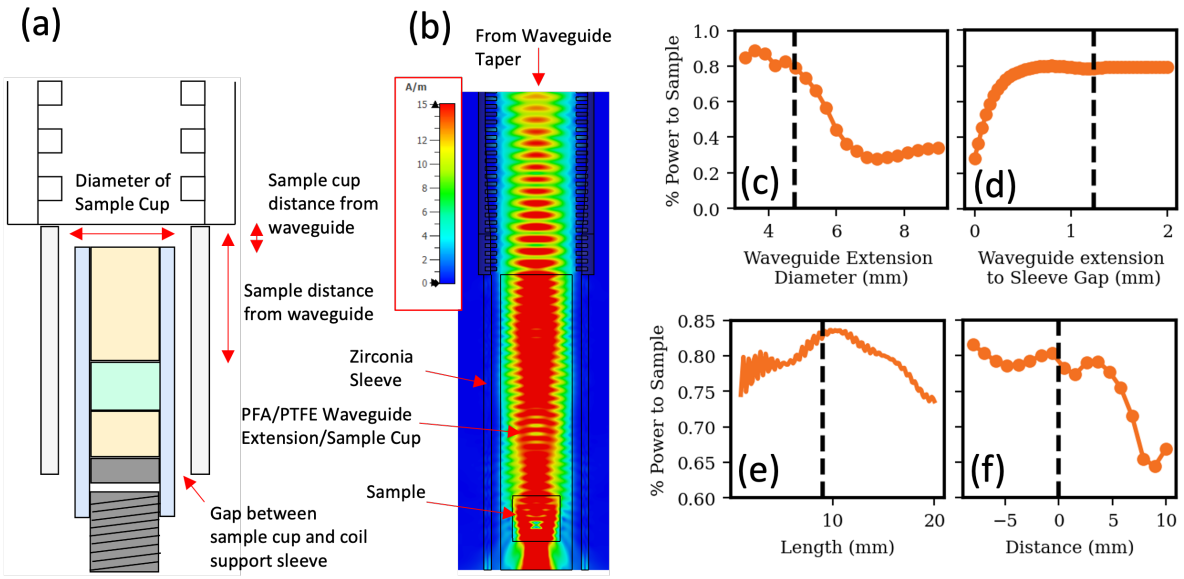

Figure 5.8: (a) Schematic of sample cup/waveguide extension simulation. (b) Cross section of the RMS μw B_1 field in the sample cup. (c) Average μw B_1 field and filling factor (i.e the percent of μw power that passes through the sample) as a function of the waveguide extension/sample cup diameter. (d) μw filling factor as a function of the gap between the waveguide extension and NMR coil support tube. (e) μw filling factor as a function of how long the waveguide extension is. (f) μw filling factor as a function of sample cup distance from waveguide. Negative numbers correspond to the top of the PTFE waveguide extension being inserted into the corrugated waveguide. For (c-f) the chosen geometry used in our probe is indicated with a dashed black line. Additionally each parametric simulation was carried out with all other geometric features held constant at the values indicated.

5.4 Results: Dual DNP/EPR Experiments

μw performance of the DNP/EPR probe

To test the EPR performance of the sample holder, the EPR nutation frequency was measured. This is a good measure of performance because equations (1) and (2) hold for EPR and NMR, and thus higher μw B_1 is an indication of higher s/n. The nutation experiment was performed using a solid echo pulse sequence where the echo pulses are varied in length (as shown in Fig. 5.9a). Here, a 90° pulse length should result in the highest detected EPR signal.

With the current optimization, our dual DNP/EPR probe yields a μw B_1 of approximately 500 kHz (500 ns 90° pulse), as measured with 0.5% BDPA in polystyrene (as shown in Fig. 5.9a-b) using a 450 mW μw source. This B_1 for EPR is comparable to values reported previously from our lab.[121] Notably this value is just an average– because the sample dimensions (3mm for this sample) are larger than a quarter of the μw wavelength ($\sim$ 0.385mm at 194 GHz) there will be large variations in B_1 field across the diameter of the sample (uneven μw power distribution across the sample can be seen in Fig. 5.8b).

To verify the validity of the simulated μw performance, the B_1 for different configurations of the sample cup/waveguide extension was measured as shown in Fig. 5.9d-h. The optimal configuration for EPR is to place the sample cup inside the waveguide as shown in Fig. 5.9d. This ensures that minimal μw power is lost to scattering and yields a 90° pulse time of 700 ns with a 120 mW μw source. Realistically, the sample cannot be inside the solid metal waveguide because this positioning prevents NMR detection which necessitates a PTFE waveguide extension. Fig. 5.9e shows a geometry closest to that used in our probe (shown in Fig. 5.7) including a length of 9mm and a 0.8mm gap between the outer tube and waveguide extension, which gives a 90° pulse of 1000 ns. The

effect of lengthening the waveguide extension to 15mm is shown in Fig. 5.9f. This geometry yields a 90° pulse of 1050 ns, which is very close to the value from the 9mm length in Fig. 5.9e, suggesting that the waveguide extension can be fairly long without losing too much μw power. This concept was demonstrated in the simulated results shown in Fig. 5.8e. Fig. 5.9g shows the scenario where the gap between the waveguide extension and coil support tube is eliminated, or equivalently where the waveguide extension has a larger diameter (3/8" in this case). Here, the 90° pulse length increases to 2000 ns (i.e a much lower B_1) which indicates that the predictions arising from the simulated results shown in Figs. 5.9c and 5.9d are correct, and that smaller waveguide diameters focus the μw power. Fig. 5.9h shows a configuration in which the top of the waveguide extension is inserted 6mm into the corrugated waveguide. Here we notice a slight increase in the B_1 field (950 ns 90° pulse). This suggests that the μw couple into the waveguide more effectively, supporting the simulated predictions in Fig. 5.8f.

Improvements to μw Design

While substantial efforts have been made to optimize this probe for EPR, there are still improvements that can be made. PTFE is a good material for μw transmission, but it still cause reflections due to its relatively high dielectric constant compared to free space (2.1 vs 1). Thus with the current waveguide extension, some μw will always be reflected off the interface between PTFE and air. This can potentially be reduced by adding specific geometric features to this interface such as a hemispheric lens or by adding anti-reflective coating to the PTFE probe elements. Furthermore, the sample diameter can be increased, allowing thinner sample volumes (and higher B_1). The position of the mirror behind the sample also plays a role in the B_1 experienced by the sample, where careful simulations could reveal a more optimal position or mirror geometry (i.e a concave instead of flat mirror). For some DNP and EPR experiments, broadband μw

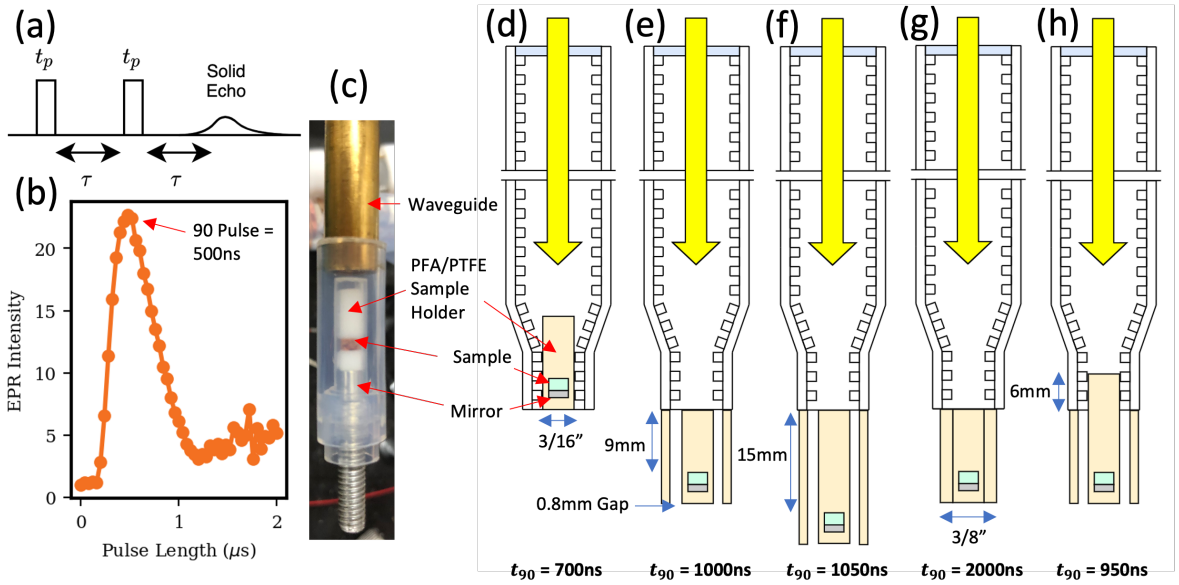

Figure 5.9: (a) Solid echo pulse sequence used for nutation experiment. (b) Nutation curve for a 0.5% BDPA in polystyrene sample using a 450mW solid state source. (c) Photo of the setup used to measure B_1 as a function of sample geometry in (d-h). Concentric PFA tubes were used to hold the waveguide extension in place. This is slightly different from the setup shown in Fig. 5.7 because the outer tube is PFA instead of Zirconia and has a larger OD, but should work to show proof of principle for simulations in Fig. 5.8. (d) The optimal arrangement for EPR detection and B_1 with the sample completely inside the waveguide. (e) Standard sample geometry arrangement with relevant dimensions labeled. (f) Geometry with a longer waveguide extension. (g) Geometry with no gap between the waveguide extension and a PFA sleeve– equivalent to a waveguide extension with a larger diameter. (h) Standard sample geometry with the waveguide extension inserted partially into the waveguide. For (d-h) the B_1 was measured with a 120mW source instead of the 450mW source used in (b).

performance is less important than high B_1 amplitude. In this case it can be beneficial to design a FP resonator between the waveguide and the mirror, and to tune the structure via precise actuation of the J arm, resulting in a resonant structure that can provide more power the sample at the expense of μw bandwidth.

RF performance of the DNP/EPR probe

The performance of the dual DNP/EPR probe for dual NMR and EPR detection, as well as DNP, was evaluated and summarized in Fig. 5.10. The EPR/NMR pulse sequences used for each measurement are shown in the inset of each figure panel. The measurements were performed of a sample consisting of 40mM 4-Amino Tempo and 1mM ^{13}C enriched Glycine in "DNP Juice" (i.e 60/30/10 d-Glycerol/D_2O/H_2O) at 23K, and include an echo-detected EPR field profile (Fig. 5.10a), an echo-detected EPR frequency profile (Fig. 5.10b), an echo-detected pump-probe ELDOR profile (Fig. 5.10c), and a ^{1}H$-^{13}$C Cross Polarization (CP) DNP profile (Fig. 5.10d), plotted on the same μw frequency axis (the field axis on Fig. 5.10a is scaled to be equivalent to the frequency axis). This allows us to compare the electron spin density (field/frequency sweep) and spin diffusion (ELDOR) to the DNP frequency profile. Here we can see that the DNP frequency profile has a dispersive shape which spans the EPR profile, indicating a cross effect mechanism. These broadband μw measurements are possible because of the non-resonant sample holder design of this dual DNP/EPR probe which makes it especially useful to perform EPR frequency dependent measurements spanning a frequency tuning range of 1 to 10 GHz. Frequency sweeps are advantageous over field sweeps because they can span a greater range compared to a room temperature field coil (in our setup, our sweep coil can reach +/-17mT or equivalently $\sim$1 GHz), they are faster than field sweeps (jumping of μw source frequency is much quicker than changing field), and most importantly, accessing multiple μw frequencies simultaneously or in rapid (μs to ms) succession is necessary to perform for two frequency (EPR) pump-probe experiments, such as ELDOR. Furthermore, μw frequency sweeping allows for the measurement of a DNP profile without retuning the NMR probe for each field position. However, our results show that the shape of the frequency sweep (Fig. 5.10b) is slightly distorted

compared to the field sweep (Fig. 5.10), in our setup due to interference from standing waves present in the probe and the quasi-optical μw bridge. The standing waves mostly affect the shape of the EPR frequency profiles or any experiment where the μw/EPR probe frequency is changing, while the shape of the ELDOR and DNP profiles are less affected as there, the μw/EPR pump frequency is stepped, but not the μw/EPR probe frequency.

Standing waves can be reduced by careful alignment of the bridge/probe (especially ensuring that the microwave beam is focused onto the waveguide of the probe and is not clipped), but this issue will always be present in some capacity. Thus, it is advanatageous to be equipped with a field sweep coil, in addition to having access to μw frequency tuning.

Next, measurements were performed of the same sample as discussed at 23 K and 8.5 T, except using a narrow-line radical of 40mM OXO-63 trityl replacing 40 mM 4-Amino TEMPO. A high concentration of trityl radicals have been shown to be a promising class of DNP polarizing agents at high field, while their underlying DNP mechanism is still subject of interest.[193, 73] Using our dual DNP/EPR probe, we measured an EPR field and frequency profile (Fig. 5.10e) that reveals a distorted/split line-shape. This line-shape is most likely due to clustering of the radicals leading to a distribution of electron-electron dipolar couplings. In Fig. 5.10f the saturation recovery of the trityl EPR resonance is measured at various frequencies of the EPR frequency profile (marked by dashed lines on Fig. 5.10e). The saturation recovery curves clearly illustrate that there are different components present in the EPR line that possess different relaxation properties. For example, the saturation recovery profile at 193.66 GHz (i.e in the "dip" region of the EPR profile) shows a much longer and distorted buildup curve, indicating the presence of multiple relaxation components with multiple T_{1e} rates.

Further interpretation of these EPR properties of this radical and their effect on DNP enhancements and properties require additional experiments. However, even the simple

EPR field and frequency profiles and the EPR frequency/field dependant relaxation measurements reveal the presence of heterogeneous electron spin populations that cannot be simply deduced from NMR-detected DNP experiments or simulations. Hence, concurrent measurements of EPR and DNP properties are key to the study of DNP mechanisms. Additional experiments that can be readily carried out (not shown here) include EPR T_m measurements, DNP buildup time profiles and DNP power profiles.

5.5 Conclusion

In this paper we have described the design principles and construction of a dual EPR/DNP probe operating in a cryo-free cryostat operating down to 8.5K temperatures. This system was constructed to simultaneously optimize cryogenic temperature, EPR and NMR performance with as few compromises as possible. This was achieved through careful design choices of NMR RF circuit components and simulation of μw/EPR structures. This probe was constructed with a focus on multi-frequency/broadband EPR and NMR performance to enable a wide variety of experiments on samples with a broad range of EPR and NMR properties as demonstrated via select EPR and DNP results on typical DNP radicals.

While much optimization has been carried out on this probe, there are still many ways this probe can be improved in terms of temperature, EPR and NMR performance, as suggested above. Furthermore, other practical improvements can be made to make the probe more versatile and operable. The "J arm" structure described above could be used as a sample exchange mechanism in which the entire probe is pulled from the cryostat for every sample. Optical fibers can be installed to allow optical irradiation (and perhaps some detection) capabilities to the probe for Triplet DNP and other light-activated NMR, EPR or DNP experiments.[194]

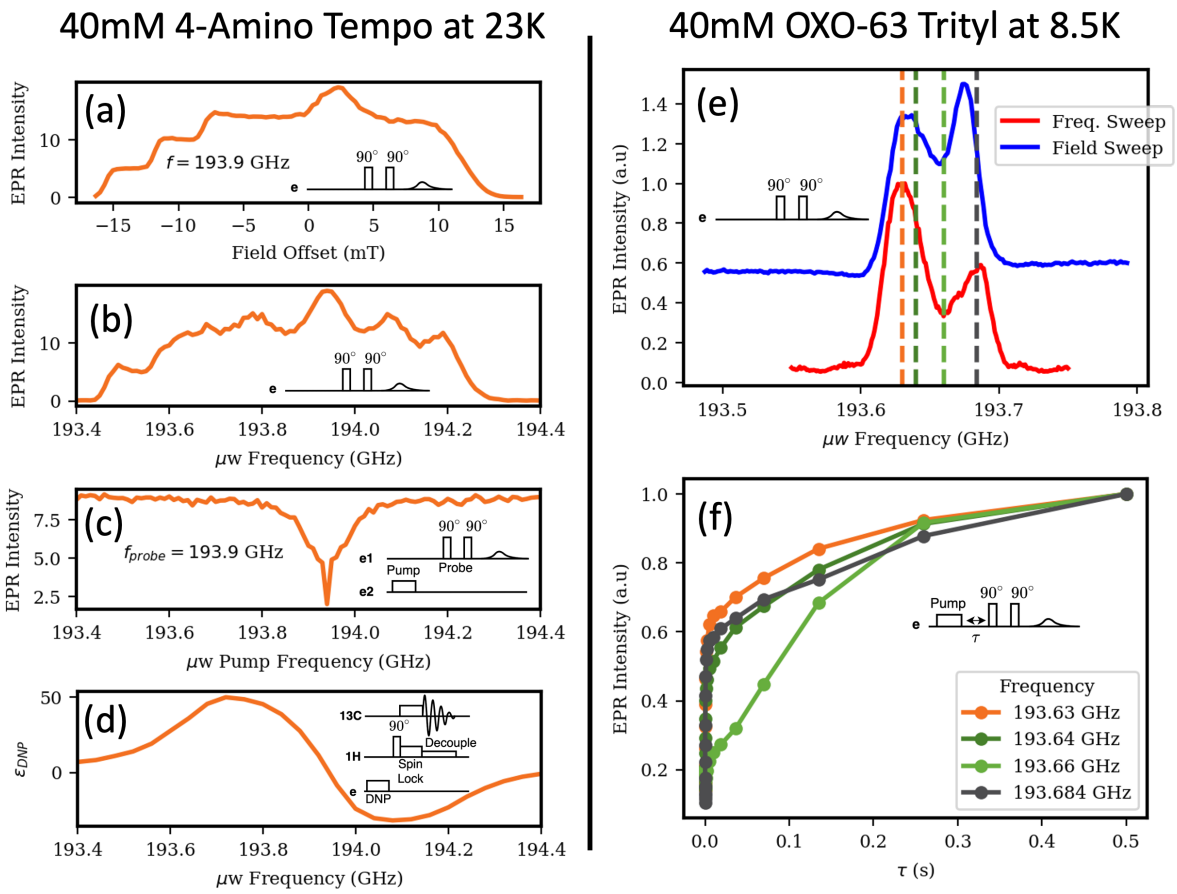

Figure 5.10: Left: EPR and DNP experiments on 4 amino tempo at 23K in DNP juice (60:30:10 d-glyercol, d2O, H2O). Inset are the pulse sequences used to acquire the data. (a) Field swept echo detected EPR spectra. (b) Frequency swept echo detected EPR spectra. Here we can see the effect of standing waves compared to the field swept spectra. (c) ELDOR profile. (d) DNP frequency profile with a 10s DNP buildup. Right: experiments on 40mM OXO-63 Trityl in DNP Juice at 8.5K. (e) Field and frequency swept echo detected EPR spectra. (f) Saturation recovery electron spin lattice relaxation measurements at different points on the EPR spectra.

Chapter 6

High Spin DNP

6.1 Introduction

DNP has revolutionized NMR spectroscopy for a number of applications including biosolids and materials characterization. This technique relies on transferring polarization from a paramagnetic electron polarizing agent (PA) to a nuclei of interest, which can boost the NMR signal intensity by orders of magnitude up to a theoretical limit of 660 for 1H nuclei.

At high magnetic fields, the cross effect (CE) mechanism has been shown to be the most effective. A crucial requirement for CE, is that two coupled electrons must be separated in EPR frequency by the nuclear Larmor frequency. To date much effort has been focused on tailoring spin 1/2 PAs to fulfill this frequency matching requirement. Recently it has been shown that mixtures of different types of radicals can more efficiently fulfill the CE frequency matching condition. This method has been shown to be effective in nitroxide-BDPA and nitroxide-trityl mixtures for 1H DNP, and in BPDA-trityl mixtures for direct C13 DNP up to moderately high fields (9.4T).[107, 103, 33, 195, 196, 197, 61] However, these specially tailored mixed spin 1/2 radical systems start to degrade in per-

formance at very high magnetic fields due to the g anisotropy of the radicals spreading out the spin density, and decreasing the number of spins that fulfill the CE frequency matching condition and can even contribute to simultaneous negative DNP enhancement which can destroy the signal. Thus there is a need for more effective mixed radical systems for high field use.

To date, the vast majority of search and optimization efforts for mixed radical development has been limited to a handful of spin 1/2 type radical moieties; namely, Trityl, BDPA, and nitroxide. Most efforts have gone towards modifying the surrounding chemical environment and/or linkers of these radical moieties. However, the g factors of these aforementioned radical moieties are limited, even when the host molecule is modified. Thus, tuning the EPR frequencies to match the CE condition is difficult without introducing a significant amount of zero field splitting which can alter the spin quantum number characteristic of the system.

An alternative solution is to find different classes of radicals for use in CE DNP systems. One option is to turn to higher spin radicals which often can have much more varied g factors, and narrow line widths. So far, DNP of exogenous high spin radicals has been demonstrated with Mn, Gd, Cr, and V.[198, 199, 200, 201, 200, 116, 202] Additionally, many material systems of interest such as catalysts, solar cells, and battery materials possess high spin endogenous metal ions that can potentially act as polarizing agent for DNP. In fact, DNP has been shown to be effective using endogenous metal centers for Mn, Gd, and Fe.[21, 199, 203]

While effective, all of these high spin systems have demonstrated much lower DNP enhancement than contemporary organic radical based spin 1/2 DNP systems, with 1H DNP enhancements rarely exceeding 10 at fields >5T. This is partially due to the polarization being spread out between the m_s sub-levels. However, all of these systems rely on a homogeneous mixture of radicals (i.e only 1 type of radical), whereas heterogeneous

mixtures (such as tempo-trityl) have been shown to be more effective for spin 1/2 organic radicals. Heterogeneous mixtures are particularly important in MAS, as homogeneous mixtures of broad line radicals such as nitroxide can undergo depolarization which greatly reduces DNP enhancement at fast spinning speeds.[47, 32]

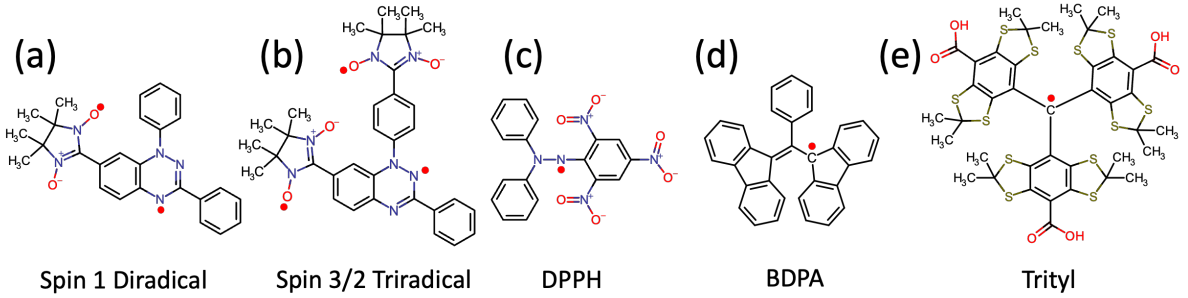

Figure 6.1: (a) Spin 1 Triradical

In theory, radicals of different spin can be used in conjunction for CE DNP as long as they fulfill the CE frequency matching condition. In this paper we seek to demonstrate for the first time, DNP using a mixture of spin 1/2 and higher spin radicals at high magnetic field (7T). The high spin radicals used are organic spin 1[204] and 3/2[205] radicals synthesized by the group of Rajca et. al as shown in Fig. 6.1a and Fig.6.1b respectively. These radicals are triplet ground state radicals with the frequency of the $\Delta m_s = 1$ EPR transition very near the $\Delta m_s = 1$ of typical DNP radicals. The spin 1/2 radicals were chosen such that their spin density optimally fulfilled the CE frequency matching condition according to high field (7T) EPR measurements, and for their solubility in organic solvents (which the higher spin radicals are soluble in). Initial EPR experiments at 7T determined that DPPH (Fig. 6.1c) matched the CE condition for teh spin 1 radical while BDPA (Fig. 6.1d) matched the CE condition for the spin 3/2 radical.

EPR and DNP measurements of the radical mixtures were then carried out at the same conditions to diagnose the DNP mechanism, and determine if indeed DNP was happening between the two types of radicals. EPR frequency profiles were taken of the

radical mixtures to verify the distribution of spin density and determine the optimal radical mixtures to match the CE condition, and the electron relaxation properties were measured. Finally, EPR nutation experiments were conducted to verify the spin state of each radical.

6.2 Methods

6.2.1 Radical Systems

BDPA (1,3-bisdiphenylene-2-phenylallyl), DPPH (2,2-Diphenyl-1-picrylhydrazyl), and 99.6% dueterated toluene (d8) were purchased from Sigma Aldrich and were used as recieved. The diradical (Fig. 6.1a) was recieved from Rajca et al. and was synthesized according to Gallagher et. al[204], and the triradical (Fig. 6.1b) was also recieved from Rajca et al. and synthesized according to Shu et. al[205]. All samples were dissolved in a mixture of 3:1 d8-toluene (fully dueterated) to Ethanol (non-dueterated).

6.2.2 High Field EPR and DNP Measurements

High field EPR and DNP measurements were carried out on our custom home-built cryogen-free 7T dual EPR/DNP spectrometer. A full description of the spectrometer[185] and probe (chapter 5) can be found elsewhere. All EPR and DNP experiments were carried with a 20uL volume of sample. Unless otherwise noted all experiments were carried out at 8.5K.

6.2.3 Pulsed X Band EPR Measurements

6.3 Results and Discussion

The goal of this paper is to show that spin 1/2 radicals can effectively participate in CE DNP with higher spin radicals. To maximize the chance of observing CE DNP, the radical mixtures used must have sufficient spin density that fulfill the CE matching condition. Thus, field swept EPR spectra were obtained to determine the suitability of various spin 1/2 radicals to undergo CE with the high spin radicals according the CE frequency matching condition. The field swept EPR spectra of higher spin radicals, as well as 3 common narrow line were measured at 6.907T and 8.5K and are shown in Fig. 6.2. Field sweeps were used to eliminate standing wave effects present in frequency sweeps, and the x axis was converted from field to frequency to easier visualize the frequency matching conditions. Here, the spin 1/2 radicals are BDPA, OXO63-Trityl, DPPH, and 4-amino tempo (4AT) and are shown above, and the higher spin radicals (spin 1 diradical and the spin 3/2 triradical) are shown below. From these spectra we can see that the higher spin radicals have relatively broad lines (similar in width to the nitroxide line of 4AT). BDPA has the narrowest line of the spin 1/2 radicals followed by OXO63 and DPPH. The EPR maxima for BDPA, DPPH, spin 1, and spin 3/2 are marked with dashed lines, with the nuclear larmor frequency (1H) indicated by black arrows. From this we can see that the maxima of DPPH and spin 1 are separated by the γ_n. Similarly BDPA and spin 3/2 are also separated by γ_n. This means that these two radical pairs have significant spin density that can fulfill the CE condition, and thus these radical pairs were chosen to be tested for DNP.

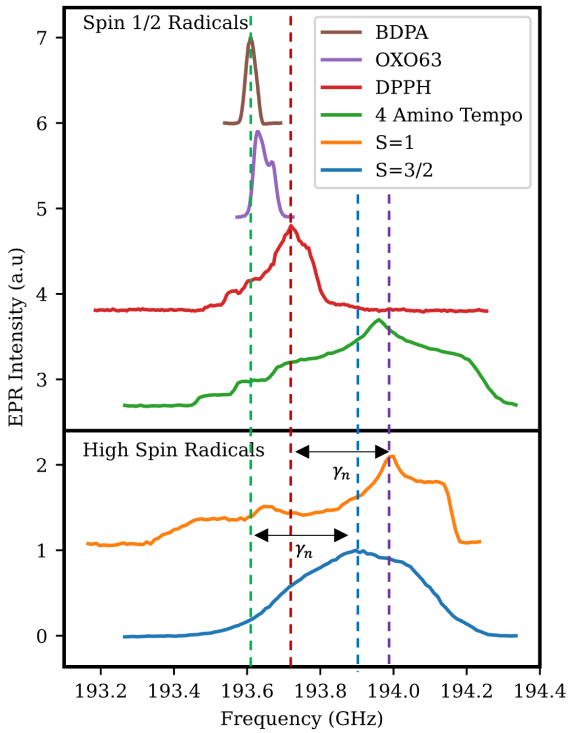

Figure 6.2: (Top) Field swept, echo detected EPR profiles of 20mM solutions of common DNP radicals including BDPA (Brown), Trityl OXO63 (purple), DPPH (red) and 4 amino tempo (green) at 7T and 8.5K. All radicals were dissolved in a mixture of 3:1 d8-toluene to EtOH except 4 amino tempo which was dissolved in a 60:40 glycerol to water mixture. (bottom) Field swept, echo detected EPR profiles of 5mM spin 1 diradical (orange) and 5mM spin 3/2 triradical (blue) in 3:1 d8-toluene to EtOH at 7T and 8.5K.

6.3.1 DPPH and spin 1 Radical

To prove that high spin and spin 1/2 radicals can undergo cross effect DNP with each other, DNP frequency profiles, EPR spectra, and electron-electron double resonance profiles (ELDOR) were acquired for the mixtures of high spin and narrow lines spin 1/2 radicals. DNP profiles and EPR spectra were also acquired for solutions of isolated high spin, and spin 1/2 radicals to test if the DNP enhancement (ϵ) was coming from CE between two radicals of the same spin. Concentrations of the radicals were set to 20mM for the spin 1/2 radicals and 5mM for the higher spin radicals. These concentrations were

chosen so that most DNP observed in the radical mixtures is a result of CE between the spin 1/2 and higher spin radicals, and not of CE between multiple higher spin radicals. To verify that the observed DNP enhancement was not a result of CE between spin 1/2 radicals, DNP was measured in solutions of only 20mM spin 1/2 radicals. DNP was also measured of only the higher spin radical at 5mM to demonstrate that very little CE DNP occurs at this concentration. To determine the effect of total radical concentration on DNP, frequency profiles of 25mM were also collected.

Fig. 6.3a shows the DNP profile for the mixture of 5mM spin 1 and 20mM DPPH radical, as well as isolated 5mM and 25mM spin 1, and 20mM DPPH. Here we can see the mixture of spin 1 and DPPH radicals gives much better DNP enhancement ($\sim$11) than the solution of just spin 1 ($\sim$2), showing that the spin 1/2 is playing an effective role in DNP. Increasing the spin 1 concentration to 25mM increases the maximum DNP enhancement to ($\sim$7). This is most likely due to increased spin concentration leading to higher inter-electron coupling and thus more CE pairs that can effectively undergo DNP. However using a homogeneous solution of spin 1 will likely lead to depolarization under MAS. The 20mM DPPH sample gave almost no noticeable DNP. This can be rationalized by the EPR spectra of 20mM DPPH in Fig. 6.2 barely spanning γ_n (i.e 294 MHz) in width, meaning that there is very little spin density that can fulfill the CE matching condition.

The shape of the DNP frequency profile for both the 5mM and 25mM spin 1 samples is identical (normalized frequency profiles in the SI). This suggests that the operative DNP mechanism is the same for both concentrations, although the efficiency is better for 25mM due to more intermolecular e-e coupling. The frequency profile for the mixed sample is shifted slightly to lower frequencies by approximately 40 MHz. Fig. 6.3b shows the EPR profile of the DPPH and spin 1 radical mixture. Here we can clearly distinguish the DPPH radical (whose EPR maxima is denoted with the dashed purple line), as well as

the spin 1 radical (EPR maxima denoted by the dashed brown line). Unexpectedly, the positive enhancement maxima does not correspond to the DPPH EPR maxima as shown in Fig. 6.2 and Fig. 6.3b, although the negative enhancement maxima does correspond to the spin 1 EPR maxima. This can be rationalized as DPPH has quite a broad EPR linewidth and significant spin density that can fulfill the CE condition away from the EPR maxima. Additionally, there exist non-zero spin density $-\gamma_n$ (-294MHz) away from the EPR maxima (at $\sim$ 193.4 GHz) which will yield negative enhancement that cancels out the positive enhancement, thus making the maximum DNP enhancement appear at a slightly lower frequency. Knowing this information, we could potentially increase DNP enhancement by using BDPA with the spin 1 radical instead of DPPH as there is negligible spin 1 spin density -294MHz away from the BDPA center frequency. However further optimization of these radical systems is beyond the scope of this paper.

ELDOR profiles were taken to trace the μw induced saturation transfer across the EPR line. Saturation transfer is necessary for CE to occur as the triple spin flip required will result in partial saturation of an electron spin γ_n away from the μw irradiation frequency (i.e pump frequency). In an ELDOR experiment, the frequency of a saturating pump pulse was swept across the entire EPR line, and the polarization of a desired spin packet (frequency) is monitored via a fixed frequency spin echo sequence as shown in Fig. 6.3c. If polarization is exchanged between spin packets at different frequencies and the detection frequency, the intensity of the spin echo will decrease. In the ELDOR curves measured here (shown in Fig. 6.3d), the detection frequency was set to the EPR maxima for DPPH (purple curve) and the spin 1 radical (brown curve). Lower values indicate more saturation transfer. The purple curve shows the saturation transfer from different portions of the EPR line to the DPPH radical. This data demonstrates that most saturation transfer to the DPPH occurs from spins $< \gamma_n$ away from the DPPH maxima, while only a slight amount of polarization is transferred from the spin 1 EPR

maxima. The brown curve shows saturation transfer to the spin 1 radical maxima. Here, the dip around 193.66 GHz shows that there is large saturation transfer from the DPPH to the spin 1 maxima. This can be explained as there is significantly more spin density at the DPPH position (193.66 GHz) that can transfer their saturation resulting in the dip in intensity for a pump frequency of 193.66 GHz.

To further prove the features of the DNP profile can be attributed to the mixture of radicals and not from just the 5mM spin 1, DNP buildup and EPR relaxation measurements were obtained. The results from these experiments are summarized in table 6.1.

DNP buildup curves were obtained for an isolated spin 1 radical, as well as the DPPH + spin 1 mixture. DNP buildup curves were measured by irradiating μw's on the frequency of maximum DNP enhancement and recording a 1H saturation recovery profile as shown in Fig.6.4a. The T_{DNP} values were measured by fitting the recovery curve to a stretched exponential equation:[206]

$$I = I_0[1 - \exp{(\frac{-t}{T_{DNP}})^{\beta}}] \tag{6.1}$$

Here, $I(t)$ was measured while I_0, T_{DNP}, and β were fit. t is the buildup time ($t_{buildup}$ in Fig. 6.4a), I is the detected NMR echo intensity, and I_0 is the maximum NMR echo intensity for an infinite buildup time, T_{DNP} is the DNP buildup constant, and β is the stretch factor. For a mono-exponential (i.e single component) buildup, β should equal 1, however for a buildup with multiple time constants T_{DNP}, β will be closer to 0.5. Errors for all fitted parameters were calculated from the covariance.

Fig.6.4b shows the fits for the DNP buildup curves for the DPPH/spin 1 mixture as well as 5mm spin 1, with the fitting parameters T_{DNP} and β shown in table 6.1. Here we can see that the DNP buildup is faster for the mixture of radicals with the

mixture having a T_{DNP} of 9.49s and the isolated spin 1 radical having a buildup of 50.46s. This can be attributed to the higher total concentration of radicals in solution and thus stronger average e-e coupling leading to a faster triple flip transition necessary for CE[90]. Furthermore the β was lower for the radical mixture (0.78 vs 0.81. This can be attributed to part of the DNP buildup for the radical mixture coming from DNP between spin 1 electrons (rather than between DPPH and spin 1). Notably, the DNP enhancement is only around 2 for the 5mM spin 1 sample, and thus the apparent DNP buildup will have a strong component coming from the much longer 1H spin lattice relaxation time.

The electron T1 relaxation rate (T_{1e}) has also been shown to be a crucial factor in determining how effective a polarizing agent will be.[31, 207] T_{1e} was measured using the pulse sequence shown in Fig. 6.4c where an initial long μw pulse destroys the magnetization of the electrons followed by a variable recovery time (t_{rec}), and then EPR echo detection. The T_{1e} values were extracted by fitting the acquired saturation recovery curve to equation 6.1, with T_{DNP} being replaced by T_{1e}.

Here, T_{1e} was measured for the EPR maxima of DPPH (193.66 GHz) and spin 1 (194 GHz) in the mixture, as well as for a sample of isolated 5mM spin 1 at 194 GHz and is shown in Fig. 6.4d with the results summarized in table 6.1. The T1e for both maxima in the radical mixture, as well as the isolated 5mM spin 1 radical were almost identical (2.03ms, 1.75ms, and 1.85ms for the DPPH, spin 1, and isolated spin 1 maxima respectively). However, the β value for the isolated 5mM spin 1 was much closer to 0.5 (0.64) while the mixed radicals were very close to unity (1.00 and 0.94). This suggests that a single relaxation process dominates the T_{1e} of the radical mixture while there are a variety of processes in the isolated 5mM spin 1 (some of which have a T_{1e} much longer than 1.85ms). The most likely culprit for relaxation in the radical mixture is e-e coupling leading to cross relaxation as the total radical concentration is much higher (25mM vs

5mM) as suggested by the ELDOR profile in Fig. 6.3c.

To further analyze this effect the EPR transverse relaxation time T_m was also measured for the radical mixtures as well as the isolated 5mM spin 1 radical. Unlike T_2 in NMR, T_m represents the transverse relaxation of only a narrow bandwidth of spin packets within the overall EPR line, and not the entire spectral linewidth (as in NMR), due to the very soft pulses used in EPR. Transverse relaxation is known to be very sensitive to spin-spin (i.e e-e) coupling, with more coupling leading to shorter time constants. T_m was measured using the pulse sequence shown in Fig. 6.4e. Here a solid echo detection pulse sequence was used, with the delay between pulses τ was varied to allow the spins to dephase for a variable amount of time. The data was fit to the following equation:

$$I = I_0 \exp \frac{-\tau}{T_m} \tag{6.2}$$

Where τ is the inter-pulse delay time, I is the measured EPR echo intensity, I_0 is the maximum echo intensity for the shortest possible delay time, and T_m is the transverse relaxation time constant.

The acquired data and fits are shown in Fig. 6.4d with the T_m fit values shown in table 6.1. Here we can see that the T_m for the isolated 5mM spin 1 is about twice as slow as for the radical mixture. This further supports our suspicion that there is larger e-e coupling present in the radical mixture which is contributing to faster T_{1e} relaxation. This additional e-e coupling is would necessarily be between the DPPH radicals and the spin 1 radicals, as the concentration of spin 1 radicals does not change.

6.3.2 BDPA and spin 3/2 Radical

DNP and EPR experiments were likewise carried out on a mixture of 20mM BDPA and 5mM of the spin 3/2 triradical. The DNP frequency profiles for the radical mixture,

as well as the solutions of the isolated radicals are shown in Fig. 6.5a. Here, the radical mixture gives the best performance, yielding a DNP enhancement of ∼2, while 5mM of the spin 3/2 radical gave a DNP enhancement of ∼1.65. Both mechanisms appear to be CE due to the DNP frequency profile spanning the entire radical mixture EPR spectra (shown in Fig. 6.5b), although the addition of 20mM BDPA shifts the DNP frequency profile to lower frequencies by ∼50 MHz. This shift can be attributed to the spin density of BDPA fulfilling the CE matching condition for more spins of a lower frequency, owing to the spin density of BDPA being much lower in frequency than the spin 3/2 radical. In fact the maximum DNP enhancement for the radical mixture is at the same frequency as the EPR maxima for BDPA as seen in Fig. 6.5b and indicated by the purple dashed line. The ELDOR profiles in Fig. 6.5c show the the diffusion of polarization to the BDPA maxima (purple curve), and to the spin 3/2 maxima (brown curve). When detecting BDPA frequency, can see that there are slight dips in ELDOR intensity along the EPR line of the spin 3/2 radical and vice versa. This indicates that saturation built up on the BDPA will transfer to the spin 3/2 and vice versa, which further suggests that CE DNP is taking place between these two radicals.

Strangely, the 20mM BDPA sample gave very little DNP enhancement (< 1.1) which contradicts other studies suggesting strong SE and OE DNP from BDPA samples at high field and cryogenic temperature.[208, 209, 88] One possible explanation is that the solution is not efficiently glassing due to slow cooling through the glass transition temperature, and that the radicals are aggregating. This behaviour has been observed for BDPA in different solvents.[210] Indeed, in this work we do not freeze quench the samples, and cooling is quite slow through the T_g of ∼117 K. Aggregation would additionally limit the e-e coupling between BDPA and the spin 3/2 radical. This aggregation theory is supported by the ELDOR spectra which shows minimal polarization transfer from the spin 1/2 (BDPA) to the higher spin radical (spin 3/2). This is compared to the ELDOR

spectra of the DPPH/spin 1 radical mixture which shows much more intense polarization transfer from the spin 1/2 (DPPH) to the higher spin radical (spin 1), which suggests less coupling between BDPA-spin 3/2 than DPPH-spin 1. As such we do not expect to see optimum DNP from the BDPA/spin 3/2 radical mixture under our conditions. However further discussion/speculation of this aggregation effect is beyond the scope of this paper.

The DNP buildup and electronic relaxation times were also measured for the spin 3/2-BDPA radical mixture as well as the 5mM isolated spin 3/2 sample as shown in Fig. 6.6 and summarized in table 6.1. The DNP buildup time (Fig.6.6a and table 6.1) for the spin 3/2-BDPA radical mixture is approximately double that of the isolated spin 3/2 radical (8.08s vs 4.16s) which suggests that the DNP pathway is different for each sample, even though the enhancements are similar. The β value for DNP buildup is very close to unity (0.99) for the isolated spin 3/2 system, but much less for the radical mixture (0.709) which indicates multiple DNP time constants for the mixture. This indicates that the radical mixture most likely has DNP occurring between spin 3/2 radicals as well as between spin 3/2 and BDPA radicals.

The T_{1e} values (Fig. 6.6b) for the spin 3/2 in the radical mixture is significantly less than for the isolated 5mM spin 3/2 sample, indicating that e-e coupling between spin BDPA and the spin 3/2 radical is providing a pathway for electron cross relaxation. Similar to the isolated spin 1 radical, the spin 3/2 radical has a lower β value than both radicals in the radical mixture suggesting that a single relaxation pathway is more dominant in mixture (likely e-e coupling between radicals). The T_m values (Fig. 6.6) also indicate that addition of BDPA to the spin 3/2 radical results in stronger cross relaxation as the T_m of the isolated spin 3/2 radical (1.341μs) is longer than for the spin 3/2 mixed with BDPA (1.190μs).

	ϵ_{DNP}	T_{DNP}[1]	$\beta(T_{DNP})$	T_{1e}	$\beta(T_{1e})$	T_m
DPPH[2]	10.9	9.49 ± 1.37	0.78 ± 0.10	2.03 ± 0.02	1.00 ± 0.02	0.465 ± 0.006
spin 1[3]	—	—	—	1.75 ± 0.03	0.94 ± 0.02	0.415 ± 0.004
spin 1 5mM[4]	1.9	50.46 ± 3.78	0.81 ± 0.03	1.85 ± 0.11	0.64 ± 0.02	0.905 ± 0.013
BDPA[5]	2	8.08 ± 1.153	0.709 ± 0.10	5.25 ± 0.10	0.79 ± 0.02	1.502 ± 0.012
spin 3/2[6]	—	—	—	2.11 ± 0.03	0.79 ± 0.01	1.190 ± 0.006
spin 3/2 5mM[7]	1.7	4.16 ± 0.59	0.99 ± 0.15	3.39 ± 0.07	0.68 ± 0.02	1.341 ± 0.020

[1] Taken at the optimal positive DNP enhancement frequency.
[2] DPPH EPR maxima (193.66 GHz) of the radical mixture.
[3] Spin 1 EPR maxima (194 GHz) of the radical mixture.
[4] Spin 1 EPR maxima (194 GHz) without DPPH.
[5] BDPA EPR maxima (193.615 GHz) of the radical mixture.
[6] Spin 3/2 EPR maxima (193.615 GHz) of the radical mixture.
[7] Spin 3/2 EPR maxima (193.9 GHz) without BDPA.

Table 6.1: Summary of DNP and EPR relaxation measurements.

6.3.3 Verification of Spin State

To differentiate between radicals with different spin quantum numbers, the nutation (B_1) frequency can be measured. For different spins, the transition between a magnetic ground and excited state can be defined by the ladder operators S^+ and S^-. For a spin 1/2 the lowering operator is shown below:

$$S^-_{1/2} = \begin{pmatrix} 0 & 0 \\ 1 & 0 \end{pmatrix}$$

Here the relative "speed" or frequency of transition between states (i.e +1/2 to -1/2) is 1. However for higher spin systems the matrix elements of the ladder operators can be larger, and thus the transition between states can be faster. For a spin 1 system the raising operator is shown below:

$$S^-_1 = \begin{pmatrix} 0 & 0 & 0 \\ \sqrt{2} & 0 & 0 \\ 0 & \sqrt{2} & 0 \end{pmatrix}$$

For a spin 1 system the transition between states (i.e -1 to 0) will happen with a relative rate of $\sqrt{2}$ or 1.414. This means that a μw pulse will tip a spin 1 electron 1.414 times faster than a spin 1/2 electron.

For a spin 3/2 system the ladder operator would be:

$$S^{-}_{3/2} = \begin{pmatrix} 0 & 0 & 0 & 0 \\ \sqrt{3} & 0 & 0 & 0 \\ 0 & 2 & 0 & 0 \\ 0 & 0 & \sqrt{3} & 0 \end{pmatrix}$$

Where the $m_s = +1/2$ to $m_s = -1/2$ transition will happen twice as fast as for a spin 1/2 electron, and the $m_s = +3/2$ to $m_s = +1/2$ transition will happen $\sqrt{3}$ times faster.

Thus we carried out a rabi nutation experiment of the radical mixtures in which the EPR echo intensity was monitored as a function of pulse length (t_p) in a solid echo pulse experiment as shown in the inset of Fig. 6.7a. Here, the detection pulse lengths were fixed and a pre-saturation pulse t_p was varied in length. This was done for the EPR maxima of each radical with the μw frequency held constant and the field varied to avoid frequency dependant standing wave effects. The resulting nutation curve is shown in Fig. 6.7a, and should be at a minimum when t_p is a 90° pulse and a maximum at integer multiples of 180°. Here we see the first minimum from Fig. 6.7a suggest that that the 90° length for the spin 3/2 radical is 800ns (a B_1 of 0.312 MHz)

However we have found measuring the 90° time from the first minimum to be occasionally misleading due to the effects of short Tm and varying excitation bandwidth. These effects are most apparent as a shift of the first minima towards longer times. Therefore, the nutation curve was Fourier transformed to capture the full B_1 frequency information, thereby obtaining the B_1 nutation spectra as shown in Fig. 6.7b. Before Fourier transforming the nutation curve, the time domain data was zero filled to 4096

total points ($\sim 400\mu$s), shifted such that the last measured point corresponds to 0 EPR intensity (not shown for the nutation curves in Fig 6.7a). The resulting B_1 spectra (Fig. 6.7b) shows a B_1 of 0.27 MHz for DPPH, and 0.38 MHz for the spin 1 radical.

Nutation curves were also obtained for the spin 3/2 and BDPA radical mixture and are shown in Fig. 6.8a. These curves were acquired and processed identically to those in Fig. 6.7a, and yielded the Fourier transformed nutation spectra shown in Fig. 6.8b.

Here we can see that the nutation frequency for BDPA is centered around 0.24 MHz while the nutation frequency for the spin 3/2 radical is centered around 0.46 MHz. The ratio between the nutation frequencies is 1.91 which is very close to the theoretical ratio of 2 between a spin 1/2 and spin 3/2 electron, confirming that the system is behaving as a spin 3/2 radical mixed with a spin 1/2 radical. We can also see that the width of the nutation spectra for BDPA is narrower than that of the spin 3/2 radical, DPPH, and the spin 1 radical. This can be at least partially attributed to the longer T_m of the BDPA which causes less dephasing during the pre-saturation pulse t_p. Notably the central nutation frequency for BDPA (0.24 MHz) is slightly different than for DPPH (0.27 MHz), although they should be the same as they are both spin 1/2 radicals. This discrepancy can be attributed to slight standing wave effects in the high field EPR probe. Even a slight change in position or geometry of the sample holder can lead to a non-neglible change in μw field distribution in the sample due to the very small wavelength of irradiation ($\sim$1.54mm). This means that nutation can vary slighly between samples, which is why here we compare nutation frequency of 2 components in the same sample.

6.4 Conclusion

In this work we have demonstrated CE DNP between radicals of different spin quantum number. For both the spin 1 and spin 3/2 radicals used, the DNP enhancement

was increased by addition of a spin 1/2 radical chosen for its favourable spin density characteristics. DNP frequency profiles and buildup measurements show that the operative CE DNP pathway changes upon the addition of spin 1/2 radical indicating that the high spin radicals undergo CE DNP with the spin 1/2 radical. EPR profiles confirm that both radicals are present in the sample, and that the features of the DNP profile can be attributed to the mixture of radicals rather than a single radical. ELDOR and electron relaxation measurements confirm that e-e coupling exists between the high spin and spin 1/2 radicals, and that polarization is exchanged between radicals, both of which are necessary for CE DNP. Finally, the spin characteristic of each high spin radical was confirmed by nutation experiments referenced to the spin 1/2 radicals.

There exists much room for growth in the area of hetero-spin CE DNP. The enhancements reported here are much less than with state of the art spin 1/2 radical systems. Although the spin density matching requirement of CE DNP was reasonably met, the e-e coupling could be further optimized (i.e via adjusting concentration or synthesis of biradicals). Furthermore the zero field splitting of higher spin radicals can spread out the electron polarization between the triplet (or quartet in the case of spin 3/2) manifold resulting in less efficient DNP, and so optimization of this parameter could additionally boost DNP.

This work also motivates the use of specially tailored exogenous spin 1/2 radicals with endogenous high spin complexes such as metal centers in proteins and catalysts for bulk, surface, and site selective DNP.

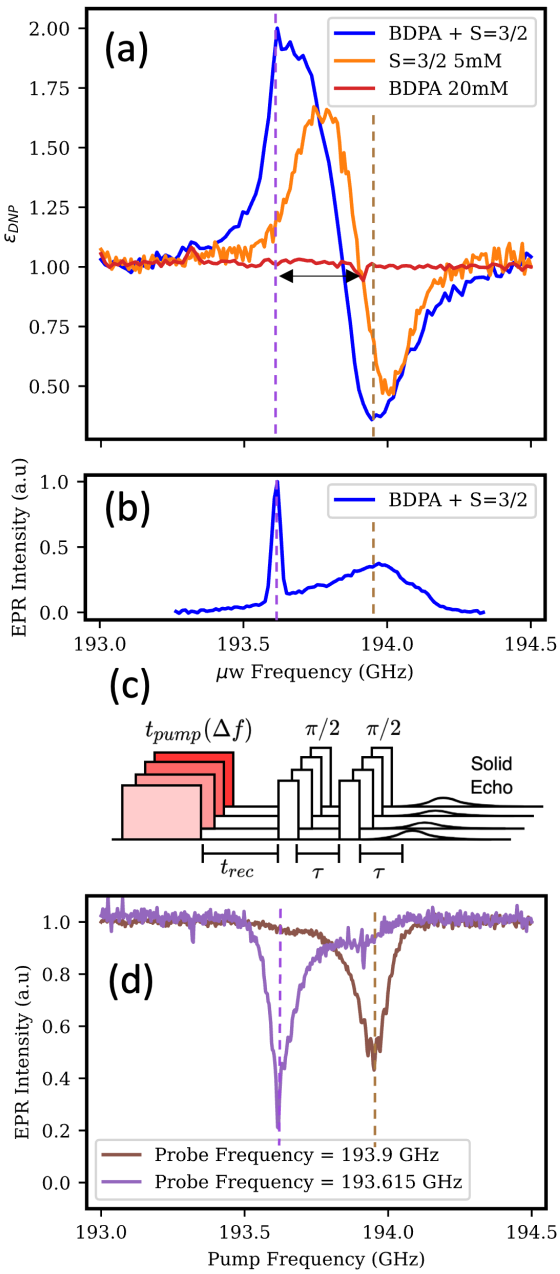

Figure 6.3: (a) DNP frequency profiles at 8.5K and 6.907 T. The DNP buildup time used was 10s. (b) EPR frequency profile of the mixed 20mM DPPH + 5mM spin 1 sample. The purple and brown dashed lines indicate the maxima for the DPPH and spin 1 EPR spectra respectively. Note that the EPR spectra was detected with a shorter echo pulse length optimized towards the spin 1 radical, and that the intensity of the DPPH on the EPR spectra is likely greater than shown. (c) Pulse sequence used for an ELDOR experiment. The frequency of a pump pulse t_{pump} is varied while the frequency of the detection pulses are held constant.(d) ELDOR profiles with the detection frequency set at the DPPH EPR maximum (purple curve) and spin 1 EPR maximum (brown curve). The purple curve has been shifted upwards for ease of viewing.

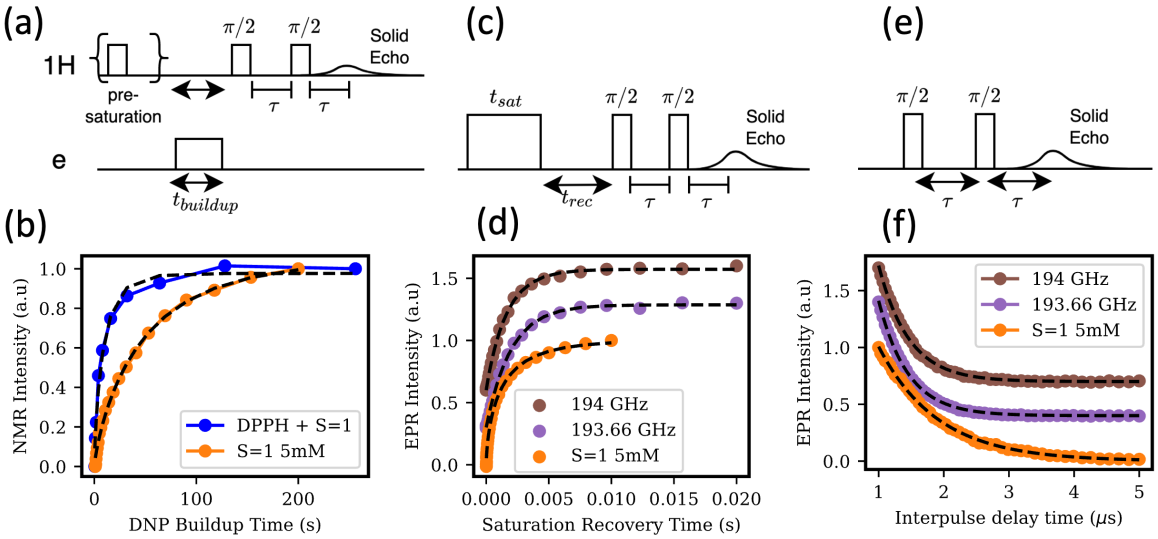

Figure 6.4: (a) Pulse sequence used to determine T_{DNP}. (b) DNP buildup curves along with the fits used to determine T_{DNP} (black dashed lines). (c) Pulse sequence used to measure T_{1e}. (d) Electron saturation recovery curves with fits used to determine T_m (black dashed lines). The purple and brown data points are shifted up for easier viewing. (e) Transverse relaxation curves used to determine T_m with the fits (black dashed lines).

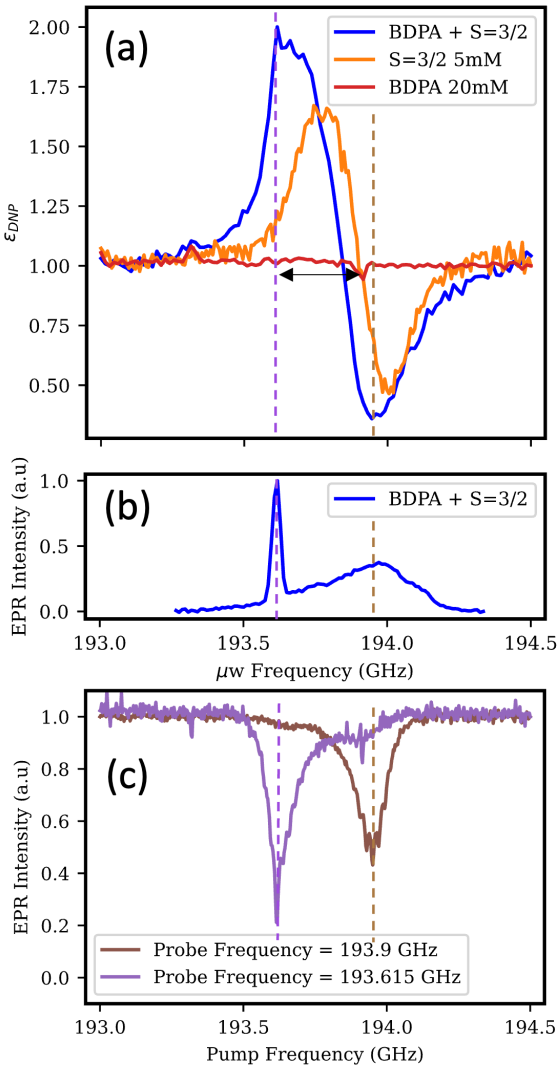

Figure 6.5: (a) DNP frequency profiles at 8.5K and 6.907 T. The DNP buildup time used was 10s. (b) EPR frequency profile of the mixed 20mM BDPA + 5mM spin 3/2 sample. The purple and brown dashed lines indicate the maxima for the BDPA and spin 3/2 EPR spectra respectively. Note that the EPR spectra was detected with an echo pulse length optimized towards the spin 3/2 radical, and that the intensity/spin population of the BDPA on the EPR spectra is greater than shown. (c) ELDOR profiles with the detection frequency set at the BDPA EPR maximum (purple curve) and spin 3/2 EPR maximum (brown curve).

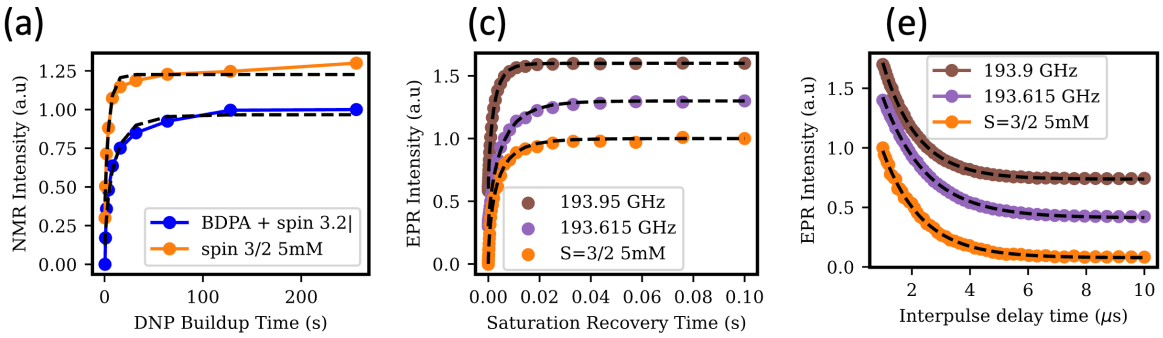

Figure 6.6: (a) DNP buildup curves along with the fits used to determine T_{DNP} (black dashed lines). (b) Electron saturation recovery curves with fits used to determine T_m (black dashed lines). The purple and brown data points are shifted up for easier viewing. (c) Transverse relaxation curves used to determine T_m with the fits (black dashed lines).

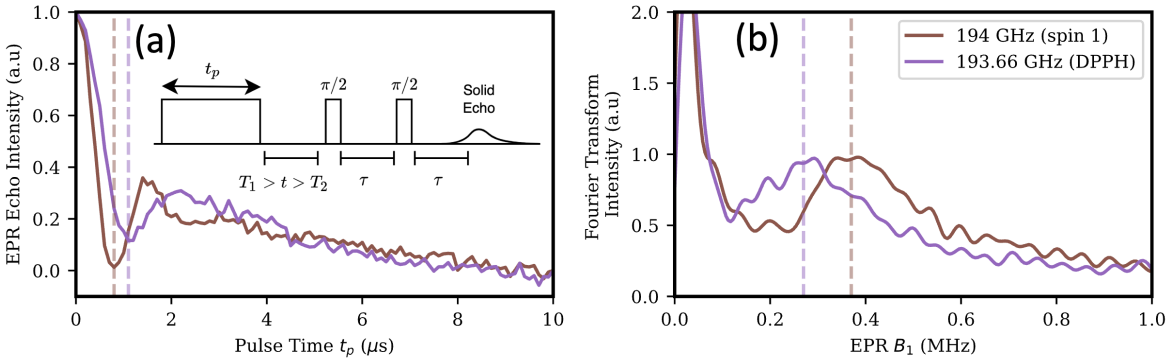

Figure 6.7: (a) Nutation curves of the DPPH EPR maxima at 193.66 GHz (purple) and spin 1 (brown). The first minima corresponding to a 90° t_p for each curve is marked with the dashed lines. Inset is the pulse sequence used to record the nutation curve. (b) Fourier transform of the nutation curves in (a).

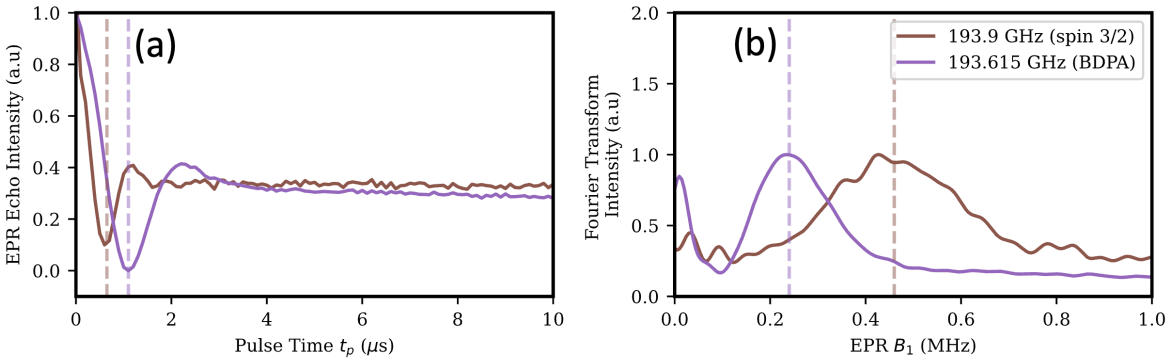

Figure 6.8: (a) Nutation curves of the BDPA EPR maxima (93.615 GHz) and spin 3/2 EPR maxima (193.9 GHz). The dashed lines indicate the first minima corresponding to 1.1μw and 0.65μw for BDPA and spin 3/2 respectively. (b) Fourier transform of the nutation curves in (a) with the central nutation frequency indicated by the dashed lines.

Chapter 7

Conclusion and Outlook

The work shown in this thesis demonstrates a multi pronged approach to understanding and enhancing the efficiency of CE DNP at high magnetic fields (7T). This approach consisted of analyzing and exploiting electron spin-spin coupling through various methods and techniques.

In chapter 3, an analysis and quantification the origin of electron-electron exchange (J) coupling in state of the art nitroxide biradicals was presented. We discovered that the previously unexplained EPR lineshape of TOTAPol and AMUPol were a result of a wide distribution of J couplings, rather than a single value. Additionally these distributions were observed to shift based on temperature. To understand the origin of these distribution we carried out rigorous testing of the "Broken Symmetry" DFT technique to find the optimal functionals, basis sets, and numerical precision necessary to predict J coupling within an order of magnitude of the small values present in DNP systems. This DFT technique lead us to discover that the rotamer states of these biradicals (i.e the angle between the nitroxide moieties) can greatly affect the value of J for each conformation which is a likely explanation for the aforementioned distribution of J. The angle between the two nitroxide moieties also determines the relative frequency of each electron and

thus their ability to meet the CE frequency matching condition. DNP simulations of various bis-nitroxide angles and J values confirm that this angle is doubly important for CE DNP efficiency. Furthermore these simulations revealed that J coupling is much more effective for DNP than dipolar coupling as it is not dependant on the relative orientation of the radical in space which can be a time varying quantity under MAS. Thus, in the future vitrification of bis-nitroxides at specific temperatures could be used to tune the value and distribution of J to optimize DNP efficiency.

Chapter 4 detailed a novel approach to manipulating heterogeneous coupled electron spin densities (i.e a Tempo-Trityl biradical) via arbitrarily shaped μw irradiation to enhance the efficiency of DNP under MAS, whereas previously broadband DNP techniques were limited to non-spinning systems. We discovered significant gains in CE DNP efficiency by using broadband μw irradiation to more effectively selectively saturate the trityl radical spin density. Furthermore we found that arbitrarily shaping the μw irradiation to match the spin density of biradicals could lead to even further gains in DNP efficiency. DNP simulations reveal that this "AWG DNP" is only expected to become more powerful at higher μw powers when more powerful sources such as frequency sweepable gyrotrons, high power solid state sources, and gyro-amplifiers become available. This technique is also expected to work well on mixed radical systems with their EPR lines broadened by strong J coupling, and in systems with fast T_{1e} such as high temperature DNP systems.

To analyze DNP mechanisms and pathways in situ, we developed a cryogen-free (8.5K) high field (6.9T) triple resonance EPR and DNP probe. This probe takes advantage of a previously built dual EPR/DNP spectrometer, but adds a novel inductively coupled double resonance NMR capability for CP and decoupling experiments while maintaining optimal broadband μw performance. Furthermore the probe was designed to be used with a cryogen free cryostat which allows almost indefinitely long experimental runs at temperatures as low as 8.5K at little cost, which would be impossible with

traditional liquid helium cyrostats.

This probe has already been used to demonstrate DNP for the first time between radical PA's with different spin quantum numbers as described in chapter 6. We first used the EPR capability of our probe to screen the spin density of various common spin 1/2 radicals and match them to novel high spin compounds synthesized by the group of Rajca et. al to optimally fulfill the CE frequency matching condition. Once suitable spin 1/2 radicals were determined they were mixed with the higher spin radicals to attempt CE DNP between paramagnetic centers of different spin. The resulting DNP frequency profiles paired with EPR nutation frequency experiments proved that DNP was indeed occurring between spin 1/2 and high spin radicals. To date, CE DNP has been limited to radicals of the same spin. This demonstration opens the door to a new class of DNP radical mixtures with potentially more favourable spin density distributions for matching the CE condition or more optimal electronic relaxation properties.

In addition to the experiments described in chapter 5 and chapter 6, this probe was designed to be modular to suit a wide variety of experimental needs. Currently modules have been constructed to carry out broadband ENDOR experiments (Fig. 7.1a) as well as light activated experiments (Fig. 7.1b) in addition to the standard double resonance NMR probe. In particular we are interested in pursuing a new class of light activated porphryin radicals for photoexcited triplet DNP which promises to allow NMR access to optical levels of polarization which far outstrip the polarization of electrons.[194]

Finally, the versatility of this probe makes it an excellent test-bed for novel DNP instrumentation. A novel butterfly style surface coil has also been implemented in the probe. This coil provides high sensitivity for both EPR and NMR/DNP experiments by increasing the RF filling factor by almost an order of magnitude whilst simultaneously maintaining excellent μw characteristics by accommodating favourable sample geometries for EPR. The geometry of this coil also makes it suitable for DNP studies of flat samples

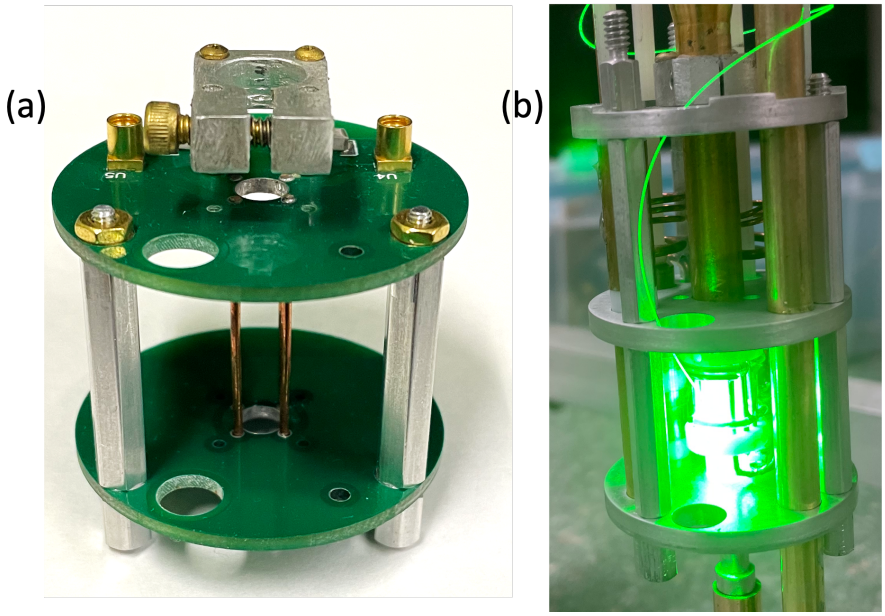

Figure 7.1: (a) ENDOR circuit for use with the dual EPR/DNP probe. (b) Fiber optic capability added to the inductively coupled double resonance NMR circuit.

such as thin films and semiconductors, as well as for potential use in a Fabry Perot resonator for applications in high field solution state Overhauser DNP. Furthermore, the combination of low Q and high B_1 make it suitable for studies of wideline quadrupolar nuclei where MAS would not be suitable.

Appendix A

Appendix A

A.1 EPR

A.1.1 Magnetic Parameter Determination

G factor The solution state X-band EPR spectra are relatively insensitive to G factor so values from literature sources have been used [57].

Hyperfine Value Isotropic hyperfine values were determined from the solution state spectra by determining the distance between the 3 hyperfine coupled peaks. This was done for each temperature point in each solvent in order to fit the spectra for J values. These values vary very slightly with temperature and solvent but are not far off from literature values.

Dipolar Coupling To get accurate fits in solution state, residual dipolar couplings needed to be included in the simulation parameters. The residual dipolar coupling included for AMUPol is shown in figure SA.2. For TOTAPol it was found that no residual dipolar coupling was necessary.

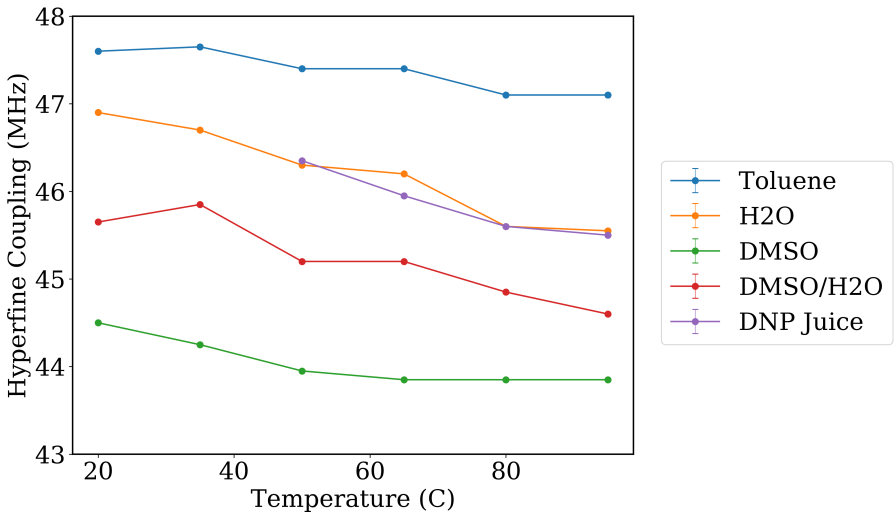

Figure A.1: Temperature Dependence of Hypefine Coupling

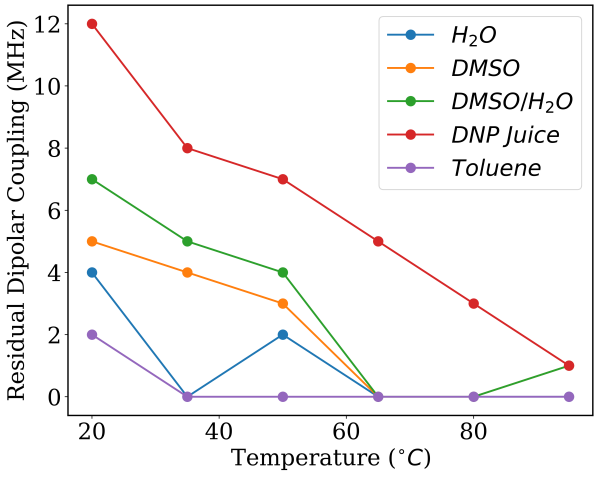

Figure A.2: Residual dipolar coupling present in solution for AMUPol

J Coupling In this paper, we describe the value of J using a Lorentzian distribution. The parameters for the distribution of J were determined via a 2 dimensional global fit; including the center of the distribution, the full width half max (FWHM) of the distribution. Details of this procedure are present in the main text. Of note, the exchange interaction can also have an anisotropic component. However, the J values we have determined experimentally is purely isotropic because we take these values in solution. Hence in simulation, we only considered the isotropic component of J as it is the relevant interaction-component in our present context.

A.1.2 Concentration Effects

Spectral broadening associated with exchange coupling can also happen due to intermolecular interactions. EPR spectra were obtained for various concentrations in H_2O in order to determine the effect of intermolecular exchange. The results are shown in figure SA.3. It was found that at $20°C$ this effect was minimized at $100\mu M$ concentration, and thus all experiments were carried out at this concentration.

A.1.3 TOTAPol

In addition to a distribution analysis; the ratio of the population of the two components in the EPR spectra can be described by the *fraction of time* the biradical spends in each conformation, given by:[62]

$$\frac{f_c}{f_e} = 3(I_2/I_1)/(2 - I_2/I_1) \tag{A.1}$$

Here, f_c is the population of the contracted high J component and f_e the population of the extended negligible J coupled component. I_1 and I_2 correspond to the integrals of the first hyperfine and inner J coupled peaks marked with red (*) respectively in figure 2.

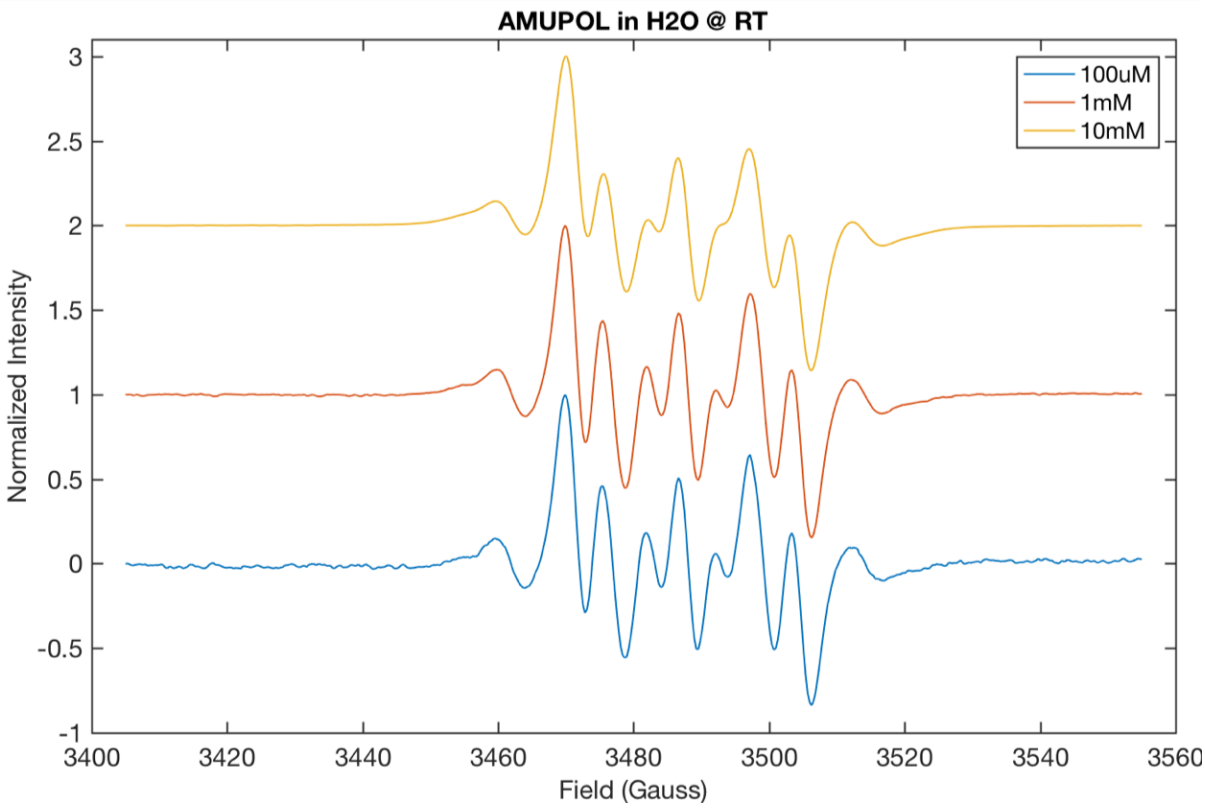

Figure A.3: Concentration dependence of AMUPol in H_2O at room temperature

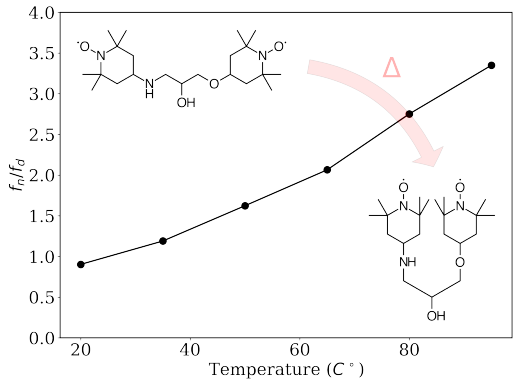

Figure A.4: Population analysis of the high and low J coupled states of TOTAPol according to eq. A.1

The results using the cage effect analysis is shown in figure SA.4. The value for f_c/f_e at $20°C$ of 0.9 agrees well with previous solution-state X band EPR analysis of TOTAPol at room temperature by Hu et. al (also 0.9).[211] Most notably, the relative population of the high J coupled structure increases substantially with temperature from 0.9 at $20°C$ to 3.5 at $95°C$. Previous studies have ignored the role of J coupling in TOTAPol; in fact, the first theory of DNP under MAS ignored the role of J coupling on the basis that TOTAPol exhibited none.[45] Here, the results show a high J coupling structure that becomes the majority component at around 30 $°C$.

A.2 DFT

A.2.1 Geometry Optimization

For truncated AMUPol, full AMUPol and extended TOTAPol the geometries were drawn and initially optimized using a universal force field (UFF) method through the program Avogadro. For all 3 molecules, the resulting geometries were then used as an input to Orca, in which we used the relatively inexpensive BP86 level of theory to obtain the initial guess. Finally, the optimum geometry was obtained at the B3LYP level

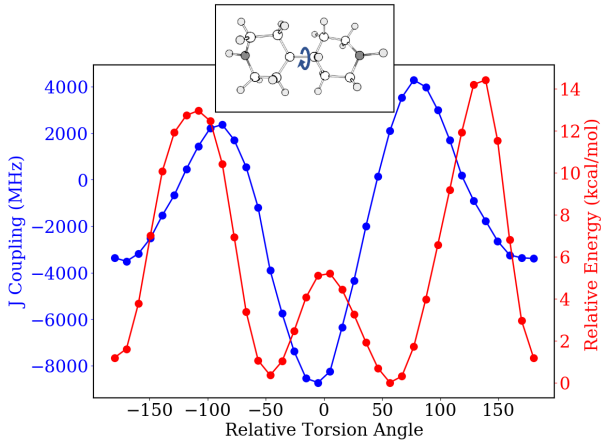

Figure A.5: Dependence of J on torsional angle between two nitroxide cyclohexane rings

of theory using a TZVP basis set, with Becke-Johnson damping of Grimme's dispersion correction included.[84, 212] For contracted TOTAPol the same method of BP86 followed by B3LYP was carried out, but the starting structure for input to the BP86 method was gained by rotation of the o-c-c-o dihedral angle of the extended conformation of TOTAPol, bringing the two hexagonal ring moieties closer. The so optimized geometries for truncated AMUPol, full AMUPol, extended TOTAPol, and contracted TOTAPol were used as starting geometries for all rotamer states. No further geometry relaxation was used when calculation J and E of rotamer states.

Broken Symmetry Testing

To ensure that the broken symmetry results were reliable, a number of tests were carried out on a model truncated AMUPol molecule. The geometry of this molecule was optimized using the above described method. The optimized geometry is shown in figure SA.6. Subsequent tests were carried out on the various rotamer states of this molecule: i.e rotation around the C-C-N-C dihedral angle (as demonstrated in figure 1c in the main text).

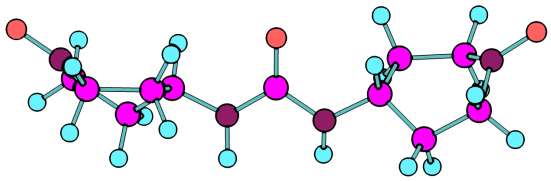

Figure A.6: Optimized geometry for truncated AMUPol molecule used in testing of broken symmetry DFT.

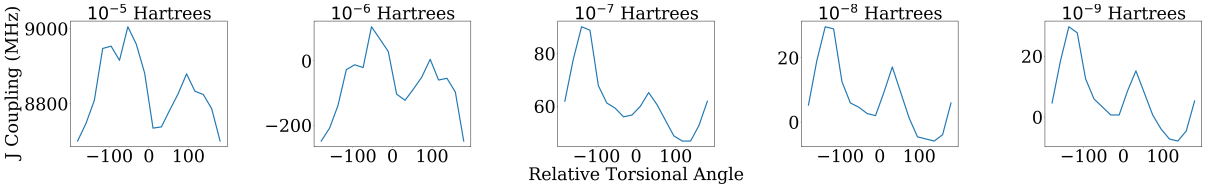

Figure A.7: Dependence of J on torsional angle between two nitroxide cyclohexane rings for the truncated AMUPol molecule at various levels of numerical precision.

Numerical Accuracy As mentioned in the main text, numerical accuracy is very important when dealing with such small energy values (MHz). Sufficient numerical accuracy was ensured by obtaining the J coupling of the above mentioned truncated biradical at different levels of SCF convergence precision. To further ensure the precision of our results, this was done for various rotamer states of the truncated AMUPol molecule as shown in figure SA.7. Here we see that the values of J do not change from a numerical accuracy (SCF energy convergence tolerance) of 10^{-8} to 10^{-9} hartrees and thus we consider this sufficient accuracy. To be safe, further calculations were carried out with an accuracy of $5 * 10^{-13}$ hartrees.

A.2.2 Full AMUPol Molecule

The geometry optimized AMUPol molecule is shown in figure SA.8a (top). The calculated structure yielded a inter-nitroxide (O-O) distance of 12.5 Åwhich is similar to

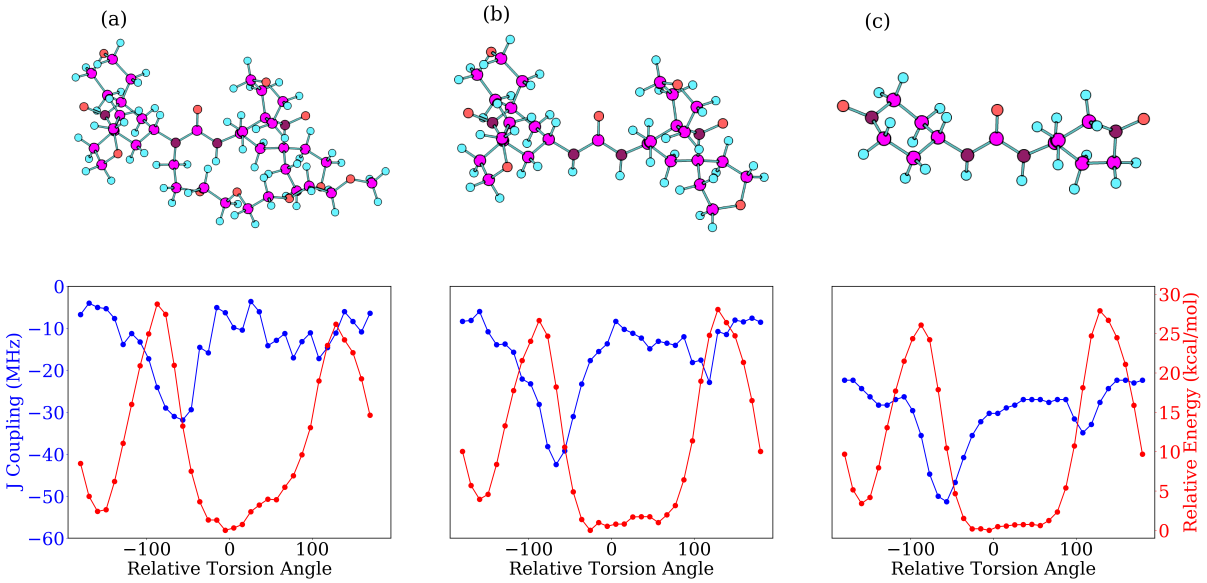

Figure A.8: Rotational dependence of J for AMUPol and various trimmed versions of AMUPol calculated at the CAM-B3LYP/SVP level.

a previously calculated (B3LYP/6-31G(d,p)) value of 12.79 Åin the literature.[49]

To investigate the effect of structural features on J, the rotational dependence of J was investigated for AMUPol and various trimmed versions of the molecule: namely removal of the R group and cyclohexane moieties (as shown in figure SA.8). To obtain the trimmed versions of the molecule, features of the optimized geometry of AMUPol were replaced with hydrogen. The placement of these hydrogens were then optimized at the B3LYP/TZVP level while keeping all other geometric parameters constant. The results are shown in figure SA.8 (top). The rotational dependence of J for each of these molecules was then calculated (figure SA.8(bottom)). In general, less geometric features leads to a smoother dependence of J on torsion angle.

A.3 DNP Simulations

A.3.1 Spin Evolution Program

`Coupling/SpinEV`$_E SI$

Appendix B

Appendix B

B.1 1. Experimental Setup

B.1.1 Magic-angle spinning DNP at 32 K and 6.9 T

A number of cryogenic DNP setups have been introduced [213, 32, 129, 214]. The NMR probe used in this experiment was a custom designed 4 mm DNP probe from Revolution NMR LLC. inspired by the design by Tycko et al. [213, 32]. The spectrometer used was a Bruker AVANCE DRX300 console. All experiments were preformed at 3 kHz spinning speed using room temperature nitrogen with a consumption rate of 10 litre/hour. The experiments were performed at low temperatures to compensate for low power output from solid-state μw sources used in our experiments. Liquid helium was used for cooling with an average flow rate of ∼3-4 litre/hour to maintain 32 K at the sample position. The radical solution was blended with ∼50 mg dry KBr for the purpose of temperature calibration inside a zirconia rotor obtained from Revolution NMR, which has the following dimension: 4 mm outer-diameter, 2.36 mm inner-diameter, and 46 mm axial-length. The sample position was fixed at the center of the rotor using teflon-

inserts placed at its both ends. The sample temperature was calibrated by measuring the spin-lattice relaxation time of ^{79}Br, as demonstrated by Thurber and Tycko. Continuous-wave μw was irradiated from tunable Virginia Diode Inc. (VDI) source, with a frequency range of 193-201 GHz and μw irradiation power of up to 350 mW, measured at right after AMC transmitter. The transmitted μw beam was guided through QO bridge, and finally reached to the corrugated wave-guide inside the 6.9 T ($\sim$7 T) wide bore magnet as described below. The sample rotor (MAS stator) was located at the end of the wave-guide. The design of the probe was an adaptation from the design of Thurber *et al.*.[213] More detailed description can be found in a recent publications from Han group [32]. We want to clarify that the experiments were performed at low temperatures to compensate for low power output from solid-state μw sources used in our experiments. Clearly as demonstrated in the main draft, the gain in enhancement with AWG over CW will be a lot more for high temperature conditions, and using higher μw power sources.

B.1.2 AWG-setup

Shaped μw pulses were generated using commercial AWG (DAx22000-8M, Chase Wavepond) integrated into the pulse forming unit of our DNP hardware [105, 38]. The AWG had 8 MB of memory and a 2.5 GHz clock frequency, providing 400 ps time resolution and over 500 MHz analog bandwidth.

Overall Microwave pathway

In Fig. B.1 the pathway of microwaves from synthesizer to probe is shown. First the microwaves are generated by a Micro-Lambda $\sim$12GHz YIG source. The microwaves are then passed through the AWG/Pulse forming unit for shaping (described below) before they are amplified (up to 350 mW) and frequency multiplied (16x to $\sim$200 GHz);

and launched as a gaussian beam into the quasi optical bridge. The quasi optical bridge directs the microwaves into the corrugated waveguide of the Revolution NMR LLC probe which itself sits in a Bruker 6.9 T wide bore superconducting magnet.

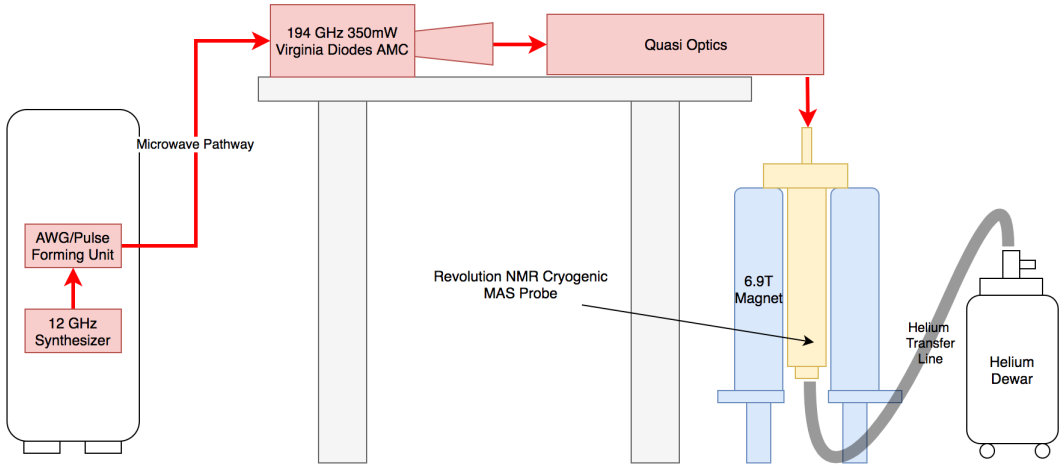

Figure B.1: **MAS DNP instrument setup.** The instrument schematic of ∼7 T MAS-DNP instrument operating at cryogenic temperatures is shown. Pathway of microwaves from the synthesizer to the probe is indicated by red arrows.

AWG pulse forming unit

In Fig. B.2 the components of microwave pulse forming unit (PFU) are shown. The input to the PFU is the 12 GHz synthesizer described above. The PFU has 2 channels which are toggled between using a fast SP4T pin diode switch. One channel is a bypass channel where microwaves pass through unaltered, and the other channel passes through an IQ mixer which is fed by the AWG unit. The second channel is the channel of interest for this paper as the AWG is what does the waveform shaping. This waveform shaping is done by injecting a time varying offset frequency into the IQ mixer, which then mixes the offset frequency with the 12 GHz carrier frequency to create a modified time varying ∼12 GHz signal. This signal is then passed to the 200 GHz 350mW VDI amplifier multiplier chain (AMC) which launches a high frequency (∼ 200 GHz) gaussian beam into the quasi

optical bridge.

Pulses are synchronized with the rotor period via a TTL signal from the MAS spin control unit which triggers the AWG to output a stored waveform every rotor period. All other switches and timing operations are done using a 300 MHz PulseBlaster ESR Pro card. The generated waveforms were verified by mixing the original 12 GHz carrier frequency with the output of the AWG channel, resulting in a down-converted signal which could be directly viewed on an oscilloscope for test purposes.

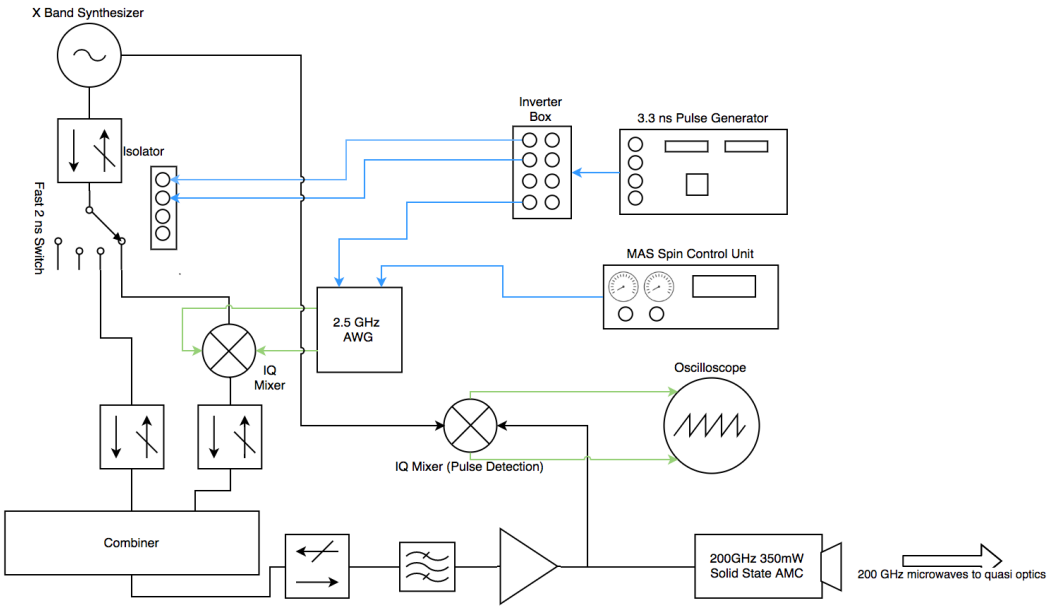

Figure B.2: **MW pulse forming and shaping unit.** Schematic of the AWG/pulse forming unit used to shape the microwave pulses. Microwave pathways are indicated by black lines. Blue lines indicate TTL control signals. Green lines indicated low frequency modulations to carrier signal.

Quasi-optical bridge

Figure B.3 shows the quasi optical setup used in this study. Here, components are arranged on a 125 mm grid. First, the microwaves are emitted as a gaussian beam with a 250mm focal length by the VDI AMC. The microwaves are directed onto a parabolic

mirror at the gaussian beam's focal point. This beam is then refocused by the parabolic mirror onto a Faraday isolator which consists of a wire grid and Faraday rotator. This device effectively rotates the polarization by 45° and prevents reflections back to the AMC. The beam then travels to another parabolic mirror which re-directs the beam downwards and focuses it onto the input of the corrugated waveguide centered in the NMR probe.

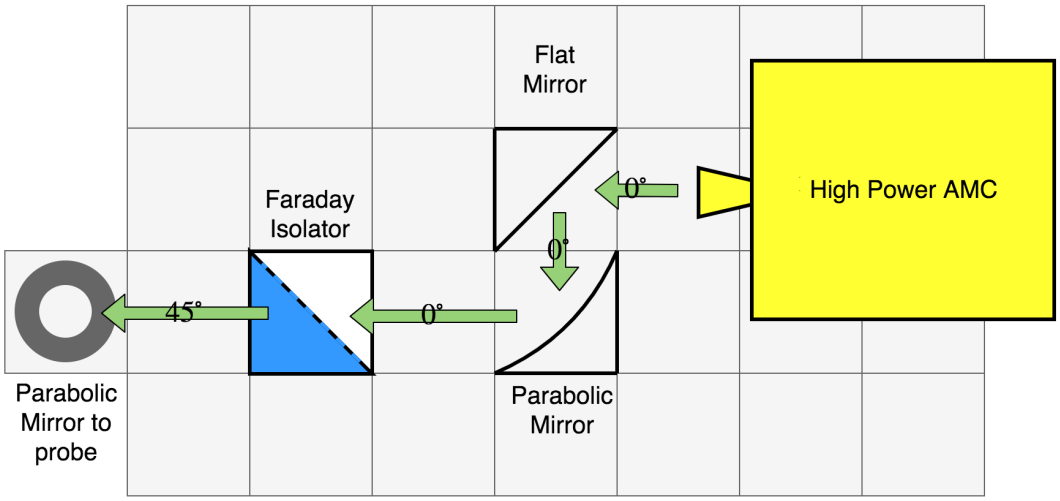

Figure B.3: **Quasi optical setup.** Top down schematic of the quasi optical bridge setup. Path of microwave beam is indicated by green arrows. Polarization of the microwave beam is indicated on the arrows.

B.1.3 AWG waveform shaping

The high frequency shaped waveforms are created by feeding the output of an AWG into the I and Q ports of an IQ mixer. Here the I and Q inputs are mixed with the 12 GHz carrier frequency, and are subsequently multiplied to $\sim$ 200 GHz as described above. The shaped output of the AWG for standard shapes is generated using analytical functions. First, a discrete set of frequency vs. time function $f(t)$ is generated. The

functions for chirp and wurst are shown below:

$$Chirp : f(t) = f_0 \pm 2\nu_{AWG}/\pi * arctan(1/tan(N\pi t/\tau_r)) \tag{B.1}$$

$$Wurst : f(t) = f_0 - \nu_{AWG} + \nu_{AWG} * (1 - cos(N\pi t/\tau_r)^n) \tag{B.2}$$

Here, f_0 is the center frequency, ν_{AWG} is the width of the frequency sweep, N is the number of blocks of the basic waveforms per rotor period, and n is the exponent or the power of the wurst function (for example for wurst3, $n = 3$). Generalized $f(t)$ functions are shown in Fig. B.4A-C. Next, the functions $f(t)$ need to be converted into a form that the AWG can directly interpret. To do this, we convert frequency $f(t)$ into phase $\phi(t)$ via integration:

$$\phi(t) = 2\pi \int f(t)dt \tag{B.3}$$

Finally, we generate the I and Q outputs of the AWG by taking the *sine* and *cosine* of the phase:

$$I = sin(2\pi\phi(t)) \tag{B.4}$$

$$Q = cos(2\pi\phi(t)) \tag{B.5}$$

The custom waveform shapes based off of frequency domain data $g(\nu)$ (such as the DNP frequency profile) are used to concentrate the power distribution across the EPR-line. First, we assign weights to each frequency bin, creating a histogram $h(\nu)$. Next we modify the concentration of the μw power distribution profile by assigning an additional

weight factor p to h to get $h(\nu)^p$. Then, a step function $f(t)$ is generated by assigning a relative length of time to each frequency bin according to its weight. This function $f(t)$ is then smoothed and processed the same way as the above chirp and wurst shapes. To illustrate the power distribution profiles for chirp, wurst3, and custom shapes, an example of the relative spectral power density of the irradiation is shown in Fig. B.4C-D.

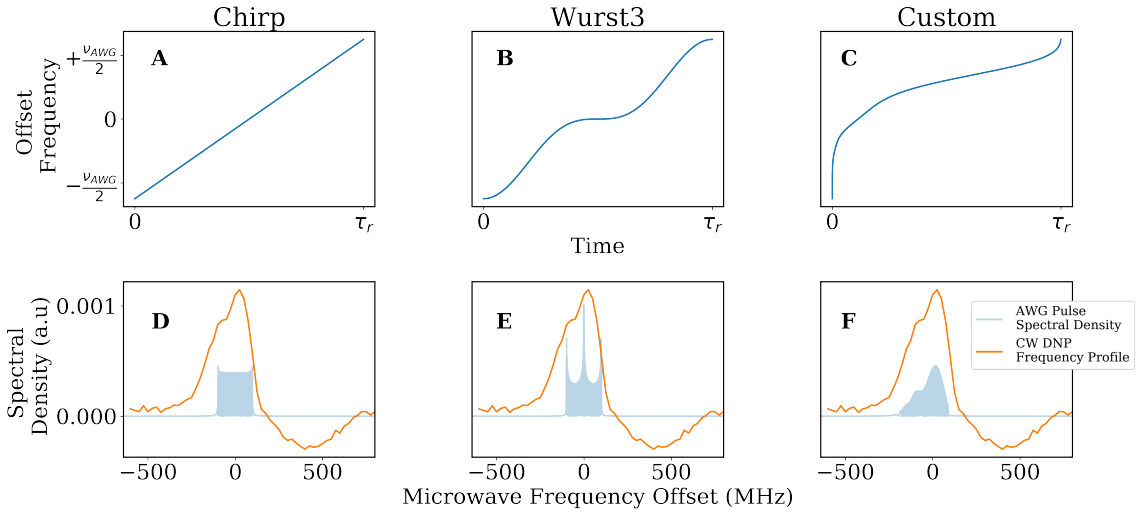

Figure B.4: **Shaped waveforms.** Generalized frequency sweep $f(t)$ (A-C) and power distribution $P(\nu)$ functions (D-F) for the shapes given to the AWG. $f(t)$ functions are shown for N = 1. Power distribution functions (blue shading) are computed using a fast Fourier transform of the calculated I and Q inputs for a pulse width of 6.25 MHz. The x axis for the AWG Pulse Spectral densities are multiplied by 16x in order to show the resulting $\Delta\nu_{AWG}$ (100 MHz) overlaid on the DNP frequency profiles. Spectral densities are not normalized. DNP frequency profiles $g(\nu)$ are overlaid for reference, and are shifted such that the maximum ϵ_{DNP} occurs at 0 MHz offset frequency.

B.2 2. Experimental results on TEMTriPol-1

B.2.1 Waveform optimization

N Optimization

Number of repeats per rotor period (N) was found to have a significant effect on ϵ_{AWG} as shown in Fig. B.5A. Here we see that DNP can be improved by about ∼10 % by choosing an adequate N, while fixing the $\Delta\nu_{AWG}$ at its optimum value. From this, we choose N = 10 for most other AWG experiments as an adequately fast repetition rate, unless mentioned otherwise. The optimum value of N depends on the available μw power as will be shown later in the numerical section. The optimum DNP enhancement, $\epsilon_{\mu won}/\epsilon_{\mu woff}$ obtained for TempTriPol-1 was ∼70 with AWG-DNP and ∼60 for AMUPol.

Chirp pulse optimization at 80K

Chirp pulses enhancements were also obtained at 80 K and the optimization results are shown in Fig. B.5B. We see the maximum effectiveness of the chirp pulse at 80 K is (∼10 %) higher relative to CW than at 32 K (shown by the black dashed line). This can be attributed to faster T_{1e} at 80 K as discussed in the main text.

Wurst pulse optimization at 32K

Wurst pulse optimization was done at multiple center frequencies to obtain the best ϵ_{DNP}. Optimization profiles with respect to $\Delta\nu_{AWG}$ for the wurst3 shape is shown in Fig. B.5C.

Effect of μw power on chirp AWG

Chirp AWG experiments were carried out at two different microwave powers to experimentally investigate the dependence of AWG effectiveness on power. The results (shown in Fig. B.5D) show that doubling the microwave power increases the effectiveness ($\epsilon_{AWG}/\epsilon_{CW}$) of chirp pulses significantly ($\sim$10 %). Additionally, with higher power, larger bandwidths ($\Delta\nu_{AWG}$) of the EPR-line can be irradiated, thus affecting more spin packets. This is illustrated using numerical simulations.

B.3 3. Numerical simulation

The Cross-Effect DNP simulations were performed using Spin-Evolution software package, for a 3-spin system, including 2 electrons and a nuclear spin, ^{1}H [65]. The calculations were done in Liouville space to incorporate for the effects of spin relaxation- which is an essential player in all the DNP mechanisms. The enhancement was measured with respect to the thermal Boltzmann polarization under static, therefore mitigating the nuclear depolarization effect. Powder averaging was performed using 100 (α, β) angles following REPULSION scheme for weighted orientation distributions. Notably, numerical results with 232 orientations showed the same trend as with 100 orientations. The simulations were performed for two kinds of PA- (1) bis-nitroxide, with e_1 and e_2 representing Tempo/nitroxide radical in the $e_1 - e_2 - ^1$H spin system, and (2) tethered TEMTriPol-1, with e_1 and e_2 representing Trityl and nitroxide radical, respectively, in the $e_1 - e_2 - ^1$H spin system. The principal axis components of the g-tensors of the electrons were taken as: Trityl: gx=2.0034, gy=2.0031, gz=2.0027, and Tempo: gx=2.0099, gy=2.0061, gz=2.0026. Unless mentioned otherwise, the spin parameters used for the calculations were as follows: the g-tensor of e_2 was related to e_1 by the Euler angles sets, (20,80,20) and (0,40,20) in bis-nitroxide and TEMTriPol-1, respectively. In both types of PA, the relative $e_1 - e_2$ dipolar tensor orientation was given by the Euler angles (10,45,60). The exact orientations of the spin tensors are not known due to existence of different molecular conformations, and therefore the choice of the above orientations are a rough estimate. The orientation of the $e_1 - ^1 H$ hyperfine coupling was randomly chosen to be (20,10,40). The $e_1 - e_2$, $e_1 - ^1 H$, and $e_2 - ^1 H$ couplings were taken to be 12.5 MHz (r_{e-e}=16$\mathring{A}$), 2.15 MHz ($r_{e_1-^1H}$=3.3$\mathring{A}$), and 0 MHz respectively. The nuclear spin-lattice relaxation rate, T_{1H}, was always set to 4s. The sample spin rate and B_0 field conditions were set to 10 kHz MAS and 6.9 T, respectively. The μw centre frequency was set around the centre of the e_1 (trityl) resonance. It was optimized for both CW and AWG schemes. An averaging over $2J$ (0MHz, 50MHz and 100MHz) was done to ac-

count for conformational distributions in TEMTriPol-1 PA for the exchange Hamiltonian: $\hat{H}_J = 2J * S_1.S_2$.

B.3.1 AWG-DNP simulation for bis-nitroxide

The AWG-DNP performance of bis-nitroxide system was calculated for different μw nutation frequency ($\nu_1^{\mu w}$) and different T_{1e}. The plot in Fig. B.6 maps the absolute DNP enhancement, $\varepsilon - {}^1H$ and relative enhancement $\varepsilon_{AWG}/\varepsilon_{CW}$, as a function sweep width $\Delta\nu_{AWG}$ for chirp waveform. It can be concluded from the plots in Fig. B.6 that for bis-nitroxides, the AWG technique can help to improve DNP efficiency by 20-30% at fast and intermediate relaxation rate compared to the spinning frequency, but only with higher μw nutation frequency. Maintaining a selective saturation with broad band irradiation is not easily achievable for bis-nitroxide under slow relaxation conditions.

B.3.2 AWG parameters optimization

There are two basic parameters for AWG irradiation: (i) the frequency sweep width $\Delta\nu_{AWG}$ and (ii) the AWG modulation rate, also denoted as $N{=}\tau_r/\tau_{AWG}$. Ideally, $\Delta\nu_{AWG}$ should be as large as the width of the narrower EPR-line in the mixed radical system, and τ_r/τ_{AWG} should also be high enough to maintain constant saturation throughout the rotor period. However, these parameters are not completely independent. Rather, they largely depend on the available μw power. The optimization of these parameters are shown in Fig. B.7 for three different μw nutation frequencies. As clear from the plots, the optimum $\Delta\nu_{AWG}$ and τ_r/τ_{AWG} increase with increase in μw nutation frequency encouraging the development of high power and AWG enabled μw source. Higher μw power ensures that the μw induced EPR transitions are more adiabatic.

B.3.3 DNP under fast electron spin relaxation

AWG irradiation helps to maintain large polarization differential between the electron spin pairs of TEMTriPol-1 PA participating in CE-DNP even at fast electron spin-lattice relaxation conditions. Figure B.8 maps absolute ${}^{1}H\varepsilon_{DNP}$ for AWG and CW irradiation and their ratios as a function T_{1e} normalized with respect to the rotor period, τ_r. Clearly, the the relative $\varepsilon_{AWG}/\varepsilon_{CW}$ increases with increasing τ_r/T_{1e} before reaching a maximum. The relative gain in enhancement using AWG irradiation can be further improved with higher μw power as shown in Fig. B.8B.

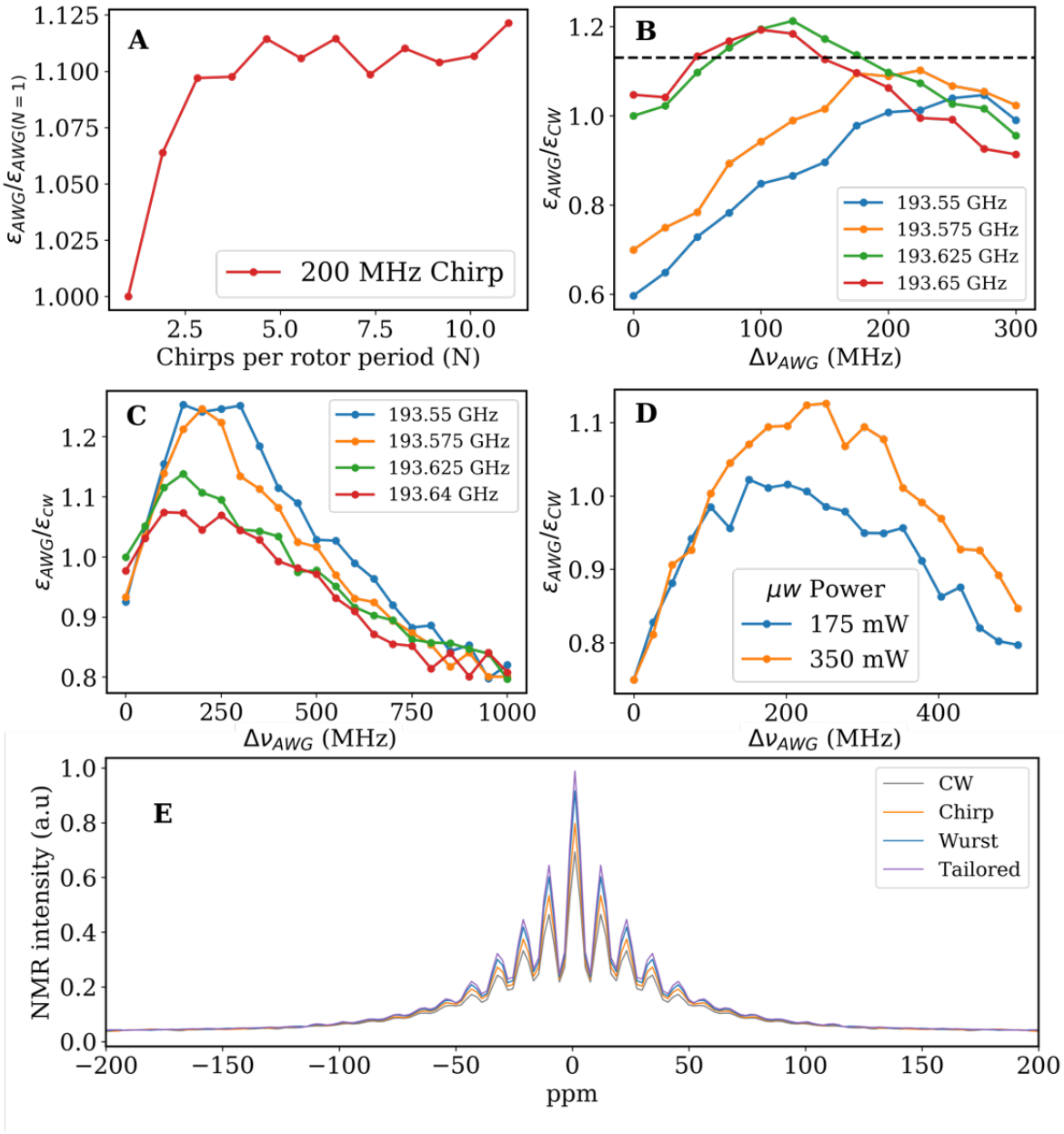

Figure B.5: **Experimental AWG-DNP optimization at 7T** (A) Effect of parameter N on ϵ_{AWG} at 32 K. (B) Optimization of the chirp pulse scheme at 80 K for various center frequencies with N=10. The dashed line indicates the maximum $\epsilon_{AWG}/\epsilon_{CW}$ for the same chirp pulse scheme at 32 K. (C) Optimization of the Wurst3 pulse scheme at 32K for various center frequencies with N=10. (D) Performance of chirp pulse shape at different μw powers at 32K, with N=10. (E) ^1H NMR spectra corresponding to maximum enhancements for various pulse schemes (Fig. 3D main text).

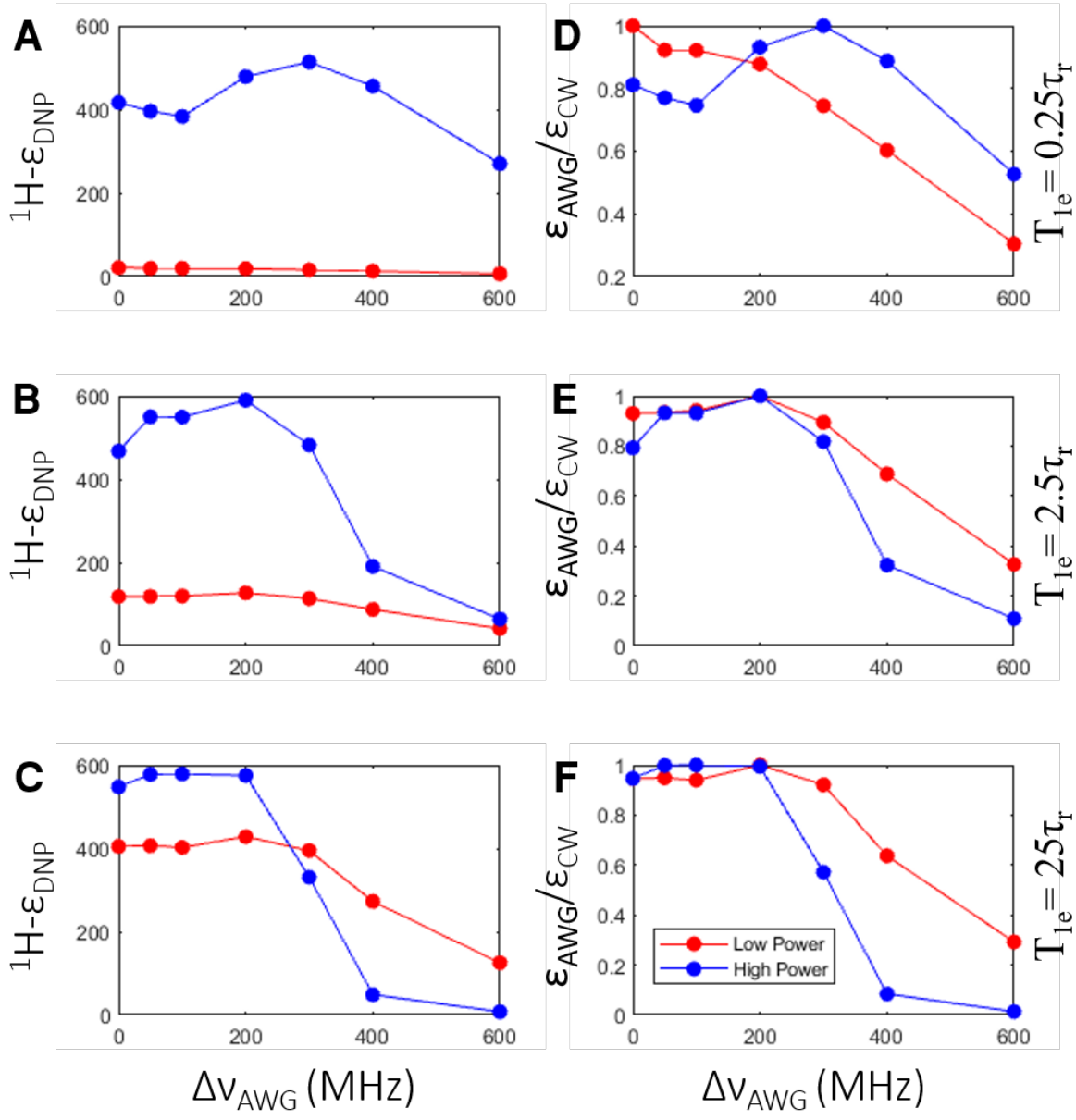

Figure B.6: **AWG-DNP on bis-nitroxide.** Numerically simulated ^{1}H DNP enhancement for $e_1 - e_2 - ^1$H spin system mimicking bis-nitroxide parameters, as a function of $\Delta\nu_{AWG}$ for two different μw nutation frequency 0.2 MHz (red) and 4 MHz (blue). Figures (A-C) map absolute enhancement and figures (D-E) map the ratio, $\varepsilon_{AWG}/\varepsilon_{CW}$ for different T_{1e}/τ_r. The simulation was performed at 10 kHz spinning using N=10 for AWG scheme.

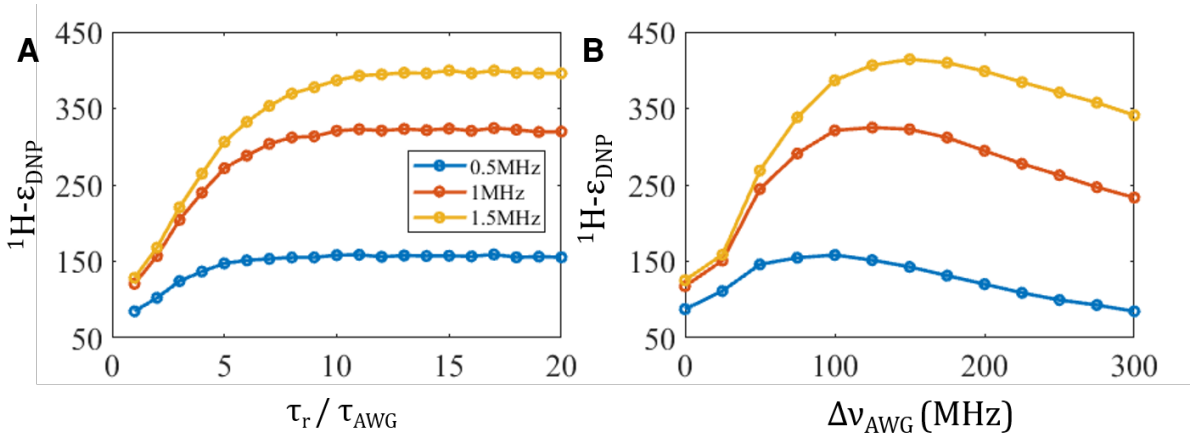

Figure B.7: **Numerically simulated AWG-DNP parameters optimization profiles.** Numerically simulated ^{1}H DNP enhancement using $e_1 - e_2 - ^1$H spin system mimicking tethered TEMTriPol-1 parameters for three different μw nutation frequencies 0.5 MHz, 1 MHz and 1.5 MHz. Figure (A) maps enhancement as a function of parameter $N = \tau_r/\tau_{AWG}$ for $\Delta\nu_{AWG}$=100MHz. Figure (B) maps enhancement as a function of $\Delta\nu_{AWG}$ for $N = \tau_r/\tau_{AWG}$=10. $T_{1e_1} = 0.25\tau_r$ and T_{1e_2}=0.5T_{1e_1}.

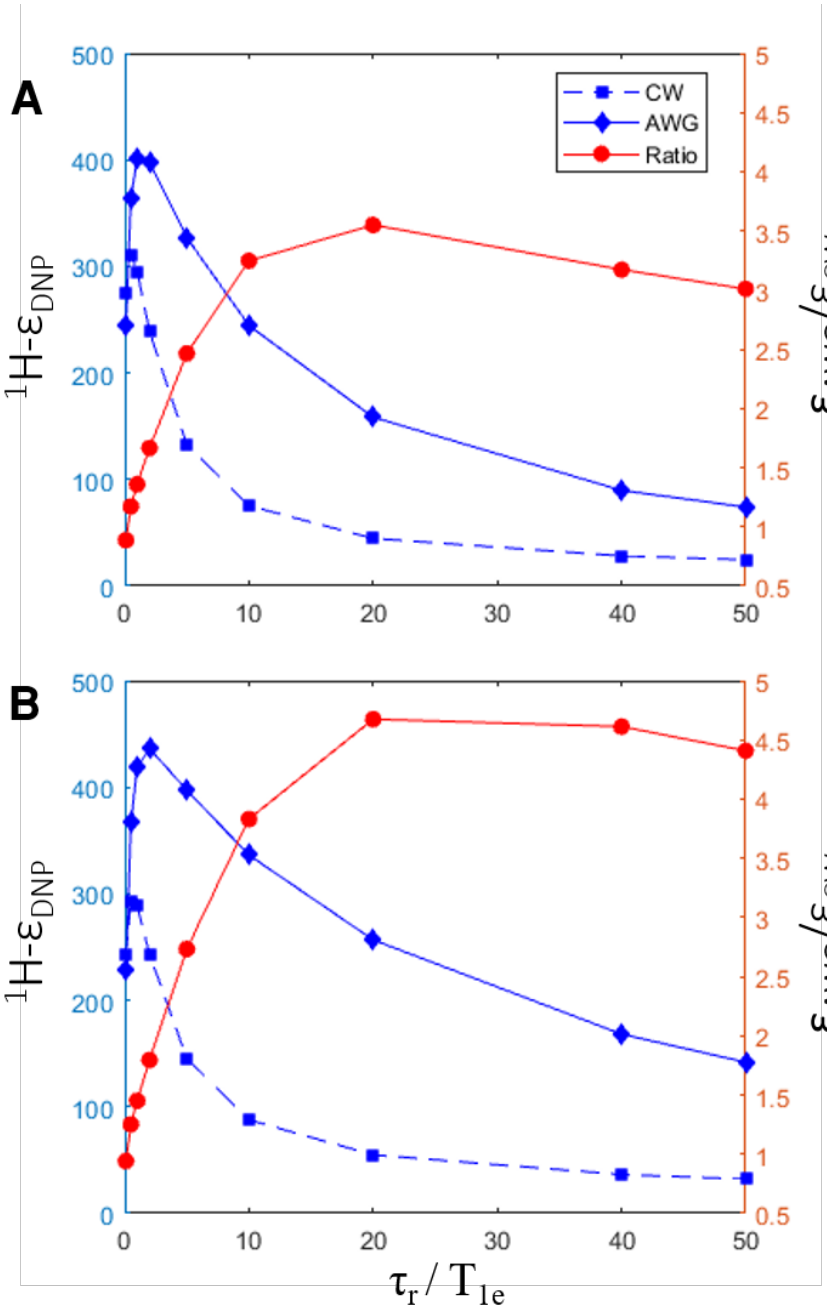

Figure B.8: **AWG-DNP under short T_{1e} conditions.** Numerically simulated ^{1}H DNP enhancement using $e_1 - e_2 - ^1$H spin-system as a function τ_r/T_{1e_1} for two different μw nutation frequencies (A) 1.5 MHz, and (B) 2.5 MHz. The left y-axis maps absolute enhancement obtained for CW (dashed-square) and AWG-chirp (solid-diamond) irradiation. The right y-axis maps the ratio, $\varepsilon_{AWG}/\varepsilon_{CW}$. The simulation was performed at 10 kHz MAS using $\Delta\nu_{AWG}$=100 MHz and N=50 for AWG scheme for the same J distribution. T_{1e_2} =0.5T_{1e_1}.

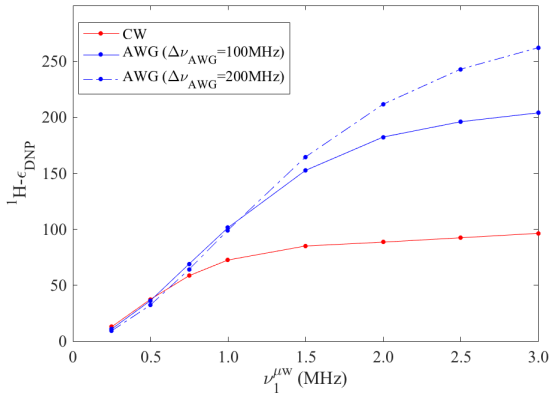

Figure B.9: **Microwave nutation frequency dependence on CW and AWG at 14 T.** Simulated ^{1}H ε_{DNP} vs. μw nutation frequency for CW and AWG (linear chirp) schemes. The simulations were performed for $e_1 - e_2 - ^1$H spin-system at 14 T B_0 field condition mimicking TEMTriPol-1 PA for MAS = 10 kHz. For AWG-DNP, N was set to 20. T_{1e_1}=$0.1\tau_r$ and T_{1e_2}= $0.5T_{1e_1}$.

Appendix C

Appendix C

C.1 Temperature Performance

C.1.1 Cryostat

When setting up the cryostat is it critically important to make sure all internal surfaces are clean and polished. Dirty/oxidized surfaces will act as good absorbers/emitters of blackbody radiation and severely affect the lowest achievable temperature. For our cryostat we noticed that over time if the vacuum jacket is not constantly maintained at a low pressure, the copper of the cold finger would oxidize, increasing the minimum unloaded crysotat temperature from 4K to 12K. This can be rectified by cleaning and polishing of the cold finger and radiation shield.

C.1.2 Sweep Coil

A picture of the sweep coil made by Bridge12 is shown in Fig. SC.1. This coil sits around the outermost cryostat shield. The coil is cooled by water flow through push-to-connect inlets/outlets on the top and bottom of the sweep coil from a Neslab ThermoFlex

Figure C.1: Picture of sweep coil.

1400 water chiller. The sweep coil is rated for a maximum current of 3.5A (with water cooling), and has a resistance of ∼25 ohms. It is powered by an Agilent 6675A DC power supply with an Agilent 59511A polarity switching device for bipolar (positive and negative voltage/current) operation.

The sweep coil was calibrated using the ^1H signal acquired from our NMR circuit. The field position (ppm) of the ^1H was monitored as a function of input current to the sweep coil and a slope of 5.413 mT/A was obtained. Over the full 3.5A range this gives a full sweep range of +/-18.95 mT or equivalently ∼0.53 GHz for a frequency sweep (centered around 194 GHz).

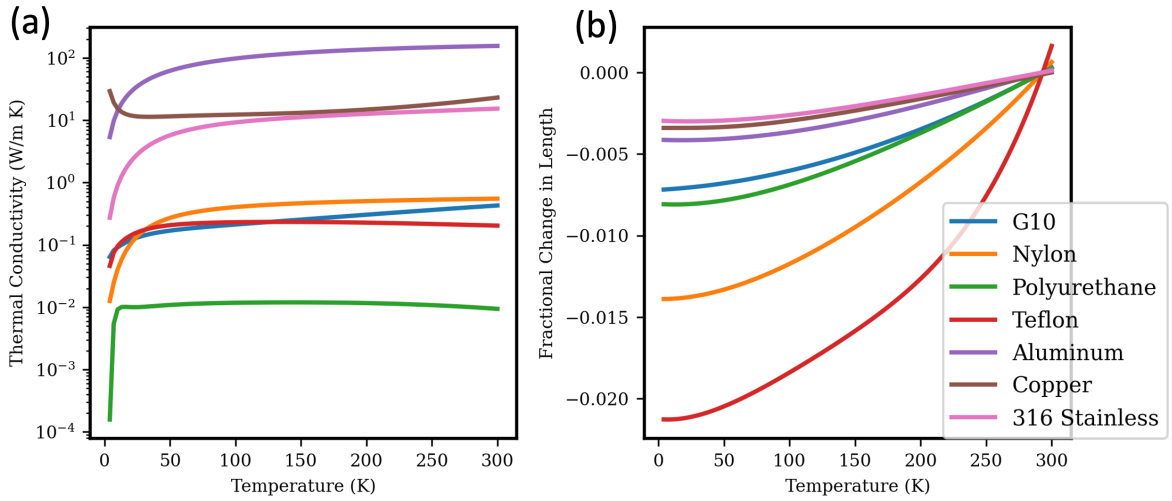

Figure C.2: a) Thermal conductivity of selected materials. b) Thermal expansion of materials expressed as the % change in length of a material from 294K.

C.1.3 Probe

Thermal properties of some selected non-magnetic materials commonly used at cryogenic temperatures are shownin Fig. SC.2. All data was taken from the NIST website $https://trc.nist.gov/cryogenics/materials/materialproperties.htm$. Fig. SC.2(a) Shows the thermal conductivity vs temperature and Fig. SC.2(b) shows thermal expansion.

Stainless steel is the best commonly available metal (besides titanium) that can be used to reduce thermal conduction, as it is widely available in many geometries and easily machinable. The 316 stainless steel portion of the J arm was a stock 1/4" OD tube from McMaster soldered onto the copper tube (also stock from McMaster).

When structural integrity is

C.2 NMR Design

C.2.1 Capacitor Tuning

The metal piston/G10 rod that tunes the variable capacitors is actuated by a simple screw mechanism located towards the top of the probe as shown in Fig. SC.3. The G10 rod is attached to a 6-32 threaded rod via a shaft collar. The threaded rod is screwed in and out of a threaded hole in the top-most baffle via 1/8" OD 316 stainless steel rod. The stainless steel rod goes through an o-ring seal at the top of the probe. Turning this rod results in the actuation of the mechanism. The screw is placed near the top of probe (near room temperature) to prevent potential jamming caused by cryogenic temperatures.

C.2.2 Vpp Measurements

The capacitor voltage handling was tested using a simple inductively coupled LC circuit of known Q and, capacitance, and inductance as shown in Fig. SC.4a. Here 3 chip capacitors are used in parallel to adjust the resonance to the desired frequency. 3 were used in series to extend their voltage handling such that they would not arc before the variable capacitor under test. Experimentally, the input power to the circuit was increased until arcing was detected via nearby pickup loop hooked up to an oscilloscope. The maximum power was then taken as an input to a simulated circuit to determine the voltage at which the variable capacitor failed.

There are a few ways to simulate the voltage in a resonant circuit such as this. One way is to use a linear network parameter simulation software such as CST studio to obtain the S parameters, and from there the voltage amplification across the capacitor can be calculated as demonstrated by Doty et. al.[215] This method is also useful for simulation more complex NMR circuits and their efficiency. However these programs are

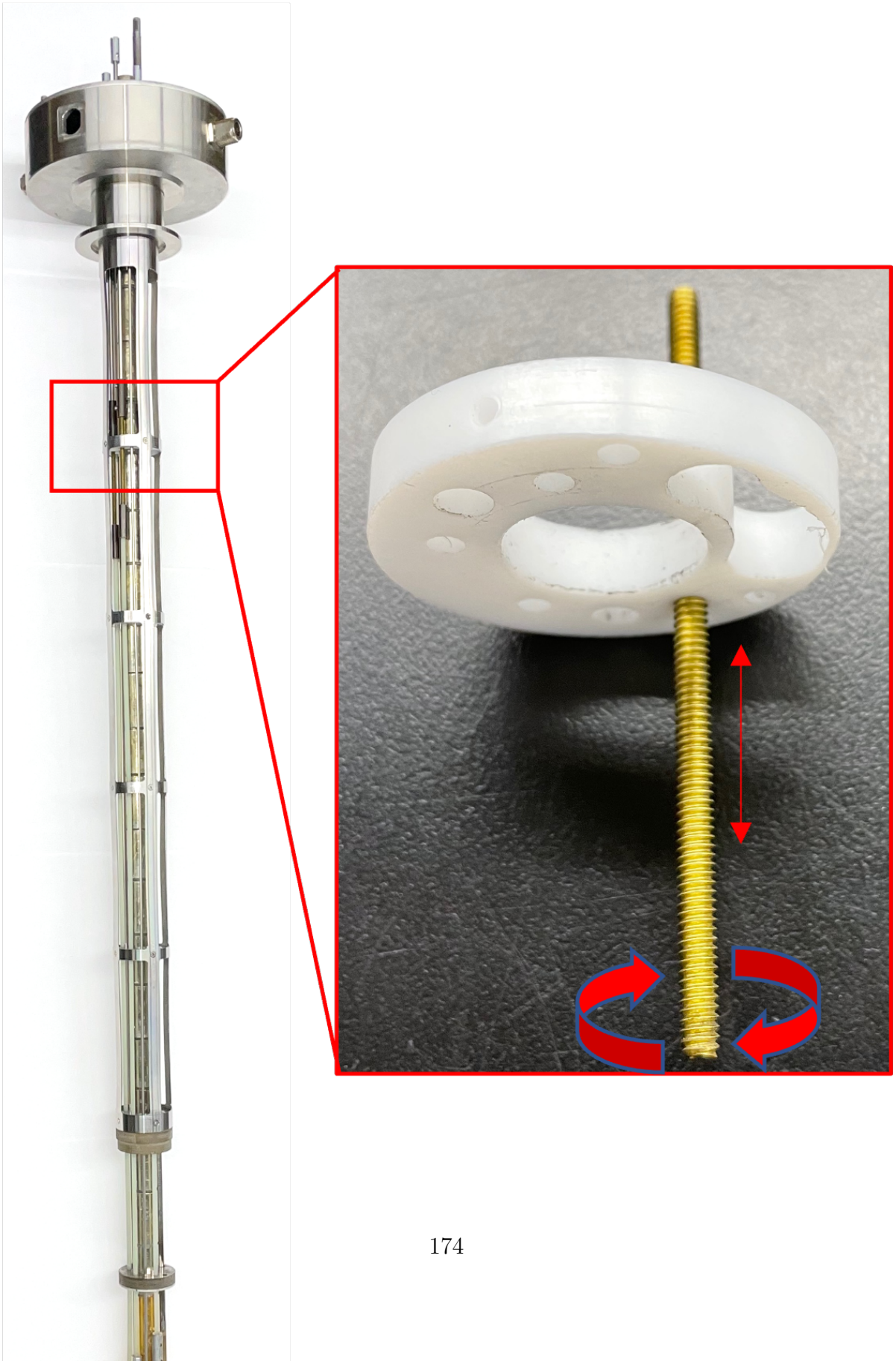

typically quite expensive. Alternatively this simple voltage calculation can also be done in the free program LTSpice as shown in Fig. SC.4c.

In this program, to simulate the voltage across the capacitor for a given input power the capacitor and inductor values from the circuit are needed, as well as the Q of the circuit and the input power. The inductor value can be determined by placing the inductor in parallel with a known valued capacitor and measuring the resulting resonant frequency with a pickup loop connected to a vector network analyzer (VNA) similar to what is shown in Fig. SC.6c. The inductance can then be determined from the following equation:

$$2 * pi * f = \frac{1}{\sqrt{LC}} \tag{C.1}$$

Where f is the resonant frequency in MHz, L is inductance in nanoHenries (nH), and C is capacitance in picoFarads (pF). The Q of the circuit can be determined by connecting the circuit to a VNA and critically coupling the circuit by adjusting the matching capacitor until the reflection parameter (S_{11}) is minimized for the resonant frequency, then the 7dB bandwidth of the resonant dip can be measured to determine Q_T according to:

$$Q_T = \frac{\Delta f(-7dB)}{f}$$

Where f is the central frequency of the resonant dip, and $\Delta f(-7dB)$ is the width of the dip at -7dB. Q_T is the Q of the isolated circuit (as opposed to Q_L which is the Q of the circuit when it is matched to 50 ohms). In many cases the Q of the inductor is much less than the capacitor, and is therefore dominant in determining the circuit Q_T via the following equation:

$$Q_T = \frac{1}{Q_{inductor}} = \frac{1}{Q_{capacitor}}$$

Therefore we can approximate $Q_T = Q_{inductor}$ where:

$$Q_{inductor} = 2\pi f R$$

Where R is the series resistance of the inductor. This resistance can be simulated as an external resistor placed in series with the inductor as shown in Fig. SC.4c as "R1" with a value of 0.3675 ohms resulting from a measured Q_T of 300.

The voltage source (V1) used to excite the simulation model was set to an rms voltage of 50 volts which corresponds to a power of 50 watts in a 50 ohm load (50 watts was the maximum input power the capacitor could handle without arcing). A 50 ohm resistor was placed in series with the voltage source to simulate the 50 ohm impedance of the transmitter.

The coupling constant between the inductors was set to 0.2 as denoted by the line "K1 L1 L2 0.2". Experimentally measuring the exact coupling constant is difficult, however as long as it is small enough (i.e below 0.3) the simulation results should be relatively consistent. This is due to the fact that with small coupling constants, most of the current will be traveling through the parallel LC portion of the circuit.[158]

The command used to simulate this circuit is ".ac lin 10000 50meg 100meg" which tells the program to run an AC (frequency domain) simulation from 50 MHz to 100 MHz with 10000 steps. Fig. SC.4d shows the resulting voltages (peak) across the capacitor C2 (which is the capacitor under test) as a function of frequency. The voltage is highest at the resonant frequency of the circuit, and can be taken as the maximum voltage handling of the capacitor. For this particular capacitor we achieved a peak voltage rating of ∼600 volts or a peak to peak voltage rating of 1200 volts at 75 MHz.

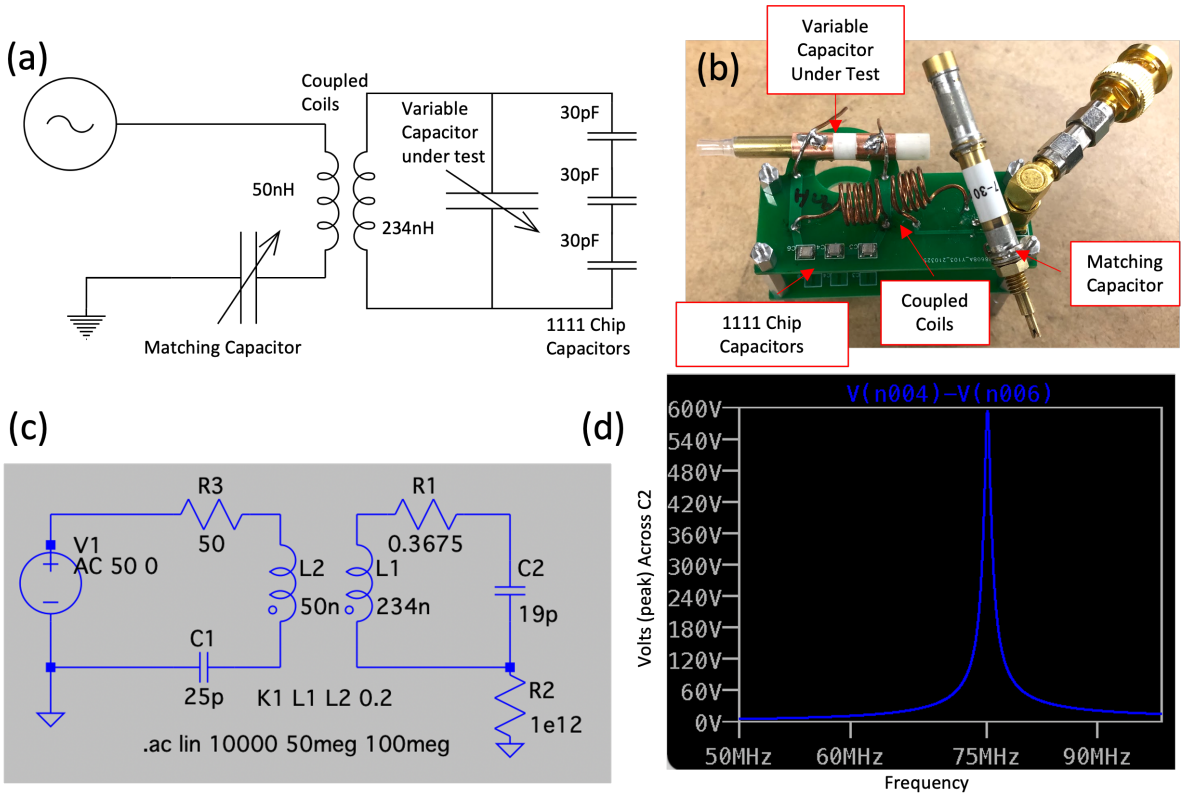

Figure C.4: (a) Schematic of circuit used to determine the RF voltage handling of the home-built capacitors. (b) picture of circuit used to test home-built capacitors. (c) LTSpice schematic used to simulate the voltage in the circuit. Note the resistor R2 is present for technical reasons but does not affect the simulation as the resistance value is very high. (d) Voltage across capacitor C2 as a function of frequency. Note that this plot shows the peak voltage which is 1/2 of the peak to peak voltage.

C.2.3 Capacitor Range

The above circuit (Fig. SC.4a-b) was used to determine the range of the variable capacitors. The variable capacitor can be adjusted until the highest and lowest resonant frequencies are observed. These frequencies and the inductor value can be plugged into equation C.1 to determine the highest and lowest total capacitance of the circuit. From there the variable capacitance can be determined from the following equation given that there are 3 series 30pF capacitors in parallel with the variable capacitor:

$$C_{total} = C_{variable} + \frac{1}{\frac{1}{30pF} + \frac{1}{30pF} + \frac{1}{30pF}}$$

C.2.4 1H Capacitor

The 1H capacitor is designed slightly differently to the X capacitor. Instead of the outer copper foil being arranged in vertically stacked rings as shown in Fig. 5.4a-c, the outer copper foil is arranged horizontally as shown in Fig. SC.5a. This was done to shorten the lead lengths from the capacitor to the sample coil, thereby reducing parasitic inductance and increasing η_{CFF}.

C.2.5 Matching Capacitor

The matching capacitor is constructed similar to the tuning capacitors described in the main text. However the voltage handling requirements are much relaxed (up to 10s of times less), thus more focus was put on capacitance range. The matching capacitors were constructed as 2 plate capacitors with one of the plates being grounded as shown in Fig. SC.5b and c. Furthermore FEP heat shrink was not used on the inner piston as discussed in the main text because the voltage handling of these matching capacitors can be much lower. Both of these factors allow the matching capacitors to have a larger

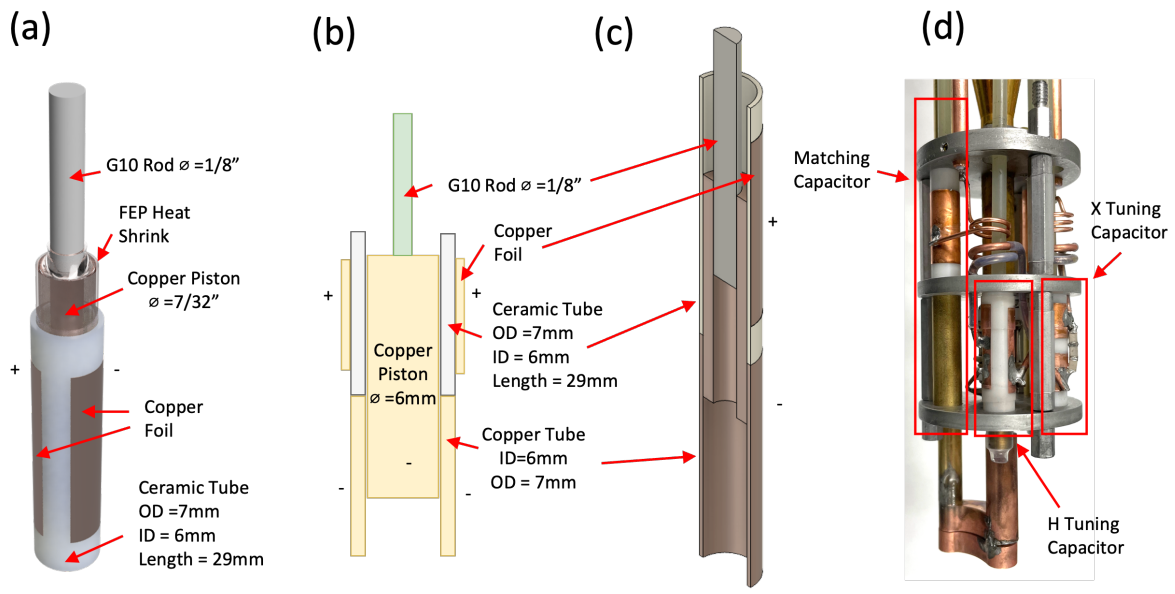

Figure C.5: (a) Rendering of the H channel tuning capacitor with the outer copper foil arranged horizontally instead of vertically. (b) Schematic of the matching capacitor. Here the ”-” end of the capacitor is grounded.(c) CAD model cross section of the matching capacitor. Noteably the inner copper piston is in electrical contact with the copper tube such that they are both grounded. (d) Picture of the RF circuit with the tuning and matching capacitors indicated inside the red boxes.

capacitance range. A picture of the circuit with the matching and tuning capacitors is shown in Fig. SC.5d.

C.2.6 Ball Shift Measurements

Ball shift measurements were used to determine the RF B_1 homogeneity of the sample coil described in the main text as well as the efficiency η_{CFF} of the circuit.[146, 216, 217]

The ball shift measurements were done by resonating the RF circuit at the frequency of interest (300 MHz and 74 MHz). The resonant frequency was monitored via a vector network analyzer connected to the input port of interest (H or X). A 1/8” aluminum ball was inserted down the vertical axis of the saddle coil (as shown in Fig. SC.6a via the apparatus shown in Fig. SC.6b. Subsequently the shift in resonant frequency as a

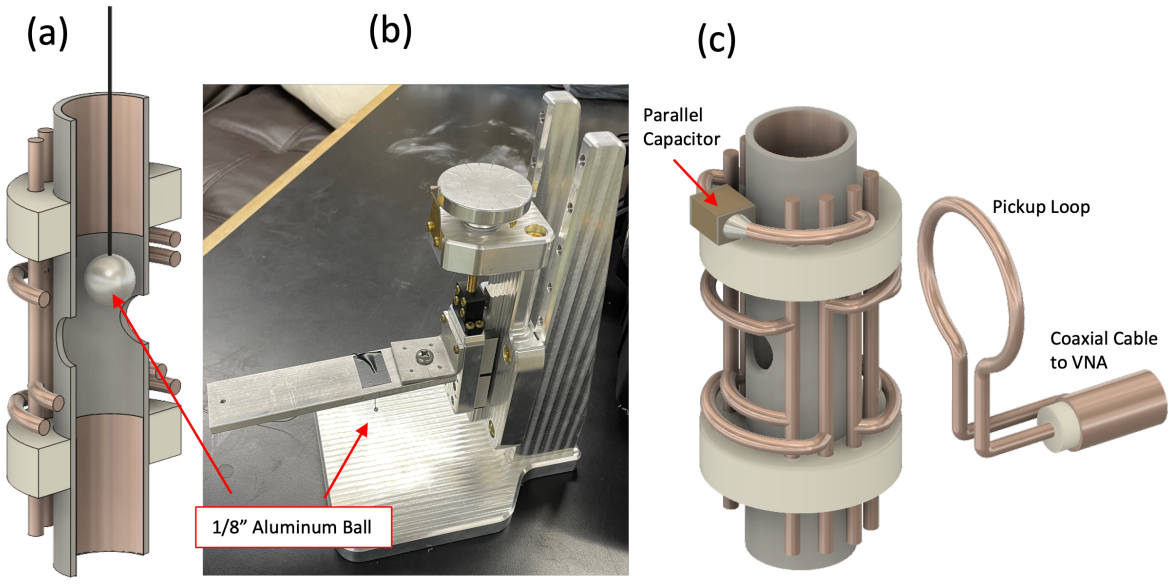

Figure C.6: (a) Cross section model of the sample coil with 1/8" aluminum ball to illustrate the ball shift measurement. The ball is moved down the length of the coil in measured increments. (b) Apparatus used to precisely move the aluminum ball in the coil. This apparatus is based on a lead screw with a 1mm pitch such that 1 complete revolution of the screw corresponds to shifting the ball by 1mm. (c) Model of the setup used to measure the isolated ball shift of the sample coil. A 1111 chip capacitor is placed directly across the leads of the coil to resonate it at the desired frequency, and a pickup loop connected to a VNA via a coaxial cable is brought near the coil to measure the frequency of the resonance.

function of the ball position was recorded to map out the B_1 field along the vertical axis of the coil. The apparatus used for the ball shift measurement is shown in Fig. SC.6 which uses a screw mechanism to vary the position of the ball in the coil.

The measurements of η_{CFF} were also done using ball shift measurements. To measure η_{CFF} the maximum frequency shift of the coil resonated using only a capacitor Δf_{coil} must be compared with the maximum frequency shift of the coil resonated using the full circuit $\Delta f_{circuit}$ described above. To measure the resonant frequency of the sample coil without the RF circuit, a pickup loop connected to a vector network analyzer was brought near the sample coil to observe the resonance as shown in Fig. SC.6c. η_{CFF} can be determined from the maximum frequency shifts Δf of each condition (observed when

the ball is in the middle of the sample coil):

$$\eta_{CFF} = \Delta f_{circuit,max} / \Delta f_{coil,max} \tag{C.2}$$

C.3 μw Design

C.3.1 Simulation Details

The μw simulations shown in this paper were carried out using the time domain solver in CST Studio. Time domain was chosen as it can give broadband information about the system with only 1 simulation run (as opposed to 1 simulation for each frequency point with a frequency domain solver). The model used consists of: (1) a TE_{11} waveguide port used to feed μw's into the simulation; (2) a TE_{11} to HE_{11} mode converter used to simulate the near Gaussian output profile of a corrugated waveguide; (3) the zirconia sleeve, PFA waveguide extension, and sample described in the main text; and (4) a waveguide port monitor on the sample to monitor how much μw power intersects the sample.

1. The excitation source was chosen to be a TE_{11} waveguide port (Fig. SC.7) because in CST waveguide ports can be used to simulate broadband excitation in the time domain. Without getting into too much detail, the program sends a shaped pulse that contains all the frequencies of interest into the simulation to excite and measure a broadband frequency response. Furthermore, TE_{11} modes can be easily converted to the desired HE_{11} mode of our actual corrugated waveguide as described below.[218, 191]

2. The TE_{11} to HE_{11} mode converter (Fig. SC.7) was constructed to have an output geometry identical to that of our actual probe. This converter is necessary because it is not possible to directly excite the HE_{11} mode in a waveguide port in CST.

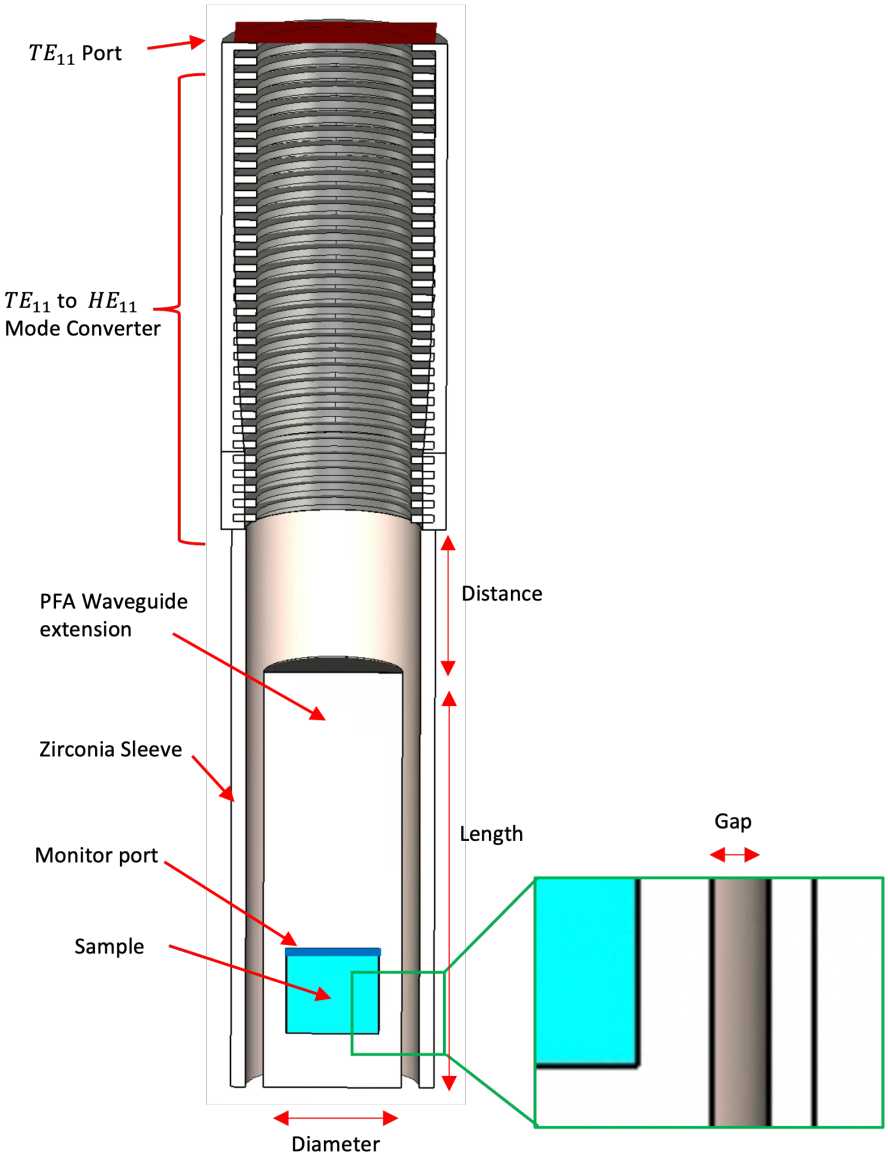

Figure C.7: Cross section of the model used to simulate the EPR performance of the sample cup. Important components are labeled, as well as the geometric features that are varied/optimized in the main text Fig. 5.8c-f.

Briefly, the mode converter is essentially a corrugated waveguide in which the corrugations gradually transition from 1/2 wavelength depth to 1/4 wavelength depth (approximatelly 0.386mm for a frequency of 194 GHz). The full design principles used to model the mode converter are based on the work of Manfred et. al.[219]

3. The sample cup materials were simulated in CST as dielectrics with different dielectric constants and loss tangents. PFA and PTFE were simulated as having identical dielectric properties and thus were combined into 1 material. The dielectric constant for PTFE was set as 2.1 with a loss tangent of 0.0002.[178] Zirconia was simulated as having a dielectric constant of 23 and loss tangent of 0.013.[220] The sample was simulated with a dielectric constant of 3.5 and loss tangent of 0.009 corresponding to a frozen solution of 60:40 Glycerol:water.[192]

4. The monitor port (indicated in Fig. SC.7) was set to have the same dimensions of the sample face closest to the waveguide. Thus, any μw power that intersected the monitor port can be assumed to also intersect the sample. The advantage of using this monitor port is that it can measure broadband power flow through it. The power measured vs frequency for a sample simulation is shown in Fig. SC.8. The total power that the waveguide port excites is 0.5 Watts, so the percentage of power than makes it to the sample is calculated by dividing each point in Fig. SC.8 by 0.5. To obtain a single number for each simulation geometry as shown in the main text, the average power over the entire frequency range is taken (i.e the average of the values Fig. SC.8 is taken). Note that the power to the sample does vary with frequency, but it fluctuates by less than 10% for the non-resonant structure we are using.

   Additionally care must be taken to measure enough modes on the port to capture the full power that intersects it. This is necessary because the μw field profiles

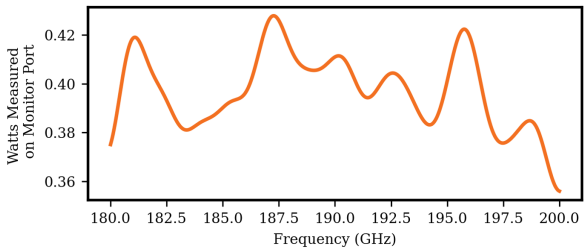

Figure C.8: Power measured by the monitor port as a function of frequency for a 0.5W excitation.

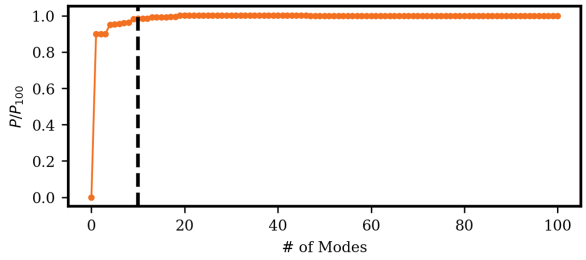

Figure C.9: Power measured by the monitor port as a function of how many modes were included, normalized to the power measured using 100 modes. More modes result in more power captured. The black dashed line indicates 10 modes which is how many were used for the simulations in the main text.

intersecting the monitor port will be a combination of many different modes. Including more modes will slow down the simulation, but will yield more accurate results as shown in Fig. SC.9. For the simulations in the main text we used 10 modes which should give better than 95% of the total power.

The model described above was used for the simulation results shown in Fig. 5.8c-f where certain geometric features of the model are varied and their effect on μw filling factor is measured. The following SI sections show μw magnetic field maps of select geometries to illustrate the effect of varying these geometric features.

C.3.2 Waveguide Extension Diameter

In Fig. 5.8c μw filling factor is measured as a function of diameter of the waveguide extension. The results suggested that larger diameter waveguide extensions lead to a lower μw filling factor. This can be attributed to the μw beam launched from the waveguide "spreading out" to fill the entire waveguide extension diameter, and thus the muw power is diluted. To illustrate this 2D slices of the RMS magentic field for samples of the results in Fig. 5.8c are shown in Fig. SC.10. Here we can see that the μw magnetic field is more intense for the smaller diameter waveguide extension (3mm vs 7mm), which is due to the beam being confined to a smaller space. The zirconia sleeve is excluded from these simulations as its effect is minimal (assuming a large enough gap exists between the sleeve and the waveguide extension as discussed in the next section), and its high dielectric constant increases simulation time significantly.

C.3.3 Waveguide Extension to Sleeve Gap

In Fig. 5.8c μw filling factor is measured as a function of diameter of the waveguide extension to sleeve gap. The results from Fig. 5.8d show that larger gaps lead to better μw filling factor. The reason for this is that for small gaps, the μw power travels into the high dielectric constant zirconia sleeve, as well as the waveguide extension which dilutes the μw power and filling factor similar to increasing the waveguide extension diameter as shown above. This effect can be qualitatively seen in Fig. SC.11 which shows 2D slices of the RMS magentic field for samples of the results in Fig. 5.8d. Here we can see that without a gap, there is a very high μw B_1 field inside the zirconia sleeve, but with a 0.3mm gap the field inside the sleeve is drastically reduced, and the field inside the waveguide extension/sample is increased.

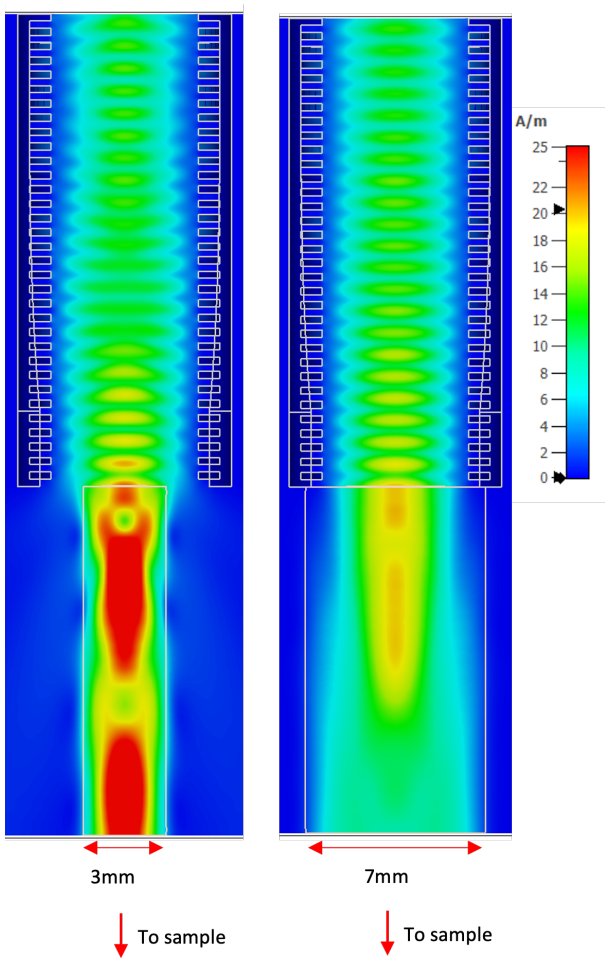

Figure C.10: 2D slice of the RMS B_1 (magnetic) field for 2 waveguide extension diameters taken from the simulations points shown in Fig. 5.8c. The sample position is below the displayed slice and is not shown.

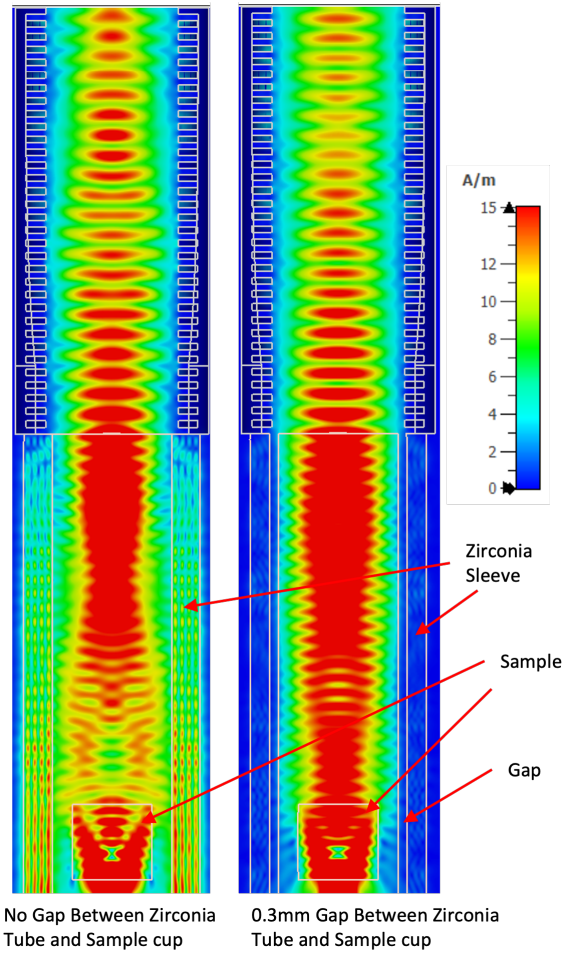

Figure C.11: 2D slice of the RMS B_1 (magnetic) field for 2 gap distances taken from the simulations points shown in Fig. 5.8d.

C.3.4 Waveguide Extension Length

The waveguide extension length parameter optimized/varied in Fig. 5.8e determines how far the sample is from the corrugated waveguide. The longer the wavegude extension length, the further the μw beam must travel outside the corrugated waveguide to reach the sample. Within the range of 0-20mm the effect of this length on μw filling factor is ¡10%. This suggests that the waveguide extension is efficient at confining the μw beam and guiding it to the sample. This means that the sample can be placed further from the waveguide without much detrimental effect on B_1. To illustrate this, 2D μw B_1 field maps of waveguide extensions with 2 different lengths are shown in Fig. SC.12

C.3.5 Distance Between Waveguide Extension and Corrugated Waveguide

The final geometric parameter discussed in the main text is the distance between the waveguide extension and the corrugated waveguide. This parameter determines where the waveguide extension is placed relative to the corrugated waveguide. Larger distances will result in an air gap between the corrugated waveguide and the waveguide extension that the μw beam will have to traverse, while negative distances correspond to the waveguide extension being inside the corrugated waveguide. Fig. 5.8f shows the effect of this distance on μw filling factor. Larger distances will result in lower μw filling factors as the μw beam has a chance to diffract before entering the waveguide extension. This can be slightly seen in Fig. SC.13 which shows 2D μw B_1 field maps of waveguide extensions with 3 different distances. Here the field map with a 7mm distance shows that the beam size becomes slightly larger than the waveguide extension before entering it, and thus some of the beam is scattered to the surrounding environment. The -5mm distance and 0mm distance models do not exhibit this behaviour.

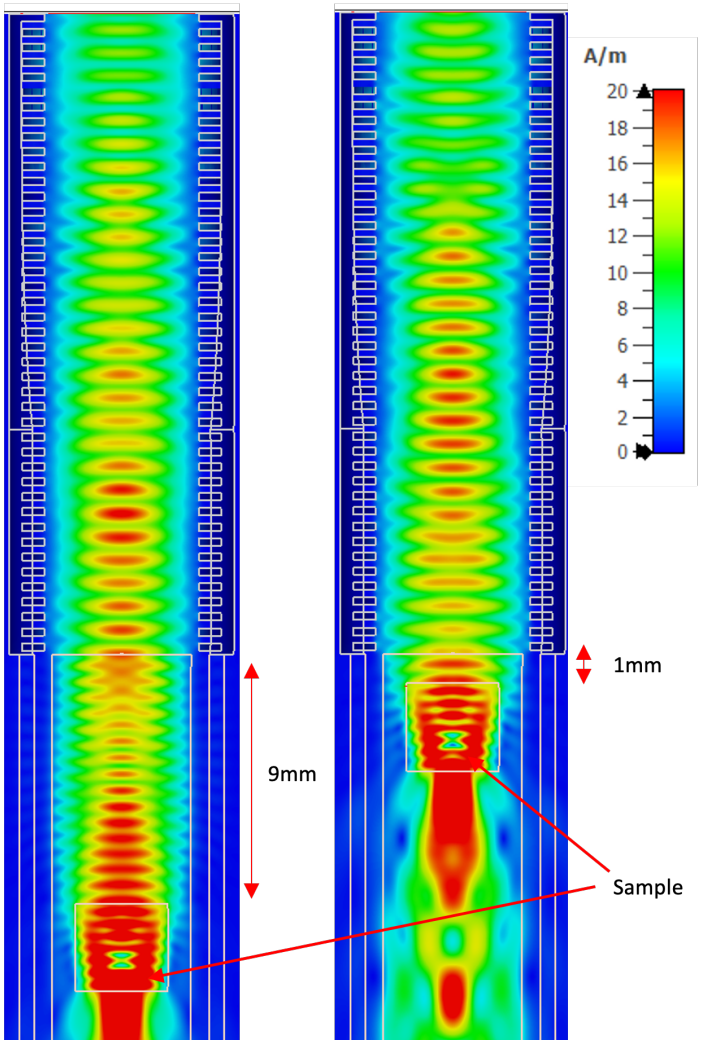

Figure C.12: 2D slice of the RMS B_1 (magnetic) field for 2 waveguide extension lengths (9mm and 1mm) taken from the simulations points shown in Fig. 5.8e.

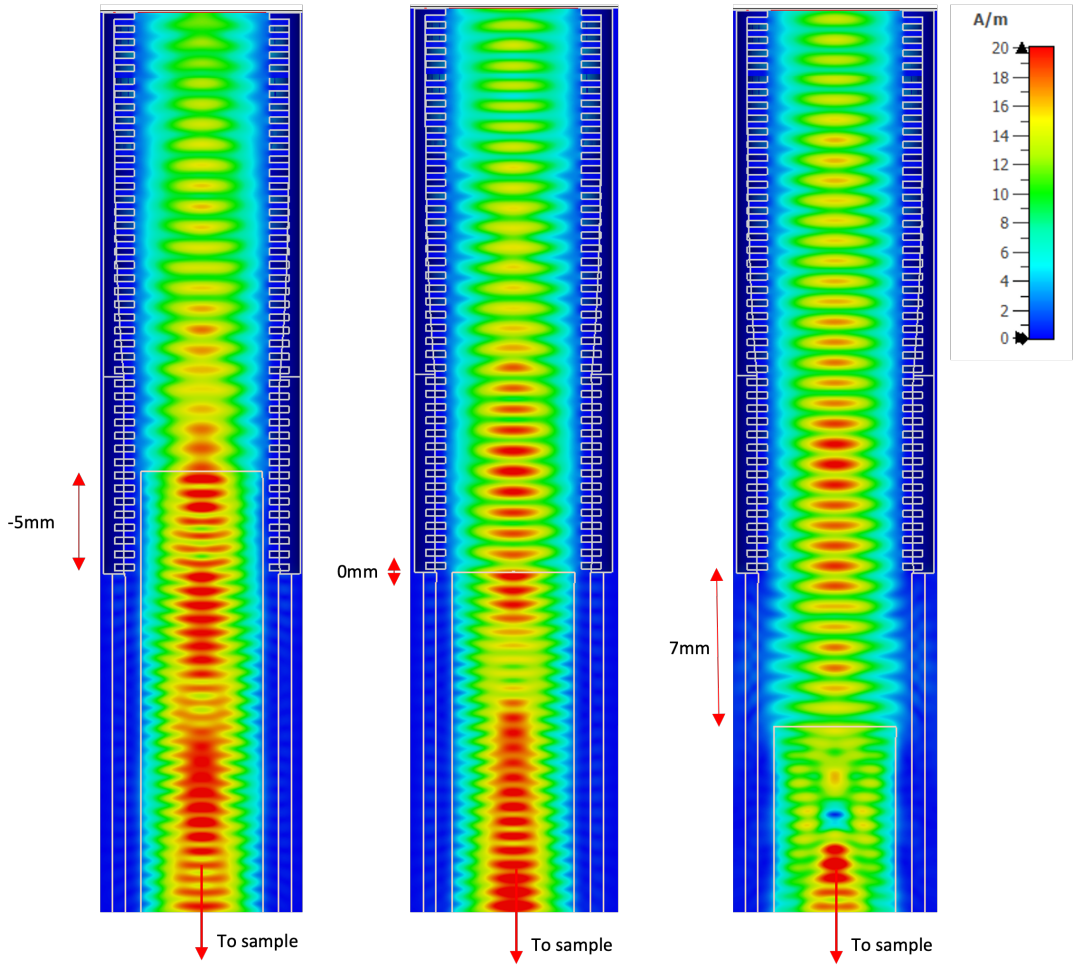

Figure C.13: 2D slice of the RMS B_1 (magnetic) field for 3 distances (-5mm, 0mm and 7mm) taken from the simulations points shown in Fig. 5.8f.

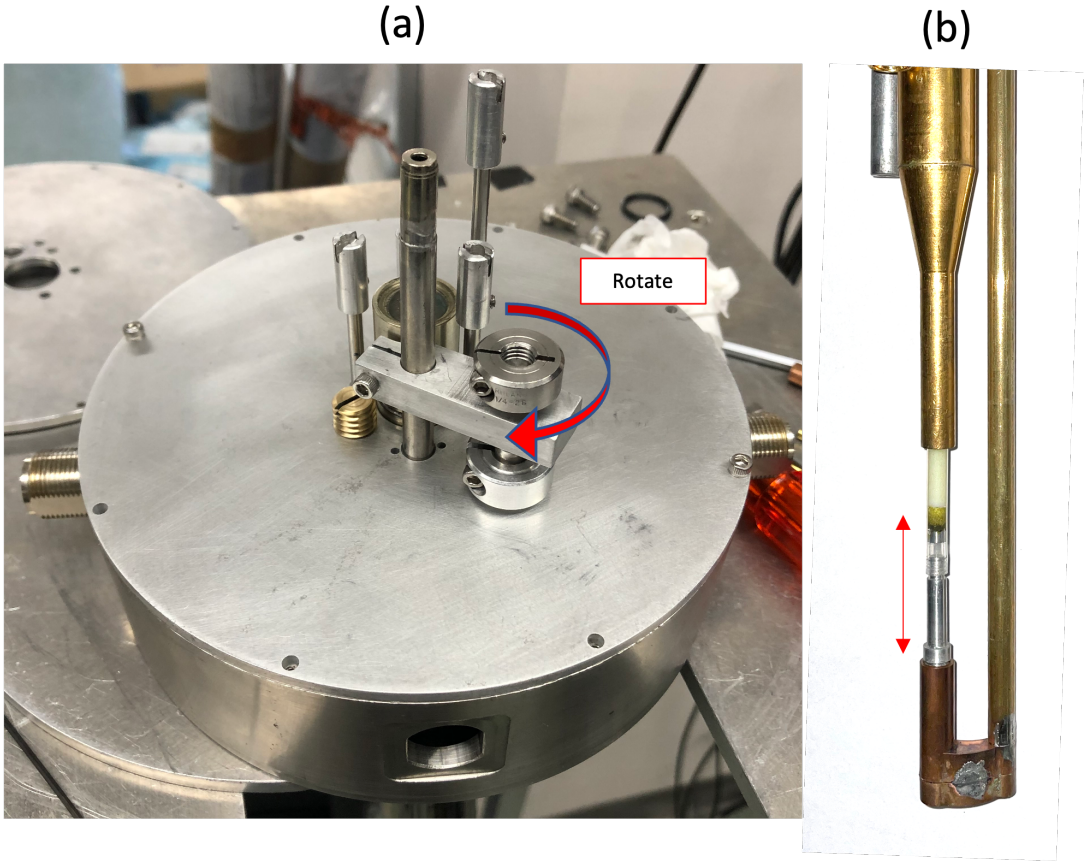

Figure C.14: (a) Picture of J arm actuator on top of the probe. (b) Picture of the sample and bottom of the J arm with the direction of actuation indicated.

C.3.6 J Arm Actuator

An actuator for the J arm has been constructed on the probe for future use in an FP resonator design. This mechanism clamps on to the J arm and shifts it up and down via a screw mechanism shown in Fig. SC.14 This in turn adjusts the distance between the sample and the corrugated waveguide. An FP resonator could be conceived by placing a semi-reflective mirror at the output of the waveguide.

Bibliography

[1] J. A. Tan, S. Garakyaraghi, K. A. Tagami, K. A. Frano, H. M. Crockett, A. F. Ogata, J. D. Patterson, and K. L. Wustholz, *Contributions from excited-state proton and electron transfer to the blinking and photobleaching dynamics of alizarin and purpurin*, *Journal of Physical Chemistry C* **121** (1, 2017) 97–106.

[2] Y. Li, A. Equbal, K. Tagami, and S. Han, *Electron spin density matching for cross-effect dynamic nuclear polarization*, *Chemical Communications* **55** (6, 2019) 7591–7594.

[3] K. Tagami, A. Equbal, I. Kaminker, B. Kirtman, and S. Han, *Biradical rotamer states tune electron J coupling and MAS dynamic nuclear polarization enhancement*, *Solid state nuclear magnetic resonance* **101** (9, 2019) 12–20.

[4] A. Equbal, K. Tagami, and S. Han, *Pulse-Shaped Dynamic Nuclear Polarization under Magic-Angle Spinning*, *Journal of Physical Chemistry Letters* **10** (12, 2019) 7781–7788.

[5] A. Equbal, K. Tagami, and S. Han, *Balancing dipolar and exchange coupling in biradicals to maximize cross effect dynamic nuclear polarization*, *Physical Chemistry Chemical Physics* **22** (2020), no. 24.

[6] A. Equbal, S. Jain, Y. Li, K. Tagami, X. Wang, and S. Han, *Role of electron spin dynamics and coupling network in designing dynamic nuclear polarization*, *Progress in Nuclear Magnetic Resonance Spectroscopy* **126-127** (2021).

[7] Y. Li, R. Chaklashiya, H. Takahashi, Y. Kawahara, K. Tagami, C. Tobar, and S. Han, *Solid-state MAS NMR at ultra low temperature of hydrated alanine doped with DNP radicals*, *Journal of Magnetic Resonance* **333** (12, 2021) 107090.

[8] S. Oh, A. Nikolaev, K. Tagami, T. Tran, D. Lee, S. Mukherjee, R. Segalman, S. Han, J. Read De Alaniz, and M. Chabinyc, *Redox-Active Polymeric Ionic Liquids with Pendant N-Substituted Phenothiazine*, *ACS Applied Materials and Interfaces* **13** (2021), no. 4.

[9] W. Gerlach and O. Stern, *Der experimentelle Nachweis der Richtungsquantelung im Magnetfeld*, *Zeitschrift für Physik 1922 9:1* **9** (12, 1922) 349–352.

[10] I. I. Rabi, J. R. Zacharias, S. Millman, and P. Kusch, *A New Method of Measuring Nuclear Magnetic Moment*, *Physical Review* **53** (2, 1938) 318.

[11] F. Bloch, *Nuclear Induction*, *Physical Review* **70** (10, 1946) 460.

[12] E. M. Purcell, H. C. Torrey, and R. V. Pound, *Resonance absorption by nuclear magnetic moments in a solid [7]*, *Physical Review* **69** (1, 1946) 37–38.

[13] A. W. Overhauser, *Polarization of nuclei in metals*, *Physical Review* **92** (10, 1953) 411–415.

[14] T. R. Carver and C. P. Slichter, *Polarization of Nuclear Spins in Metals*, *Physical Review* **92** (10, 1953) 212.

[15] D. A. Hall, D. C. Maus, G. J. Gerfen, S. J. Inati, L. R. Becerra, F. W. Dahlquist, and R. G. Griffin, *Polarization-enhanced NMR spectroscopy of biomolecules in frozen solution*, *Science* **276** (5, 1997) 930–932.

[16] A. Potapov, W. M. Yau, R. Ghirlando, K. R. Thurber, and R. Tycko, *Successive Stages of Amyloid-β Self-Assembly Characterized by Solid-State Nuclear Magnetic Resonance with Dynamic Nuclear Polarization*, *Journal of the American Chemical Society* **137** (7, 2015) 8294–8307.

[17] B. J. Wylie, B. G. Dzikovski, S. Pawsey, M. Caporini, M. Rosay, J. H. Freed, and A. E. McDermott, *Dynamic nuclear polarization of membrane proteins: covalently bound spin-labels at protein-protein interfaces*, *Journal of biomolecular NMR* **61** (4, 2015) 361–367.

[18] Y. Su, L. Andreas, and R. G. Griffin, *Magic angle spinning NMR of proteins: high-frequency dynamic nuclear polarization and (1)H detection*, *Annual review of biochemistry* **84** (6, 2015) 465–497.

[19] A. N. Smith, M. A. Caporini, G. E. Fanucci, and J. R. Long, *A method for dynamic nuclear polarization enhancement of membrane proteins*, *Angewandte Chemie (International ed. in English)* **54** (1, 2015) 1542–1546.

[20] F. A. Perras, T. Kobayashi, and M. Pruski, *Natural Abundance 17O DNP Two-Dimensional and Surface-Enhanced NMR Spectroscopy*, *Journal of the American Chemical Society* **137** (7, 2015) 8336–8339.

[21] T. Wolf, S. Kumar, H. Singh, T. Chakrabarty, F. Aussenac, A. I. Frenkel, D. T. Major, and M. Leskes, *Endogenous Dynamic Nuclear Polarization for Natural Abundance 17 O and Lithium NMR in the Bulk of Inorganic Solids*, *Journal of the American Chemical Society* **141** (1, 2019) 451–462.

[22] T. Kobayashi, F. A. Perras, I. I. Slowing, A. D. Sadow, and M. Pruski, *Dynamic Nuclear Polarization Solid-State NMR in Heterogeneous Catalysis Research*, 12, 2015.

[23] W. R. Grüning, A. J. Rossini, A. Zagdoun, D. Gajan, A. Lesage, L. Emsley, and C. Copéret, *Molecular-level characterization of the structure and the surface chemistry of periodic mesoporous organosilicates using DNP-surface enhanced NMR spectroscopy*, *Physical Chemistry Chemical Physics* **15** (7, 2013) 13270–13274.

[24] P. Berruyer, L. Emsley, and A. Lesage, *DNP in Materials Science: Touching the Surface*, *eMagRes* **7** (2018), no. 4 93–104.

[25] H. Nagashima, J. Trébosc, J. Trébosc, Y. Kon, K. Sato, O. Lafon, O. Lafon, J. P. Amoureux, J. P. Amoureux, and J. P. Amoureux, *Observation of Low-γ Quadrupolar Nuclei by Surface-Enhanced NMR Spectroscopy*, *Journal of the American Chemical Society* **142** (6, 2020) 10659–10672.

[26] A. Lesage, M. Lelli, D. Gajan, M. A. Caporini, V. Vitzthum, P. Miéville, J. Alauzun, A. Roussey, C. Thieuleux, A. Mehdi, G. Bodenhausen, C. Copéret, and L. Emsley, *Surface enhanced NMR spectroscopy by dynamic nuclear polarization*, *Journal of the American Chemical Society* **132** (11, 2010) 15459–15461.

[27] M. Lelli, D. Gajan, A. Lesage, M. A. Caporini, V. Vitzthum, P. Miéville, F. Héroguel, F. Rascón, A. Roussey, C. Thieuleux, M. Boualleg, L. Veyre, G. Bodenhausen, C. Copéret, and L. Emsley, *Fast characterization of functionalized silica materials by silicon-29 surface-enhanced NMR spectroscopy using dynamic nuclear polarization*, *Journal of the American Chemical Society* **133** (2, 2011) 2104–2107.

[28] V. Vitzthum, P. Miéville, D. Carnevale, M. A. Caporini, D. Gajan, C. Copéret, M. Lelli, A. Zagdoun, A. J. Rossini, A. Lesage, L. Emsley, and G. Bodenhausen, *Dynamic nuclear polarization of quadrupolar nuclei using cross polarization from protons: surface-enhanced aluminium-27 NMR*, *Chemical Communications* **48** (1, 2012) 1988–1990.

[29] A. Equbal, S. K. Jain, Y. Li, K. Tagami, X. Wang, and S. Han, *Role of electron spin dynamics and coupling network in designing dynamic nuclear polarization*, *Progress in Nuclear Magnetic Resonance Spectroscopy* **126-127** (10, 2021) 1–16.

[30] A. Zagdoun, G. Casano, O. Ouari, M. Schwarzwälder, A. J. Rossini, F. Aussenac, M. Yulikov, G. Jeschke, C. Copéret, A. Lesage, P. Tordo, and L. Emsley, *Large molecular weight nitroxide biradicals providing efficient dynamic nuclear*

polarization at temperatures up to 200 K, *Journal of the American Chemical Society* **135** (8, 2013) 12790–12797.

[31] D. J. Kubicki, G. Casano, M. Schwarzwälder, S. Abel, C. Sauvée, K. Ganesan, M. Yulikov, A. J. Rossini, G. Jeschke, C. Copéret, A. Lesage, P. Tordo, O. Ouari, and L. Emsley, *Rational design of dinitroxide biradicals for efficient cross-effect dynamic nuclear polarization*, *Chemical Science* **7** (12, 2016) 550–558.

[32] A. Lund, A. Equbal, and S. Han, *Tuning nuclear depolarization under MAS by electron T1e*, *Physical Chemistry Chemical Physics* **20** (2018), no. 37 23976–23987.

[33] V. K. Michaelis, A. A. Smith, B. Corzilius, O. Haze, T. M. Swager, and R. G. Griffin, *High-Field 13 C DNP with a Radical Mixture*, *Journal of the American Chemical Society* **135** (2013), no. 8 2935–2938.–2938.

[34] G. Mathies, M. A. Caporini, V. K. Michaelis, Y. Liu, K. N. Hu, D. Mance, J. L. Zweier, M. Rosay, M. Baldus, and R. G. Griffin, *Efficient Dynamic Nuclear Polarization at 800 MHz / 527 GHz with Trityl-nitroxide Biradicals*, *Angewandte Chemie (International ed. in English)* **54** (9, 2015) 11770.

[35] F. J. Scott, E. P. Saliba, B. J. Albert, N. Alaniva, E. L. Sesti, C. Gao, N. C. Golota, E. J. Choi, A. P. Jagtap, J. J. Wittmann, M. Eckardt, W. Harneit, B. Corzilius, S. Th. Sigurdsson, and A. B. Barnes, *Frequency-agile gyrotron for electron decoupling and pulsed dynamic nuclear polarization*, *Journal of Magnetic Resonance* **289** (4, 2018) 45–54.

[36] P. T. Judge, E. L. Sesti, N. Alaniva, E. P. Saliba, L. E. Price, C. Gao, T. Halbritter, S. T. Sigurdsson, G. B. Kyei, and A. B. Barnes, *Characterization of frequency-chirped dynamic nuclear polarization in rotating solids*, *Journal of Magnetic Resonance* **313** (4, 2020) 106702.

[37] S. Takahashi, L. C. Brunel, D. T. Edwards, J. Van Tol, G. Ramian, S. Han, and M. S. Sherwin, *Pulsed electron paramagnetic resonance spectroscopy powered by a free-electron laser*, *Nature 2012 489:7416* **489** (9, 2012) 409–413.

[38] I. Kaminker, R. Barnes, and S. Han, *Arbitrary waveform modulated pulse EPR at 200 GHz*, *Journal of Magnetic Resonance* **279** (6, 2017) 81–90.

[39] J. A. Parkinson, A. Abragam, and M. Goldman, *Reports on Progress in Physics Principles of dynamic nuclear polarisation Recent citations Exploiting Endogenous Surface Defects for Dynamic Nuclear Polarization of Silicon Micro-and Nanoparticles Grzegorz Kwiatkowski et al Principles of dynamic nuclear p*, Tech. Rep. 41, 1978.

[40] C. F. Hwang and D. A. Hill, *New effect in dynamic polarization*, *Physical Review Letters* **18** (1, 1967) 110–112.

[41] D. S. Wollan, *Dynamic nuclear polarization with an inhomogeneously broadened ESR line. I. Theory*, *Physical Review B* **13** (5, 1976) 3671–3685.

[42] T. Maly, G. T. Debelouchina, V. S. Bajaj, K.-N. Hu, C.-G. Joo, M. L. Mak–Jurkauskas, J. R. Sirigiri, P. C. A. van der Wel, J. Herzfeld, R. J. Temkin, and R. G. Griffin, *Dynamic nuclear polarization at high magnetic fields*, *The Journal of Chemical Physics* **128** (2, 2008) 052211.

[43] A. Equbal, A. Leavesley, S. K. Jain, and S. Han, *Cross-Effect Dynamic Nuclear Polarization Explained: Polarization, Depolarization, and Oversaturation*, *Journal of Physical Chemistry Letters* **10** (2, 2019) 548–558.

[44] C. Song, K. N. Hu, C. G. Joo, T. M. Swager, and R. G. Griffin, *TOTAPOL: A biradical polarizing agent for dynamic nuclear polarization experiments in aqueous media*, *Journal of the American Chemical Society* **128** (2006), no. 35 11385–11390.

[45] K. R. Thurber and R. Tycko, *Theory for cross effect dynamic nuclear polarization under magic-angle spinning in solid state nuclear magnetic resonance: The importance of level crossings*, *Journal of Chemical Physics* **137** (8, 2012) 084508.

[46] F. Mentink-Vigier, Akbey, Y. Hovav, S. Vega, H. Oschkinat, and A. Feintuch, *Fast passage dynamic nuclear polarization on rotating solids*, *Journal of Magnetic Resonance* **224** (11, 2012) 13–21.

[47] F. Mentink-Vigier, Akbey, H. Oschkinat, S. Vega, and A. Feintuch, *Theoretical aspects of Magic Angle Spinning - Dynamic Nuclear Polarization*, *Journal of Magnetic Resonance* **258** (9, 2015) 102–120.

[48] K.-N. Hu, H.-h. Yu, T. M. Swager, and R. G. Griffin, *Dynamic Nuclear Polarization with Biradicals*, *Journal of the American Chemical Society* **126** (2004), no. 35 10844–10845.

[49] C. Sauvée, M. Rosay, G. Casano, F. Aussenac, R. T. Weber, O. Ouari, and P. Tordo, *Highly efficient, water-soluble polarizing agents for dynamic nuclear polarization at high frequency*, *Angewandte Chemie - International Edition* **52** (10, 2013) 10858–10861.

[50] C. Sauvée, G. Casano, S. Abel, A. Rockenbauer, D. Akhmetzyanov, H. Karoui, D. Siri, F. Aussenac, W. Maas, R. T. Weber, T. Prisner, M. Rosay, P. Tordo, and O. Ouari, *Tailoring of Polarizing Agents in the bTurea Series for Cross-Effect Dynamic Nuclear Polarization in Aqueous Media*, *Chemistry - A European Journal* **22** (4, 2016) 5598–5606.

[51] T. A. Siaw, M. Fehr, A. Lund, A. Latimer, S. A. Walker, D. T. Edwards, and S. I. Han, *Effect of electron spin dynamics on solid-state dynamic nuclear polarization performance*, *Physical Chemistry Chemical Physics* **16** (2014), no. 35 18694–18706.

[52] S. A. Walker, D. T. Edwards, T. A. Siaw, B. D. Armstrong, and S. Han, *Temperature dependence of high field 13C dynamic nuclear polarization processes with trityl radicals below 35 Kelvin*, *Physical Chemistry Chemical Physics* **15** (8, 2013) 15106–15120.

[53] L. Lumata, M. E. Merritt, C. R. Malloy, A. D. Sherry, and Z. Kovacs, *Impact of Gd3+on DNP of [1-13C]pyruvate doped with trityl OX063, BDPA, or 4-oxo-TEMPO*, 5, 2012.

[54] J. H. Ardenkjaer-Larsen, S. Macholl, and H. Jóhannesson, *Dynamic Nuclear Polarization with Trityls at 1.2 K*, *Applied Magnetic Resonance* **34** (8, 2008) 509–522.

[55] S. Macholl, H. Jóhannesson, and J. H. Ardenkjaer-Larsen, *Trityl biradicals and13C dynamic nuclear polarization*, *Physical Chemistry Chemical Physics* **12** (5, 2010) 5804–5817.

[56] Y. Matsuki, T. Maly, O. Ouari, H. Karoui, F. Le Moigne, E. Rizzato, S. Lyubenova, J. Herzfeld, T. Prisner, P. Tordo, and R. G. Griffin, *Dynamic nuclear polarization with a rigid biradical*, *Angewandte Chemie - International Edition* **48** (6, 2009) 4996–5000.

[57] P. Gast, D. Mance, E. Zurlo, K. L. Ivanov, M. Baldus, and M. Huber, *A tailored multi-frequency EPR approach to accurately determine the magnetic resonance parameters of dynamic nuclear polarization agents: Application to AMUPol*, *Physical Chemistry Chemical Physics* **19** (2, 2017) 3777–3781.

[58] F. A. Perras, A. Sadow, and M. Pruski, *In Silico Design of DNP Polarizing Agents: Can Current Dinitroxides Be Improved?*, *ChemPhysChem* **18** (8, 2017) 2279–2287.

[59] C. Zener, *Non-Adiabatic Crossing of Energy Levels*, *Proceedings of the Royal Society A: Mathematical, Physical and Engineering Sciences* **137** (9, 1932) 696–702.

[60] J. Soetbeer, P. Gast, J. J. Walish, Y. Zhao, C. George, C. Yang, T. M. Swager, R. G. Griffin, and G. Mathies, *Conformation of bis-nitroxide polarizing agents by multi-frequency EPR spectroscopy*, *Physical Chemistry Chemical Physics* **20** (2018), no. 39 25506–25517.

[61] F. Mentink-Vigier, G. Mathies, Y. Liu, A.-L. Barra, M. A. Caporini, D. Lee, S. Hediger, R. G. Griffin, and G. De Paëpe, *Efficient cross-effect dynamic nuclear polarization without depolarization in high-resolution MAS NMR*, *Chemical Science* **8** (11, 2017) 8150–8163.

[62] V. N. Parmon, A. I. Kokorin, and G. M. Zhidomirov, *Conformational structure of nitroxide biradicals use of biradicals as spin probes*, 1977.

[63] A. I. Kokorin, *Regularities of the spin exchange coupling through a bridge in nitroxide biradicals*, *Applied Magnetic Resonance* **26** (3, 2004) 253–274.

[64] K. Yamaguchi, Y. Takahara, and T. Fueno, *Ab-Initio Molecular Orbital Studies of Structure and Reactivity of Transition Metal-OXO Compounds*, in *Applied Quantum Chemistry*, pp. 155–184. Springer Netherlands, Dordrecht, 1986.

[65] M. Veshtort and R. G. Griffin, *SPINEVOLUTION: A powerful tool for the simulation of solid and liquid state NMR experiments*, *Journal of Magnetic Resonance* **178** (2, 2006) 248–282.

[66] S. Stoll and A. Schweiger, *EasySpin, a comprehensive software package for spectral simulation and analysis in EPR*, *Journal of Magnetic Resonance* **178** (1, 2006) 42–55.

[67] F. Neese, *The ORCA program system*, *Wiley Interdisciplinary Reviews: Computational Molecular Science* **2** (1, 2012) 73–78.

[68] U. Ekström, L. Visscher, R. Bast, A. J. Thorvaldsen, and K. Ruud, *Arbitrary-order density functional response theory from automatic differentiation*, *Journal of Chemical Theory and Computation* **6** (2010), no. 7 1971–1980.

[69] L. Noodleman, *Valence bond description of antiferromagnetic coupling in transition metal dimers*, *The Journal of Chemical Physics* **74** (5, 1981) 5737–5743.

[70] R. Caballol, O. Castell, F. Illas, I. D. Moreira, and J. P. Malrieu, *Remarks on the proper use of the broken symmetry approach to magnetic coupling*, *Journal of Physical Chemistry A* **101** (1997), no. 42 7860–7866.

[71] C. Riplinger, J. P. Y. Kao, G. M. Rosen, V. Kathirvelu, G. R. Eaton, S. S. Eaton, A. Kutateladze, and F. Neese, *Interaction of radical pairs through-bond and through-space: Scope and limitations of the point-dipole approximation in electron paramagnetic resonance spectroscopy*, *Journal of the American Chemical Society* **131** (7, 2009) 10092–10106.

[72] J. P. Malrieu and G. Trinquier, *A recipe for geometry optimization of diradicalar singlet states from broken-symmetry calculations*, *Journal of Physical Chemistry A* **116** (8, 2012) 8226–8237.

[73] A. Equbal, Y. Li, A. Leavesley, S. Huang, S. Rajca, A. Rajca, and S. Han, *Truncated Cross Effect Dynamic Nuclear Polarization: An Overhauser Effect Doppelgänger*, *Journal of Physical Chemistry Letters* **9** (5, 2018) 2175–2180.

[74] A. Hudson and G. R. Luckhurst, *The electron resonance line shapes of radicals in solution*, *Chemical Reviews* **69** (1969), no. 2 191–225.

[75] M. Margittai and R. Langen, *Fibrils with parallel in-register structure constitute a major class of amyloid fibrils: Molecular insights from electron paramagnetic resonance spectroscopy*, 11, 2008.

[76] K. Yamaguchi, M. Okumura, J. Maki, T. Noro, H. Namimoto, M. Nakano, and T. Fueno, *MO theoretical studies of magnetic interactions in clusters of nitronyl nitroxide and related species*, *Chem. Phys. Lett.* **190** (1992) 353–360.

[77] V. Barone, A. Di Matteo, F. Mele, I. D. P. Moreira, and F. Illas, *Through-bond and through-space effects in the magnetic properties of nitroxide biradicals by an integrated QM/MM approach including solvent effects*, *Chemical Physics Letters* **302** (1999), no. 3-4 240–248.

[78] V. S. Bryantsev, T. K. Firman, and B. P. Hay, *Conformational analysis and rotational barriers of alkyl- And phenyl-substituted urea derivatives*, *Journal of Physical Chemistry A* **109** (2005), no. 5 832–842.

[79] M. F. Ottaviani, A. Modelli, O. Zeika, S. Jockusch, A. Moscatelli, and N. J. Turro, *EPR analysis and DFT computations of a series of polynitroxides*, *Journal of Physical Chemistry A* **116** (2012), no. 1 174–184.

[80] A. Leavesley, D. Shimon, T. A. Siaw, A. Feintuch, D. Goldfarb, S. Vega, I. Kaminker, and S. Han, *Effect of electron spectral diffusion on static dynamic nuclear polarization at 7 Tesla*, *Physical Chemistry Chemical Physics* **19** (2, 2017) 3596–3605.

[81] O. Kwon and G. Chung, *Density functional and multireference perturbation theory calculations of bis-nitronyl nitroxide biradical*, *Bulletin of the Korean Chemical Society* **29** (11, 2008) 2140–2144.

[82] O. Castell, R. Caballol, R. Subra, and A. Grand, *Ab Initio study of ullman's nitroxide biradicals. Exchange coupling versus structural characteristics analysis*, *Journal of Physical Chemistry®* **99** (1995), no. 1 154–157.

[83] M. E. Ali, A. S. Roy, and S. N. Datta, *Molecular tailoring and prediction of strongly ferromagnetically coupled trimethylenemethane-based nitroxide diradicals*, *Journal of Physical Chemistry A* **111** (2007), no. 25 5523–5527.

[84] F. Weigend and R. Ahlrichs, *Balanced basis sets of split valence, triple zeta valence and quadruple zeta valence quality for H to Rn: Design and assessment of accuracy*, *Physical Chemistry Chemical Physics* **7** (2005), no. 18 3297–3305.

[85] C. A. Naleway, L. A. Curtiss, and J. R. Miller, *Superexchange-Pathway Model for Long-Distance Electronic Couplings*, *J. Phys. Chem.* **95** (1991), no. 22 8434–8437.

[86] W. Zhai, Y. Feng, H. Liu, A. Rockenbauer, D. Mance, S. Li, Y. Song, M. Baldus, and Y. Liu, *Diastereoisomers of l-proline-linked trityl-nitroxide biradicals: Synthesis and effect of chiral configurations on exchange interactions*, *Chemical Science* **9** (2018), no. 19 4381–4391.

[87] C. D. Jeffries, *Polarization of Nuclei by Resonance Saturation in Paramagnetic Crystals*, *Physical Review* **106** (4, 1957) 164.

[88] T. V. Can, M. A. Caporini, F. Mentink-Vigier, B. Corzilius, J. J. Walish, M. Rosay, W. E. Maas, M. Baldus, S. Vega, T. M. Swager, and R. G. Griffin, *Overhauser effects in insulating solids*, *The Journal of chemical physics* **141** (8, 2014).

[89] A. Equbal, Y. Li, A. Leavesley, S. Huang, S. Rajca, A. Rajca, and S. Han, *Truncated Cross Effect Dynamic Nuclear Polarization: An Overhauser Effect Doppelgänger HHS Public Access*, *J Phys Chem Lett* **9** (2018), no. 9 2175–2180.

[90] Y. Hovav, A. Feintuch, and S. Vega, *Theoretical aspects of dynamic nuclear polarization in the solid state - The cross effect*, *Journal of Magnetic Resonance* **214** (1, 2012) 29–41.

[91] K. R. Thurber and R. Tycko, *Perturbation of nuclear spin polarizations in solid state NMR of nitroxide-doped samples by magic-angle spinning without microwaves*, *The Journal of Chemical Physics* **140** (5, 2014) 184201.

[92] A. S. Lilly Thankamony, J. J. Wittmann, M. Kaushik, and B. Corzilius, *Dynamic nuclear polarization for sensitivity enhancement in modern solid-state NMR*, 11, 2017.

[93] T. V. Can, J. J. Walish, T. M. Swager, and R. G. Griffin, *Time domain DNP with the NOVEL sequence*, *The Journal of Chemical Physics* **143** (8, 2015) 054201.

[94] G. Mathies, S. Jain, M. Reese, and R. G. Griffin, *Pulsed Dynamic Nuclear Polarization with Trityl Radicals*, *Journal of Physical Chemistry Letters* **7** (1, 2016) 111–116.

[95] S. K. Jain, G. Mathies, and R. G. Griffin, *Off-resonance NOVEL*, *The Journal of Chemical Physics* **147** (10, 2017) 164201.

[96] K. O. Tan, C. Yang, R. T. Weber, G. Mathies, and R. G. Griffin, *Time-optimized pulsed dynamic nuclear polarization*, *Science Advances* **5** (1, 2019) eaav6909.

[97] Y. Hovav, A. Feintuch, S. Vega, and D. Goldfarb, *Dynamic nuclear polarization using frequency modulation at 3.34 T*, *Journal of Magnetic Resonance* **238** (1, 2014) 94–105.

[98] A. Bornet, J. Milani, B. Vuichoud, A. J. Perez Linde, G. Bodenhausen, and S. Jannin, *Microwave frequency modulation to enhance Dissolution Dynamic Nuclear Polarization Dedicated to To Martial Rey, as a token of appreciation.*, *Chemical Physics Letters* **602** (5, 2014) 63–67.

[99] K. R. Thurber, W. M. Yau, and R. Tycko, *Low-temperature dynamic nuclear polarization at 9.4 T with a 30 mW microwave source*, *Journal of Magnetic Resonance* **204** (6, 2010) 303–313.

[100] I. Kaminker and S. Han, *Amplification of Dynamic Nuclear Polarization at 200 GHz by Arbitrary Pulse Shaping of the Electron Spin Saturation Profile*, *J. Phys. Chem. Lett* **9** (2018) 44.

[101] D. Mance, P. Gast, M. Huber, M. Baldus, and K. L. Ivanov, *The magnetic field dependence of cross-effect dynamic nuclear polarization under magic angle spinning*, *The Journal of chemical physics* **142** (6, 2015) 234201.

[102] Y. Liu, F. A. Villamena, A. Rockenbauer, Y. Song, and J. L. Zweier, *Structural factors controlling the spin-spin exchange coupling: EPR spectroscopic studies of highly asymmetric trityl-nitroxide biradicals*, *Journal of the American Chemical Society* **135** (2, 2013) 2350–2356.

[103] D. Wisser, G. Karthikeyan, A. Lund, G. Casano, H. Karoui, M. Yulikov, G. Menzildjian, A. C. Pinon, A. Purea, F. Engelke, S. R. Chaudhari, D. Kubicki, A. J. Rossini, I. B. Moroz, D. Gajan, C. Copéret, G. Jeschke, M. Lelli, L. Emsley, A. Lesage, and O. Ouari, *BDPA-Nitroxide Biradicals Tailored for Efficient Dynamic Nuclear Polarization Enhanced Solid-State NMR at Magnetic Fields up to 21.1 T*, *Journal of the American Chemical Society* **140** (10, 2018) 13340–13349.

[104] K. Sato, R. Hirao, I. Timofeev, O. Krumkacheva, E. Zaytseva, O. Rogozhnikova, V. M. Tormyshev, D. Trukhin, E. Bagryanskaya, T. Gutmann, V. Klimavicius, G. Buntkowsky, K. Sugisaki, S. Nakazawa, H. Matsuoka, K. Toyota, D. Shiomi, and T. Takui, *Trityl-Aryl-Nitroxide-Based Genuinely g-Engineered Biradicals, As Studied by Dynamic Nuclear Polarization, Multifrequency ESR/ENDOR, Arbitrary Wave Generator Pulse Microwave Waveform Spectroscopy, and Quantum Chemical Calculations*, *Journal of Physical Chemistry A* **123** (7, 2019) 7507–7517.

[105] T. A. Siaw, A. Leavesley, A. Lund, I. Kaminker, and S. Han, *A versatile and modular quasi optics-based 200 GHz dual dynamic nuclear polarization and electron paramagnetic resonance instrument*, *Journal of Magnetic Resonance* **264** (3, 2016) 131–153.

[106] A. Equbal, K. Tagami, and S. Han, *Pulse-Shaped Dynamic Nuclear Polarization under Magic-Angle Spinning*, *Journal of Physical Chemistry Letters* **10** (12, 2019) 7781–7788.

[107] K. N. Hu, V. S. Bajaj, M. Rosay, and R. G. Griffin, *High-frequency dynamic nuclear polarization using mixtures of TEMPO and trityl radicals*, *The Journal of Chemical Physics* **126** (1, 2007) 044512.

[108] F. Mentink-Vigier, I. Marin-Montesinos, A. P. Jagtap, T. Halbritter, J. Van Tol, S. Hediger, D. Lee, S. T. Sigurdsson, and G. De Paëpe, *Computationally Assisted Design of Polarizing Agents for Dynamic Nuclear Polarization Enhanced NMR: The AsymPol Family*, *Journal of the American Chemical Society* **140** (9, 2018) 11013–11019.

[109] F. Mentink-Vigier, A. L. Barra, J. Van Tol, S. Hediger, D. Lee, and G. De Paëpe, *De novo prediction of cross-effect efficiency for magic angle spinning dynamic nuclear polarization*, *Physical Chemistry Chemical Physics* **21** (1, 2019) 2166–2176.

[110] Kupče and R. Freeman, *Adiabatic Pulses for Wideband Inversion and Broadband Decoupling*, *Journal of Magnetic Resonance, Series A* **115** (8, 1995) 273–276.

[111] E. A. Nanni, A. B. Barnes, Y. Matsuki, P. P. Woskov, B. Corzilius, R. G. Griffin, and R. J. Temkin, *Microwave field distribution in a magic angle spinning dynamic nuclear polarization NMR probe*, *Journal of magnetic resonance (San Diego, Calif. : 1997)* **210** (5, 2011) 16–23.

[112] E. P. Saliba, E. L. Sesti, F. J. Scott, B. J. Albert, E. J. Choi, N. Alaniva, C. Gao, and A. B. Barnes, *Electron Decoupling with Dynamic Nuclear Polarization in Rotating Solids*, *Journal of the American Chemical Society* **139** (5, 2017) 6310–6313.

[113] E. A. Nanni, S. M. Lewis, M. A. Shapiro, R. G. Griffin, and R. J. Temkin, *Photonic-band-gap traveling-wave gyrotron amplifier*, *Physical Review Letters* **111** (12, 2013) 235101.

[114] I. V. Sergeyev, F. Aussenac, A. Purea, C. Reiter, E. Bryerton, S. Retzloff, J. Hesler, L. Tometich, and M. Rosay, *Efficient 263GHz magic angle spinning DNP at 100K using solid-state diode sources*, *Solid State Nuclear Magnetic Resonance* **100** (8, 2019) 63–69.

[115] A. Purea, C. Reiter, A. I. Dimitriadis, E. de Rijk, F. Aussenac, I. Sergeyev, M. Rosay, and F. Engelke, *Improved waveguide coupling for 1.3mm MAS DNP probes at 263GHz*, *Journal of Magnetic Resonance* **302** (5, 2019) 43–49.

[116] B. Corzilius, A. A. Smith, A. B. Barnes, C. Luchinat, I. Bertini, and R. G. Griffin, *High-field dynamic nuclear polarization with high-spin transition metal ions*, *Journal of the American Chemical Society* **133** (4, 2011) 5648–5651.

[117] J. Leggett, R. Hunter, J. Granwehr, R. Panek, A. J. Perez-Linde, A. J. Horsewill, J. McMaster, G. Smith, and W. Köckenberger, *A dedicated spectrometer for dissolution DNP NMR spectroscopy*, *Physical Chemistry Chemical Physics* **12** (5, 2010) 5883–5892.

[118] J. Granwehr, J. Leggett, and W. Köckenberger, *A low-cost implementation of EPR detection in a dissolution DNP setup*, *Journal of Magnetic Resonance* **187** (8, 2007) 266–276.

[119] A. A. Smith, B. Corzilius, J. A. Bryant, R. Derocher, P. P. Woskov, R. J. Temkin, and R. G. Griffin, *A 140 GHz pulsed EPR/212 MHz NMR spectrometer for DNP studies*, *Journal of Magnetic Resonance* **223** (10, 2012) 170–179.

[120] A. Feintuch, D. Shimon, Y. Hovav, D. Banerjee, I. Kaminker, Y. Lipkin, K. Zibzener, B. Epel, S. Vega, and D. Goldfarb, *A Dynamic Nuclear Polarization spectrometer at 95 GHz/144 MHz with EPR and NMR excitation and detection capabilities*, *Journal of Magnetic Resonance* **209** (4, 2011) 136–141.

[121] T. A. Siaw, A. Leavesley, A. Lund, I. Kaminker, and S. Han, *A versatile and modular quasi optics-based 200 GHz dual dynamic nuclear polarization and electron paramagnetic resonance instrument*, *Journal of Magnetic Resonance* **264** (3, 2016) 131–153.

[122] J. H. Freed, *New technologies in electron spin resonance*, *Annual Review of Physical Chemistry* **51** (10, 2000) 655–689.

[123] R. Tycko, *NMR at Low and Ultralow Temperatures*, *Accounts of Chemical Research* **46** (9, 2013) 1923–1932.

[124] V. Aladin and B. Corzilius, *Methyl dynamics in amino acids modulate heteronuclear cross relaxation in the solid state under MAS DNP*, *Solid State Nuclear Magnetic Resonance* **99** (7, 2019) 27–35.

[125] A. H. Linden, W. T. Franks, Akbey, S. Lange, B. J. Van Rossum, and H. Oschkinat, *Cryogenic temperature effects and resolution upon slow cooling of protein preparations in solid state NMR*, *Journal of Biomolecular NMR* **51** (11, 2011) 283–292.

[126] Y. Matsuki, S. Nakamura, S. Fukui, H. Suematsu, and T. Fujiwara, *Closed-cycle cold helium magic-angle spinning for sensitivity-enhanced multi-dimensional solid-state NMR*, *Journal of Magnetic Resonance* **259** (10, 2015) 76–81.

[127] Y. Li, R. Chaklashiya, H. Takahashi, Y. Kawahara, K. Tagami, C. Tobar, and S. Han, *Solid-state MAS NMR at ultra low temperature of hydrated alanine doped with DNP radicals*, *Journal of Magnetic Resonance* **333** (12, 2021) 107090.

[128] K. Thurber and R. Tycko, *Low-temperature dynamic nuclear polarization with helium-cooled samples and nitrogen-driven magic-angle spinning.*, *Journal of magnetic resonance (San Diego, Calif. : 1997)* **264** (3, 2016) 99–106.

[129] D. Lee, E. Bouleau, P. Saint-Bonnet, S. Hediger, and G. De Paëpe, *Ultra-low temperature MAS-DNP*, *Journal of Magnetic Resonance* **264** (3, 2016) 116–124.

[130] E. L. Sesti, N. Alaniva, P. W. Rand, E. J. Choi, B. J. Albert, E. P. Saliba, F. J. Scott, and A. B. Barnes, *Magic angle spinning NMR below 6K with a computational fluid dynamics analysis of fluid flow and temperature gradients*, *Journal of Magnetic Resonance* **286** (1, 2018) 1–9.

[131] P. Chen, B. J. Albert, C. Gao, N. Alaniva, L. E. Price, F. J. Scott, E. P. Saliba, E. L. Sesti, P. T. Judge, E. W. Fisher, and A. B. Barnes, *Magic angle spinning spheres*, *Science Advances* **4** (9, 2018).

[132] M. S. Conradi, *Low-temperature NMR techniques*, *Concepts in Magnetic Resonance* **5** (7, 1993) 243–262.

[133] N. H. Balshaw, *Practical Cryogenics: an introduction to laboratory cryogenics.* No. 01865. 2001.

[134] R. S. Khandpur, *Cryostat*, in *Compendium of Biomedical Instrumentation*, pp. 561–565. Wiley, 2, 2020.

[135] D. Arčon, I. Heinmaa, and R. Stern, *Chapter 8: Low-temperature NMR: Techniques and Applications*, in *New Developments in NMR*, vol. 2018-January, pp. 233–261. Royal Society of Chemistry, 3, 2018.

[136] T. Cheng, A. P. Gaunt, I. Marco-Rius, M. Gehrung, A. P. Chen, J. J. van der Klink, and A. Comment, *A multisample 7 T dynamic nuclear polarization polarizer for preclinical hyperpolarized MR*, *NMR in Biomedicine* **33** (5, 2020) e4264.

[137] R. Balzan, L. Fernandes, A. Comment, L. Pidial, B. Tavitian, and P. R. Vasos, *Dissolution dynamic nuclear polarization instrumentation for real-time enzymatic reaction rate measurements by NMR*, *Journal of Visualized Experiments* **2016** (2, 2016).

[138] K. R. Thurber, W.-M. Yau, and R. Tycko, *Low-temperature dynamic nuclear polarization at 9.4T with a 30mW microwave source*, *Journal of Magnetic Resonance* **204** (6, 2010) 303–313.

[139] A. Comment, B. van den Brandt, K. Uffmann, F. Kurdzesau, S. Jannin, J. Konter, P. Hautle, W. Wenckebach, R. Gruetter, and J. van der Klink, *Design and performance of a DNP prepolarizer coupled to a rodent MRI scanner*, *Concepts in Magnetic Resonance Part B: Magnetic Resonance Engineering* **31B** (10, 2007) 255–269.

[140] K. Kouřil, H. Kouřilová, S. Bartram, M. H. Levitt, and B. Meier, *Scalable dissolution-dynamic nuclear polarization with rapid transfer of a polarized solid*, *Nature Communications* **10** (12, 2019) 1–6.

[141] J. H. Ardenkjær-Larsen, S. Bowen, J. R. Petersen, O. Rybalko, M. S. Vinding, M. Ullisch, and N. C. Nielsen, *Cryogen-free dissolution dynamic nuclear polarization polarizer operating at 3.35 T, 6.70 T, and 10.1 T*, *Magnetic Resonance in Medicine* **81** (3, 2019) 2184–2194.

[142] M. Baudin, B. Vuichoud, A. Bornet, G. Bodenhausen, and S. Jannin, *A cryogen-consumption-free system for dynamic nuclear polarization at 9.4T*, *Journal of Magnetic Resonance* **294** (9, 2018) 115–121.

[143] A. Kiswandhi, P. Niedbalski, C. Parish, Q. Wang, and L. Lumata, *Assembly and performance of a 6.4 T cryogen-free dynamic nuclear polarization system*, *Magnetic Resonance in Chemistry* **55** (9, 2017) 846–852.

[144] V. Parma, *Cryostat Design*, tech. rep.

[145] D. I. Hoult, *The NMR receiver: A description and analysis of design*, 1978.

[146] F. D. Doty, *Probe Design and Construction*, .

[147] F. D. Doty, *Solid State NMR Probe Design*, .

[148] A. Webb, *Magnetic Resonance Technology: Hardware and System Component Design.* 5, 2016.

[149] L. R. Becerra, G. J. Gerfen, B. F. Bellew, J. A. Bryant, D. A. Hall, S. J. Inati, R. T. Weber, S. Un, T. F. Prisner, A. E. McDermott, K. W. Fishbein, K. E. Kreischer, R. J. Temkin, D. J. Singel, and R. G. Griffin, *A Spectrometer for Dynamic Nuclear Polarization and Electron Paramagnetic Resonance at High Frequencies*, *Journal of Magnetic Resonance, Series A* **117** (11, 1995) 28–40.

[150] M. L. Guy, L. Zhu, and C. Ramanathan, *Design and characterization of a W-band system for modulated DNP experiments*, *Journal of Magnetic Resonance* **261** (12, 2015) 11–18.

[151] J. H. Walton and M. S. Conradi, *Probe tuning adjustments-Need they be in the probe?*, *Journal of Magnetic Resonance (1969)* **81** (2, 1989) 623–627.

[152] F. D. Doty, R. R. Inners, and P. D. Ellis, *A multinuclear double-tuned probe for applications with solids or liquids utilizing lumped tuning elements*, *Journal of Magnetic Resonance (1969)* **43** (6, 1981) 399–416.

[153] H. Kovacs, D. Moskau, and M. Spraul, *Cryogenically cooled probes - A leap in NMR technology*, 5, 2005.

[154] J. Thoris, B. Leon, A. Dubois, and J. C. Bobo, *Dielectric breakdown of cold gaseous helium in large gaps*, *Cryogenics* **10** (4, 1970) 147–149.

[155] T. A. Siaw, S. A. Walker, B. D. Armstrong, and S. I. Han, *Inductively coupled NMR probe for versatile dynamic nuclear polarization operation at 7 T: Observation of 61 ± 2% 1H polarization at 4 K*, *Journal of Magnetic Resonance* **221** (8, 2012) 5–10.

[156] M. Decorps, P. Blondet, H. Reutenauer, J. P. Albrand, and C. Remy, *An inductively coupled, series-tuned NMR probe*, *Journal of Magnetic Resonance (1969)* **65** (10, 1985) 100–109.

[157] P. L. Kuhns, M. J. Lizak, S.-H. Lee, and M. S. Conradi, *Inductive Coupling and Tuning in NMR Probes; Applications*, tech. rep., 1988.

[158] A. P. Zens, *Using magnetic coupling to improve multiple resonance NMR probe circuits*, *Journal of Magnetic Resonance* **316** (6, 2020) 106741.

[159] B. M. Wood and R. F. Code, *High-performance cryogenic pulsed NMR spectrometer*, *Review of Scientific Instruments* **52** (1981), no. 3 386–390.

[160] A. P. Reyes, H. N. Bachman, and W. P. Halperin, *Versatile 4 K nuclear magnetic resonance probe and cryogenic system for small-bore high-field Bitter magnets*, *Review of Scientific Instruments* **68** (6, 1998) 2132.

[161] A. S. Lipton, R. W. Heck, J. A. Sears, and P. D. Ellis, *Low temperature solid-state NMR experiments of half-integer quadrupolar nuclides: caveats and data analysis*, *Journal of Magnetic Resonance* **168** (5, 2004) 66–74.

[162] A. A. Nevzorov, S. Milikisiyants, A. N. Marek, and A. I. Smirnov, *Multi-resonant photonic band-gap/saddle coil DNP probehead for static solid state NMR of microliter volume samples*, *Journal of Magnetic Resonance* **297** (12, 2018) 113–123.

[163] D. W. Alderman and D. M. Grant, *An efficient decoupler coil design which reduces heating in conductive samples in superconducting spectrometers*, *Journal of Magnetic Resonance (1969)* **36** (12, 1979) 447–451.

[164] David M Pozar, *Microwave engineering*, vol. 8. John Wiley & Sons, 1989.

[165] W. B. Lynch, K. A. Earle, and J. H. Freed, *1-mm wave ESR spectrometer*, *Review of Scientific Instruments* **59** (8, 1988) 1345–1351.

[166] G. M. Smith, J. C. Lesurf, R. H. Mitchell, and P. C. Riedi, *High performance MM-wave electron spin resonance spectrometer*, in *IEEE MTT-S International Microwave Symposium Digest*, vol. 3, pp. 1677–1680, IEEE, 1995.

[167] P. P. Woskov, V. S. Bajaj, M. K. Hornstein, R. J. Temkin, and R. G. Griffin, *Corrugated waveguide and directional coupler for CW 250-GHz gyrotron DNP experiments*, *IEEE Transactions on Microwave Theory and Techniques* **53** (6, 2005) 1863–1869.

[168] T. Maly and J. R. Sirigiri, *Simplified THz Instrumentation for High-Field DNP-NMR Spectroscopy*, *Applied Magnetic Resonance* **43** (7, 2012) 181–194.

[169] V. Weis, M. Bennati, M. Rosay, J. A. Bryant, and R. G. Griffin, *High-Field DNP and ENDOR with a Novel Multiple-Frequency Resonance Structure*, tech. rep., 1999.

[170] V. Denysenkov and T. Prisner, *Liquid state Dynamic Nuclear Polarization probe with Fabry-Perot resonator at 9.2 T*, *Journal of Magnetic Resonance* **217** (4, 2012) 1–5.

[171] Y. Fuiiil, Y. Ishikawa, Y. Koizumi, T. Omija, I. Ohya, S. Mitsudo, S. Miura, H. Yamamori, H. Kikuchi, and A. Fukuda, *Development of Millimeter-Wave Fabry-Perot Resonator for Simultaneous Electron-Spin and Nuclear-Magnetic Resonance Measurement at Low Temperatures*, in *International Conference on Infrared, Millimeter, and Terahertz Waves, IRMMW-THz*, vol. 2018-September, IEEE Computer Society, 10, 2018.

[172] T. Prisner, V. Denysenkov, and D. Sezer, *Liquid state DNP at high magnetic fields: Instrumentation, experimental results and atomistic modelling by molecular dynamics simulations*, *Journal of Magnetic Resonance* **264** (3, 2016) 68–77.

[173] J. Van Tol, L. C. Brunel, and R. J. Wylde, *A quasioptical transient electron spin resonance spectrometer operating at 120 and 240 GHz*, *Review of Scientific Instruments* **76** (7, 2005) 074101.

[174] O. Jakdetchai, V. Denysenkov, J. Becker-Baldus, B. Dutagaci, T. F. Prisner, and C. Glaubitz, *Dynamic nuclear polarization-enhanced NMR on aligned lipid bilayers at ambient temperature*, *Journal of the American Chemical Society* **136** (11, 2014) 15533–15536.

[175] E. J. Reijerse, *High-frequency EPR instrumentation*, *Applied Magnetic Resonance* **37** (11, 2010) 795–818.

[176] F. H. Cho, V. Stepanov, and S. Takahashi, *A high-frequency electron paramagnetic resonance spectrometer for multi-dimensional, multi-frequency, and multi-phase pulsed measurements*, *Review of Scientific Instruments* **85** (7, 2014) 075110.

[177] J. P. Crenn, *Optical propagation of the HE11 mode and Gaussian beams in hollow circular waveguides*, *International Journal of Infrared and Millimeter Waves* **14** (1993), no. 10 1947–1973.

[178] J. W. Lamb, *Miscellaneous data on materials for millimetre and submillimetre optics*, *International Journal of Infrared and Millimeter Waves* **17** (1996), no. 12 1997–2034.

[179] B. D. Armstrong, D. T. Edwards, R. J. Wylde, S. A. Walker, and S. Han, *A 200 GHz dynamic nuclear polarization spectrometer*, *Physical Chemistry Chemical Physics* **12** (5, 2010) 5920–5926.

[180] A. Lund, M. F. Hsieh, T. A. Siaw, and S. I. Han, *Direct dynamic nuclear polarization targeting catalytically active 27Al sites*, *Physical Chemistry Chemical Physics* **17** (9, 2015) 25449–25454.

[181] D. H. Fabini, T. A. Siaw, C. C. Stoumpos, G. Laurita, D. Olds, K. Page, J. G. Hu, M. G. Kanatzidis, S. Han, and R. Seshadri, *Universal Dynamics of Molecular Reorientation in Hybrid Lead Iodide Perovskites*, *Journal of the American Chemical Society* **139** (11, 2017) 16875–16884.

[182] A. Leavesley, C. B. Wilson, M. Sherwin, and S. Han, *Effect of water/glycerol polymorphism on dynamic nuclear polarization*, *Physical Chemistry Chemical Physics* **20** (2018), no. 15 9897–9903.

[183] S. K. Jain, T. A. Siaw, A. Equbal, C. B. Wilson, I. Kaminker, and S. Han, *Reversal of Paramagnetic Effects by Electron Spin Saturation*, *Journal of Physical Chemistry C* **122** (3, 2018) 5578–5589.

[184] A. Leavesley, S. Jain, I. Kamniker, H. Zhang, S. Rajca, A. Rajca, and S. Han, *Maximizing NMR signal per unit time by facilitating the e–e–n cross effect DNP rate*, *Physical Chemistry Chemical Physics* **20** (11, 2018) 27646–27657.

[185] A. Leavesley, I. Kaminker, and S. Han, *Versatile Dynamic Nuclear Polarization Hardware with Integrated Electron Paramagnetic Resonance Capabilities*, *eMagRes* **7** (2018), no. 4 133–154.

[186] E. H. Williams, *Magnetic Properties of Copper-Nickel Alloys*, *Physical Review* **38** (8, 1931) 828.

[187] C. Lau, M. C. Kaufman, E. J. Doyle, G. R. Hanson, W. A. Peebles, G. Wang, and A. Zolfaghari, *Circular Corrugated Miter Bend and Gap Losses for Broadband Frequency Applications*, *IEEE Transactions on Microwave Theory and Techniques* **67** (1, 2019) 38–49.

[188] N. Simon, *Cryogenic Properties of Inorganic Insulation Materials for ITER Magnets: A Review*, tech. rep., Oak Ridge Operations, Oak Ridge, TN, 12, 1994.

[189] F. Bonetto, E. Anoardo, and M. Polello, *Saddle coils for uniform static magnetic field generation in NMR experiments*, *Concepts in Magnetic Resonance Part B: Magnetic Resonance Engineering* **29B** (2, 2006) 9–19.

[190] L. F. Fuks and W. Anderson, *Perturbation Method for Finding the RF Field of an NMR Probe*, 1997.

[191] A. Patel, R. Goswami, A. Vala, K. Mahant, H. Mewada, P. Bhatt, K. Sathyanarayan, and S. V. Kulkarni, *Millimeter-wave TE ¡sub¿01¡/sub¿ –TE ¡sub¿11¡/sub¿ –HE ¡sub¿11¡/sub¿ mode converter using overmoded circular waveguide*, *Journal of Electromagnetic Waves and Applications* **32** (9, 2018) 1768–1778.

[192] D. J. Kubicki, A. J. Rossini, A. Purea, A. Zagdoun, O. Ouari, P. Tordo, F. Engelke, A. Lesage, and L. Emsley, *Amplifying Dynamic Nuclear Polarization of Frozen*
}Solutions by Incorporating Dielectric Particles, Journal of the American Chemical Society **136** *(11, 2014) 15711.*

[193] A. Equbal, Y. Li, T. Tabassum, and S. Han, Crossover from a Solid Effect to Thermal Mixing 1H Dynamic Nuclear Polarization with Trityl-OX063, The journal of physical chemistry letters **11** *(5, 2020) 3718–3723.*

[194] T. Hamachi, K. Nishimura, H. Kouno, Y. Kawashima, K. Tateishi, T. Uesaka, N. Kimizuka, and N. Yanai, Porphyrins as Versatile, Aggregation-Tolerant, and Biocompatible Polarizing Agents for Triplet Dynamic Nuclear Polarization of Biomolecules, Journal of Physical Chemistry Letters **12** *(3, 2021) 2645–2650.*

[195] Y. Li, A. Equbal, T. Tabassum, and S. Han, 1H Thermal Mixing Dynamic Nuclear Polarization with BDPA as Polarizing Agents, Journal of Physical Chemistry Letters **11** *(2020) 9195–9202.*

[196] L. Lumata, M. Merritt, C. Khemtong, S. J. Ratnakar, J. Van Tol, L. Yu, L. Song, and Z. Kovacs, The efficiency of DPPH as a polarising agent for DNP-NMR spectroscopy, RSC Advances **2** *(11, 2012) 12812–12817.*

[197] *G. Menzildjian, A. Lund, M. Yulikov, D. Gajan, L. Niccoli, G. Karthikeyan, G. Casano, G. Jeschke, O. Ouari, M. Lelli, and A. Lesage, Efficient Dynamic Nuclear Polarization up to 230 K with Hybrid BDPA-Nitroxide Radicals at a High Magnetic Field,* Journal of Physical Chemistry B **125** *(12, 2021) 13329–13338.*

[198] *T. Chakrabarty, N. Goldin, A. Feintuch, L. Houben, M. Leskes, T. Chakrabarty, N. Goldin, M. Leskes, A. Feintuch, L. Houben, and W. Vch, Paramagnetic Metal-Ion Dopants as Polarization Agents for Dynamic Nuclear Polarization NMR Spectroscopy in Inorganic Solids,* ChemPhysChem **19** *(9, 2018) 2139–2142.*

[199] *A. L. Paterson, F. A. Perras, M. F. Besser, and M. Pruski, Dynamic Nuclear Polarization of Metal-Doped Oxide Glasses: A Test of the Generality of Paramagnetic Metal Polarizing Agents,* Journal of Physical Chemistry C **124** *(10, 2020) 23126–23133.*

[200] *M. Kaushik, T. Bahrenberg, T. V. Can, M. A. Caporini, R. Silvers, J. Heiliger, A. A. Smith, H. Schwalbe, R. G. Griffin, and B. Corzilius, Gd(III) and Mn(II) complexes for dynamic nuclear polarization: small molecular chelate polarizing agents and applications with site-directed spin labeling of proteins,* Physical Chemistry Chemical Physics **18** *(10, 2016) 27205–27218.*

[201] *B. Corzilius, V. K. Michaelis, S. A. Penzel, E. Ravera, A. A. Smith, C. Luchinat, and R. G. Griffin, Dynamic nuclear polarization of 1H, 13C, and 59Co in a tris(ethylenediamine)cobalt(III) crystalline lattice doped with Cr(III),* Journal of the American Chemical Society **136** *(8, 2014) 11716–11727.*

[202] *S. K. Jain, C. J. Yu, C. B. Wilson, T. Tabassum, D. E. Freedman, and S. Han, Dynamic Nuclear Polarization with Vanadium(IV) Metal Centers,* Chem **7** *(2, 2021) 421–435.*

[203] *A. Harchol, G. Reuveni, V. Ri, B. Thomas, R. Carmieli, R. H. Herber, C. Kim, and M. Leskes, Endogenous Dynamic Nuclear Polarization for Sensitivity Enhancement in Solid-State NMR of Electrode Materials,* Journal of Physical Chemistry C **124** *(4, 2020) 7082–7090.*

[204] *N. Gallagher, H. Zhang, T. Junghoefer, E. Giangrisostomi, R. Ovsyannikov, M. Pink, S. Rajca, M. B. Casu, and A. Rajca, Thermally and Magnetically Robust Triplet Ground State Diradical,* Journal of the American Chemical Society **141** *(3, 2019) 4764–4774.*

[205] *C. Shu, M. Pink, T. Junghoefer, E. Nadler, S. Rajca, M. B. Casu, and A. Rajca, Synthesis and Thin Films of Thermally Robust Quartet (S = 3/2) Ground State Triradical,* Journal of the American Chemical Society **143** *(4, 2021) 5508–5518.*

[206] A. Narayanan, J. S. Hartman, and A. D. Bain, Characterizing Nonexponential Spin-Lattice Relaxation in Solid-State NMR by Fitting to the Stretched Exponential, Journal of Magnetic Resonance, Series A **112** *(1, 1995) 58–65.*

[207] A. Zagdoun, A. J. Rossini, M. P. Conley, W. R. Grüning, M. Schwarzwälder, M. Lelli, W. T. Franks, H. Oschkinat, C. Copéret, L. Emsley, and A. Lesage, Improved Dynamic Nuclear Polarization Surface-Enhanced NMR Spectroscopy through Controlled Incorporation of Deuterated Functional Groups, Angewandte Chemie International Edition **52** *(1, 2013) 1222–1225.*

[208] A. Gennaro, A. Karabanov, A. Potapov, and W. Köckenberger, Heteronuclear DNP of 1H and 19F nuclei using BDPA as a polarizing agent, Physical Chemistry Chemical Physics **22** *(4, 2020) 7803–7816.*

[209] L. Delage-Laurin, R. S. Palani, N. Golota, M. Mardini, Y. Ouyang, K. O. Tan, T. M. Swager, and R. G. Griffin, Overhauser Dynamic Nuclear Polarization with Selectively Deuterated BDPA Radicals, Journal of the American Chemical Society **143** *(12, 2021) 20281–20290.*

[210] S. Mandal and S. T. Sigurdsson, On the Limited Stability of BDPA Radicals, Chemistry – A European Journal **26** *(6, 2020) 7486–7491.*

[211] K. N. Hu, C. Song, H. H. Yu, T. M. Swager, and R. G. Griffin, High-frequency dynamic nuclear polarization using biradicals: A multifrequency EPR lineshape analysis, Journal of Chemical Physics **128** *(2, 2008) 052302.*

[212] S. Grimme, S. Ehrlich, and L. Goerigk, Effect of the damping function in dispersion corrected density functional theory, Journal of Computational Chemistry **32** *(5, 2011) 1456–1465.*

[213] K. R. Thurber and R. Tycko, Biomolecular solid state NMR with magic-angle spinning at 25 K, Journal of magnetic resonance (San Diego, Calif. : 1997) **195** *(12, 2008) 179.*

[214] Y. Matsuki, T. Idehara, J. Fukazawa, and T. Fujiwara, Advanced instrumentation for DNP-enhanced MAS NMR for higher magnetic fields and lower temperatures, Journal of magnetic resonance (San Diego, Calif. : 1997) **264** *(3, 2016) 107–115.*

[215] F. D. Doty, Guide to simulating complex NMR probe circuits, Concepts in Magnetic Resonance Part A: Bridging Education and Research **47A** *(3, 2018) e21463.*

[216] E. K. Paulson, R. W. Martin, and K. W. Zilm, Cross polarization, radio frequency field homogeneity, and circuit balancing in high field solid state NMR probes, Journal of Magnetic Resonance **171** *(12, 2004) 314–323.*

[217] L. C. Maier and J. C. Slater, Field Strength Measurements in Resonant Cavities, Journal of Applied Physics **23** *(6, 2004) 68.*

[218] M. S. Choe, K. H. Kim, and E. Choi, A comprehensive analysis of a TE ¡sub¿11¡/sub¿ to HE ¡sub¿11¡/sub¿ mode converter for an oversized F-band corrugated waveguide, Journal of Electromagnetic Waves and Applications **27** *(11, 2013) 2221–2238.*

[219] T. Manfred, A. Jacobs, and M. S. Ayza, Design of Short High-Power Te11-He11 Mode Converters in Highly Overmoded Corrugated Waveguides, IEEE Transactions on Microwave Theory and Techniques **39** *(1991), no. 2 301–309.*

[220] Y. Oh, V. Bharambe, B. Mummareddy, J. Martin, J. McKnight, M. A. Abraham, J. M. Walker, K. Rogers, B. Conner, P. Cortes, E. MacDonald, and J. J. Adams, Microwave dielectric properties of zirconia fabricated using NanoParticle Jetting™, Additive Manufacturing **27** *(5, 2019) 586–594.*